Quantum transport in magnetic topological insulators

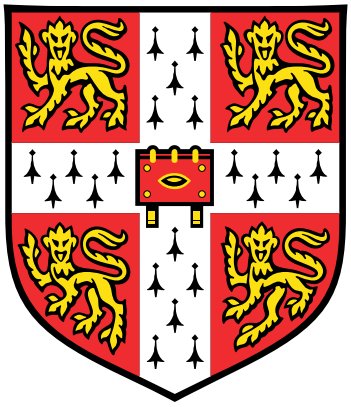

Shu-Wei Wang

Department of Physics
University of Cambridge

This dissertation is submitted for the degree of
Doctor of Philosophy

Queens' College

November 2019

Declaration

I hereby declare that except where specific reference is made to the work of others, the contents of this dissertation are original and have not been submitted in whole or in part for consideration for any other degree or qualification in this, or any other university. This dissertation is my own work and contains nothing which is the outcome of work done in collaboration with others, except as specified in the text and Acknowledgements. This dissertation contains fewer than 60,000 words including appendices, bibliography, footnotes, tables and equations and has fewer than 150 figures.

Shu-Wei Wang
November 2019

Acknowledgements

The process of doing a Ph.D. degree is usually full of challenge, and sometimes can be frustrating. However, no matter how hard the time is, when I remind myself how privileged I am to be able to work with the outstanding people in the world-renowned Cavendish Lab, I feel everything is worth it.

This thesis cannot be completed without the help and support from many people. First of all, I would like to express my immense gratitude to my supervisor Charles Smith, for giving me the opportunity to study in such an amazing institute. Charles seems to have an incredible ability that he always can find the resources I need for research and my personal life. He was extremely patient in our every discussion and gave me countless inspiring advice when I was stuck by the problems in my experiments. I also appreciate that he gave me a huge freedom to work independently and let me design experiments to test my own ideas these years. I learnt a lot from him not only in terms of physics, but also the attitude as a scientist. I owe a great deal to Charles and his kindness.

I am also grateful to Malcolm, who introduced a lot of interesting research to me in the early years of my Ph.D. and encouraged me to choose magnetic topological insulators as the topic of my thesis. Without him, I probably dared not choose such a challenging topic for my Ph.D. study. The very useful measurement and presentation skills he taught me when I just started my Ph.D. still benefit me in many ways today.

I was fortunate to have the sample supply from Dr. Cui-Zu Chang and Dr. Di Xiao at the Pennsylvania State University. They have always been very responsive and supportive in our collaboration. My Ph.D. research is impossible to be done without their help.

I would like to thank my colleagues in the Cavendish Lab who helped me in different ways throughout these 4 years. I was impressed by the willingness of Prof. Chris Ford on helping students. More than once he spent hours to help me solve CryoMeas problems like I was his student. Joanna is one of the most generous and reliable people I have seen. She is the kind of experienced scientist that every student wants to work with. Luke kindly helped me proofread my draft and gave me very useful suggestions that greatly improved the quality of the thesis. Huw and Berry at the electronic workshop customised many electronics for me, which was a tremendous help for my experiments. I also want to express my appreciation

to the staff at Mott hub and technicians of the cleanroom and gas liquefiers for constantly supporting the research in the Cavendish Lab.

Thanks to Gulzat, Jinggao, Yuqing, Hangtian, Tzu-Kan, Teng and Chong for the chats and jokes over the coffee breaks and meals. Thanks to Moda who was so careful and patient when helping me with my experiments at Fridge1. Moreover, I really enjoyed the time hunting with Vivek and Wooi Kiat. It was fun and always could relax my nerves from the hard work. Special thanks go to my best comrade, Ziwei, who gave me lots of useful suggestions for my experiments. I guess he is one of the last few people on earth who can understand the mysterious problems I have encountered when using OX1 and LSM.

I also would like to acknowledge the financial support from the Cambridge Overseas Trust, Semiconductor Physics Group, and Taiwanese Government that made my Ph.D. study in Cambridge possible.

In addition, I have to mention my good friends from the Cambridge Taiwanese Society. The events they organised and the food they prepared sometimes gave me an illusion that I was still in Taiwan. My life in U.K. was much enjoyable with their company.

Finally, I would like to thank my dearest parents, who always encourage me to pursue the life I want and provide me with unconditional support. Thanks to my sister, Yi-Ying, who is so optimistic and keeps sharing her positive energy with me. I also would like to thank my wife, Hui-Ru, who knows all the ups and downs in my Ph.D. and supports me, no matter what. I am blessed to have you all as my family.

Abstract

This thesis is focused on the study of carrier transport behaviour in magnetically doped topological insulator (TI) materials. Magnetic TIs have been predicted to possess many exotic properties, such as the quantum anomalous Hall (QAH) effect, in which the edge states propagate adiabatically, similar to the quantum Hall effect, but without the need of an external magnetic field. In addition to the potential of being used for low-dissipation power transmission and for metrology as a resistance standard, the QAH effect also allows the exploration of a variety of new physics. However, it has been observed that dissipation mechanisms, which theoretically should be absent in the QAH effect, still exist in real measurements and impede the application of the QAH effect on further studies. Thus, this thesis presents the experiments designed to investigate the nature of dissipation in the QAH effect and discusses the possible ways to improve the QAH effect for future experiments.

The first part of the thesis introduces the study of the magnetic and electric properties of V-doped $(Bi,Sb)_2Te_3$ films. Transport measurements and various scanning probe microscopy (SPM) techniques are employed to probe the relation between magnetic domain structures and carrier transport behaviour in the samples during the QAH phase transition as well as in the QAH regime. Patch-like structures ranging from several hundred nanometers to 2 μm with a stray magnetic field strength lower than 1 G are observed in the magnetic images, which may originate from the domains of the magnetic TI films. The activation energy extracted from Arrhenius plots of longitudinal resistance versus temperature is ~ 4 μeV (i.e. ~ 47 mK). Such a small energy scale implies that the Fermi level is far away from the centre of the magnetic gap and the bulk conduction may dominate the transport. Thermal effects arising from the complicated interplay between the electronic and spin system in our samples are observed and the possible origins of them are discussed.

The second part of the thesis is dedicated to the study of transport properties of a Cr-doped $(Bi,Sb)_2Te_3$ sandwich heterostructure. The QAH effect with a non-vanishing longitudinal resistance $\sim 0.0667\ h/e^2$ is observed, suggesting the presence of dissipative conducting channels in the sample. By multi-terminal measurements, we verify the existence of non-chiral edge states. A possible candidate of these non-chiral edge states is the quasi-helical states on the side surface of the sample that become dissipative due to the broken time-

reversal symmetry. It is shown that the backscatterings of these quasi-helical states have a magnetic field dependence and contribute to the dissipation in parallel with the residual surface and bulk states. A theoretical model is employed to understand the interactions between different kind of conducting channels. Based on this model, we speculate that a transition between different dominant dissipation mechanisms in the QAH effect occurs at a transition field $H^* \sim 2.5$ T at the base temperature, which suggests a mean free path ~ 20 nm in this Cr-doped $(Bi,Sb)_2Te_3$ sample. The activation energy exhibits a magnetic field dependence as well, ranging from 35.0 μeV at $\mu_0 H = 0$ T to 16.2 μeV at $\mu_0 H = \pm 5$ T, which agrees with the transition behaviour observed at H^* and indicates that it may also result from the shift between different dominant dissipation mechanisms in the QAH regime. The magnetic gap of the sample is estimated to be at least larger than 43.7 μeV. Moreover, H^* is found to have a temperature dependence, which is probably due to the increasing number of diffusive conducting states at higher temperatures according to our analysis. Finally, we demonstrate that the electron temperature can differ from the sample temperature due to Joule heating at millikelvin temperatures. The inferred electron temperature is found to be proportional to the source-drain current in our measurements. Because so far the QAH effect can only be observed at millikelvin temperatures and Joule heating should always play an important role in this regime, the relation obtained in our experiments will be useful for future studies on the QAH effect.

Table of contents

List of figures

List of tables

Nomenclature

Physics constants

e	Elementary charge
h	Planck constant
$\hbar$	$\frac{h}{2\pi}$
π	$\simeq 3.14159265359\ldots$

Acronyms / Abbreviations

1D	One-dimensional
2D	Two-dimensional
2DES	Two-dimensional electron system
3D	Three-dimensional
AFM	Atomic force microscopy
BST	Bismuth antimony telluride
Cr-BST	Chromium-doped bismuth antimony telluride
DOS	Density of states
EFM	Electrostatic force microscopy
KPM	Kelvin probe microscopy
MFM	Magnetic force microscopy
PLL	Phase-locked loop

QAHE Quantum anomalous Hall effect

QAH Quantum anomalous Hall

QHE Quantum Hall effect

QH Quantum Hall

QSHE Quantum spin Hall effect

QSH Quantum spin Hall

SGM Scanning gate microscopy

SHPM Scanning Hall probe microscopy

SOC Spin-orbit coupling

SPM Scanning probe microscopy

TI Topological insulator

V-BST Vanadium-doped bismuth antimony telluride

ZF Zero-field

Chapter 1

Introduction

1.1 Motivation of the study

Modern civilisation relies heavily on electronics. Mobile phones, internet, personal computers, and all sorts of electronic applications have become an indispensable part in our everyday life. One important issue that scientists and engineers always want to overcome is the heat dissipation in electrical and electronic devices. Heat dissipation is caused by the energy loss of electrons due to their collisions with the atoms of the lattice while travelling in the power cables or the leads on the circuit boards. This heat dissipation can give rise to two major problems. The first one is overheating that can lead to malfunction of instruments or even safety hazard for life. Hence the cooling mechanism of the electrical and electronic devices must be carefully designed to ensure the heat generated can be removed from the system fast enough to maintain the working temperature of the devices. The second problem is energy waste in the power transmission process. After electricity is generated by power plants, it usually has to run in a transmission line for a long distance before reaching the mains power socket in an office or room. A significant portion of electrical energy can be lost during this transmission process due to the scattering between electrons and lattice, and turn into thermal energy that just dissipates into surroundings as waste heat, lowering the efficiency of power transmission. This is not only a waste of energy, but also increases the cost of electricity generation.

One possible solution appeared after superconductivity was discovered by Dutch physicist Heike Kamerlingh Onnes in 1911. In a superconductor, the electrons can travel through the lattice in the absence of scattering with the lattice, resulting in vanishing electrical resistance and thus zero energy dissipation. Since this discovery, scientists have found many materials that possess superconductivity. However, superconductivity only occurs when materials are below the superconducting critical temperatures that are usually lower than 200

K ($\sim -73.15\,^{\circ}$C). To date, finding new materials with higher critical temperatures and the conditions that can elevate the critical temperatures remains one of the biggest challenges in condensed matter physics.

Interestingly, quantum mechanics provides more than one possibility for the electrons to be free from backscattering in macroscopic transport that results in heat dissipation. In 1980, Klaus von Klitzing made the groundbreaking discovery of quantum Hall effect (QHE) [1]. As we shall see in more detail in Chapter 2, when the two-dimensional electron system (2DES) is in the plateau regime of quantum Hall state, only the electrons at the physical edges of the device will be able to conduct charges. These edge states cannot be backscattered and hence the longitudinal resistance of the 2DES drops to zero. This vanishing resistance has a different origin to the superconductors but is another way to realise dissipationless conduction. However, like superconductors, achieving the QHE also requires special conditions, typically a cryogenic environment with a large external magnetic field. Although the QHE has been observed at room temperature on graphene [2], the magnetic field needed is higher than 25 T, which is roughly 1,000,000 times of the geomagnetic field [3]. It is impractical to apply such a high magnetic field in the electronic devices used in everyday life.

To this end, it seems the QHE is again not a viable solution for low dissipation power transmission. Luckily, this is not the end of the story. Topology comes into play here and offers another hope. As we will see in Chapter 3, an effect that resembles the QHE can be obtained in strong spin-orbit coupling (SOC) materials with ferromagnetic order even in the absence of an external magnetic field. This effect is called the quantum anomalous Hall effect (QAHE), and the material with strong SOC that can satisfy the above conditions is called a topological insulator (TI). The TI is a new class of matter and was experimentally realised in 2007 for the first time [4]. It has a unique electronic band structure that makes the interior of the material insulating, while the surface is conducting. When the TI is doped with magnetic elements, ferromagnetism can be induced in the material and, under appropriate conditions, leads to the observation of the QAHE.

In an ideal QAHE, only the dissipationless boundary states can carry electrical current and there should be no backscattering. However, dissipation can still be observed in terms of finite longitudinal resistance in real experiments, suggesting that some kind of dissipative states conduct in parallel with the dissipationless states. Such a problem can tremendously undermine the utility of the QAHE in applications.

What is the origin of these dissipative states? How do they interact with each other and the dissipationless states? How can we reduce the unwanted dissipation and achieve better QAHE? These are the questions that this thesis tries to answer.

1.2 Thesis outline

In this thesis, some basic transport models and theories in mesoscopic physics are introduced in Chapter 2. The theories about topological orders in matter and experimental discoveries on these topological phases are then reviewed in Chapter 3. The experimental techniques used in this thesis are described in Chapter 4. In Chapter 5, the transport and scanning probe microscopy (SPM) experiments carried out on the magnetic topological insulators V-doped $(Bi,Sb)_2Te_3$ are presented and discussed. Chapter 6 contains the results and analyses of the transport measurements on a Cr-doped $(Bi,Sb)_2Te_3$ heterostructure. Finally, Chapter 7 concludes the results in this thesis and provides some ideas for the future work.

Chapter 2

Transport theory

2.1 Drude model

In 1900, Paul Drude proposed a model to describe the transport of electrons in materials, which was later called the Drude model [5]. The Drude model simplifies the behaviour of electrons in a solid by ignoring the long-range electron-electron interaction and electron-ion interaction during the propagation. Conducting electrons are treated like an ideal gas drifting in the background of ions that are much heavier than the electrons. When an electron collides with the ions, it will be scattered and move in a straight line between collisions, while the ions are assumed to remain still after the collisions.

In the Drude model, the equation of motion of electrons travelling in a velocity $\mathbf{v}$ can be written as

$$m\frac{\mathrm{d}\mathbf{v}}{\mathrm{d}t} = -e\mathbf{E} - e\mathbf{v}\times\mathbf{B} - \frac{m\mathbf{v}}{\tau}, \tag{2.1}$$

where $\mathbf{E}$ is the external electric field, $\mathbf{B}$ is the external magnetic field, e is the elementary charge, $\mathbf{v}$ is the velocity of electrons, and τ is the mean free time between collisions.

When the system is in equilibrium, $\mathrm{d}\mathbf{v}/\mathrm{d}t = 0$ and Eq. 2.1 becomes

$$-\frac{e\tau}{m}\mathbf{E} = \mathbf{v} + \frac{e\tau}{m}\mathbf{v}\times\mathbf{B}. \tag{2.2}$$

Let us first consider the case without a magnetic field. Then Eq. 2.2 can be reduced to

$$-\frac{e\tau}{m}\mathbf{E} = \mathbf{v}. \tag{2.3}$$

Since the current density of electrons driven by an external electric field can be expressed as

$$\mathbf{J} = -ne\mathbf{v}, \tag{2.4}$$

where n is the concentration of conducting electrons, we can substitute Eq. 2.4 into Eq. 2.3 and obtain

$$\mathbf{J} = \frac{ne^2\tau}{m}\mathbf{E}. \tag{2.5}$$

Eq. 2.5 describes the relation between the electric field $\mathbf{E}$ and current density $\mathbf{J}$, similar to the Ohm's law

$$J = \sigma E, \tag{2.6}$$

where σ is defined as the electrical conductivity. Hence, we can write the conductivity as

$$\sigma = \frac{ne^2\tau}{m} \equiv ne\mu, \tag{2.7}$$

where

$$\mu = \frac{e\tau}{m} \tag{2.8}$$

is the electron mobility, which characterises how quickly an electron can move in a material under an applied electric field.

Now, let us consider the situation in the presence of a magnetic field. By substituting Eq. 2.4 into Eq. 2.2, we obtain

$$\frac{ne^2\tau}{m}\mathbf{E} = \begin{pmatrix} 1 & \omega_c\tau \\ -\omega_c\tau & 1 \end{pmatrix}\mathbf{J}, \tag{2.9}$$

where $\omega_c = eB/m$ is the cyclotron frequency. Again, we can rearrange Eq. 2.9 into

$$\mathbf{J} = \frac{1}{1+(\omega_c\tau)^2}\begin{pmatrix} 1 & -\omega_c\tau \\ \omega_c\tau & 1 \end{pmatrix}\frac{ne^2\tau}{m}\mathbf{E} \tag{2.10}$$

to compare with the Ohm's law. It can be seen that the electrical conductivity under a magnetic field becomes a tensor, which can be written as

$$\boldsymbol{\sigma}_\mathbf{B} = \frac{\sigma}{1+(\omega_c\tau)^2}\begin{pmatrix} 1 & -\omega_c\tau \\ \omega_c\tau & 1 \end{pmatrix} \equiv \begin{pmatrix} \sigma_{xx} & \sigma_{xy} \\ \sigma_{yx} & \sigma_{yy} \end{pmatrix}. \tag{2.11}$$

In a homogeneous and isotropic substance $\sigma_{xx} = \sigma_{yy}$ and $\sigma_{xy} = -\sigma_{yx}$. Thus, we can rewrite Eq. 2.10 as

$$\begin{pmatrix} J_x \\ J_y \end{pmatrix} = \begin{pmatrix} \sigma_{xx} & \sigma_{xy} \\ -\sigma_{xy} & \sigma_{xx} \end{pmatrix}\begin{pmatrix} E_x \\ E_y \end{pmatrix}. \tag{2.12}$$

If the current only flows in the x-direction (i.e. $J_y = 0$), we have $E_x/E_y = \sigma_{xx}/\sigma_{xy}$, which can be substituted back into Eq. 2.12 to calculate the resistivity as

$$\begin{aligned} \rho_{xx} &\equiv \frac{E_x}{j_x} = \frac{\sigma_{xx}}{\sigma_{xx}^2 + \sigma_{xy}^2}, \\ \rho_{xy} &\equiv \frac{E_y}{j_x} = \frac{\sigma_{xy}}{\sigma_{xx}^2 + \sigma_{xy}^2}. \end{aligned} \tag{2.13}$$

Since in practice the physical quantity measured in experiments is usually the resistance or resistivity rather than the conductance or conductivity, Eq. 2.13 is useful for the conversion between the experimental observables and the intrinsic property of materials in real magnetotransport measurements.

2.2 Landauer-Büttiker formalism

In 1957, Rolf Landauer proposed a formula that can describe the relation between the electrical conductance and the scattering properties of a 1D system in a two-terminal configuration [6]. The Landauer formula was later generalised to multi-terminal configurations by Markus Büttiker, which then became the so-called Landauer-Büttiker formalism [7, 8]. In this section, we will briefly introduce the principle of the Landauer-Büttiker formalism and how to implement it in data analysis.

Considering a device with a Hall bar geometry that is widely used in transport measurements, as shown in Fig. 2.1. On each terminal there is a metallic electrode that can be regarded as an electron reservoir with an effectively infinite number of degrees of freedom, and electrons will lose their phase coherence once they enter these metallic electrodes. If the chemical potential of the electrode i is μ_i, the Landauer-Büttiker formalism gives

$$I_i = N\frac{e}{h}\sum_j (T_{ij}\mu_i - T_{ji}\mu_j), \tag{2.14}$$

where I_i is the current passing through electrode i, N is the number of conducting channels, and T_{ij} is the transmission probability of the states going from the ith to jth electrodes. The matrix T_{ij} contains the scattering information for the device, and hence Eq. 2.14 allows us to calculate the resistance of different measurement configurations without dealing with complicated parameters.

In reality, transport measurements are usually performed by applying a constant current source and measuring the voltage drop between contacts, therefore a more common form of

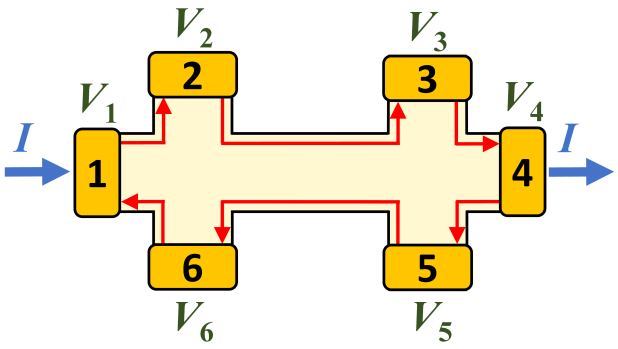

Figure 2.1: An example of the Landauer-Büttiker formalism for a Hall bar device with metallic electrodes on its six terminals. The voltage on electrode i is V_i, and the current flowing into/out of electrode i is I_i. When a bias V is applied on electrode 1 and grounded at electrode 4, the current flows into the device from electrode 1 and leaves the device from electrode 4. Furthermore, we assume there is only one channel travelling in the clockwise direction along the edge of the device to simplify the calculation, as indicated by the red arrows.

the Landauer-Büttiker formalism is

$$I_i = N\frac{e^2}{h}\sum_j (T_{ij}V_i - T_{ji}V_j), \tag{2.15}$$

where $V_i = \mu_i/e$.

Ideally, the electrodes used as voltage probes have no net current flow in/out, hence $I_i = 0$ for the voltage probes. On the other hand, the source electrode has a voltage $V_i \neq 0$ and a current $I_i \neq 0$, while the drain electrode has a voltage of zero and a current that equals the negative value of the current at the source electrode.

A simple example is illustrated as follows. As shown in Fig. 2.1, when a bias V is applied on electrode 1 and grounded at electrode 4, current should flow into the device from electrode 1 and leave the device from electrode 4. Thus, we have $V_1 = V$, $V_4 = 0$, $I_1 = -I_4 \neq 0$ and $I_2 = I_3 = I_5 = I_6 = 0$. Assuming that there is only one channel travelling in the clockwise direction along the edge of the device, then $N = 1$ and $T_{i,i+1} = 1$, with all other $T_{ij} = 0$. With these conditions, the Landauer-Büttiker formalism can be written as

$$\begin{pmatrix} I_1 \\ 0 \\ 0 \\ I_4 \\ 0 \\ 0 \end{pmatrix} = \frac{e^2}{h} \begin{pmatrix} 1 & 0 & 0 & 0 & 0 & -1 \\ -1 & 1 & 0 & 0 & 0 & 0 \\ 0 & -1 & 1 & 0 & 0 & 0 \\ 0 & 0 & -1 & 1 & 0 & 0 \\ 0 & 0 & 0 & -1 & 1 & 0 \\ 0 & 0 & 0 & 0 & -1 & 1 \end{pmatrix} \begin{pmatrix} V \\ V_2 \\ V_3 \\ 0 \\ V_5 \\ V_6 \end{pmatrix}. \tag{2.16}$$

By solving the equations, we can obtain the relations

$$\begin{aligned} V_1 =& V_2 = V_3 = V \\ V_4 =& V_5 = V_6 = 0 \\ I_1 =& \frac{e^2}{h} V \\ I_4 =& \frac{-e^2}{h} V, \end{aligned} \tag{2.17}$$

which in turn enables us to calculate the resistance between different contact combinations.

Although the example above seems a bit unrealistic, it is actually a case that can occur in the QHE, as will be discussed in Chapter 3. Therefore, the Landauer-Büttiker formalism is an extremely important tool for the description of ballistic transport in low-dimensional systems, such as quantum point contacts and the edge conduction in the QHE, and will be frequently used in the later discussions.

Chapter 3

Topological order

3.1 Introduction

The term topology originates from a branch of mathematics that studies the properties of objects under deformation. The deformation can either be continuous or discontinuous. For example, a continuous deformation can be the extension, contraction, or distortion of an object. In contrast, a discontinuous change may be carving a hole on an object, breaking an object into multiple parts, or gluing multiple objects together. If an object can be continuously transformed from shape A to shape B, then A and B can be categorised into the same topological class. The topological class of an object can be classified by a number g representing its topological genus. Some good examples illustrating this concept can be found in a café. A doughnut and a coffee cup, despite how different they look, belong to the same topological genus, $g = 1$, because they both have one hole. A pretzel has three holes and hence is in a different topological genus $g = 3$. An apple or banana has no hole and should be categorised into yet another different topological genus $g = 0$ (see Fig. 3.1). The topological properties have nothing to do with the geometric shapes, colours or the materials of the object, but solely depend on the number of holes on the object.

The question that may arise at this point is why and how the concept of topology is introduced into physics. The answer is related to the development of the theory of phase transition. Before 1970s, the mainstream theory for explaining phase transition phenomena was Landau's theory [9], in which every phase transition implies that an underlying symmetry of matter is broken. This theory predicts that a 2D crystal is thermodynamically unstable at any finite temperature because of the thermal fluctuation in the atomic scale [9, 10]. Since there is no stable ordered phase, there should also be no symmetry breaking, and thus no phase transition. However, the 2D XY model proposed by John Kosterlitz and David Thouless in 1973 shows that a phase transition is possible in a 2D magnetic system at finite

(a) (b) (c) (d)

Figure 3.1: Examples of different topological genera. (a) A doughnut and (b) a coffee cup both have one hole and thus belong to the same topological genus $g = 1$. (c) A pretzel with three holes belongs to $g = 3$. (d) A banana or an apple is $g = 0$.

temperatures, which is now called the Kosterlitz–Thouless transition (K-T transition) [11]. They find that a non-zero integer changes its value when the K-T transition occurs. This is similar to the change of the topological number of an object in topology when its topological property is changed. The subtle connection between topology and the phases of matter started to be noticed by scientists from this point.

In 1980, Klaus von Klitzing observed the quantum Hall effect (QHE), in which the Hall conductance of a two-dimensional electron system (2DES) is quantised to the value of (ne^2/h) in a strong magnetic field [1], where n is an integer. The discovery of QHE was striking to physicists and could not be explained by Landau's symmetry breaking theory. In 1982, Thouless, Kohomoto, Nightingale and den Nijs (referred to as TKNN hereafter) introduced the concept of topology to explain the QHE and successfully obtained the quantised conductance [12] from the theoretical perspective. It turns out that the integer n corresponds to the Chern number C in the Gauss-Bonnet theory in topology. Nevertheless, the relation between topology and the QHE was still not clear at that point, so n was given another name called the TKNN number, describing the number of edge modes in the QHE, e.g. $n = 1$ means there is one edge state propagating along the sample edge, $n = 2$ means there are two edge states, and so on. Nowadays the Chern numbers are also called $\mathbb{Z}$ topological invariants (where $\mathbb{Z}$ stands for the group of integers), that can be used to characterise the topological properties of an electron's wave function.

With the successful explanation of the mechanism of the QHE using topology, more and more physicists started to explore the relation between topology and the phases of matter. Additional topological properties of different phases and phase transitions are thus further investigated since then.

In 2005, Charles Kane and Eugene Mele suggested that the Haldane model [13] can be realised in graphene by its intrinsic spin-orbit coupling (SOC), which can break the

time-reversal symmetry of the 2DES and lead to quantised Hall resistance, like the QHE [14, 15]. However, this effect is not exactly the same as the ordinary QHE because the influence of spins to the system must be taken into account. Therefore, this effect is named the quantum spin Hall effect (QSHE). Moreover, when considering both the spin-up and spin-down electrons in the system, the outcome is a system with time-reversal symmetry. Clearly, this effect has a different symmetry than the QHE (in which the time-reversal symmetry is broken by the external magnetic field) and hence should belong to a different topological class. Compared to the $\mathbb{Z}$ topological invariants that TKNN used in their theory for the QHE, Kane and Mele suggested that the QSHE should be described by a new topological order - $\mathbb{Z}_2$ topological invariants. The $\mathbb{Z}_2$ topological invariants are in a different category to the $\mathbb{Z}$ topological invariants in topology, implying that the phase characterised by $\mathbb{Z}_2$ topological invariants is a new phase of matter. In 2007, Laurens Molenkamp's group experimentally realised the first $\mathbb{Z}_2$ phase with HgTe/CdTe quantum well and observed the QSHE [4].

The next thing scientists want to know is whether the QSHE can be observed in a 3D system, i.e. can the $\mathbb{Z}_2$ phase be realised in 3D systems. In the 2D case, $\mathbb{Z}_2$ has only two possibilities, either an even number or an odd number. While the system is just an ordinary insulator without any propagating states when $\mathbb{Z}_2$ is an even number, edge states are allowed to exist in the system if $\mathbb{Z}_2$ is an odd number. In the 3D case, however, $\mathbb{Z}_2$ can have more than two possibilities [16–19], and thus the 3D case is regarded as a different phase to the 2D one. The 3D case of $\mathbb{Z}_2$ phase is then named the topological insulator (TI) [17]. Shortly after the theoretical prediction, the TI phase was also experimentally realised in a bismuth antimony alloy in 2008 [20].

It turns out that if a system has non-zero Chern numbers, it can show an effect similar to the QHE, no matter how it is achieved (e.g. with or without an external magnetic field). Therefore, to discriminate the systems with non-zero Chern numbers $\mathcal{C}$ from the "trivial" insulators ($\mathcal{C} = 0$), these systems are categorised as Chern insulators.

From the brief history above, we can see that the QHE plays an important role in the discovery and development of the study of topological phases. Therefore, we will have a short review of the theory of the QHE in the next section and bring in some ideas for the introduction of TIs later in this chapter.

3.2 Quantum Hall effect

3.2.1 Hall effect

In 1879, Edwin Hall found that when applying a magnetic field perpendicular to the direction of the electric current in a conductor, a voltage difference transverse to the flow of current and perpendicular to the magnetic field direction can be generated across the conductor [21]. This effect is known as the Hall effect, and the voltage across the conductor is called the Hall voltage.

Consider a 2DES with the shape of a "Hall bar" with length L and width W as shown in Fig. 3.2. An electric current I in the x-direction is passed from electrode 1 to electrode 4, and an external magnetic field B in the $+z$-direction is applied on the 2DES. The moving electrons will experience a Lorentz force F_m in the $-y$-direction and turn toward the lower edge. As a result, negative charges start to accumulate at the lower edge and create an electric field E_y pointing from the lower edge to upper edge. This electric field leads to an electrostatic force in the opposite direction of the Lorentz force. When the accumulation of the charge reaches the point that the Coulomb force F_e generated by this transverse electric field E_y is equivalent to the Lorentz force caused by the out-of-plane magnetic field B, the trajectories of electrons become straight again and the system is in equilibrium.

In the equilibrium state, F_e equals to F_m, i.e.

$$eE_y = evB. \tag{3.1}$$

From the Drude model, we know $j = nev$. In the 2DES shown in Fig. 3.2, j is the 2D current density I/W. Thus, the Hall voltage becomes

$$V_{xy} = E_y W = \frac{IB}{ne} \tag{3.2}$$

and hence the Hall resistance is

$$R_{xy} = \frac{B}{ne}. \tag{3.3}$$

The longitudinal resistance R_{xx} can be obtained by

$$R_{xx} = \frac{V_{xx}}{I}, \tag{3.4}$$

where the V_{xx} is the voltage drop between electrode 2 and 3.

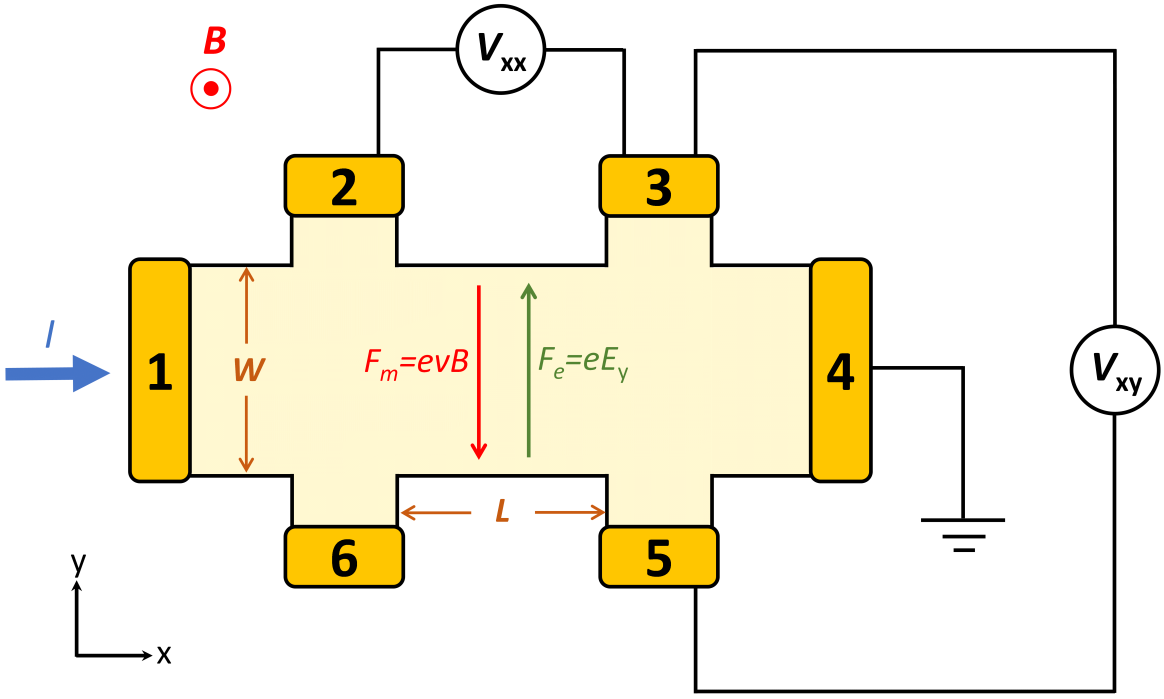

Figure 3.2: The Hall measurement setup. A current I enters the Hall bar device (with channel width W and length L) from the electrode 1 and leaves from electrode 4. A magnetic field B perpendicular to the plane of the device is applied and causes a Lorentz force F_m to the travelling electrons. The electrons then are deflected and accumulate at the lower edge, creating an electric field E_y and hence a Coulomb force F_e opposite to F_m. When F_e is equivalent to F_m, the electrons again move without deflection and the system reaches an equilibrium state. The longitudinal voltage drop V_{xx} can be obtained by measuring the voltage difference between electrode 2 and 3, while the Hall voltage V_{xy} is obtained by measuring the voltage difference between electrode 3 and 5.

With Eq. 3.3 and 3.4, the longitudinal resistivity ρ_{xx} and Hall resistivity ρ_{xy} can be obtained by

$$\begin{aligned} \rho_{xx} &\equiv \frac{E_x}{j_x} = \frac{R_{xx}}{\square} \\ \rho_{xy} &\equiv \frac{E_y}{j_x} = R_{xy}, \end{aligned} \tag{3.5}$$

where the $\square$ is the number of squares in the channel that the current flows through and can be determined by the aspect ratio of the channel L/W.

3.2.2 Semiclassical approach to the quantum Hall effect

In the Hall effect, the Hall voltage is generated by moving charge carriers deflected by the Lorentz force accumulating on one side of the Hall bar. The deflection of electron trajectories

will become larger if the applied magnetic field is further increased. When the magnetic field is sufficiently large, electrons in the interior of the Hall bar will move in closed orbits, as shown in Fig. 3.3. These electrons cannot carry current from the source to drain anymore and hence the bulk of the Hall bar becomes insulating. However, the electrons near the edge of the Hall bar can bounce off the edges and continue to travel in skipping orbits. Therefore, these edge states are one-way and must move in opposite directions at opposite edges. This leads to the chirality of edge states and results in the suppression of backscattering during transport.

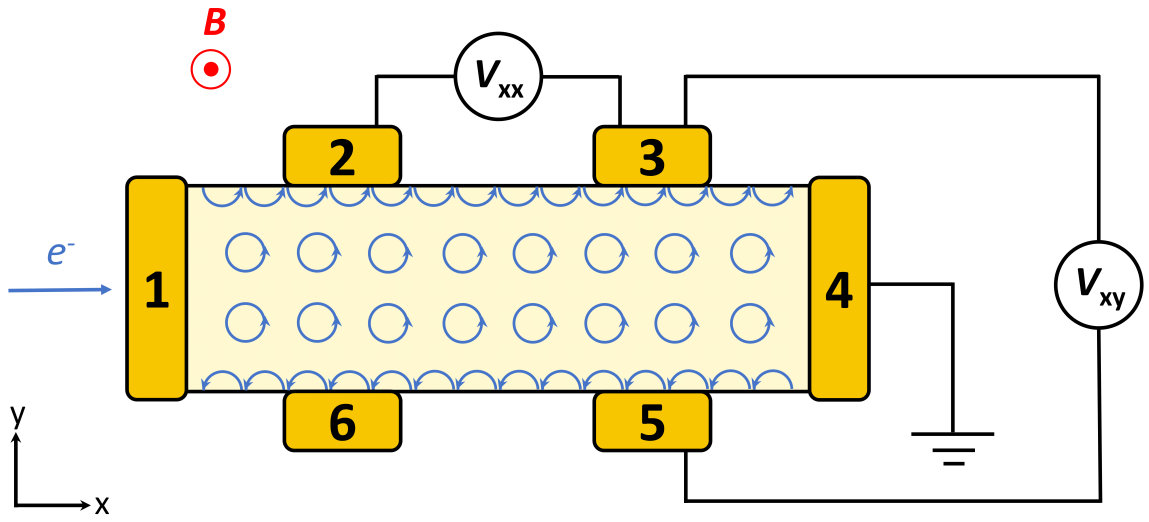

Figure 3.3: In a strong magnetic field, the charge carriers in the bulk of sample move in closed orbits and cannot conduct current from the source to drain. Charge carriers near the edges of the sample collide with the edges and move along the sample perimeter in skipping orbits. The travelling directions of these edge states are opposite at the opposite edges.

The conduction of edge states can be understood by the Landauer-Büttiker formalism [7, 8, 6, 22]

$$I_i = \frac{e^2}{h} \sum_j (T_{ij} V_i - T_{ji} V_j), \tag{3.6}$$

where the I_i is the current flowing through ith electrode, V_i is the voltage on ith electrode, and T_{ij} is the transmission probability of the states going from the ith to the jth electrodes. Thus, for a measurement setup like Fig 3.3, Eq. 3.6 allows us to write down the equation of each

electrode as

$$I_1 = \frac{e^2}{h}(T_{12}V_1 - T_{61}V_6) \tag{3.7}$$

$$I_2 = \frac{e^2}{h}(T_{23}V_2 - T_{12}V_1) \tag{3.8}$$

$$I_3 = \frac{e^2}{h}(T_{34}V_3 - T_{23}V_2) \tag{3.9}$$

$$I_4 = \frac{e^2}{h}(T_{45}V_4 - T_{34}V_3) \tag{3.10}$$

$$I_5 = \frac{e^2}{h}(T_{56}V_5 - T_{45}V_4) \tag{3.11}$$

$$I_6 = \frac{e^2}{h}(T_{61}V_6 - T_{56}V_5) \tag{3.12}$$

Now, there are several conditions that can be used to solve these equations. Firstly, the current is passed between the source and drain and there is no net current flowing on the voltage probes or floating electrodes. Secondly, the total current flowing through the system should be conserved. Therefore, we have $I_1 = I$, $I_4 = -I$, and $I_i = 0$ for all other probes. If the bias applied on electrode 1 is V, we have $V_1 = V$ and $V_4 = 0$. Finally, for chiral edge states, the transmission probability is given by $T_{i,i+1} = 1$ for i =1 to 6 (consider $i = 7$ as $i = 1$) and all other $T_{ij} = 0$. With these conditions, we then can solve the equations and obtain $V_1 = V_2 = V_3 = V$ and $V_4 = V_5 = V_6 = 0$. This implies that the chiral edge states do not lose energy before reaching the drain, and therefore we have

$$\rho_{xx} = \frac{V_3 - V_2}{I} = 0 \tag{3.13}$$

$$\rho_{xy} = \frac{V_3 - V_5}{I} = \frac{h}{e^2}. \tag{3.14}$$

Equation 3.13 and 3.14 suggest that the measured longitudinal resistance will be zero and the Hall resistance can be determined by a combination of physical constants, independent of the sample-specific details. Furthermore, it is immediately evident that the form of the Hall resistivity is similar to that of 1D transport in the quantum point contact. Therefore, the edge transport can be regarded as quasi-one-dimensional (quasi-1D), with n being the number of conducting chiral edge channels.

This is exactly what was discovered in von Klitzing's experiment in 1980 [1], in which a series of plateaux appeared in the Hall resistivity with the values $\rho_{xy} = h/ne^2$ while $\rho_{xx} = 0$ for integers n (Fig. 3.4). To date, the quantised Hall resistivity can be measured to the precision of one part in 10^9 [23], and such an accuracy makes the QHE an ideal way for defining the

international standard of resistance. The von Klitzing constant $R_K = h/e^2 = 25812.807...\ \Omega$ hence becomes the definition of a resistance quantum in metrology.

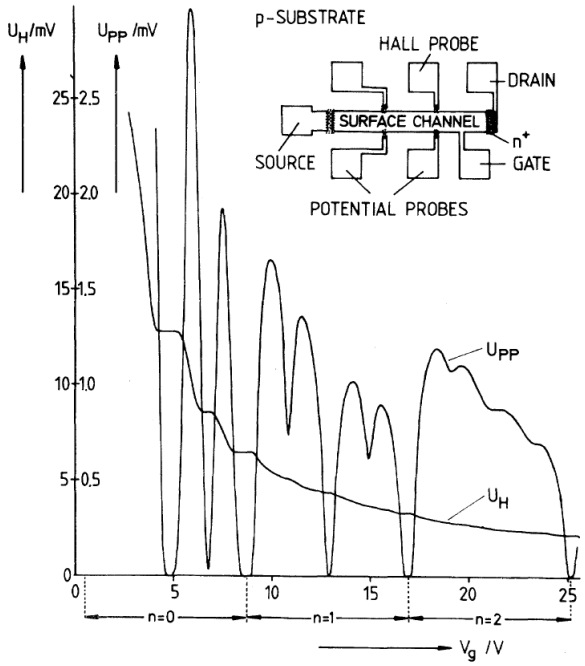

Figure 3.4: The first discovery of the quantum Hall effect [1].

Now we have seen that the Landauer-Büttiker formalism can provide a theoretical explanation for the observation of the QHE. However, the derivation above involved a mixture of classical and quantum mechanical concepts. In the next section we will treat the system quantum-mechanically using the Hamiltonian and wavefunction of carriers.

3.2.3 Quantum mechanical approach to the quantum Hall effect

Consider a 2DES on the xy-plane. For an electron of charge $-e$ and mass m moving in a magnetic field $\mathbf{B} = \nabla \times \mathbf{A}$, the Lagrangian is

$$\mathcal{L} = \frac{1}{2} m\dot{\mathbf{x}}^2 - e\dot{\mathbf{x}} \cdot \mathbf{A} \tag{3.15}$$

and the canonical momentum $\mathbf{P}$ can be obtained by

$$\mathbf{P} = \frac{\partial \mathcal{L}}{\partial \dot{\mathbf{x}}} = m\dot{\mathbf{x}} - e\mathbf{A} \tag{3.16}$$

Using Eq. 3.15 and 3.16, the Hamiltonian can be calculated as

$$\mathcal{H} = \dot{\mathbf{x}} \cdot \mathbf{P} - \mathcal{L} = \frac{1}{2m}(\mathbf{P} + e\mathbf{A})^2. \tag{3.17}$$

For a magnetic field **B** perpendicular to the plane of the 2DES, there is more than one way to choose the vector potential **A** to satisfy $\nabla \times \mathbf{A} = B\hat{z}$. Here, we choose the Landau gauge

$$\mathbf{A} = -yB\hat{x}, \tag{3.18}$$

that is commonly used for solving this problem. Then Eq. 3.17 becomes

$$\mathcal{H} = \frac{1}{2m}(P_x - eyB)^2 + \frac{1}{2m}P_y^2, \tag{3.19}$$

where P_x and P_y are the x and y components of **P**, respectively. By applying this Hamiltonian on the electrons' wavefunction ψ, we can solve the eigenenergy of the system.

Because the Landau gauge we chose is translational invariant in the x-direction but not in the y-direction, we can deduce that the form of the wavefunction should be

$$\psi(x,y) = e^{ik_x x} f(y). \tag{3.20}$$

Therefore, we have

$$\mathcal{H}\psi = \left[\frac{1}{2m}P_y^2 + \frac{1}{2m}(\hbar k_x - eyB)^2\right]\psi, \tag{3.21}$$

which can be rearranged and becomes

$$\mathcal{H}\psi = \left[\frac{1}{2m}P_y^2 + \frac{1}{2}m\omega_c^2\left(y - \frac{\hbar k_x}{eB}\right)^2\right]\psi, \tag{3.22}$$

where $\omega_c = eB/m$ is the cyclotron frequency.

Remarkably, the Hamiltonian in Eq. 3.22 actually resembles the Hamiltonian of a quantum harmonic oscillator with the centre shifted to $\hbar k_x/eB$. Thus, the form of its eigenvalues should be given by

$$E_n = (n + \frac{1}{2})\hbar\omega_c, \tag{3.23}$$

for integers $n \geq 0$. From Eq. 3.23, we see that the energy spectrum becomes a series of equally-spaced discrete states due to the confining potential from **B**. This is called Landau quantisation and the energy levels are Landau levels.

Despite the similarity of Hamiltonian, there are two important differences between Landau quantisation and a quantum harmonic oscillator.

Firstly, the centre of the parabolic magnetic potential is not at the origin and the displacement is determined by $\hbar k_x/eB$. This implies that the displacement in the y-direction is affected by the momentum in the x-direction. If we consider a 2DES in a rectangular sample like Fig. 3.3, with the dimensions of L in the x-direction and W in the y-direction, the physical edges of the sample in the y-direction act like a infinite potential well for the electrons inside. When k_x increases, the centre of magnetic potential will shift toward the boundary of the infinite potential well. When $\hbar k_x/eB > W/2$ the centre will be pushed beyond the physical edges. This is where the condition for Landau quantisation is no longer valid. Hence, it is useful to introduce a quantity called the magnetic length $l_B = \sqrt{\hbar/eB}$, which is essentially the size of the cyclotron orbits of electrons. The l_B should be much smaller than the width of the channel for the orbits of electrons to stay inside the sample and for the Landau levels to exist.

Secondly, the Landau levels are degenerate. The energy of a Landau level corresponds to more than one state. To calculate the degeneracy, again we consider a sample with length L and width W. Since the translational invariance is reserved in the x-direction, the length L gives a periodic boundary condition $k_x = 2N\pi/L$ for Eq. 3.20. In the y-direction, the translational invariance is broken by our choice of $\mathbf{A}$, but there is still a boundary condition imposed by the finite width W. As discussed above, the centre of the harmonic oscillator-like Hamiltonian should sit inside the sample. Hence, we have

$$\left|\frac{\hbar k_x}{eB}\right| \leq \frac{W}{2}. \tag{3.24}$$

By combining these two boundary conditions, we get

$$|N| \leq \frac{eBLW}{2h}. \tag{3.25}$$

Considering both positive and negative N values, we can rewrite Eq. 3.25 and obtain the upper bound of the number of electrons in one Landau level

$$N \leq \frac{eBA}{h}, \tag{3.26}$$

where $A = LW$ is the area of the 2DES. Therefore, the degeneracy per unit area per Landau level is

$$\frac{N}{A} = \frac{eB}{h}. \tag{3.27}$$

Apparently, the degeneracy of a Landau level is proportional to B. To understand why, we introduce another important physical quantity called the magnetic flux quantum $\Phi_0 = h/e$,

which is the magnetic flux encircled by the orbit of one electron (and the area of the orbit is $2\pi l_B^2$). Equation 3.27 then becomes $N = BA/\Phi_0$, i.e. the number of states in a Landau level actually means the number of flux quanta in a magnetic field. Therefore, the larger the magnetic field is, the higher the degeneracy will be.

Next, we take into account the transverse electric field $E = V/W$ caused by the Hall effect. This electric field will add an electric potential energy eEy into the Hamiltonian in Eq. 3.22, and the new Hamiltonian is

$$\mathcal{H}' = \frac{1}{2m}P_y^2 + \frac{1}{2}m\omega_c^2\big(y - \frac{\hbar k_x}{eB}\big)^2 + eEy. \tag{3.28}$$

By some rearrangement, we can move all the terms containing y into the harmonic oscillator term and write the Eq. 3.28 in the form of

$$\mathcal{H}' = \frac{1}{2m}P_y^2 + \frac{1}{2}m\omega_c^2\big(y - y_0\big)^2 + eEy_0 + \frac{1}{2}m\frac{E^2}{B^2}, \tag{3.29}$$

where

$$y_0 = \frac{\hbar k_x}{eB} - \frac{mE}{eB^2} \tag{3.30}$$

can be again seen as the centre of the harmonic oscillator potential. y_0 is also referred to as the guiding centre. The eigenenergy of this Hamiltonian is

$$E_{n,k} = (n + \frac{1}{2})\hbar\omega_c + eEy_0 + \frac{1}{2}m\frac{E^2}{B^2}.$$

One can see that, in addition to the harmonic oscillator energy, two extra terms appear in the eigenenergy. The second term eEy_0 is the electric potential energy and its value depends on k_x, meaning that the energy now becomes a function of momentum. This implies that the state is no longer a standing wave but a wavepacket travelling in the x-direction. The third term is actually equivalent to $\frac{1}{2}mv_x^2$ and thus can be thought of as the kinetic energy of the moving state.

We can go one step further to explore more interesting properties of this system. Let us consider a gedankenexperiment proposed by Robert Laughlin [24]. Imagine that we wrap the 2DES into a cylinder, as shown in Fig. 3.5. Now the source and drain electrodes become two rings with circumference L located at the two ends of this cylinder, respectively. The magnetic field lines become radial after wrapping and are still normal to the surface of the 2DES. In this geometry, there is no longer "edges" connecting the source and drain. With a magnetic field, the electrons injected from the source electrode will have spiral trajectories on the cylindrical surface and if the magnetic field is strong enough, the electrons may even form

circular orbits around the surface of the cylinder, creating a "Hall voltage" between the two ends of the cylinder. To be able to utilise the Hamiltonian derived above for later discussion, we define the x-direction to be parallel to the rim of the cylinder, while the y-direction is parallel to the axis of the cylinder because the Hall voltage now lays between the two ends of the cylinder.

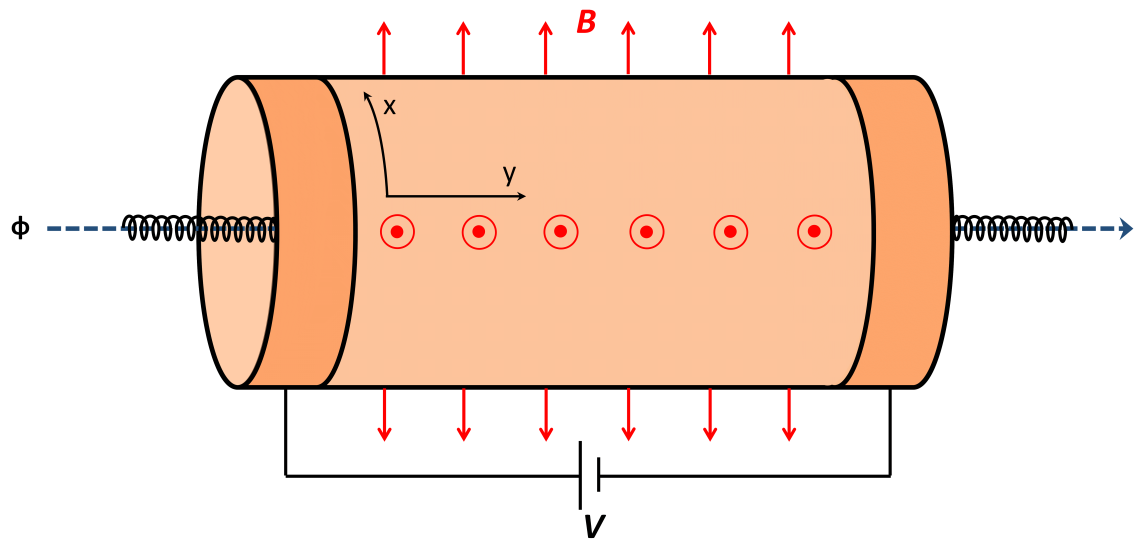

Figure 3.5: The device geometry used in Laughlin's gedankenexperiment [24].

Then we place a solenoid with uniform magnetic flux ϕ on the axis of the cylinder, which generates a magnetic field $\mathbf{B}_\phi$ in the y-direction inside the cylinder. Remarkably, although $\mathbf{B}_\phi$ only exists inside the cylinder, the corresponding vector potential $\mathbf{A}_\phi$ has a finite component on the surface that affects electrons' wavefunction according to the Aharonov-Bohm effect [25]. We can find the relation between ϕ and $\mathbf{A}_\phi$ by

$$\phi = \int \mathbf{B}_\phi \cdot \mathrm{d}\mathbf{S} = \int (\nabla \times \mathbf{A}_\phi) \cdot \mathrm{d}\mathbf{S} = \oint \mathbf{A}_\phi \cdot \mathrm{d}\mathbf{l} = L|A_\phi|, \tag{3.31}$$

and hence obtain

$$\mathbf{A}_\phi = \frac{\phi}{L}\hat{x}. \tag{3.32}$$

Since the $\mathbf{B}_\phi$ is not on the surface where the electrons are, when a change $\Delta\phi$ occurs, the corresponding change $\Delta\mathbf{A}_\phi$ only has the effect like a gauge transformation [24, 26], which adds a Aharonov-Bohm phase $\exp(ie\Delta A_\phi x/\hbar)$ to the electrons' wavefunction, i.e.

$$\psi(x,y) \to \psi(x,y)\mathrm{e}^{(ie\Delta A_\phi x/\hbar)}. \tag{3.33}$$

Moreover, since the electrons move around a loop, the wavefunction should obey the periodic boundary condition $\psi(x,y) = \psi(x+L,y)$, which means

$$\begin{aligned}\psi(x,y)\mathrm{e}^{(ie\Delta A_\phi x/\hbar)} &= \psi(x+L,y)\mathrm{e}^{(ie\Delta A_\phi (x+L)/\hbar)} \\ &= \psi(x,y)\mathrm{e}^{(ie\Delta A_\phi x/\hbar)}\mathrm{e}^{(ie\Delta A_\phi L/\hbar)} \\ &= \psi(x,y)\mathrm{e}^{(ie\Delta A_\phi x/\hbar)}\mathrm{e}^{(ie\Delta\phi/\hbar)}.\end{aligned} \tag{3.34}$$

To make the left and right of Eq 3.34 equivalent, $\Delta\phi$ must satisfy

$$\Delta\phi = n \times \frac{h}{e}. \tag{3.35}$$

This implies that, for a self-connected current loop, a continuous gauge transformation is not allowed and the change of flux must be quantised.

In addition, since ΔA_ϕ only acts as a gauge transformation, the change of $\Delta\phi$ must map the system back to itself [24]. Therefore, ΔA_ϕ simply changes the Hamiltonian in terms of the mapping

$$y_0 \to y_0 - \frac{\Delta A_\phi}{B}, \tag{3.36}$$

which merely affects the wavefunction through the location of its guiding centre.

From our discussion about the translational invariance in the x-direction, we know that the available k_x is spaced by $2\pi/L$. Thus, the available y position is spaced by h/eBL. Consequently, what happens every time when the $\Delta\phi$ satisfies Eq. 3.35 is that the guiding centre shifts in the y-direction by a length of h/eBL. The electrons in each current loop are translated to the position that was originally occupied by the next current loop. At one end of the cylinder, the electron in the last current loop flows out of the sample, while at the other end another electron flows into the sample to occupy the first current loop. Thus, when n Landau levels are filled, n electrons are moved from one end to the other, and the required energy E for this operation is neV. If the current loops carry a current I, then we can write

$$I = \frac{dE}{d\phi} = \frac{neV}{h/e} = \frac{ne^2V}{h}, \tag{3.37}$$

and therefore,

$$\frac{V}{I} = \frac{h}{ne^2}. \tag{3.38}$$

Again, we obtain the result that Hall resistance is quantised to h/ne^2, same as the semiclassical approach.

Some may wonder whether what we derived from Laughlin's imagined cylindrical system can actually occur in real-world experiments. In fact, the Corbino disks that are commonly used in measurements nowadays are topologically equivalent to this cylindrical system. The advantage of using this Laughlin's geometry is that we can keep the translational invariance and continue to use Cartesian coordinates for calculation, which makes the derivation more concise.

As a final remark, it should be noted that the spin of carriers is not considered in the derivation above. If we take into account the spin degeneracy, the number of available states per Landau level will be doubled (because one Landau level actually consists of a spin-up level and a spin-down level). In that case, we should introduce a parameter called the filling factor ν, which means the number of filled "spin-split" Landau levels and is given by

$$\nu = g_d \times n,$$

where g_d is the degree of degeneracy of the system, and hence $g_d = 2$ for a system with spin degeneracy. Similarly, if a system possesses other degeneracies (e.g. valley degeneracy), the available states per Landau level will increase accordingly.

3.2.4 Extended states and localised states

We have arrived at the conclusion that the Hall resistance can be quantised under a strong magnetic field. However, the derivations in the previous sections only tell us that the Hall resistance should be quantised at one point, where n Landau levels are completely filled. The theories we have considered so far cannot explain why the quantised Hall resistance persists over a range of magnetic fields in experiments.

To understand the observation of Hall plateax in a real experiment, we must consider a sample in the real world, too. In the theoretical discussion, we considered the sample to be a perfectly pure material without any kind of disorder. However, a real sample may contain impurities and structural defects such as vacancies or lattice dislocations. As a result, the Landau levels, which theoretically should be delta functions, are broadened due to the presence of disorder (as shown in Fig. 3.6). The broadened Landau level spectrum consists of two kinds of states. The centre of each Landau levels is the extended state, in which the carriers are able to move through the sample and conduct current. The tails of each Landau level become the localised state, in which the carriers' movement are restricted to isolated islands and cannot contribute to the electrical conduction.

Assuming that we tune the Fermi level from an energy near the nth Landau level. When the Fermi level enters the energy range of localised states, part of the broadened Landau

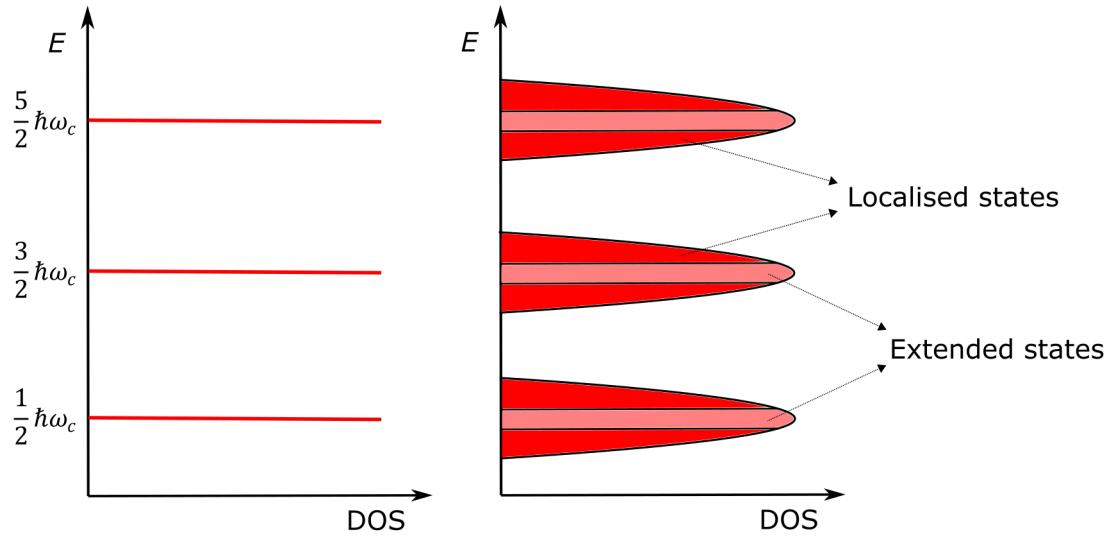

Figure 3.6: The relation between the energy (E) and density of states (DOS) of Landau levels. Theoretically, the Landau levels should be a series of delta functions separated by an energy difference of $\hbar\omega_c$ (left). However, in a real sample the Landau levels are broadened due to the presence of disorder (right). The broadened Landau level spectrum consists of two kinds of states: extended states in the centre and localised states in the tails of each Landau level.

level starts to be filled. However, the filled states can only form small isolated islands in the bulk. If we keep tuning the Fermi level, more states continue to be filled and the islands may grow larger. Before the islands grow large enough to connect with each other and form a continuous conducting channel from the source to drain, the bulk will remain insulating. Since the conductivity does not change in this process, plateaux with finite width thus appear in the Hall resistance. On the other hand, when the Fermi level coincides with the energy of extended states, the bulk becomes conducting, resulting in the transition between plateaux.

3.3 Topological invariants

3.3.1 The topological order of the quantum Hall effect

We have seen that Laughlin's gedankenexperiment can provide a good explanation for the quantisation of Hall resistance. However, Laughlin's argument relies on the gauge invariance and boundary conditions of the cylindrical geometry, which does not explicitly show why the QHE is insensitive to the details of the device. Therefore, Thouless, Kohomoto, Nightingale and den Nijs (TKNN) proposed an alternative approach for understanding the QHE by using the Kubo formula for a 2DES [12, 27, 28]. In TKNN's formulation, the topological nature of the QH phase is revealed for the first time, despite that it requires the condition

of non-interacting electrons moving in a uniform magnetic field and a periodic substrate potential. TKNN's formulation was generalised by later work to an interacting, non-periodic Hamiltonian in a realistic geometry [29–31], demonstrating the deep connection between the QHE and topology.

Let us begin with calculating the expectation value of current density j_x of a 2DES in the presence of an electric field E. Let $|\psi_n\rangle$ be the eigenstate of the many-body Hamiltonian $\mathcal{H}$. If E is not too large, we can simply add a term $\Delta\mathcal{H} = eEy$ to the Hamiltonian according to the perturbation theory so that $\mathcal{H}' = \mathcal{H} + \Delta\mathcal{H}$. To the first order in perturbation theory, the change of ground state is

$$\left|\psi_0'\right\rangle = |\psi_0\rangle + \sum_{n>0} \frac{\langle\psi_n|\, eEy\,|\psi_0\rangle}{E_0 - E_n} |\psi_n\rangle\,, \tag{3.39}$$

and hence the current density can be obtained by

$$\begin{aligned}\langle j_x\rangle &= \left\langle\psi_0'\right| j_x \left|\psi_0'\right\rangle \\ &= \left(\langle\psi_0| + \sum_{m>0} \frac{\langle\psi_0|\, eEy\,|\psi_m\rangle}{E_0 - E_m} \langle\psi_m| \right) j_x \left(|\psi_0\rangle + \sum_{n>0} \frac{\langle\psi_n|\, eEy\,|\psi_0\rangle}{E_0 - E_n} |\psi_n\rangle \right).\end{aligned} \tag{3.40}$$

Since there is no current flowing in the x-direction in the ground state before introducing eEy, we have $\langle\psi_0|\, j_x\,|\psi_0\rangle = 0$. In addition, we can ignore the E^2 term to take the first-order approximation for our calculation. In this way, Eq. 3.40 can be written as

$$\langle j_x\rangle = eE \sum_{n>0} \frac{\langle\psi_n|y|\psi_0\rangle\langle\psi_0|\, j_x\,|\psi_n\rangle + \langle\psi_n|\, j_x\,|\psi_0\rangle\langle\psi_0|y|\psi_n\rangle}{E_0 - E_n}. \tag{3.41}$$

Here, we can make use of the commutation relation $[\mathcal{H}, y] = (-i\hbar/m)P_y$ and replace P_y by $j_y = (e/m)P_y$ to obtain

$$\langle\psi_n|\,[\mathcal{H}, y]\,|\psi_0\rangle = (E_n - E_0)\langle\psi_n|y|\psi_0\rangle = (-i\hbar/e)\langle\psi_n|\, j_y\,|\psi_0\rangle\,. \tag{3.42}$$

From Eq 3.42, we see that

$$\langle\psi_n|y|\psi_0\rangle = \frac{-i\hbar}{e(E_n - E_0)}\langle\psi_n|\, j_y\,|\psi_0\rangle\,. \tag{3.43}$$

Substituting Eq. 3.43 into Eq. 3.41 leads to

$$\sigma_{xy} = i\hbar \sum_{n>0} \frac{\langle\psi_n|\, j_y\,|\psi_0\rangle\langle\psi_0|\, j_x\,|\psi_n\rangle - \langle\psi_n|\, j_x\,|\psi_0\rangle\langle\psi_0|\, j_y\,|\psi_n\rangle}{(E_n - E_0)^2}. \tag{3.44}$$

This is the Kubo formula for the Hall conductivity.

The Kubo formula is a more general argument and enables us to directly calculate the Hall conductivity of a 2DES. Now we employ the approach proposed by Niu and Thouless [31], which is closely related to the idea of Laughlin's gedankenexperiment, to calculate the Hall conductivity.

Figure 3.7(a) shows a typical strip-like device that is usually used for the measurements of the QHE. A magnetic field is applied normal to the device plane, while a current is passed from A to C and the Hall voltage is measured by a voltmeter between B and D. Let us consider a device shown in Fig. 3.7(b), in which A and C in Fig. 3.7(a) are connected by the same 2D material as the sample and form a "current lead". The circuit for measuring the Hall voltage in Fig. 3.7(a) is also replaced by a loop of the same 2D material, which we call the "voltage lead". The rectangular part and the two loops are all in the same approximately uniform magnetic field normal to their 2D plane. Then, we thread two solenoids with flux Φ_J and Φ_V through the loops of the current lead and voltage lead, respectively. In this geometry, if we change Φ_J or Φ_V, an electromotive force (emf) can be induced around the corresponding loop, similar to Laughlin's gedankenexperiment. For example, if we change Φ_V, an electric field E will be generated around the voltage lead, causing a current to flow along the direction normal to E which can be detected by the change of Φ_J. Therefore, this device is actually equivalent to the device in Fig. 3.7(a).

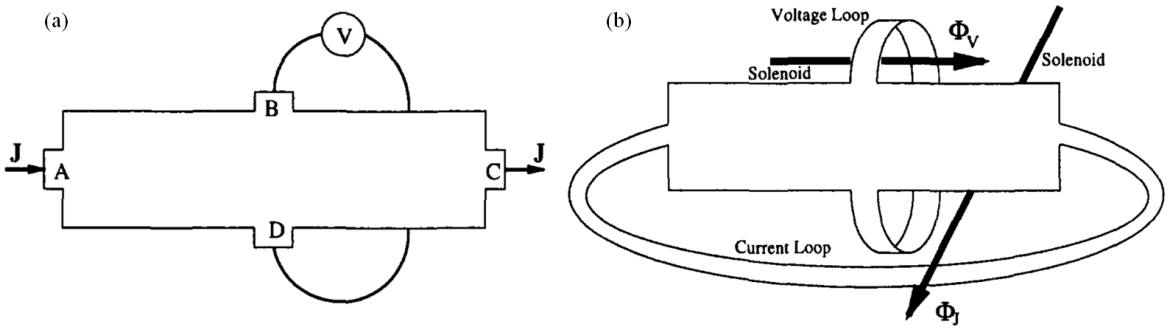

Figure 3.7: The device with realistic boundary conditions considered by Niu and Thouless [31]. The graphs are reproduced from [32]. (a) A typical strip-like device usually used for the measurements of the QHE. A uniform magnetic field normal to the plane is applied, while a current is passed from A to C and the transverse voltage is measured between B and D. (b) A device transformed from the strip-like device in (a), with A and C connected by a strip which we call the "current lead", and B and D connected by a strip which we call the "voltage lead". The rectangular part and the two loops are all made of the same 2D material and in the same approximately uniform magnetic field. This device is equivalent to the device in (a).

For the two inductive loops, we have two relations

$$j_x = \frac{\partial \mathcal{H}}{\partial \Phi_J} \quad \text{and} \quad j_y = \frac{\partial \mathcal{H}}{\partial \Phi_V}, \tag{3.45}$$

that can be substituted into Eq 3.44. Moreover, the first order perturbation theory gives

$$\left| \frac{\partial \psi_0}{\partial \Phi_J} \right\rangle = \sum_{n>0} \frac{\langle \psi_n | \frac{\partial \mathcal{H}}{\partial \Phi_J} | \psi_0 \rangle}{E_0 - E_n} | \psi_n \rangle \quad \text{and} \quad \left| \frac{\partial \psi_0}{\partial \Phi_V} \right\rangle = \sum_{n>0} \frac{\langle \psi_n | \frac{\partial \mathcal{H}}{\partial \Phi_V} | \psi_0 \rangle}{E_0 - E_n} | \psi_n \rangle \tag{3.46}$$

With the aid of Eq 3.45 and Eq 3.46, we can rewrite Eq 3.44 as

$$\begin{aligned} \sigma_{xy} &= i\hbar \left(\left\langle \frac{\partial \psi_0}{\partial \Phi_J} \middle| \frac{\partial \psi_0}{\partial \Phi_V} \right\rangle - \left\langle \frac{\partial \psi_0}{\partial \Phi_V} \middle| \frac{\partial \psi_0}{\partial \Phi_J} \right\rangle \right) \\ &= i\hbar \left(\frac{\partial}{\partial \Phi_J} \left\langle \psi_0 \middle| \frac{\partial \psi_0}{\partial \Phi_V} \right\rangle - \frac{\partial}{\partial \Phi_V} \left\langle \psi_0 \middle| \frac{\partial \psi_0}{\partial \Phi_J} \right\rangle \right). \end{aligned} \tag{3.47}$$

As we discussed in Laughin's argument, the change of Φ_J and Φ_V must be quantised to h/e to obey the periodic boundary conditions on the current lead and voltage lead, respectively. This means the flux space (Φ_V, Φ_J) is a torus with a periodicity h/e. Hence, we can integrate Eq. 3.47 over the entire flux space and then divide it by the unit area h^2/e^2 in the flux space to calculate the average value of σ_{xy},

$$\sigma_{xy} = i\hbar \frac{e^2}{h^2} \int_0^{h/e} \mathrm{d}\Phi_J \int_0^{h/e} \mathrm{d}\Phi_V \left(\frac{\partial}{\partial \Phi_J} \left\langle \psi_0 \middle| \frac{\partial \psi_0}{\partial \Phi_V} \right\rangle - \frac{\partial}{\partial \Phi_V} \left\langle \psi_0 \middle| \frac{\partial \psi_0}{\partial \Phi_J} \right\rangle \right). \tag{3.48}$$

To further reduce this equation, we introduce a dimensionless variable θ, which is defined as

$$\theta_i \equiv \frac{2\pi \Phi_i}{\Phi_0}, \qquad 0 \leq \theta \leq 2\pi \tag{3.49}$$

where the subscript i can be a variable in the parameter space of interest, such as V and J in this case. According to Berry's work [33], the integration around a closed loop in a parameter space can result in an additional geometric phase, which is now called the Berry phase. To compute the Berry phase, we start with the Berry connection, which is defined as

$$\mathcal{A}_i \equiv i \langle \psi_0 | \frac{\partial}{\partial \theta_i} | \psi_0 \rangle . \tag{3.50}$$

The Berry curvature is then given by

$$\mathcal{F}_{ij} \equiv \nabla_\theta \times \mathcal{A} = \frac{\partial \mathcal{A}_i}{\partial \theta_j} - \frac{\partial \mathcal{A}_j}{\partial \theta_i} = i\left(\frac{\partial}{\partial \theta_j} \left\langle \psi_0 \middle| \frac{\partial \psi_0}{\partial \theta_i} \right\rangle - \frac{\partial}{\partial \theta_i} \left\langle \psi_0 \middle| \frac{\partial \psi_0}{\partial \theta_j} \right\rangle \right). \tag{3.51}$$

It can be seen that Eq. 3.51 has a very similar form to the term in the parentheses of Eq. 3.48. Thus, we can rewrite Eq. 3.48 as

$$\begin{aligned} \sigma_{xy} &= \frac{e^2}{2\pi h} \int_0^{2\pi} \mathrm{d}\theta_J \int_0^{2\pi} \mathrm{d}\theta_V \mathcal{F}_{VJ} \\ &= \frac{e^2}{2\pi h} \int_0^{2\pi} \mathrm{d}\theta_J \int_0^{2\pi} \mathrm{d}\theta_V (\nabla_\theta \times \mathcal{A}) \end{aligned} \tag{3.52}$$

By the Stoke's theorem, Eq 3.52 can be written as

$$\sigma_{xy} = \frac{e^2}{2\pi h} \oint \mathcal{A} \cdot \mathrm{d}^2\theta \tag{3.53}$$

Remarkably, the integral above is exactly the expression of the Berry phase. The boundary conditions of this system tell us that the Berry phase can only be an integer multiple of 2π after circling a closed loop in the parameter space. Consequently, Eq. 3.53 becomes

$$\sigma_{xy} = \frac{\mathcal{C}e^2}{h}, \tag{3.54}$$

where $\mathcal{C}$ is the Chern number. Similar to Eq. 3.38, the quantisation of Hall conductance is obtained.

3.3.2 The Chern number

The Chern number is named after Shiing-Shen Chern, who generalised the Gauss-Bonnet theorem and introduced the Chern class in topology. In the generalised Gauss-Bonnet theorem, the topological genus (denoted by the Chern number) of a manifold can be obtained by integrating the Gaussian curvature over the surface of a manifold. This is similar to integrating the Berry curvature over the area of a parameter space or, in other words, the Berry phase around the area. Clearly, the Berry phase only differs from the Chern number by a factor of 2π, implying that they are essentially the same idea. Because the Chern number solely depends on the number of "holes" surrounded by the path of integral in a parameter space and cannot vary continuously, it is insensitive to the local details on the path. This

explains the robustness of QHE on different samples, at different temperatures, or even in different materials.

Once again, in Eq. 3.54 we find the quantisation of Hall conductivity just like in the different approaches in the previous sections. The TKNN formulation using the Kubo formula is much more general than Laughlin's argument. With the knowledge of Berry's work on the geometric phase and Chern class in topology, the QHE is related to the topological order. For this reason, the Chern number is called a topological invariant, which is a fundamental characteristic of matter and will be the key idea for discussing other topological phases in condensed matter physics in the following sections.

3.4 Quantum spin Hall effect

3.4.1 Haldane model

Now we know that the topological invariant of matter is the fundamental reason of the QHE. In principle, as long as a system has a non-zero Chern number, we should be able to observe some behaviours like the QHE. Therefore, a further question is whether it is possible to induce a similar effect without an external magnetic field.

This was investigated by Duncan Haldane in 1988 [13]. In his work, a 2D system composed of carbon atoms interconnecting in a honeycomb network is considered. Such a structure was hypothetical at that point, but became possible after Andre Geim and Konstantin Novoselov successfully isolated individual graphene flakes in 2004 and proved the material is stable under ambient condition [34].

Each primitive cell of graphene contains two atoms, located on the two sublattices, A and B, as shown in Fig. 3.8. The two sublattices result in two inequivalent points, K and K', in the reciprocal lattice in momentum space.

The band structure of graphene calculated by the tight-binding method [35–37] is shown in Fig. 3.9. It can be clearly seen that the conduction band and valence band touch at six K- and K'-points of the Brillouin zone at zero energy. Since there is no prevailing type of charge carrier at the K-point and K'-point, they are called the charge neutrality point. The K- and K'-points are degenerate in energy and give rise to the valley degeneracy in graphene.

The dispersion relation of graphene at low energy (within about 1 eV of the charge neutrality point) is linear and the Hamiltonian can be written as [39]

$$\mathcal{H} = \mathbf{h}(\mathbf{q}) \cdot \sigma = \hbar v_F \mathbf{q} \cdot \sigma, \tag{3.55}$$

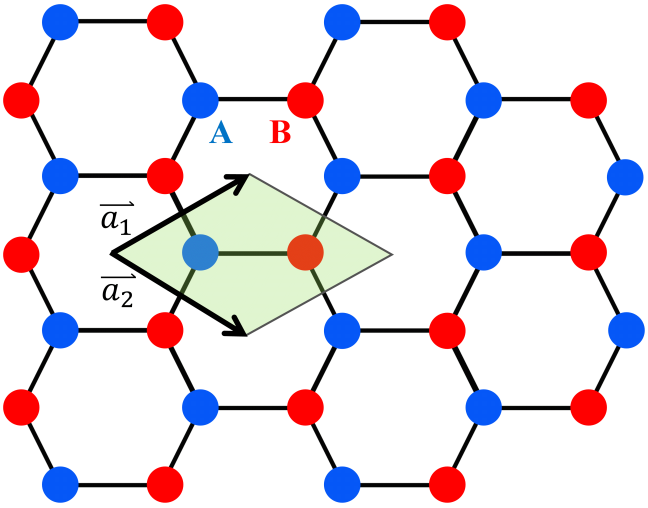

Figure 3.8: The crystal structure of graphene. The blue and red circles represent the sublattice A and B, respectively. The green region is a primitive cell of graphene defined by the two lattice vectors of graphene $\overrightarrow{a_1}$ and $\overrightarrow{a_2}$.

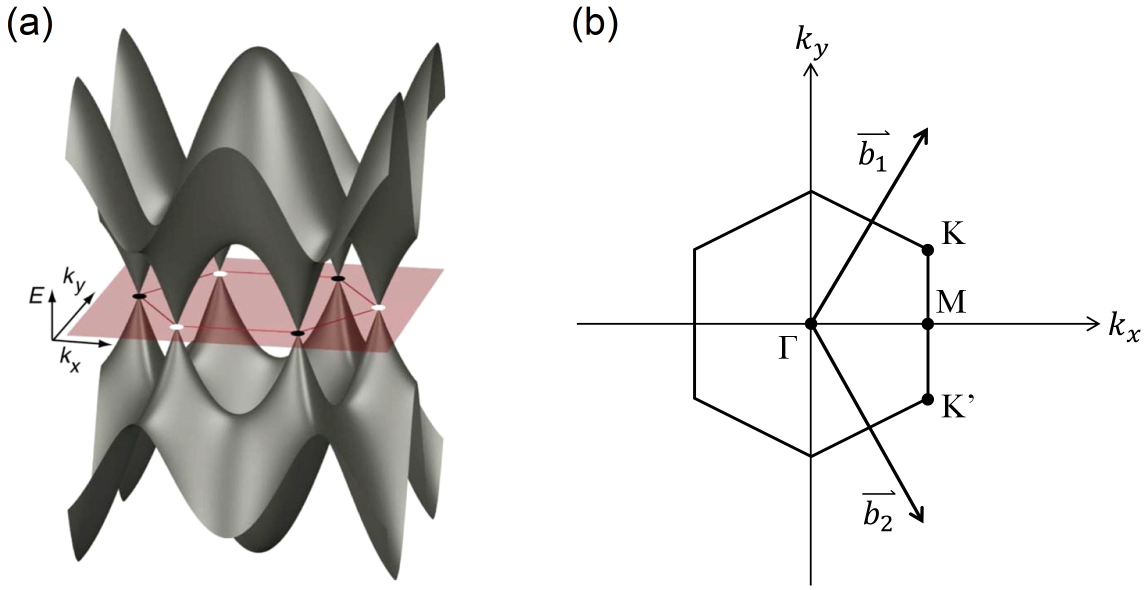

Figure 3.9: (a) The band structure of graphene calculated by tight-binding model. The conical energy spectrum near the charge neutrality points has a linear dispersion relation. (Image is reproduced from [38]). (b) The first Brillouin zone of graphene. K and K' are the points where the valence and conduction band meet, i.e. the charge neutrality points. $\overrightarrow{b_1}$ and $\overrightarrow{b_2}$ are the reciprocal lattice vectors.

where v_F is the Fermi velocity , $\mathbf{q} = \mathbf{k} - \mathbf{K}$ is the wave vector relative to the K point in the momentum space, and $\sigma = (\sigma_x, \sigma_y, \sigma_z)$ are Pauli matrices. This linear dispersion relation implies that the effective mass of charge carriers around the charge neutrality point is zero

and the Fermi velocity is as high as about 1/300 of the speed of light in vacuum. The relativistic carrier transport behaviour can be described by the Dirac equation and thus the charge neutrality point is also named the Dirac point.

Both the inversion symmetry ($\mathcal{P}$) and time-reversal symmetry ($\mathcal{T}$) are preserved in graphene lattice, which requires the z-component of $\mathbf{h}(\mathbf{k})$ to be zero since

$$\mathcal{P}\mathbf{h}_z(\mathbf{k}) = -\mathbf{h}_z(-\mathbf{k}) \quad \text{and} \quad \mathcal{T}\mathbf{h}_z(\mathbf{k}) = \mathbf{h}_z(-\mathbf{k}) \tag{3.56}$$

both need to be unchanged under the operation. The Dirac point is obviously a solution of this condition because Eq. 3.56 is satisfied at K- and K'-point. Therefore, we can say that the Dirac point is protected by inversion and time-reversal symmetry. On the other hand, it also means that if we break the inversion or time-reversal symmetry, the degeneracy at Dirac point can be lifted.

For example, if an extra term $m\sigma_z$ is added to Eq. 3.55,

$$\mathcal{H} = \hbar v_F \mathbf{q} \cdot \boldsymbol{\sigma} + m\sigma_z, \tag{3.57}$$

an energy difference between the sublattice A and B can be generated, breaking the inversion symmetry at the Dirac point. Since the carbon atoms in sublattice A and B are no longer equivalent after introducing $m\sigma_z$, $\mathbf{h}_z(\mathbf{k})$ is allowed to be non-zero, rendering the carrier a finite effective mass m at the K-point. Moreover, because the time-reversal symmetry still holds, the effective mass at the K'-point should also be m. This is the case of an trivial insulator.

In Haldane's model [13], instead of breaking the inversion symmetry, the time-reversal symmetry of graphene lattice is broken by a magnetic field that is zero on average but still preserves the lattice symmetry. Likewise, this condition also allows $\mathbf{h}_z(\mathbf{k})$ to be non-zero and leads to massive Dirac fermion. However, the inversion symmetry requires the mass of the carrier at the K- and K'-point to have opposite signs. In this case, it is no longer an ordinary insulator but a quantum Hall-like state with non-zero Chern numbers.

Therefore, it seems that the graphene lattice provides a suitable environment for realising the Haldane model. Nevertheless, the distribution of magnetic field in the Haldane model is still fairly unrealistic in practice. As we shall see in Sec. 3.4.2, the key to solve this problem is to consider a relativistic effect that originates from the interaction between an electron's spin and orbital motion in a potential.

3.4.2 The $\mathbb{Z}_2$ topological invariant

In 2005, Kane and Mele made a major breakthrough on the theoretical study of Haldane model and found that the imagined magnetic field in the Haldane model may be generated by the intrinsic SOC of graphene lattice [14, 15]. Furthermore, if both spin-up and spin-down carriers are taken into account, the system can be seen as a combination of two spinful Haldane models that propagate in opposite directions and the time-reversal symmetry is preserved.

Remarkably, for a time-reversal invariant system with an odd number of half-integer spin particles, Kramers' theorem requires that the eigenstates of the time-reversal invariant Hamiltonian are at least twofold degenerate, i.e. there must be more than one eigenstate with the same energy. In a system with weak SOC, the spin-orbit interaction is negligible and the Kramers' theorem is simply the case of energy degeneracy between spin-up and spin-down particles. However, in a system with strong SOC, the Kramers' theorem describes a non-trivial situation.

Let us briefly digress here to discuss the band topology of a system with edge states in it. We know that a vacuum is equivalent to a trivial insulator with $\mathcal{C} = 0$, and a quantum Hall insulator has $\mathcal{C} \neq 0$. It can be imagined that the gap must close somewhere between the quantum Hall insulator and vacuum in order to let the Chern number change from zero to non-zero. Therefore, there must be finite DOS at the boundary between the quantum Hall insulator and vacuum. An example is shown in Fig. 3.10(a), one edge mode appears at the interface between the quantum Hall state and the trivial insulator, which can be represented by a line connecting the conduction band and valence band in the band diagram in Fig. 3.10(b).

Now, there are two kinds of possible band structures for the Kramers degeneracy in a 2D time-reversal invariant system. In a similar way as Fig. 3.10, the band diagrams of these two possibilities are plotted in Fig. 3.11. Note that only half of the Brillouin zone ($0 \leq k \leq \pi/a$) is shown because in a time-reversal invariant system the band structure should be symmetric about $k = 0$. Furthermore, since $k = 0$ is where the momentum equals to zero, and $k = \pi/a$ is the same as $k = -\pi/a$, these two points, labelled as Γ_a and Γ_b in Fig. 3.11, are time-reversal invariant. When there are edge modes existing in the energy gap, the Kramers' theorem requires the Γ_a and Γ_b point to be twofold degenerate because these two points must be their own Kramer partner. Apart from these two special points, the Kramers degeneracy can be lifted by the SOC, just like the Zeeman splitting of the spin degeneracy, and their Kramers partners are located in $-\pi/a < k < 0$. As a result, there are two ways that the two Kramers degenerate points Γ_a and Γ_b can be connected. If they are connected pairwise, the edge states intersect the Fermi level an even number of times as in Fig. 3.11(a). Then the edge

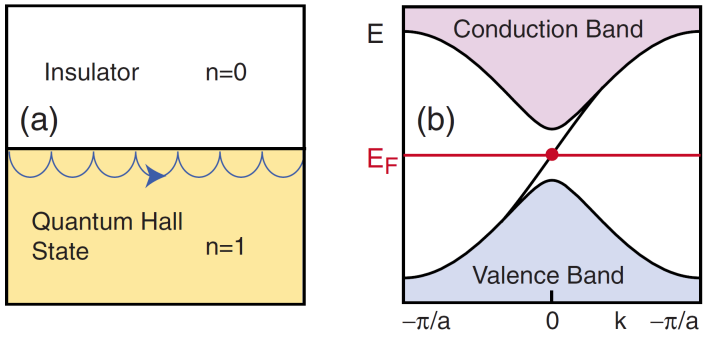

Figure 3.10: The chiral edge state existing at the interface between a topologically trivial insulator and a quantum Hall insulator, adapted from [39]. (a) The chiral edge state propagates along the boundary between a trivial insulator (with TKNN number $n = 0$) and a quantum Hall insulator (with TKNN number $n = 1$). (b) The band structure of a 2D system described by the Haldane model. The line connecting the conduction band and the valence band represents the edge state.

states can be pushed out of the gap and eliminated from the system by smoothly altering the Hamiltonian. However, when the edge states intersect the Fermi level an odd number of times as in Fig. 3.11(b), the edge states cannot be removed and there will always be at least one Kramers pair in the gap. Therefore, the number of the Kramers pairs is actually a topological property of the system, and has only two possibilities - even or odd. More importantly, this is a different topological class to the TKNN number of $\mathbb{Z}$ topological invariant. Hence it was named by Kane and Mele as $\mathbb{Z}_2$ topological invariant ν with the definition of

$$\nu \equiv N_K \bmod 2, \tag{3.58}$$

where N_k is the number of Kramers pairs in the energy gap. In this way, ν can only be zero or one. Only when $\nu = 1$, i.e. when the number of Kramers pairs is odd, the edge states in the system are robust.

A 2D system with $\nu = 1$ can exhibit the quantum spin Hall effect (QSHE), which is the first $\mathbb{Z}_2$ topological phase observed in experiments [4]. In the QSHE, each edge of the sample has one Kramers pair that consists of two states with opposite spins propagating in opposite directions as shown in Fig. 3.12.

The QSHE is given this name due to its similarity to the QHE - the edge states in both effects are topologically protected. However, unlike the QHE, the QSHE does not require an external magnetic field and, more importantly, its time-reversal symmetry is not broken. Therefore, although in the QSHE the left-moving state and right-moving state propagate on top of each other at the edge, there is no scattering between them because reversing their travelling directions requires their spins to be flipped, which is not allowed without

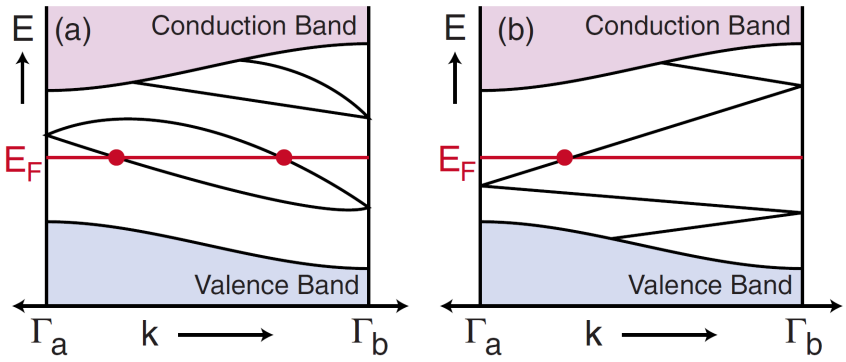

Figure 3.11: The band diagram of a 2D time-reversal invariant system between two Kramers degenerate points Γ_a ($k = 0$) and Γ_b ($k = \pi/a$), adapted from [39]. The edge mode may cross the Fermi level E_F (a) an even number of times or (b) an odd number of times. Topologically protected edge states can arise in the latter case.

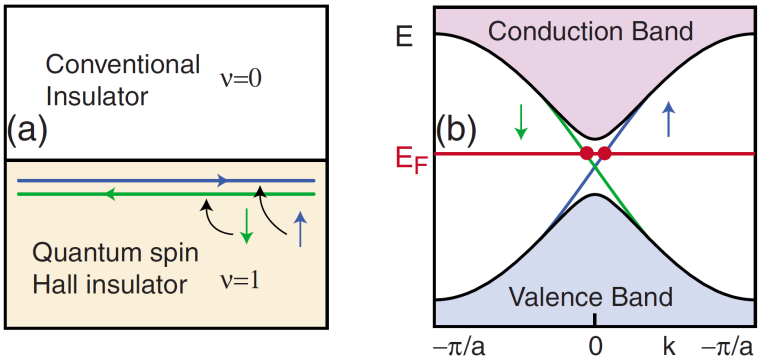

Figure 3.12: The helical edge states existing at the interface between a topologically trivial insulator and a quantum spin Hall insulator, adapted from [39]. (a) The helical edge states propagating along the boundary between a trivial insulator ($\nu = 0$) and a quantum spin Hall insulator ($\nu = 1$) consist of a right mover with up spin and a left mover with down spin. (b) The band diagram of a QSHE system. There are two edge modes with opposite spins connecting the conduction band and the valence band in $k > 0$ and $k < 0$ regime, respectively. They form the spin-polarised left-moving and right-moving edge states in (a).

the presence of magnetic scatterers to break the time-reversal symmetry. Such an edge state with its spin direction locked to the direction of linear momentum is referred to as a helical edge state [40]. It is worth noting that the helical edge states cannot even be backscattered by circling a non-magnetic impurity. As shown in Fig. 3.13, there are two ways in which the helical edge state may reverse its direction after moving around a non-magnetic impurity - either clockwise or counterclockwise. Travelling clockwise along the blue trace rotates the spin by an angle of π, while travelling counterclockwise along the red trace rotates the spin by an angle of $-\pi$ [41]. As a result, the rotation angle of spin via these two scattering paths differs by 2π, which introduces a Berry phase of π and thus adds a factor of -1 to the

wavefunction [41]. Consequently, the two scattering paths always interfere destructively and the backscattering is suppressed. We can also say that the robustness of helical edge states is protected by the time-reversal symmetry.

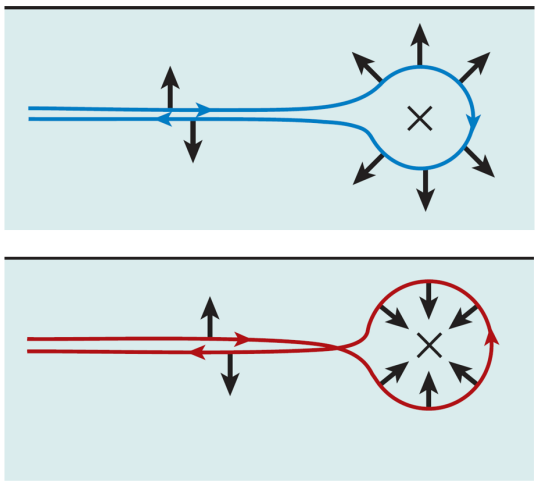

Figure 3.13: The helical edge state may scatter around a non-magnetic impurity in clockwise or counterclockwise direction and reverse its travelling direction. However, moving clockwise along the blue curve will rotate the spin by an angle π, while counterclockwise along the red curve will rotate the spin by $-\pi$. The total rotation angle of spin differs by 2π between the two scattering paths, and introduces a factor of -1 to the wavefunction, which causes a destructive interference between the two scattering paths and suppresses the backscattering. The figure is adapted from [42].

In a simple two-terminal measurement performed on a strip-like device, the longitudinal resistance of a QHE system is h/ne^2 for integers n, which can be easily calculated as described in Sec. 3.2.2. For a QSHE system, there is a right-moving state carrying a conductance quantum of e^2/h at one edge, and another right-moving state with the opposite spin carrying e^2/h at the opposite edge propagating from the source to drain. Consequently, the two-terminal conductance is expected to be $2e^2/h$. In a multi-terminal measurement, the case of the QSHE is a bit more complicated. But just like the QHE, the Landauer-Büttiker formalism can also be used to describe the conduction of helical edge states in the QSHE, as will be discussed in the following section.

Up to this point, we have introduced the basic theory of the $\mathbb{Z}_2$ topological phase. However, there is actually a gap between the theoretical prediction and experimental realisation. In the next section, we will briefly review some of the important works regarding the experimental realisation of the QSHE and the measurements of the helical edge transport.

3.4.3 Experimental realisation of the quantum spin Hall insulator

Although Kane and Mele proposed the first theoretical model of the QSHE in 2005 [14, 15], it was soon pointed out that the SOC in graphene is much weaker than their estimation and the QSHE may only be observed at temperatures below 0.01 K [43, 44], which is unrealistic for current instruments.

At about the same time, Andrei Bernevig and Shou-Cheng Zhang independently proposed a different system with the potential of exhibiting the QSHE based on the SOC induced by strain gradients in conventional semiconductors [45]. However, this model is also experimentally difficult to realise.

The main problem with the above two models is the weak SOC in the proposed systems. Nevertheless, these two models do provide theorists with some conceptual guides for the search for suitable systems. Namely, the candidates for the QSHE should be the materials with stronger SOC, typically composed of heavy elements.

In 2006, Bernevig, Hughes, and Zhang (BHZ) put forward the first model of this kind, which is a quantum well system in the heterostructure of HgTe and CdTe [46]. In most semiconductors, the conduction band formed by s-like orbitals sits above the valence band formed by p-like orbitals. But for some semiconductors composed of heavy elements, such as HgTe, the strong spin-orbit interaction can push the p-like band above the s-like band, causing a band inversion, as shown in Fig. 3.14(a). In contrast, the CdTe, a material with a similar lattice constant but much weaker SOC, has a normal band progression with the s-like band lying above the p-like band. As a result, in the BHZ model, when the HgTe layer is sandwiched by two CdTe layers and forms a quantum well, the band structure shown in Fig. 3.14(b) is produced [46]. The strength of SOC in this system can be tuned by the thickness of the HgTe layer d. When the HgTe layer is thin, the spin-orbit interaction is small and the properties of the quantum well are dominated by the CdTe layers, which leads to a band structure like a conventional insulator, as shown in the left panel of Fig. 3.14(b). When the HgTe layer is thicker than the critical thickness $d_c \approx 6.3$ nm, band inversion occurs and gives rise to a topologically non-trivial band structure, as shown in the right panel of Fig. 3.14(b). Consequently, in order to connect the inverted band to vacuum, the gap must close and reopen at the sample boundary, leading to the existence of helical edge modes [46].

BHZ also proposed the ways to measure the QSHE in the HgTe/CdTe quantum well. Because the QSHE preserves the time-reversal symmetry, it cannot be observed by measuring the Hall voltage in the presence of an external magnetic field, which will just destroy the QSHE. Therefore, the simplest way is to measure the longitudinal conductance of a strip-like device. They predicted that when the band structure is trivial, the system should behave like a conventional insulator with very high resistance if the Fermi level is tuned into the bulk

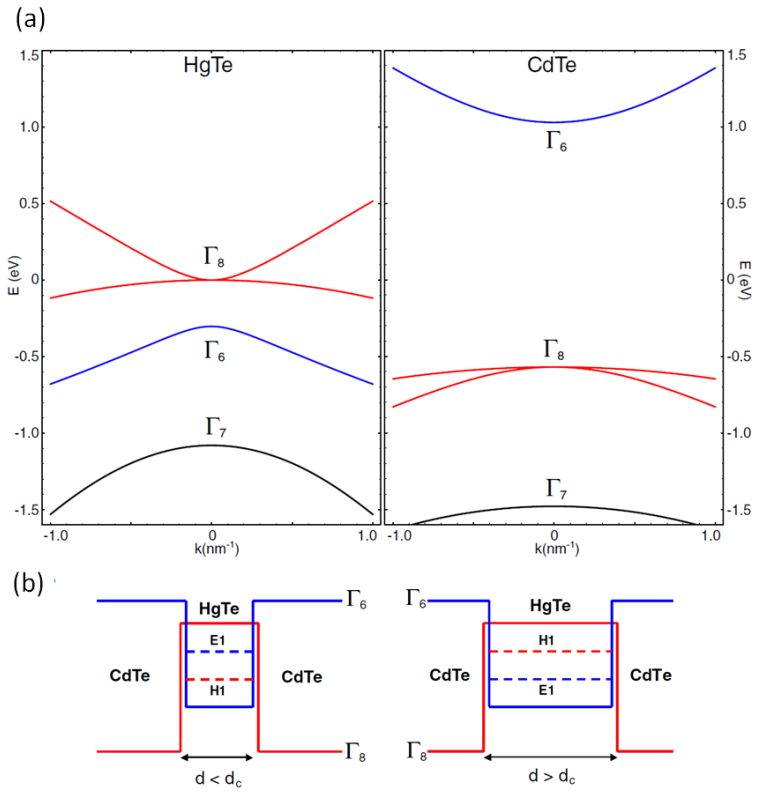

Figure 3.14: (a) The bulk band structures of the HgTe and CdTe near the Γ point. The s-like band Γ_6 and the p-like band Γ_8 are indicated by the blue and red curves, respectively. While the band structure of CdTe is like a conventional insulator, the band structure of HgTe is inverted due to strong SOC. (b) The band structure of CdTe/HgTe/CdTe quantum well at the Γ point. The thickness of HgTe layer d can affect the strength of SOC for the quantum well. In a thin quantum well, as shown in the left panel, the CdTe layers dominate the properties of the quantum well and the bands are ordered as a conventional insulator. When the well thickness d becomes greater than the critical thickness $d_c \approx 6.3$ nm, as shown in the right panel, a topological phase transition will occur and the bands are inverted. The figures are adapted from [47].

gap. On the other hand, if the bands are inverted and become topologically non-trivial, there must exist helical edge states that can contribute finite conductance. In such a measurement, because each of the two edges contains one state with a conductance quantum e^2/h moving from the source to drain, the measured conductance should be quantised to $2e^2/h$.

Soon after BHZ's theoretical prediction, Laurens Molenkamp's group successfully grew high mobility HgTe/CdTe quantum well samples and confirmed the quantised resistance of the QSHE, as shown in Fig. 3.15 [4], in which the three measurements performed on devices with different channel widths at different temperatures all plateau at a longitudinal resistance of $h/2e^2$ after the Fermi level is tuned into the bulk gap.

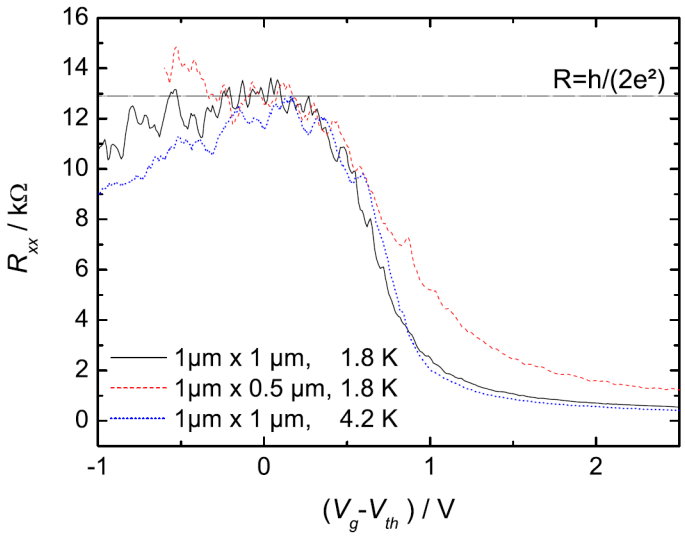

Figure 3.15: The longitudinal resistance (R_{xx}) measured as a function of gate voltage (V_g) in the QSH regime on a strip-like HgTe/CdTe quantum well device. The threshold voltage V_{th} is defined as the voltage needed to reach the QSH regime. The three curves correspond to the measurements performed on devices with different channel widths at different temperatures. They all plateau at $R_{xx} = h/2e^2$, independent of the channel width, suggesting that it is caused by edge states. The figure is adapted from [47].

With the experimental confirmation of the QSHE, one can examine further properties of the helical edge states. For instance, if the conductance does come from the edge transport, it should be independent of not only the channel width but also the channel length. Furthermore, since the edge transport necessarily leads to non-local signals, some four-terminal and non-local measurements should be useful for understanding the behaviour of helical edge states.

Figure 3.16 shows the schematic of a Hall bar. In the case of QHE, the transmission probability of chiral edge states is $T_{i,i+1} = 1$ for $i = 1$ to 6, and all other $T_{ij} = 0$. However, in the QSHE, a Kramers pair of helical edge states travel in opposite directions at any given edge, which makes $T_{i,i+1} = T_{i+1,1} = 1$, and all the others vanish for every electrode. If a current I is injected from electrode 1 to electrode 4 and the corresponding voltage on electrode 1 is V, using the Landauer-Büttiker formalism we can write

$$\begin{pmatrix} I \\ 0 \\ 0 \\ -I \\ 0 \\ 0 \end{pmatrix} = \frac{e^2}{h} \begin{pmatrix} 2 & -1 & 0 & 0 & 0 & -1 \\ -1 & 2 & -1 & 0 & 0 & 0 \\ 0 & -1 & 2 & -1 & 0 & 0 \\ 0 & 0 & -1 & 2 & -1 & 0 \\ 0 & 0 & 0 & -1 & 2 & -1 \\ -1 & 0 & 0 & 0 & -1 & 2 \end{pmatrix} \begin{pmatrix} V \\ V_2 \\ V_3 \\ 0 \\ V_5 \\ V_6 \end{pmatrix}. \tag{3.59}$$

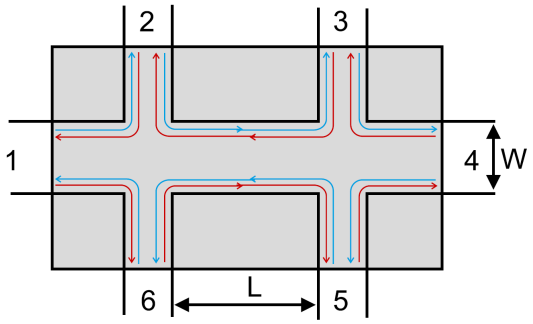

Figure 3.16: The schematic diagram showing the helical edge transport in a Hall bar. The blue and red arrows indicate the edge channels with up spin and down spin, respectively. Adapted from [47].

By solving Eq. 3.59, the voltage of each electrode can be obtained

$$\begin{pmatrix} V_1 \\ V_2 \\ V_3 \\ V_4 \\ V_5 \\ V_6 \end{pmatrix} = \begin{pmatrix} V \\ 2V/3 \\ V/3 \\ 0 \\ V/3 \\ 2V/3 \end{pmatrix}. \tag{3.60}$$

According to Eq. 3.60, we can compute the multi-terminal resistance of various measurement setups. For example, the four-terminal longitudinal resistance $R_{14,23} = h/2e^2$ and the Hall resistance $R_{14,35} = 0$. This is verified in the experiments performed by Molenkamp's group, as shown in Fig. 3.17 [4], in which four-terminal measurements were carried out on four different samples. The quantum well thickness is 5.5 nm for sample I (denoted by the black curve), and 7.3 nm for sample II, III, and IV (denoted by the blue, green, and red curves, respectively). The device dimensions ($L \times W$) are 20.0×13.3 μm^2 for sample I and II, 1.0×1.0 μm^2 for sample III, and 1.0×0.5 μm^2 for sample IV.

For sample I, because the well thickness is smaller than d_c, the band structure remains a trivial insulator. Therefore, it shows a resistance over 10 MΩ (which is the detection limit of the instrument used in the experiment) when the Fermi level is tuned into the bulk gap. In contrast, the well thickness of the other three samples is larger than d_c and the band inversion is induced, leading to finite conductance and hence much lower resistance. For sample III and IV, both curves plateau at $G = 2e^2/h$, consistent with the value deduced by the Landauer-Büttiker formalism. Therefore, the BHZ model is unambiguously confirmed by this experiment.

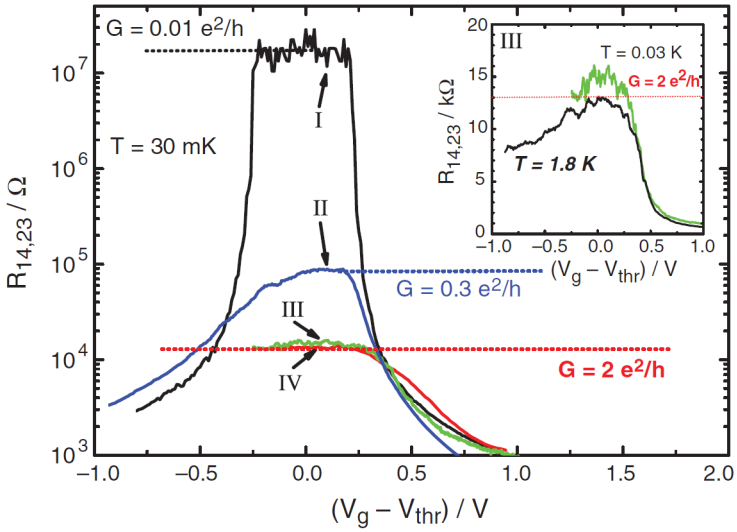

Figure 3.17: The four-terminal resistance ($R_{14,23}$) of a HgTe/CdTe quantum well as a function of gate voltage (V_g) in the QSH regime at $B = 0$ T and $T = 30$ mK. The threshold voltage V_{thr} is defined as the voltage at the maximum resistance. The well thickness is 5.5 nm for sample I (denoted by the black curve), and 7.3 nm for sample II, III, and IV (denoted by the blue, green, and red curves, respectively). Sample I is the only sample without band inversion due to its insufficiently thick quantum well. The device sizes ($L \times W$) are 20.0×13.3 μm^2 for sample I and II, 1.0×1.0 μm^2 for sample III, and 1.0×0.5 μm^2 for sample IV. The figure is adapted from [4].

One question that arises here is why the blue curve plateaus at $G = 0.3e^2/h$. This actually brings up another important factor in the helical edge transport: while we mentioned that the helical edge states are immune to backscattering from elastic scatterers, they are not robust against inelastic scatterers due to finite experimental temperatures in reality. The typical mobility of the HgTe/CdTe quantum well samples used in this experiment is about 10^5 cm^{2}V^{-1}s^{-1}, corresponding to an elastic mean free path $l_{\text{mfp}} \approx 1$ μm. On the other hand, the inelastic mean free path l_{in} is estimated to be several times larger than l_{mfp} due to the suppression of phonons and the reduced electron–electron interaction at low temperatures. Therefore, l_{in} is possibly on the order of a few microns. As the channel length of sample II is significantly larger than l_{in}, the inelastic backscattering is more likely to occur and results in a higher resistance and non-quantised values. In principle, the results calculated in the Landauer-Büttiker formalism are valid as long as the distance between the voltage probes is shorter than l_{in}. This is a scattering mechanism that should be considered when dealing with the transport of helical edge states in real experiments.

In addition to the measurement of $R_{14,23}$, other combinations of two-terminal and four-terminal measurements were also conducted to inclusively check the prediction of the

Landauer-Büttiker formalism for the helical edge transport [48], as shown in Fig. 3.18. The resistance of $R_{14,14}$, $R_{13,13}$, $R_{14,23}$, and $R_{13,54}$ as a function of gate voltage are presented. The blue dashed lines indicate the expected values for each setup calculated in the Landauer-Büttiker formalism, and $V^* = V_g - V_{th}$. The insets in Fig. 3.18(a) and (b) show the layout of the device, and the light yellow square on top of the Hall bar is the gate for adjusting the Fermi level. All the curves match the values predicted by the Landauer-Büttiker formalism quite well.

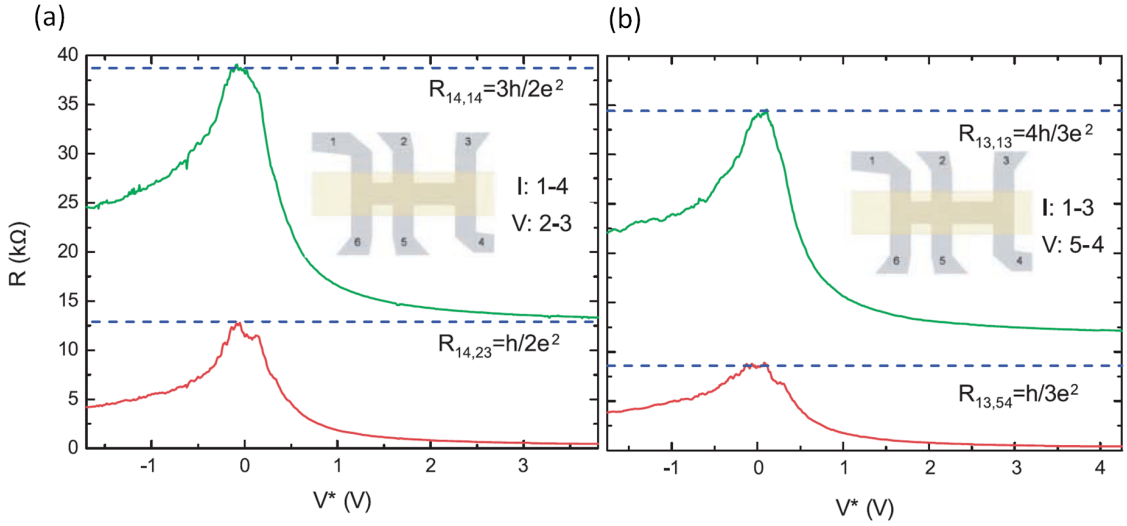

Figure 3.18: The two-terminal and four-terminal resistance of four different setups of a HgTe/CdTe quantum well as a function of gate voltage in the QSH regime. The blue dashed lines indicate the theoretical values for each setup, and $V^* = V_g - V_{th}$. The insets show the layout of the device, and the light yellow square on top of the Hall bar is the gate for adjusting the Fermi level. Adapted from [48].

Last but not least, one of the most important signatures of edge transport is the non-local signal. To unequivocally check whether the quantised conductance of $2e^2/h$ measured in small devices is not merely an outcome of ballistic transport (due to $L < l_{\text{mfp}}$) but indeed caused by edge transport, non-local measurements were performed by Roth *et al.* on a H-bar device and were also shown to be consistent with the Landauer-Büttiker calculation [48].

From the transport measurements described above, we see that the voltage difference between neighbouring voltage probes does not vanish even though they are connected by dissipationless edge states in the QSH regime. This seeming paradox can actually be explained by taking into account the nature of the materials of electrodes used in the experiments. In the BHZ model, the electrodes are assumed to be something that can purely measure the potential of helical edge states without affecting them. However, for a real device, the electrodes are usually made of metallic materials, which are n-type to the semiconductor

samples under test. When the edge states enter the *n*-type electrode, they effectively see a potential reservoir and are forced to equilibrate with it by scattering with the large number of bulk states inside the electrodes. Moreover, the helical edge states that come from opposite directions have different potentials before reaching the electrode, but are required to relax to the same potential as the *n*-type electrode afterwards. Consequently, dissipation occurs inside the electrodes and the voltage difference between two neighbouring voltage probes is created. That is to say, even the electrodes that merely work as voltage probes can introduce additional dissipation, and the measured resistance can be affected by the number of electrodes in the current path. This effect can be clearly observed in Fig. 3.18, in which $R_{14,14}$ and $R_{13,13}$ essentially have the same channel length, and $R_{14,23}$ and $R_{13,54}$ are basically an equivalent four-terminal configuration, yet the measured quantised conductance values are different.

It should be noted that the dissipationless transport of helical edge states is guaranteed by Kramers' theorem, which relies on the quantum phase coherence of wavefunctions. Contact with the metallic electrodes leads to decoherence between the wavefunctions of the incoming and outgoing states. Therefore, dissipation occurs when the phase coherence is destroyed in the electrodes. In contrast, although the phase decoherence effect of metallic electrodes also exists in a QH system, the voltage probes do not cause additional dissipation because all the chiral edge states travel in the same direction and thus the conduction is not affected by the decoherence mechanism.

3.5 Topological insulators

3.5.1 3D Topological insulators

After the realisation of QSH insulators, a question that naturally arises is whether the $\mathbb{Z}_2$ topological phases also exist in 3D systems. In the case of the QHE, it has been pointed out by theoretical studies that the existence of the QH phase in 3D systems is possible and can be viewed as the stacking of 2D QH systems [49–51]. Thus, there are three independent Chern numbers in a 3D QH system with the same meaning as the Chern number in a 2D QH system and can be used to calculate the transport behaviour in a 3D QHE. Can we find the analogue for the time-reversal symmetric system?

In 2006, the theories that generalise the $\mathbb{Z}_2$ topological order in a 2D system to 3D were developed by three different groups [16–19], and the connection between the topological order and the boundary states became clearer. Thus, the material with non-trivial topological band structures was given the generic name of a "topological insulator (TI)" [17], to distinguish it from the ordinary insulators with trivial band structures. For this reason, the

materials demonstrating the QSHE are often called 2D topological insulators in the literature thereafter.

Let us start from the band structure of a 3D TI. Similar to the 2D case (i.e. the QSH insulator) discussed in Sec. 3.4, the topological phase in a 3D system requires an inverted band structure. With band inversion, some boundary modes connecting the conduction band to the valence band are inevitably created. In addition, like the 2D case, the Kramers theorem requires the degeneracy of the time-reversal invariant points at certain positions in the Brillouin zone of a 3D TI. For example, in a surface Brillouin zone shown in Fig. 3.19, $\Gamma_1, \Gamma_2, \Gamma_3$, and Γ_4 are the four time-reversal invariant points that must be their own Kramers partners. Outside these four points, the Kramers degeneracy can be lifted by the SOC. Again, the key question is how these time-reversal invariant points are connected. Namely, does the intersection between the surface band and the Fermi level cross the line connecting Γ_i and Γ_j an even number of times or an odd number of times? Such a relation between the four Γ points can be described by four $\mathbb{Z}_2$ topological invariants denoted by $(\nu_0; \nu_1, \nu_2, \nu_3)$ [16, 17, 19]. As will be discussed later, ν_0 counts the number of Kramers degenerate points (modulo 2) inside the Fermi surface and has a similar meaning as the 2D $\mathbb{Z}_2$ topological invariants, while (ν_1, ν_2, ν_3) can be interpreted as the Miller indices of the orientation of the layers constituting the 3D TI.

The simplest way to construct a 3D TI is to stack the 2D TI layers, which is similar to the idea of constructing a 3D QH system mentioned in the beginning of this section. In this way, the QSH states in the weakly coupled 2D layers can stack along the y-direction and give rise to a surface Brillouin zone shown in Fig. 3.19(a), in which the intersection between the surface band and the Fermi level is depicted by the red curves. It can be seen that the red curve crosses the line connecting Γ_1 and Γ_2 and the line connecting Γ_3 and Γ_4 once each. Although this satisfies the condition of odd-number crossing and allows the presence of topological surface states, the surface states generated in this fashion are not protected by the time-reversal symmetry and can be easily destroyed by disorder. In the example in Fig. 3.19(a), the red curves (i.e. the Fermi surface) enclose an even number of degenerate points and hence this system has $\nu_0 = 0$. A 3D TI of this kind is called a weak topological insulator.

In contrast, a system with $\nu_0 = 1$ is called a strong topological insulator. An example of the strong topological insulator is shown in Fig. 3.19(b), in which the Fermi surface encloses an odd number of degenerate points, leading to $\nu_0 = 1$. Such a system cannot be built out of 2D TIs and is essentially a different topological phase to the QSHE [16, 19]. The example shown in Fig. 3.19(b) is the simplest case of a strong topological insulator, i.e. the Fermi surface encloses only one Γ point. Since the time-reversal symmetry requires any states at $\mathbf{k}$ to have their Kramers partners at $-\mathbf{k}$, the surface band near the Γ point is actually a

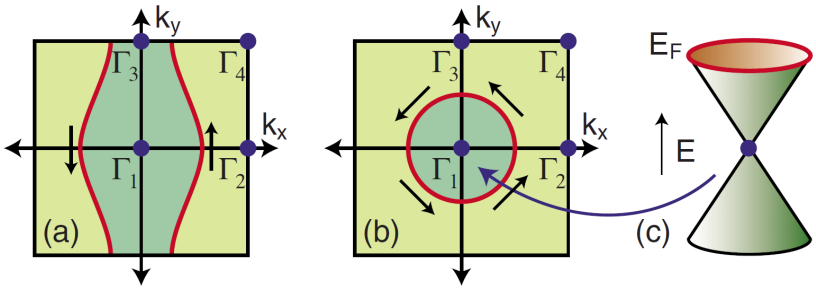

Figure 3.19: The surface Brillouin zone of a 3D time-reversal invariant system, adapted from [39]. Four time-reversal invariant points Γ_1, Γ_2, Γ_3 and Γ_4 appear at $(0,0)$, $(\pi/a,0)$, $(0,\pi/a)$ and $(\pi/a,\pi/a)$, respectively. (a) A weak topological insulator, in which an even number of Kramers degenerate points are enclosed by the Fermi surface (red curves). (b) A strong topological insulator, in which an odd number of Kramers degenerate points are enclosed by the Fermi surface (red circle). (c) In the simplest case of strong topological insulator, the Fermi surface encloses only one Dirac point and the dispersion forms a single Dirac cone. The black arrows in (a) and (b) indicate how the spin direction changes at different $\mathbf{k}$.

Dirac cone, as shown in Fig. 3.19(c). Moreover, because the two states of a Kramers pair carry opposite spins, the spin of one state at $\mathbf{k}$ must rotate around the Fermi surface and reverse its direction at $-\mathbf{k}$, as denoted by the arrows around the red circle in Fig. 3.19(b). As discussed in Sec. 3.4.2, the rotation of spin can introduce a Berry phase into the wavefunction. Circling the Dirac point rotates the spin by 2π and results in a Berry phase of π that can cause destructive interference and suppression of backscattering. This is why the surface states of a strong topological insulator are robust against disorder. In some sense it is similar to the helical edge states in the QSHE. Nevertheless, the transport of the topological surface states is diffusive rather than ballistic [39].

In summary, the strong topological insulator is the truly interesting 3D topological phase we are looking for. In the discussions hereafter, the 3D TIs without explicitly noting "weak" or "strong" should be referred to as strong topological insulators.

3.5.2 Experimental realisation of 3D topological insulators

Shortly after the theoretical models of 3D TIs were proposed, Fu and Kane predicted several materials as potential candidates for 3D TIs [52], including $Bi_{1-x}Sb_x$ alloy, α-Sn and strained HgTe. In 2008, Zahid Hasan's group successfully observed the topological surface states on $Bi_{1-x}Sb_x$ alloy using the angle-resolved photoemission spectroscopy (ARPES) and identified the first 3D TI [20].

Bismuth antimony alloy is a well-known material that has been extensively studied for its thermoelectric properties. Pure bismuth is a semimetal with normal band ordering, while

pure antimony is a semimetal with non-trivial band ordering. If the concentration of antimony in the alloy is continuously increased, the gap of bismuth will close and reopen in a certain range of x, as explained in Fig. 3.20.

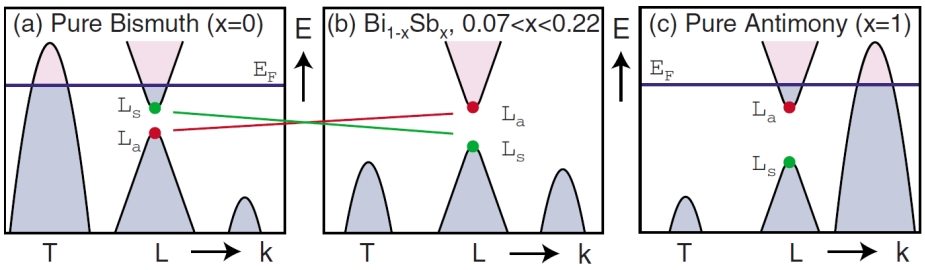

Figure 3.20: The evolution of the band structure of $Bi_{1-x}Sb_x$ alloy with the change of antimony concentration x, adapted from [39]. (a) Pure bismuth is a semimetal with indirect band gap. The top of valence band at the T point is higher than the minimum of conduction band, creating pockets of holes near the T point. As the concentration of antimony x increases, the maximum of valence band at T becomes lower. When $x \approx 0.04$, the gap between L_a and L_s closes and a Dirac cone forms at the L point. The gap will be reopened with an inverted order if x is further increased. (b) When $x > 0.07$, the top of valence band at T point falls below the bottom of conduction band at L point, and the alloy becomes an insulator with a direct band gap. After $x > 0.22$, the valence band on the right side of L point can rise and exceed the bottom of conduction band at L point. The system then becomes a semimetal again, as shown in (c).

In the experiments of Hsieh *et al.*, the surface states are found to emerge around $x = 0.1$ and the surface bands are directly mapped out using ARPES [20]. When $x = 0.1$, the alloy shows a direct bulk gap with five surface bands crossing the Fermi level between the Γ and M point in the Brillouin zone, as shown in Fig. 3.21, suggesting this system has a non-zero $\mathbb{Z}_2$ invariant ν_0 and therefore topological surface states.

Later, Hasan's group also performed a spin-resolved ARPES measurement which unequivocally confirmed the predicted spin texture of the surface bands and the π Berry phase of $Bi_{1-x}Sb_x$ [53]. The robustness of surface states against non-magnetic impurities was directly verified by Roushan *et al.* using scanning tunnelling spectroscopy and spin ARPES [54].

However, although the 3D $\mathbb{Z}_2$ phase is confirmed by these experiments, $Bi_{1-x}Sb_x$ is not an ideal system for further characterisation and study of TIs due to its complicated band structure and small band gap. This motivated the search for other 3D TIs in similar type of materials with simpler band structures.

In 2009, Zhang *et al.* predicted Bi_2Te_3, Bi_2Se_3 and Sb_2Te_3 as potential candidates for the second generation of 3D TI [55]. This "X_2Y_3" family has an inverted band structure owing to the strong SOC originating from Bi and Te atoms. Therefore, Sb_2Se_3, a material with a

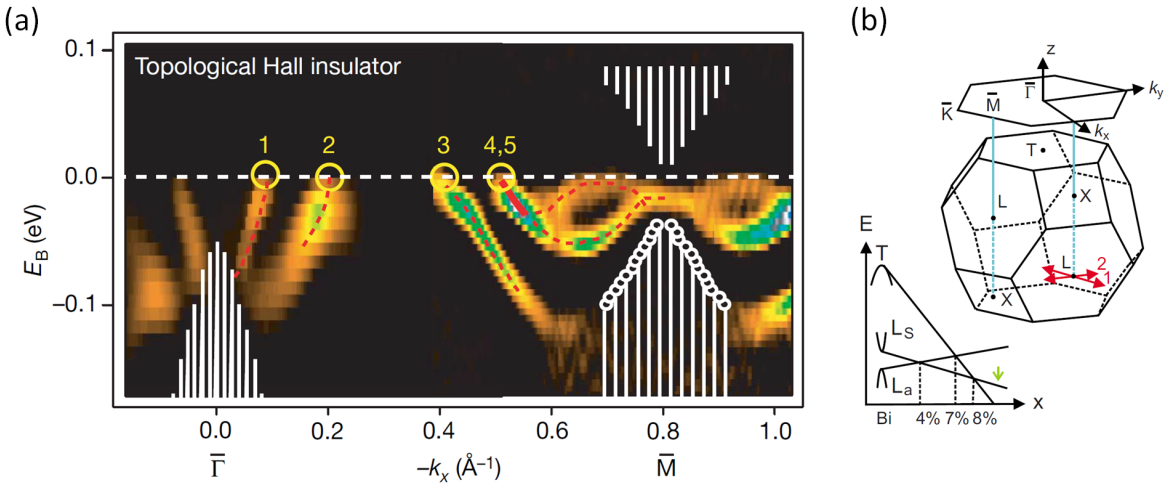

Figure 3.21: (a) The ARPES image of the band structure of $Bi_{0.9}Sb_{0.1}$ along the Γ-M direction. The white shaded regions represent bulk bands and the coloured regions are the density of surface states (red lines are guides to the eye). The surface bands cross the Fermi level five times, as indicated by the yellow circles, suggesting that this system has non-zero $\mathbb{Z}_2$ invariant ν_0 and topological surface states. (b) A schematic diagram showing the projection of the 3D Brillouin zone on the (111) surface. The images are adapted from [20].

similar "X_2Y_3" composition, does not have sufficiently strong SOC and is not a 3D TI. The band structures of these four materials obtained by the *ab initio* calculation are shown in Fig. 3.22 [55]. These materials have larger band gaps and simpler band structures compared to $Bi_{1-x}Sb_x$. In addition, since they are pure compounds rather than alloys like $Bi_{1-x}Sb_x$, the synthesis of high quality samples is relatively easier. Purer TI samples naturally result in clearer surface bands, which is favourable for experiments. Shortly after the theoretical prediction, the first 2nd-generation TI was experimentally realised by Xia *et al.* [56]. More detailed studies on the 2nd-generation 3D TIs have been carried out in a number of works [57–61], and show that these materials belong to the topological class $(\nu_0;\nu_1\nu_2\nu_3) = (1;000)$ instead of (1;111) of the $Bi_{1-x}Sb_x$.

Among the 2nd generation of 3D TIs, the most remarkable one is Bi_2Se_3. The crystal structure of Bi_2Se_3 is schematically shown in Fig. 3.23(a) [55]. The building block of Bi_2Se_3 is one quintuple layer (QL), which is composed of two layers of bismuth and three layers of selenium. This QL-based structure is the same as for Sb_2Te_3 and Bi_2Te_3, and is a crucial factor that affects the properties of TIs. The band structure measured by ARPES is shown in Fig. 3.23(d) [62]. The surface bands of Bi_2Se_3 have a highly symmetric single Dirac cone, and the large band gap of ∼0.3 eV means the topological behaviour can survive at room temperature [58], which substantially increases its potential for use in practical applications.

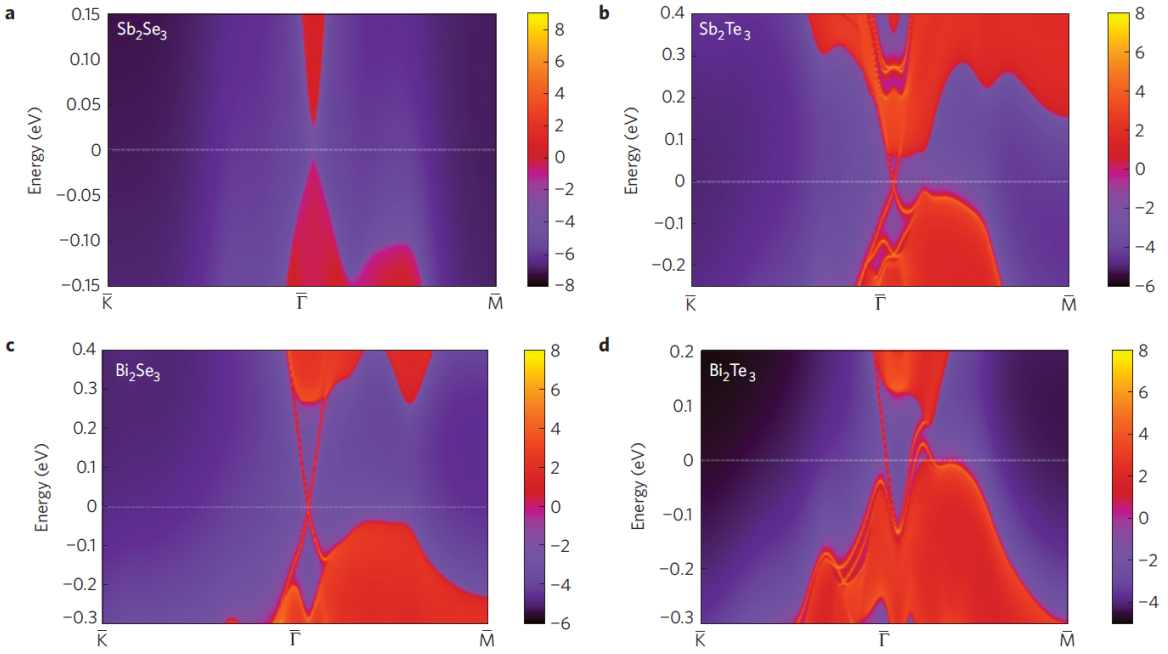

Figure 3.22: *Ab initio* calculations of the band structures of the 2nd-generation 3D TIs (a) Sb_2Se_3, (b) Sb_2Te_3, (c) Bi_2Se_3, and (d) Bi_2Te_3. The warmer colours represent higher local DOS. The SOC in Sb_2Se_3 is too weak to induce surface states. In contrast, clear Dirac surface bands can be observed as red lines crossing around the Γ point in the other three compounds. Note that the Dirac point of Bi_2Te_3 is buried in the bulk valence band. Images are adapted from [55].

Due to these advantages, Bi_2Se_3 has become the most frequently used material for studying many of the predicted properties in 3D TIs.

The experiments investigating the properties of 3D TIs introduced so far are mostly ARPES measurements. One may wonder if it is possible to use transport measurements to study the behaviour of the surface states in 3D TIs, just like in the research of QHE and QSHE. A major advantage of ARPES is that the contribution from the surface and bulk can be well distinguished. On the other hand, in transport measurements the signals from the surface and bulk are almost always mixed together, and the topological signatures of surface states can be smeared out by the residual bulk states.

Some transport measurements did report the observation of quantum oscillation in the surface states of 3D TIs, but these surface signals are generally quite small compared to the bulk signals co-existing in the systems [63–66]. The influence of residual bulk states may depend on, for instance, the doping from air after a fresh sample starts to be exposed in atmosphere, or mid-gap states caused by impurities introduced during the sample growth.

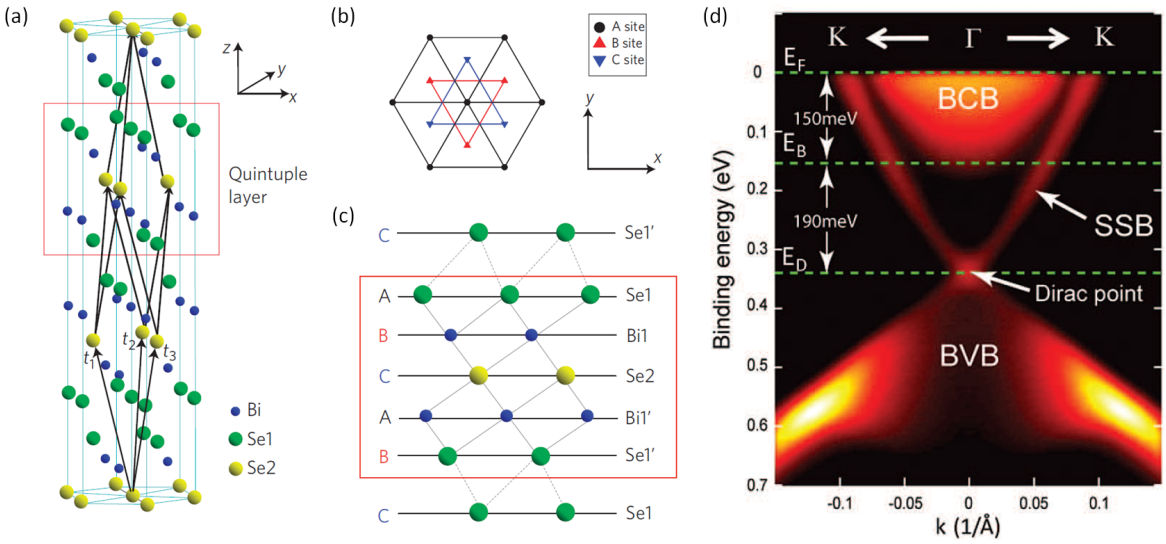

Figure 3.23: (a) The crystal structure of Bi_2Se_3. t_1, t_2, and t_3 are the primitive lattice vectors. A QL structure is indicated by the red square. (b) A top view of the crystal structure along the z-direction. The three different positions between layers in one QL are denoted by A, B and C. (c) A side view of the crystal structure. The stacking order in a QL is A(Se1)–B(Bi1)–C(Se2)–A(Bi1')–B(Se1'). The Se1' (Bi1') layer corresponds to the Se1 (Bi1) layer with an inversion operation using the Se2 atoms as inversion centres. (d) The band structure of Bi_2Se_3 measured by ARPES. The Dirac cone is symmetric about the Γ point, and a bulk gap of ∼0.3 eV can be useful for practical applications at room temperature. Images are adapted from [55, 62].

For some samples, the Fermi level even crosses the bulk bands intrinsically, resulting in a large number of bulk carriers.

Several solutions have been proposed to reduce the bulk carriers, including increasing the surface-to-volume ratio of samples [63], tuning the Fermi level into the bulk gap by doping complementary elements [61, 58, 60, 62] or electric gating [67, 68], and making ternary or quaternary compounds of $Bi_{2-x}Sb_xTe_{3-y}Se_y$ (where $0 \leq x \leq 2$ and $0 \leq y \leq 3$). The approach using $Bi_{2-x}Sb_xTe_{3-y}Se_y$ is particularly useful because it allows the tuning of the Fermi energy, the position of the Dirac point, and the size of the bulk gap, leading to TI systems with significantly less bulk conduction and much more prominent surface signals in transport measurements [65, 69].

Since the transport measurements can provide important insights into the behaviour of topological states that cannot be probed by ARPES measurements, the ability of preparing high quality TI samples directly relates to most of the recent experimental breakthroughs. Therefore, eliminating the residual bulk contribution is one of the most crucial and urgent works in the research of 3D TIs.

3.6 Quantum anomalous Hall effect

3.6.1 Breaking the time-reversal symmetry of topological insulators

The anomalous Hall effect is an analogue of the Hall effect except the time-reversal symmetry of the system is broken by the magnetisation of the material itself rather than an external magnetic field. It was first discovered by Hall in his subsequent study [70] of the Hall effect in 1881. After the realisation of the Hall effect, the spin Hall effect [71, 72], and their quantum versions, QHE and QSHE, researchers started to question whether the quantised version of the anomalous Hall effect, i.e. the quantum anomalous Hall effect (QAHE) could also be found.

The first theoretical model of the QAHE was proposed by Liu *et al.* in a Mn-doped HgTe/CdTe quantum well system [73], as shown in Fig. 3.24. The magnetisation induced by Mn atoms can lift the spin degeneracy of the 2D bulk bands and introduce a spin-splitting of $2G_E$ for the electron bands $|E1,\pm\rangle$ and $2G_H$ for the hole bands $|H1,\pm\rangle$. The energy gap can be given by $E_g^+ = 2M_0 + (G_E - G_H)$ for the spin-up bands and $E_g^- = 2M_0 - (G_E - G_H)$ for the spin-up bands, where $2M_0$ is the gap size before spin-splitting. If $|G_E|$ and $|G_H|$ are large enough and $G_E G_H < 0$, i.e. the spin-splitting for $|E1,\pm\rangle$ and $|H1,\pm\rangle$ have opposite signs, the spin-up bands and the spin-down bands will be shifted in opposite directions. As shown in Fig. 3.24(a), the spin-down bands $|E1,-\rangle$ and $|H1,-\rangle$ will move closer and eventually touch each other, returning to the trivial band ordering, while the spin-up bands $|E1,+\rangle$ and $|H1,+\rangle$ will move further away from each other and the inverted band structure remains. Consequently, one of the counterpropagating helical edge states is destroyed, leaving only a single spin-polarised chiral edge state propagating along the edges of the quantum well, as shown in Fig. 3.24(b).

However, the spins of Mn in the HgTe/CdTe quantum well are in fact paramagnetic rather than ferromagnetic [74], which means an external magnetic field is still required to maintain the magnetisation of the material, hindering the verification of QAHE.

Later, a different system that can host the QAHE was proposed by Yu *et al.* [75]. Instead of using the 1D boundaries of a 2D QSH system, this approach uses the 2D boundaries of a 3D TI to realise the QAHE. As shown in Fig. 3.25, when the ferromagnetism is induced in a 3D TI by dopants, a magnetisation perpendicular to the surface plane can break the time-reversal symmetry and open a magnetic gap in the surface bands, making both the 3D bulk and 2D surface insulating. Nevertheless, an exception occurs at the domain boundary between the magnetisations with opposite directions. At the domain boundary, the magnetisation reverses direction and the magnetic gap will close due to the absence of out-of-plane magnetisation. The resulting gapless states at the domain boundary are developed from the topological

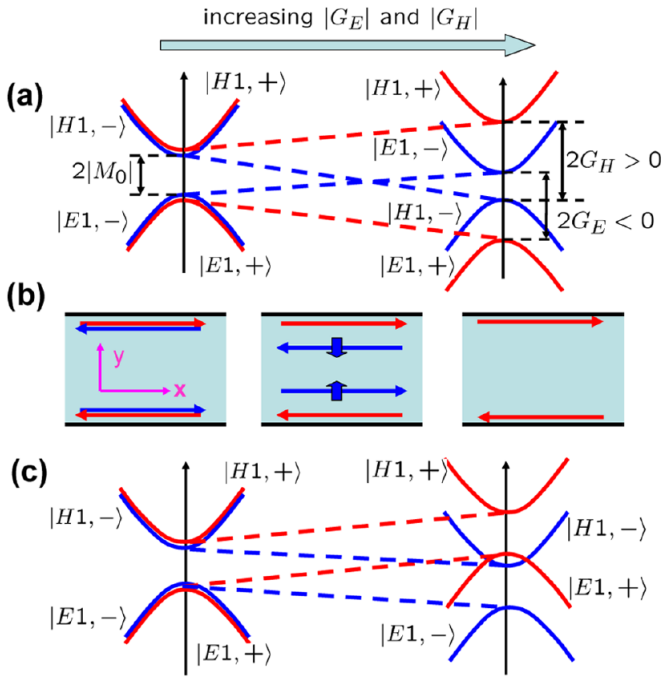

Figure 3.24: An example showing the evolution of the band structure of a TI with spin-splitting. (a) When G_E and G_H have different signs, the spin-down bands (blue) is driven back to the trivial band ordering, while the spin-up bands (red) remains topologically non-trivial. (b) Schematics showing how the helical edge states evolve during the band crossing in (a). One of the helical states is removed in this process, leaving a single spin-polarised chiral edge state conducting in the system. (c) When G_E and G_H have the same sign, the $|H1,-\rangle$ and $|E1,+\rangle$ touch each other without opening a gap, and the QAHE cannot be attained. Adapted from [73].

surface states and thus preserve the helical property despite their Kramers partners being removed by the broken time-reversal symmetry. As a result, we are left with a spin-polarised chiral edge mode propagating along the domain walls, giving rise to the QAHE.

For a thin film of 3D TI with a uniform magnetisation normal to the top and bottom surfaces, as shown in Fig. 3.26(a), such a reversal of magnetisation must take place on the side surface to change from inward (at the bottom) to outward (at the top), which effectively makes the side surface a domain wall. Due to the size confinement, the 2D conduction on the side surface can be suppressed and the side surface becomes a quasi-1D channel. The QAH states then are predicted to exist at the top and bottom corners of the side surface.

Since this system is no longer time-reversal invariant, it cannot be characterised by the $\mathbb{Z}_2$ topological invaraints anymore. As discussed earlier in this chapter, such a topological phase without time-reversal symmetry should be described by the $\mathbb{Z}$ topological invaraints, i.e. Chern numbers, like the QHE.

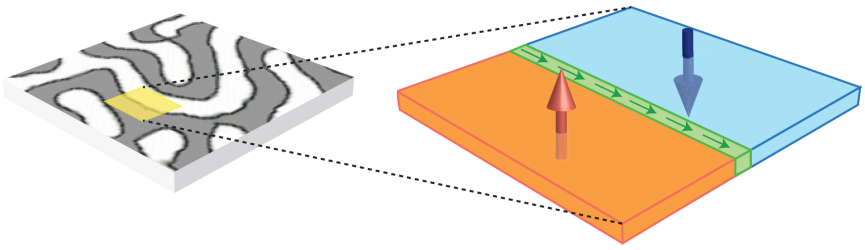

Figure 3.25: The left panel shows the magnetic domains that form on the surface of a 3D TI because of the induced ferromagnetism. The white and grey regions are the domains with the downward and upward magnetisation, respectively. The right panel shows the closeup image of the highlighted region in the left panel. At the domain boundary, the magnetic gap vanishes due to the reversal of magnetisation (i.e. from the red arrow to the blue arrow), leading to the presence of the spin-polarised chiral edge mode, i.e. the QAH state, in the domain wall (green region). Adapted from [76].

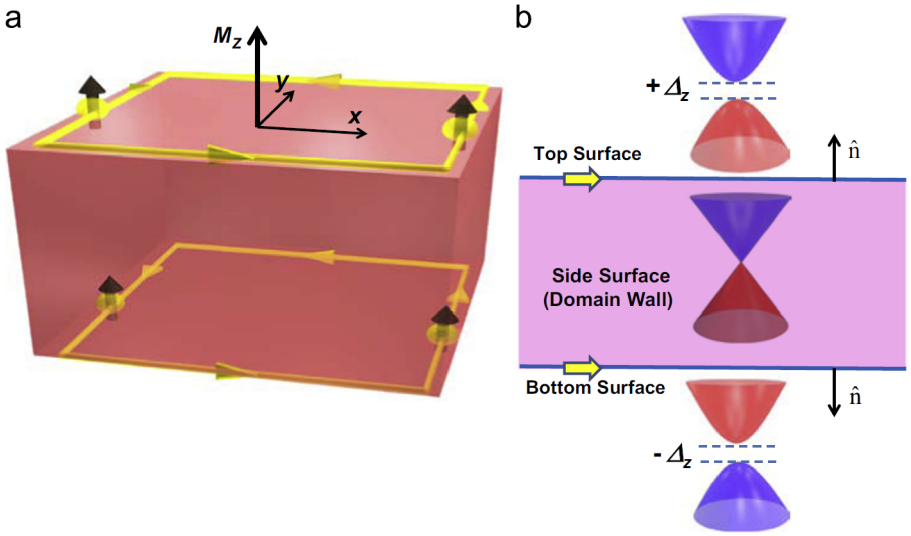

Figure 3.26: (a) A thin film of 3D TI with a uniform magnetisation M_z normal to the top and bottom surfaces. The reversal of magnetisation must take place on the side surface to change from inward (at the bottom) to outward (at the top), which effectively makes the side surface a domain wall. Therefore, the QAH states appear at the top and bottom corners of the side surface. (b) A schematic showing the band structures of different surfaces. On the top and bottom surfaces, a magnetic gap is opened in the surface bands due to the out-of-plane magnetisation, whereas on the side surface this gap is closed because the out-of-plane magnetisation vanishes here. Adapted from [77].

Wang *et al.* argued that the Chern number of such a thin film QAH system can be tuned by the thickness of the film and the size of the magnetic gap [78]. Since the thickness can be precisely controlled by the molecular beam epitaxy (MBE) growth, and the gap size can also be finely adjusted by the doping level of magnetic elements during the MBE growth,

this idea should enable the creation of materials with selected Chern numbers. Nonetheless, there are still some constraints in practice. For instance, if the film is too thick, the 2D conduction on the side surface will obscure the 1D transport behaviour. If the film is too thin, the wavefunctions of surface states from the top and bottom surfaces will hybridise and form a gap [79–81]. When this hybridisation gap becomes larger than the magnetic gap, the QAHE will disappear. In addition, a larger magnetic gap necessarily requires a stronger exchange coupling from the magnetic dopants. To date, finding the elements that can generate sufficiently strong exchange coupling in TIs remains to be one of the biggest challenges in this field. Because of these reasons, currently the only achievable phase is the QAHE with $\mathcal{C} = 1$.

Since the Chern number represents the number of conducting edge channels, for the thin film shown in Fig. 3.26(a), the top surface and bottom surface should have $\mathcal{C} = 1$ and $\mathcal{C} = -1$, respectively. If this thin film can be made into a Hall bar, we should observe a vanishing longitudinal resistance and a quantised Hall resistance in multi-terminal measurements, similar to that in the QHE.

However, the manifestation of QAHE is different from the QHE in a subtle but important way. Let us first consider the effect of a magnetic field on a 3D TI. When the surface of a 3D TI is under a perpendicular magnetic field, the single Dirac point on the surface allows the existence of a Landau level at zero energy. This zero Landau level is particle-hole symmetric, which means the Hall conductivity should be equal but with opposite signs when this Landau level is completely empty or full. As a result, since the conductivity must vary in units of e^2/h, the Hall conductivity of such a time-reversal symmetry broken TI should be determined by

$$\sigma_{xy} = (n + \frac{1}{2})\frac{e^2}{h}, \tag{3.61}$$

for integers $n \geq 0$ [52, 82, 83]. This is a familiar form that was seen in the study of the QHE on graphene [84, 85], except the four-fold degeneracy (2 spins $\times$ 2 valleys) of graphene turns Eq. 3.61 into $4(n + \frac{1}{2})\frac{e^2}{h}$, leading to quantised values of $2e^2/h$, $6e^2/h$, $10e^2/h\ldots$ and so on. However, for the QHE in TIs, the single Dirac point necessarily results in half-integer quantised values. This inference is also true for a QAH system (though there is no Landau level forms in the QAHE, as will be discussed later). The half-integer quantised values seemingly cause a problem because the Chern numbers should always be integers, and the existence of a half conducting channel is unreasonable. Fortunately, this paradox can be resolved because a closed surface does not have a boundary. In other words, the top and bottom surfaces of the thin film TI must be connected by the side surface, and hence the simultaneous measurement of the top and bottom surfaces is inevitable in reality [39, 83]. Since the top and bottom surfaces have $\mathcal{C} = 1$ and $\mathcal{C} = -1$, respectively, the side surface in

between has to be $\mathcal{C} = 0$. Consequently, the two states at the top and bottom corners of the side surface each contribute $e^2/2h$ and give rise to a total conductance of e^2/h. Therefore, a Hall plateau at h/e^2 accompanied by a vanishing longitudinal resistance in four-terminal measurements is the unique signature of the QAHE.

The next section will briefly review the experimental approaches for realising the QAHE, as well as the challenge and questions in the research of magnetic TIs.

3.6.2 Experimental realisation of the quantum anomalous Hall effect

In principle, there are two ways to induce ferromagnetism in TIs. The first one is to utilise the proximity effect [82]. For instance, when a TI film is brought into proximity of a magnetic material, the spins in the TI may be affected by the exchange effect from the magnetic material, and hence introduce magnetism into the TI film. This idea has been carried out in several systems, including growing different TI films on magnetic insulators such as EuS [86, 87] and YIG [88, 89], and confirmed that ferromagnetism can be successfully induced in TI films by the proximity effect.

Nevertheless, the proximity-induced ferromagnetism is usually quite weak due to the surface roughness and impurities trapped in the interface between the two materials. Thus, although the anomalous Hall effect has been observed in these heterostructures, the quantised version still has not been achieved so far.

The second approach towards magnetic TIs is by doping transition metal atoms into the TI materials. The ferromagnetic order is then possible to be induced by the exchange coupling from the unfilled d-orbitals of the dopants.

In 2010, Chen *et al.* realised the first magnetic TI system of this kind [62]. By controlling the doping level of Fe or Mn atoms, a magnetic gap was opened at the surface Dirac point of Bi_2Se_3, as shown in the ARPES image of Fig. 3.27. The feature of the QAH states was not detected in this paper, probably because the measurement was performed on a Bi_2Se_3 bulk crystal, in which the surface states could be overwhelming. Nonetheless, they demonstrated that magnetic doping is a viable way for introducing magnetism into TIs and paved the way for the realisation of the QAHE in magnetically doped TI systems.

As introduced in Sec 3.5.2, the use of $Bi_{2-x}Sb_xTe_{3-y}Se_y$ can effectively reduce the bulk carriers and provide a flexible tunability for the band structures of TIs. By carefully choosing x and y, it is possible to prepare a TI with both its Fermi level and Dirac point locating inside a highly insulating bulk gap. With additional magnetic doping and sample thickness control, a magnetic TI with desired band structures is not unattainable. Therefore, the $Bi_{2-x}Sb_xTe_{3-y}Se_y$ family became the most promising platform for realising the QAHE.

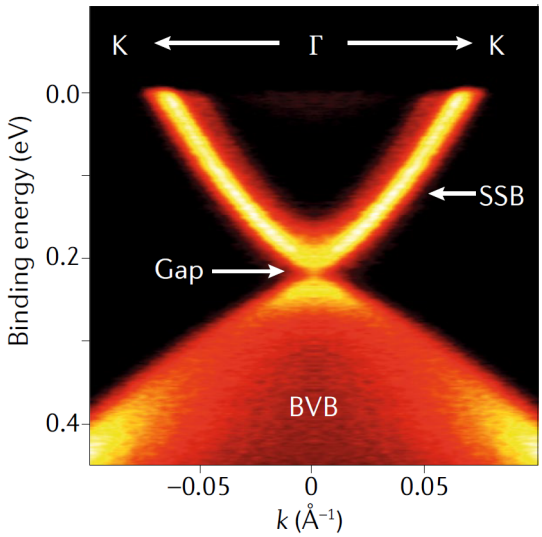

Figure 3.27: The ARPES measurement showing a magnetic gap that is opened at the surface Dirac point by the Fe atoms doped in the Bi_2Se_3 bulk crystal. The gap size is estimated to be at least 7 meV. Adapted from [62]

In the next few years, numerous theoretical studies and systematically designed band-engineering experiments were conducted to seek the optimal condition for realising the QAHE, including finding the appropriate x and y parameters for $Bi_{2-x}Sb_xTe_{3-y}Se_y$ [90–92], the suitable magnetic dopants [62, 75, 93–95] and substrates [96–98], and the proper thickness of TI films [96, 97, 99, 100]. A large number of properties related to various magnetic TI systems were investigated in these studies and the quality of samples became progressively better with the improved sample-growth parameters. In 2013, the QAHE was finally observed by Chang *et al.* in a 5 QL Cr-doped $(Bi,Sb)_2Te_3$ film on $SrTiO_3$ (STO) substrate at 30 mK and the predicted Hall resistance of h/e^2 was verified [93], as shown in Fig. 3.28.

In Fig. 3.28(a), the ρ_{yx} curve exhibits a square-shaped magnetic hysteresis loop at all V_g values, which clearly indicates a long-range ferromagnetic order with out-of-plane magnetisation forming in the TI film. The two sharp transition regions between the ρ_{yx} plateaux in Fig. 3.28(a) and the two prominent peaks shown in the ρ_{xx} curves in Fig. 3.28(b) appear around the coercive field (H_c), suggesting that the magnetisation reversal process drives the sample into a multi-domain state that allows backscattering to take place through its 2D surfaces. When the sample is fully magnetised, ρ_{yx} saturates at $\pm h/e^2$ while ρ_{xx} becomes extremely low. Moreover, when the external magnetic field is ramped back to zero, the magnetisation of the sample does not disappear, giving rise to the quantised ρ_{yx} even at zero external magnetic field, which is exactly the expected behaviour of the QAHE. When the

zero-field (ZF) ρ_{yx} and ρ_{xx} are converted to conductance, $\sigma_{yx}(0)$ and $\sigma_{xx}(0)$ were found to be 0.987 e^2/h and 0.096 e^2/h, respectively. Chang *et al.* ascribed the deviation of $\sigma_{yx}(0)$ from e^2/h and non-zero $\sigma_{xx}(0)$ and $\rho_{xx}(0)$ to the residual dissipative conduction channels in the sample. Therefore, higher magnetic fields were applied in the attempt to localise the residual dissipative states. It turns out that ρ_{xx} does drop with the increasing external magnetic field and vanish completely above 10 T, supporting their argument regarding the possible origin of the non-zero $\rho_{xx}(0)$.

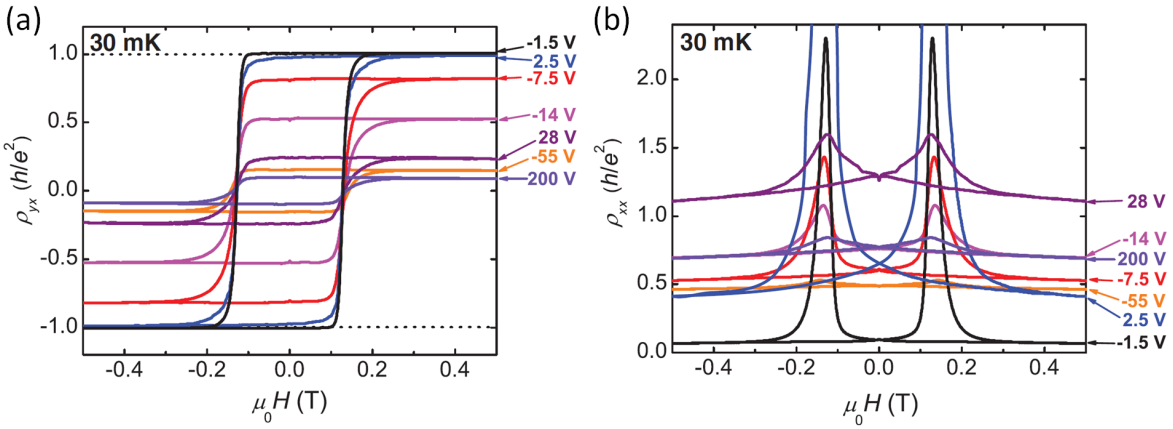

Figure 3.28: The first observation of QAHE on a 5 QL $Cr_{0.15}(Bi_{0.1}Sb_{0.9})_{1.85}Te_3$ on $SrTiO_3$ substrate at 30 mK. (a) The magnetic field dependence of Hall resistance (ρ_{yx}) at different gate voltage (V_g) values. The ρ_{yx} plateaus at h/e^2 in the fully-magnetised state at $V_g = -1.5$ V. (b) The magnetic field dependence of sheet longitudinal resistance (ρ_{xx}) at different V_g values. The zero-field ρ_{xx} is found to be as low as 0.098 h/e^2. Adapted from [93].

However, it is worth noting that the QAHE observed in different samples can be quite different in detail. For example, three studies that observed the QAHE in Cr-doped $(Bi,Sb)_2Te_3$ samples saw slightly different ρ_{xx} butterfly structures and ρ_{yx} hysteresis loops, as shown in Fig. 3.29. Firstly, if we compare the high magnetic field sweeps performed on different samples, as shown in Fig. 3.29(a), (b), (e) and (f), it can be seen that the longitudinal resistance approaches zero in two different ways. In Fig. 3.29(b) and (f), the longitudinal resistance drops asymptotically to zero beyond the coercive field, while in Fig. 3.29(e) a change in slope occurs beyond the coercive field and the lowest longitudinal resistance obtained turns out to be in the low magnetic field regime. Secondly, in the low magnetic field regime, the Hall resistance in Fig. 3.29(c) has a sharper transition around the coercive field than that in Fig. 3.28(a) and the inset of Fig. 3.29(f). Finally, the longitudinal resistance in Fig. 3.29(d) shows small lumps around 0 T (which has also been observed in [101, 102]), while such structures are not present in Fig. 3.28(b) and the inset of Fig. 3.29(f). Of course there are other different features between the QAHE observed in these samples, such as the

value of the coercive field, the magnetic field with minimum longitudinal resistance, and many more. The discrepancy between the QAHE observed in different samples may arise from the different origins of dissipative states in the samples, such as the thermal activation [101], variable range hopping [93], residual bulk and surface conduction, and gapless edge states [103, 104]. These possible dissipative conduction mechanisms are almost definitely associated with the non-vanishing ZF longitudinal resistance in the QAHE observed so far. Therefore, it is important to keep in mind that the manifestation of the QAHE is not as sample-independent as the QHE, probably due to the alloying nature of the magnetic TI materials.

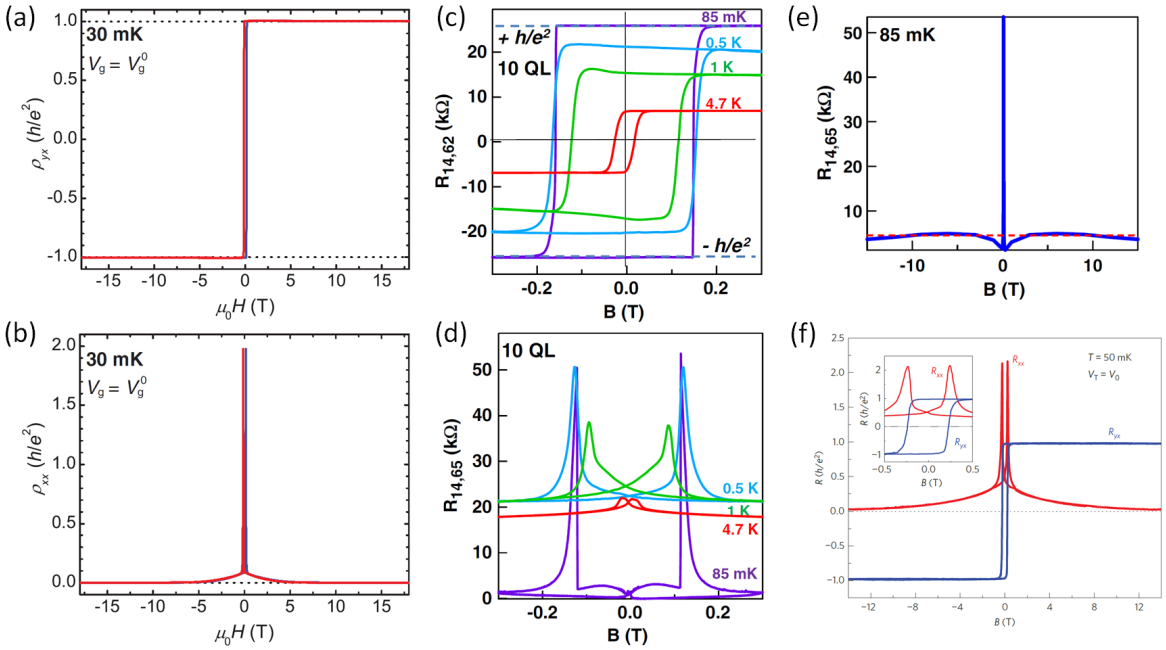

Figure 3.29: The comparison between the QAHE observed on different Cr-doped $(Bi,Sb)_2Te_3$ samples. (a) and (b) show the high magnetic field sweeps performed on the 5 QL $Cr_{0.15}(Bi_{0.1}Sb_{0.9})_{1.85}Te_3$ film on STO (111) substrate by Chang *et al.* [93]. (c) and (d) show the low magnetic field sweeps and (e) shows the high magnetic field sweeps performed on the 10 QL $Cr_{0.24}(Bi_{0.3}Sb_{0.7})_{1.76}Te_3$ film on GaAs substrate by Kou *et al.* [104]. (f) shows the high magnetic field sweep performed on the 8 QL $Cr_{0.22}(Bi_{0.2}Sb_{0.8})_{1.78}Te_3$ film on InP (111) substrate by Checkelsky *et al.* [105]. The inset in (f) is the closeup image of the low field regime in the main plot. Figures are adapted from [93, 104, 105].

After two years, Chang *et al.* realised the second QAH system in the V-doped $(Bi,Sb)_2Te_3$ samples [106], as shown in Fig. 3.30. Remarkably, the QAHE in V-doped $(Bi,Sb)_2Te_3$ exhibits a more precise quantised value than the Cr-doped $(Bi,Sb)_2Te_3$ samples. At 25 mK, the Hall resistance at zero magnetic field, $\rho_{yx}(0)$, reaches 1.00019 ± 0.00069 h/e^2 ($\sim 25817.8 \pm 17.7$ Ω), while the longitudinal resistance at zero magnetic field, $\rho_{xx}(0)$,

drops to $0.00013 \pm 0.00007\ h/e^2$ ($\sim 3.35 \pm 1.76\ \Omega$), which corresponds to a Hall conductance $\sigma_{yx}(0) = 0.9998 \pm 0.0006\ e^2/h$ and a sheet longitudinal conductance $\sigma_{xx}(0) = 0.00013 \pm 0.00007\ e^2/h$, respectively. In addition, as can be seen in Fig. 3.30(a), the V-doped $(Bi,Sb)_2Te_3$ film has a higher coercive field, which implies that the ferromagnetic order formed in V-doped TIs is more robust against external perturbation compared to the Cr-doped TIs. The ZF cooling curves of ρ_{xx} and ρ_{yx} for another $V_{0.11}(Bi_{0.29}Sb_{0.71})_{1.89}Te_3$ film (with the same thickness) are shown Fig. 3.30(b). An upturn of the ρ_{yx} curve at ~ 23 K signals the onset of the anomalous Hall effect, implying a Curie temperature of $T_C \sim 23$ K and the fact that a spontaneous magnetisation occurred in the sample during the cooling process without an external magnetic field. Furthermore, a phase transition from the semiconducting to the QAH regime below 2.5 K was also observed without the aid of an external magnetic field. This self-driven ferromagnetism and QAHE is absent in the Cr-doped TIs, and can be useful for future applications without the need of an applied magnetic field. Lastly, as shown in Fig. 3.30(c), the QAHE in this V-doped TI can be observed at 120 mK, which is much higher than the Cr-doped TIs. The red traces in Fig. 3.30(c) represent the magnetic field sweeps starting from the virgin state, and the blue traces are magnetic field sweeps after magnetic training. The similarity between them suggests that the sample has already become magnetised before the magnetic training, supporting the observation of spontaneous magnetisation observed in Fig. 3.30(b).

In summary, the V-doped TIs has a self-driven magnetisation and QAHE as well as higher H_c and T_C compared to the Cr-doped TIs, suggesting the long-range ferromagnetic order in V-doped TIs is stronger than that in Cr-doped TIs. This may in turn imply that the QAHE with higher critical temperatures is more likely to be found in V-doped TIs.

Just like in the QSHE, non-local measurements were also carried out on the Cr-doped and V-doped TIs to probe the edge transport behaviour of the QAHE [104, 107]. Kou *et al.* analysed the non-local signal measured in their 10 QL $Cr_{0.24}(Bi_{0.3}Sb_{0.7})_{1.76}Te_3$ film and argued that gapless states may exist on the side surfaces of such a thicker TI film, causing the non-vanishing longitudinal resistance at zero magnetic field [104].

Chang *et al.* performed a series of more comprehensive measurements to investigate the transport behaviour of the QAHE using a 4 QL V-doped $(Bi,Sb)_2Te_3$ film [107]. In their study, two-terminal, three-terminal, as well as four-terminal local and non-local measurements of different configurations were carried out to distinguish the contribution from various types of conducting channels in the sample. From the results, they speculated that both chiral and non-chiral edge states exist in their sample and contribute to the total non-local signals together. A possible origin of the non-chiral edge states is the side surface, similar to the conclusion of Kou *et al.* [104]. However, in contrast to the 10 QL Cr-doped TI film used by

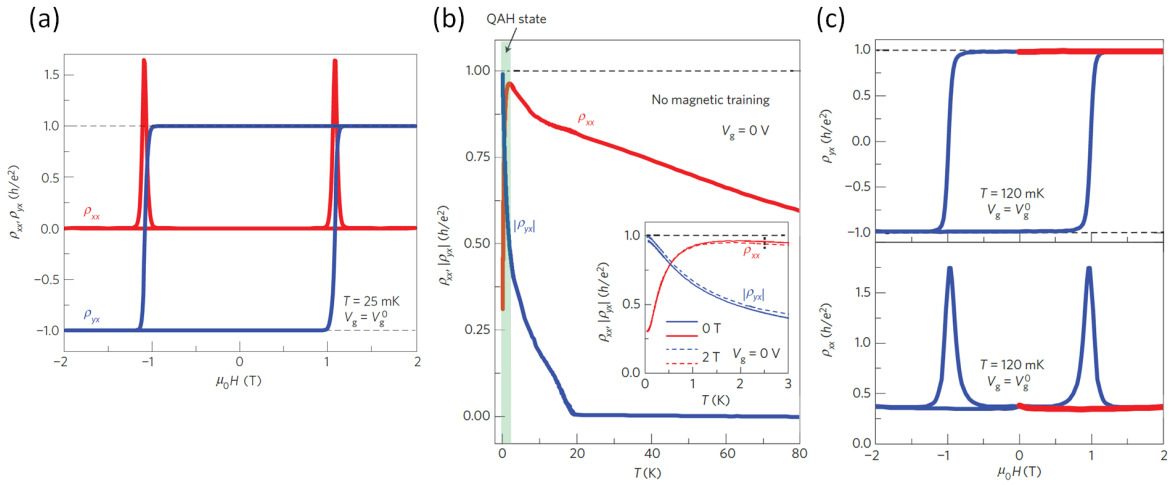

Figure 3.30: The first observation of QAHE on a 4 QL $V_{0.11}(Bi_{0.29}Sb_{0.71})_{1.89}Te_3$ on STO (111) substrate. (a) The magnetic field dependence of ρ_{xx} and ρ_{yx} when the Fermi level is tuned to the charge neutrality point. A clear QAHE with $\rho_{yx}(0) = 1.00019 \pm 0.00069\ h/e^2$ and $\rho_{xx}(0) = 0.00013 \pm 0.00007\ h/e^2$ is observed. (b) The ZF cooling curves of ρ_{xx} and ρ_{yx} for another $V_{0.11}(Bi_{0.29}Sb_{0.71})_{1.89}Te_3$ film show the onset of spontaneous magnetisation and anomalous Hall effect at $\sim$ 23 K, followed by a phase transition from the semiconducting to the QAH regime below 2.5 K. The inset shows that the cooling curves under the external magnetic fields of 0 T (solid line) and 2 T (dashed line) almost overlap with each other, suggesting that the sample can be driven into a magnetised state during the cooling process without an external magnetic field. (c) The QAHE observed in the V-doped TI at 120 mK. The red traces represent the magnetic field sweeps starting from the virgin state, and the blue traces are the magnetic field sweeps after magnetic training. Adapted from [106].

Kou *et al.*, their 4 QL V-doped film is much thinner and the 2D gapless states on the side surfaces may be gapped and become quasi-1D channels due to the quantum confinement effect. Consequently, the magnetic TI system will only show pure dissipationless transport when the Fermi level is tuned into the mini-gap of the non-chiral edge channels, as shown in Fig. 3.31(a), and this is a possible cause of the non-vanishing ZF longitudinal resistance. The size of the mini-gap is estimated to be $\sim$ 50 μeV, which is consistent in order of magnitude with the observations from other groups [101, 108–110]. Since it is much smaller than the magnetic gap, it may well be the reason why the critical temperature of the QAHE is two orders of magnitude smaller than the Curie temperature. In addition, they also pointed out that some carriers near the top of surface valence band can be thermally-excited to the non-chiral edge channels, resulting in 2D holes conducting in the system as well. The transport scenario deduced for their magnetic TI system is schematically illustrated in Fig. 3.31(b). Other mid-gap states like acceptor or donor states may also exist and cause additional dissipation.

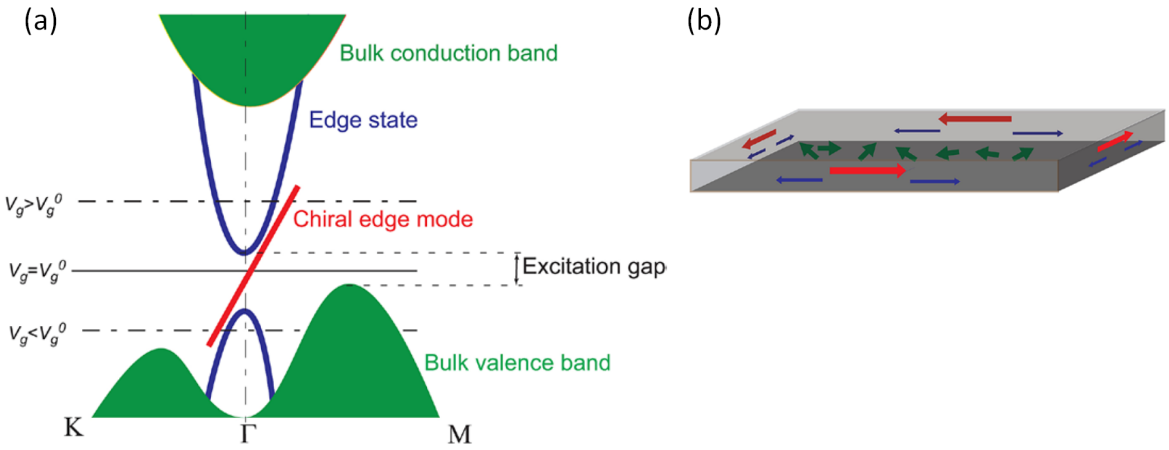

Figure 3.31: (a) The speculated band structure of the V-doped $(Bi,Sb)_2Te_3$ film used by Chang *et al.*. The green regions represent the bulk bands that consist of both 3D bulk bands and 2D surface bands of the top and bottom surfaces of the magnetic TI. The space between the green regions is the magnetic gap induced by the ferromagnetic order. Two different types of edge channels, chiral edge states (red) and non-chiral edge states (blue) can be found inside the gap. The non-chiral edge states may originate from the 2D gapless states on the side surface of TI that are gapped and become quasi-1D channels due to the quantum confinement effect. A pure dissipationless chiral edge transport occurs only when the Fermi level is located inside the mini-gap of the non-chiral edge channels. The small size of the excitation gap may be the reason why the QAHE can only be observed at the temperatures that are two orders of magnitude lower than the Curie temperature. Furthermore, the carriers near the top of bulk valence band can be thermally excited to the non-chiral edge channels owing to the small energy difference between them, causing additional dissipation. (b) The speculated transport scenario in the V-doped $(Bi,Sb)_2Te_3$ sample. The QAH states, non-chiral edge states and residual (2D + 3D) bulk states are denoted by red, blue, and green, respectively. Adapted from [106].

The best QAHE observed so far has a Hall resistance quantised to within one part per million of h/e^2, and a longitudinal resistivity under 10 mΩ at zero magnetic field [110]. Although the precision is already quite impressive, it still cannot match the part-per-billion precision of the Hall resistance and ultralow longitudinal resistance obtained in the QHE [23, 111]. Moreover, the critical temperature of QAHE is limited to several tens to a hundred millikelvin, which is much lower than the QHE, diminishing the potential of practically using the QAHE for metrology or low-dissipation electronics as well as spintronic devices. The finite longitudinal resistance and ultralow critical temperature are possibly associated with the dissipative states existing in magnetic TI systems. Up to now, there is still no clear conclusion about how the different conducting modes interact with each other and affect the QAHE in magnetic TIs. Therefore, investigating the effect of various conducting states and possible sources of disspation in magnetic TIs is one of the main goals of this thesis.

Chapter 4

Experimental techniques

4.1 Introduction

The scanning probe microscopy (SPM) is one of the most powerful tools for studying the surface and local electronic properties of semiconductor devices. In 1981, Gerd Binnig and Heinrich Rohrer performed the first successful SPM experiment using the scanning tunnelling microscopy (STM) they invented [112]. In an STM experiment, a biased conductive tip scans over a metallic surface, and the tunnelling current between the sample surface and the tip is recorded and kept constant by adjusting the tip position above the surface using a feedback loop. The change in tip position recorded during the scan is then converted into a map containing the information of the surface topography and density of states. Although STM can routinely achieve the subatomic resolution, the limitation is that both the tip and sample surface have to be conductive. In 1986, Binnig and scientists in IBM developed the atomic force microscopy (AFM), in which neither the tip nor the sample has to be a conductor [113]. The AFM can directly sense the force between the tip and the sample surface down to the order of piconewtons. Using the same principle of a feedback loop as the STM, the information of the tip position in AFM measurements can be converted into a map of surface topography of the sample. To this end, the basic working principle of SPM techniques is established. In other words, if there is some kind of interaction between the tip and the surface, with the aid of feedback loops, the information of the sample surface related to the interaction can be extracted. In the next three decades, more and more different types of SPM techniques were developed depending on the need of experiments. In this chapter, the SPM techniques used in the experiments in this thesis will be briefly introduced.

4.2 Atomic force microscopy

The atomic force microscopy (AFM) is a technique commonly used for characterising the surface topography of samples. The magnetic TI devices studied in this thesis were manually scratched by metal tips or scalpels to avoid possible contamination and doping from fabrication processes, which inevitably resulted in a lot of debris and build-up of the TI film on the sample surface. Therefore, we always performed AFM scans to search for relatively clean regions prior to further SPM experiments. In addition, as will be discussed in Chapter 5 and Chapter 6, this thesis focuses on the carrier transport behaviour near the edge of the magnetic TI devices. The signal of edge transport is usually very weak and can easily be overwhelmed by other signals. It is therefore crucial to find a smooth and straight film edge without too much variation in the topography so that unwanted signals caused by topographical features can be minimised and the scanning tip can be brought as close as possible to the sample surface to maximise the sensitivity as well as the spatial resolution of the scan.

The AFM used in our experiments is performed by a home-made SPM system. The basic operation principle is shown by the block diagram shown in Fig. 4.1.

The tip is located at the end of a cantilever that connects to a micro-fabricated chip for handling. The entire probe chip is made of heavily-doped Si, which is conductive and allows us to bias the tip in certain types of measurements. The back side of the cantilever (i.e. the side facing the laser and photodetector) usually is coated by materials with high reflectiviy, such as Al or Pt, to enhance the reflectance of the laser beam and prevent light from interfering within the cantilever. Depending on the type of SPM techniques, different materials may be deposited on the tip side of the cantilever. The specifications for the various tips used in different SPM experiments in this thesis can be found in Appendix A. The probe chip then is installed onto a tip holder with a piezoelectric actuator ("dither") underneath. The thickness of the dither can be adjusted by a voltage, and thus the cavity length between the cantilever and the optical fibre can be tuned by the dither.

If a laser is shone on the back of the cantilever, the laser beam can be reflected back to an optical fibre and read by a photodetector. The interference between the incident and reflected signals gives rise to a beat frequency that can be used for optical heterodyne detection [114]. When the tip position is changed, the intensity of the interference signal will change accordingly. Therefore, in the extension/contraction process of the dither, the detected intensity of the interference signal will oscillate as a function of the cavity length due to the alternating constructive and destructive interference conditions. Figure 4.2(a) shows a typical relation between the intensity (I) and the cavity length (z) when varying the thickness of the dither by applying a DC voltage. Clearly, the tip will be most sensitive to the

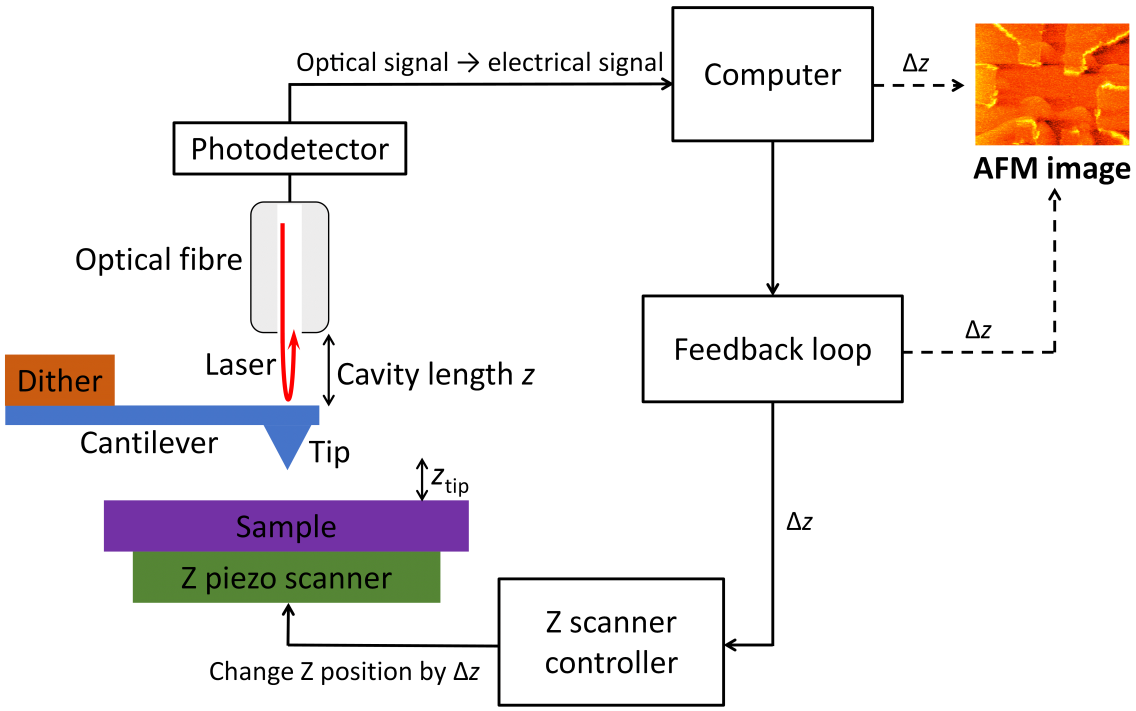

Figure 4.1: The block diagram showing the principle of the AFM. The probe is fixed on a dither that can be used to adjust the cavity length (i.e. the distance between the cantilever and the optical fibre). The laser is used to detect the change in cavity length due to the dither or tip-sample interactions. The computer is used for data acquisition and analysis. For the constant height scan of contact mode AFM, the PC can directly export the topography map by reading the deflection of the tip. For the constant force scan of contact mode AFM, the signal will be sent to a feedback loop for computing the complementary Z displacement for the Z scan controller to maintain a constant deflection of the tip. The adjustment in the Z direction made by the feedback loop then can be displayed as the topography map.

change of tip position when the cavity length is at the points with maximum gradient $\partial I/\partial z$, as indicated by the orange line in Fig. 4.2(a). For this reason, we usually have to tune the dither to this "working point" before most of our SPM experiments.

The earliest and most straightforward operation mode of AFM is the contact mode, in which the tip is brought into hard contact with the sample surface [113]. The topography of the sample surface hence will directly change the deflection of the cantilever during the scan. Such contact mode operation is called the constant height scan. The surface topography then can be imaged by measuring the deflection of cantilever. The constant height mode is only suitable for samples with relatively flat surface since the tip may be damaged or the cavity length may shift away from the "working point" if the variation in topography is too large. Thus, there is another contact mode operation called the constant force scan, in which the deflection of the cantilever is kept at constant during the scan by a feedback loop controlled

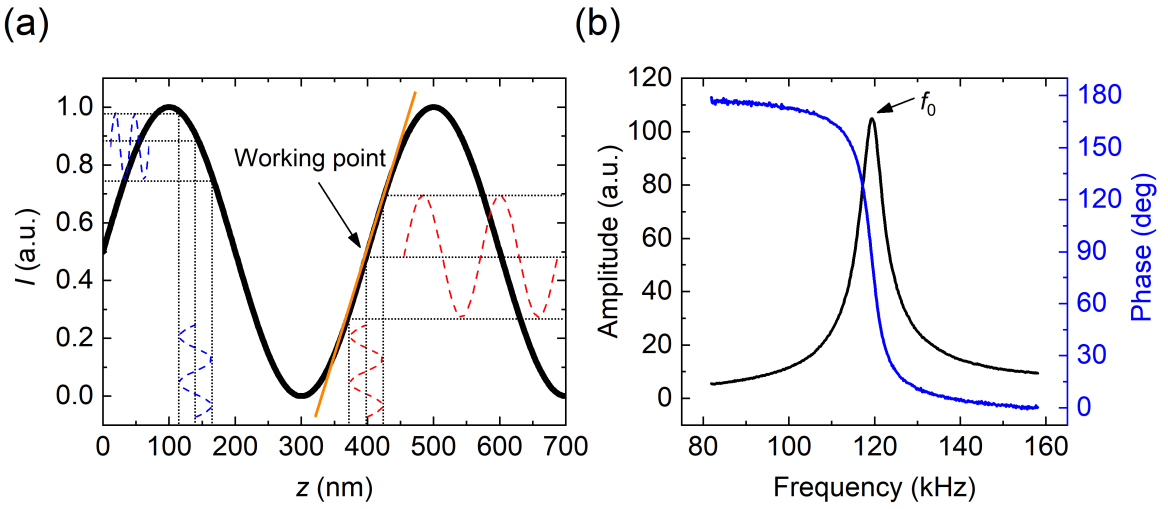

Figure 4.2: (a) The intensity I of the interference signal as a function of cavity length z. The thick black curve shows the oscillation of I due to the alternating constructive and destructive interference conditions as z changes. The orange line indicates the "working point", where the $\partial I/\partial z$ is maximum. Blue and red dashed curves show the change in I corresponding to the change in z at different z values. With the same Δz, ΔI is much larger at the "working point" than the other points. (b) The amplitude of detected signal as a function of driving frequency. The amplitude of detected signal shows a peak at its resonant frequency f_0, where the phase of tip oscillation is 90° out of phase with the driving AC voltage.

by the computer. The adjustment of tip-sample distance made by the feedback loop then can be displayed as the surface topography [114].

Although the deflection of cantilever is caused by the force between the tip and the sample surface, the physical quantity directly measured in these AFM scans is not the force but the stiffness of the cantilever (i.e. the force gradient $\partial F/\partial z$). Therefore, the force should be calculated from the Δz using Hooke's law $F = -kz$ by measuring the ΔI in Fig. 4.2(a).

The contact mode AFM is not frequently used in our measurement because the tip can be worn quickly in this scan mode. Most of the time our purpose of obtaining the topography map is just to find a clean region and prepare for other SPM experiments. Thus, the more useful AFM operation for our experiments is the tapping mode, in which the tip is very close to the sample without touching the surface. As shown in Fig. 4.3, the force-distance relation between the tip and the sample surface can be described by the green curve according to the approximation of the Lennard-Jones potential [115, 116]. While the contact mode is operated in the repulsive regime, the tapping mode is operated near the boundary between the repulsive and attractive regime. When a high frequency AC voltage is applied onto the dither, the cantilever will be shaken by rapid contraction and extension motions of the dither. If the tip originally is sufficiently close to the surface, the tip can briefly enter the repulsive regime

and touch the surface during its oscillation. When the tapping frequency is sufficiently higher than the scan rate, the tip can still obtain sufficient resolution of the surface topography without rubbing on the sample surface continuously, which is advantageous for the SPM experiments afterwards.

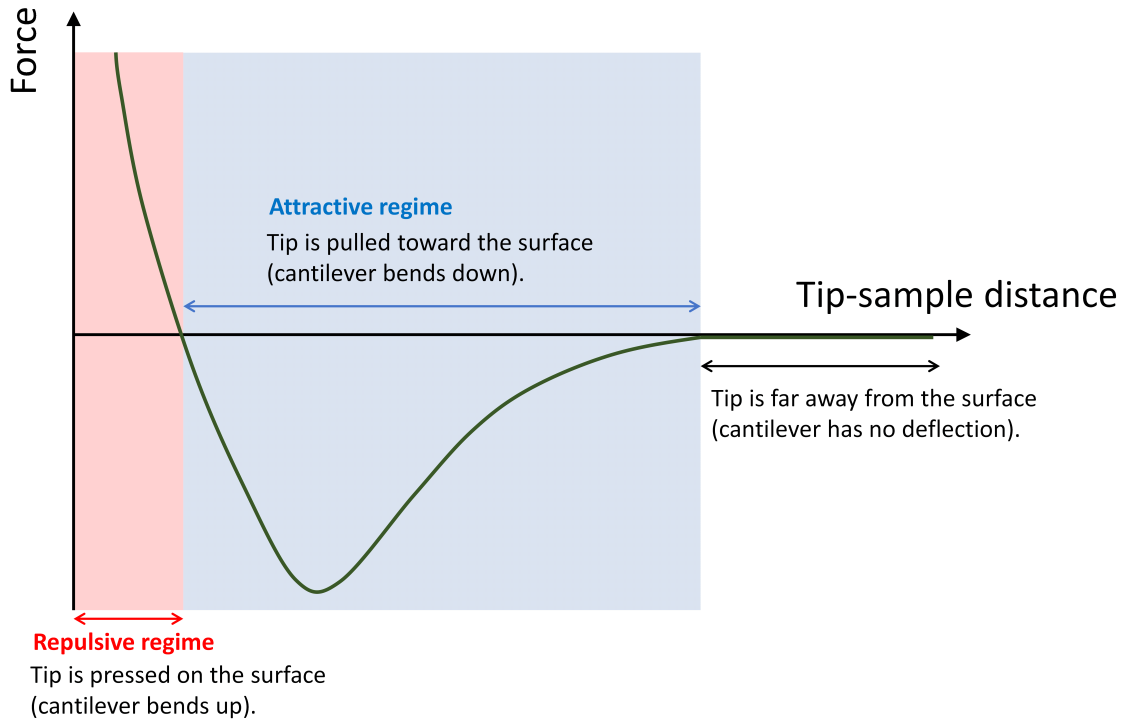

Figure 4.3: The force-distance relation between the tip and the sample surface according to the approximation of the Lennard-Jones potential. The green curve is the force sensed by the tip as a function of the tip-sample distance. The red and blue regions correspond to the repulsive and attractive regimes, respectively.

Such an operation with the tip oscillating during SPM scans is referred to as dynamic mode, which is the foundation of other SPM techniques that will be introduced later. In dynamic mode, we first sweep the frequency of the AC driving voltage on the dither to find the tip's natural resonant frequency f_0. As shown in Fig. 4.2(b), the amplitude of the oscillation signal will show a peak at f_0, where the phase of the tip oscillation is 90° out of phase with the AC driving voltage. When the AC driving voltage with desired frequency is applied onto the dither, the interference intensity I will be modulated around the working point, as shown by the red dashed curves in Fig. 4.2(a). Since the tip-sample interaction can lead to the change in oscillation frequency of the tip, the amplitude-frequency curve in Fig. 4.2(b) will shift toward higher or lower frequency depending on whether the interaction is repulsive or attractive. A phase-locked loop (PLL) is used to detect this frequency shift

Δf by monitoring the change in phase and maintain the tip oscillation to be at 90° out of phase with the AC drive by constantly adjusting the driving frequency. As a result, the tip will always be on resonance throughout the scan [114]. If the tip-sample distance is z_{tip}, the frequency shift Δf is given by

$$\Delta f = \frac{-f_0}{2k}\frac{\partial F}{\partial z_{\text{tip}}}, \tag{4.1}$$

where k is the spring constant of the tip.

For our tapping mode AFM, a PID loop is further used to maintain the oscillation amplitude at a setpoint value by controlling the Z-scanner so that the tapping force can be kept at a constant during the scan. The adjustment made by the PID loop then is recorded as the surface topography of the sample [114].

4.3 Electrostatic force microscopy

The electrostatic force microscopy (EFM) is a type of non-contact SPM that probes the electrostatic interaction between the tip and the sample using a biased tip. The block diagram in Fig. 4.4 shows how EFM is performed using our home-made SPM system.

The EFM is operated in dynamic mode with the tip being held at a distance such that it only senses the long-range electrostatic force without entering the repulsive regime in Fig. 4.3. The tip therefore does not touch the surface during the scan. When the tip is DC biased, opposite charges accumulate on the tip and the sample surface and effectively form a capacitor [114]. If the tip-sample distance is z_{tip}, for a voltage difference ΔV between the tip and the sample, the energy stored in this capacitor can be written as

$$U = \frac{1}{2}C\Delta V^2, \tag{4.2}$$

where C is the capacitance between the tip and the sample. The work done by the battery supplying the bias to maintain ΔV between the tip and sample should be $-2U$, and the total energy of the entire system should be $-U$. By definition, the force resulting from this potential energy can be obtained by

$$F = \frac{\partial U}{\partial z_{\text{tip}}} = \frac{1}{2}\Delta V^2\left(\frac{\partial C}{\partial z_{\text{tip}}}\right). \tag{4.3}$$

Since $\partial C/\partial z_{\text{tip}} < 0$, this electrostatic force is always attractive. Remarkably, this long-range electrostatic force can be detected when the tip is several hundreds nanometers away from the sample and the sensitivity of EFM can achieve the order of piconewtons [117].

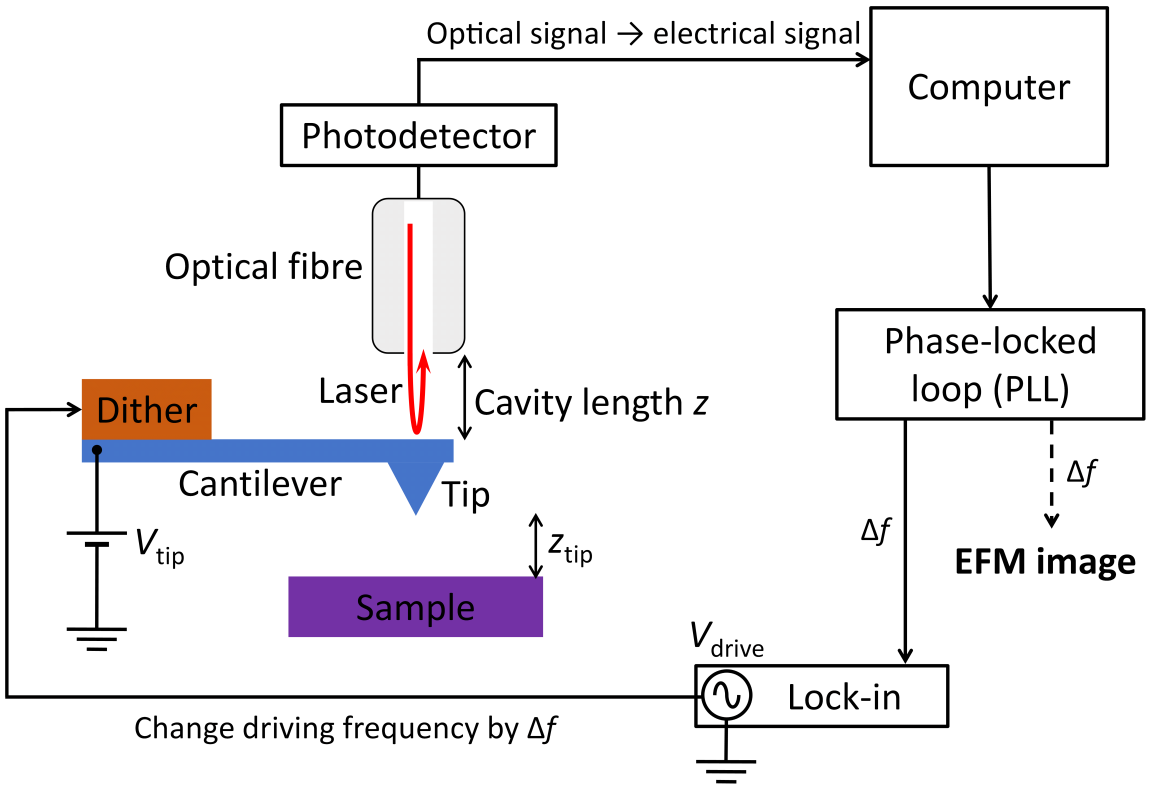

Figure 4.4: The block diagram showing how EFM is performed on our home-made SPM system. The lock-in supplies an AC driving voltage V_{drive} to the dither which vibrates the cantilever. The tip is biased by a DC voltage V_{tip}. The PLL tracks the phase shift during the scan and compensates it by adjusting the frequency of V_{drive}. The adjustment made by the PLL, i.e. the frequency shift (Δf) is recorded and displayed as the EFM image.

According to Eq. 4.1, the frequency shift in the EFM can be expressed as

$$\Delta f = \frac{-f_0}{4k} \Delta V^2 \frac{\partial^2 C}{\partial z_{\text{tip}}^2}. \tag{4.4}$$

Because $\Delta f \propto \Delta V^2$, when sweeping the tip bias (V_{tip}) the response of Δf will be a parabolic curve, as shown in Fig. 4.5, which can be used to check the performance of EFM before actual EFM scans.

In a high vacuum environment, the Q-factor of the tip usually becomes very high, and the tapping mode AFM is no longer viable because the PID loop cannot provide sufficiently quick feedback to the SPM system. Consequently, in low-temperature measurements that normally are performed under high vacuum, we have to rely on EFM rather than AFM to distinguish the topographical features on the sample surface. For instance, higher topographical features should generally contribute to a stronger EFM contrast than lower features. The region

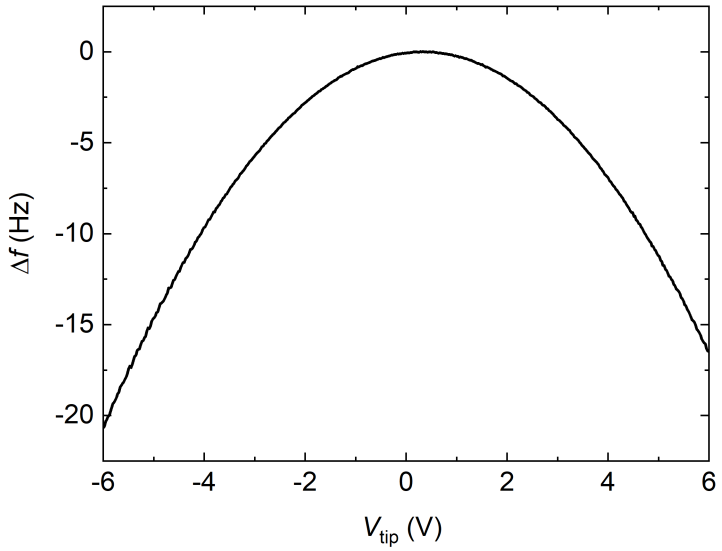

Figure 4.5: An example showing the parabolic relation between the tip bias (V_{tip}) and the frequency shift (Δf).

covered with magnetic TI films will also have a different contrast from that of the bare substrate due to different capacitive conditions. These distinctions can be used as signposts to find the area for further SPM experiments. However, there is a caveat about the "topography" imaged by EFM. Since the grounding conditions can affect the capacitance between the tip and the surface features, if there are two topographical features with the same physical height but different grounding conditions, their contrast in the EFM image will be different. In addition, charges trapped on the sample surface can give rise to features in EFM images as well. Therefore, the interpretation of EFM images is not as straightforward as the AFM images and can be complicated in some situations.

4.4 Kelvin probe microscopy

The Kelvin probe microscopy (KPM) is a non-contact SPM technique closely related to EFM. Both require a biased conductive tip and utilise the electrostatic force to probe the sample surface. However, they are used to study different physical properties.

The principle of EFM was briefly described in Sec. 4.3. However, the story is actually simplified and some details are ignored in the introduction. In fact, ΔV between the tip and sample is not simply the voltage difference between the tip and sample. Since the tip and sample in most cases are not made of the same material, there usually exists a difference between their work functions. This difference, when expressed in terms of a voltage, is called the contact potential difference (V_{CPD}), which has a typical value on the order of a few

hundred millivolts [118]. Therefore, taking V_{CPD} into account, the complete relation should be

$$\Delta V = V_{\mathrm{tip}} - V_{\mathrm{sample}} - V_{\mathrm{CPD}}, \tag{4.5}$$

where V_{sample} is the bias on the sample, which is usually chosen to be zero. The effect of V_{CPD} can be clearly seen in Fig. 4.5, in which the apex of the parabola is not at $V_{\mathrm{tip}} = 0$ but shifted to ~ 360 mV due to the presence of V_{CPD}.

The value of V_{CPD} depends on the material under the tip, the local electronic states and structures on the sample surface [118]. For instance, dust on the surface of a magnetic TI film will give rise to a different contrast from the film underneath in KPM images. The contrast arising from the regions with higher DOS on a magnetic TI film will also be stronger than that from the regions with lower DOS. The measurements of V_{CPD} is the scope of KPM.

The block diagram of the KPM performed on our SPM system is shown in Fig. 4.6. In a KPM measurement, in addition to the setup for the EFM, a second lock-in is employed to add an extra modulation to the tip bias. Generally, the frequency of this AC modulation (V_{AC}) is set to be at a few kHz so that it is not commensurate with the oscillatory motion of the cantilever, which is usually around 100 kHz. As shown in Fig. 4.5, a small modulation in the tip bias must lead to a small oscillation in the Δf signal. The response of Δf to V_{AC} can be measured with a built-in digital lock-in detector. This $\delta\Delta f$ is then sent to a separate PID controller, which will try to nullify $\delta\Delta f$ by constantly regulating the DC component of the tip bias [118, 119]. In other words, the apex of the parabola in Fig. 4.5 will always be kept at 0 V during a KPM scan by adjusting V_{DC}. The adjustment on V_{DC} made by the PID loop then is recorded as a V_{CPD} signal and displayed as a KPM image, which can be regarded as a direct measurement of the contact potential (or work function) of the sample surface.

In contrast to the EFM, which is directly based on the electrostatic force exerted on the sample surface by the biased tip and the frequency shift in EFM is used for detecting the electric field, the KPM probes the surface potential of the sample and the frequency shift in KPM is used as an input for the PID controller to compute the DC offset of tip bias needed tor compensate the change in frequency shift. The EFM is much more sensitive to topographic features than the KPM and hence is still used as the alternative approach for mapping the topography in our SPM experiments. But KPM allows us to study a sample from a different perspective and can reveal other important properties of the sample surface.

4.5 Magnetic force microscopy

The magnetic force microscopy (MFM) is a SPM technique that is very similar to the EFM. While EFM studies the electrostatic interactions between the tip and the sample, MFM

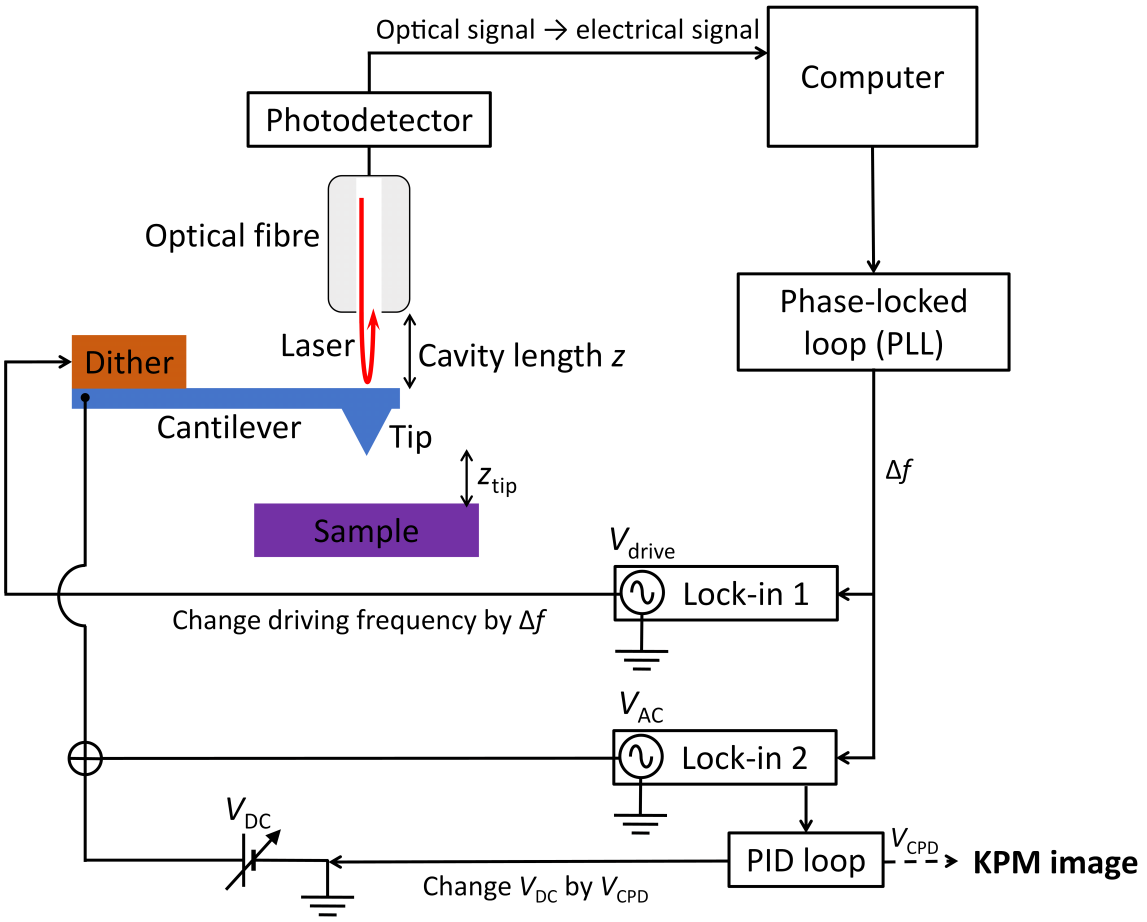

Figure 4.6: The block diagram showing how KPM is performed on our home-made SPM system. The lock-in 1 is used to supply an AC driving voltage V_{drive} to the dither and shake the cantilever. The PLL can track the phase shift during the scan and compensate it by adjusting the frequency of V_{drive}. The tip is biased by a DC voltage (V_{DC}) with a small AC modulation (V_{AC}). A PID loop is used to compute the voltage required to nullify the contact potential difference (V_{CPD}) and adjust the V_{DC} accordingly. The adjustment made by the PID loop, i.e. V_{CPD}, is then recorded and displayed as the KPM image.

studies the magnetic interactions between the tip and the sample. The experimental setup of the MFM is the same as the EFM setup shown in Fig. 4.4, except the tip is replaced by a magnetic tip. A magnetic tip can either be directly made out of magnetic materials, or be fabricated by covering a non-magnetic tip with a magnetic coating.

In MFM measurements, the magnetic force between the tip and the sample surface can be expressed as

$$F = -\mu_0 (m \cdot \nabla) H, \tag{4.6}$$

where μ_0 is the permeability in vacuum, H is the magnetic stray field from the sample surface, and m is the magnetic moment of the tip (approximated as a dipole) [114]. However, the actual magnetic interactions between the tip and sample is usually much more complicated. For instance, because the stray magnetic field from the sample can affect the magnetisation of the tip, and vice versa, the magnetic states of both can change during the scan, leading to non-linear responses. Furthermore, if the stray magnetic field of the tip is sufficiently strong, the magnetic structures of the sample can be altered, just like storing or erasing data from a hard drive of a computer, hindering the study of the sample's magnetic properties. In addition, any applied magnetic field can also affect the magnetisation of the tip and cause serious difficulty when studying the motion of domains and domain walls in the samples under external magnetic fields. Finally, similar to the AFM and EFM, the MFM does not directly measure the magnetic force but measures the force gradient, hence the magnitude and direction of the magnetisation on the sample surface cannot be directly obtained from the MFM data. To extract the quantitative information from MFM images, computer simulations with the details such as the shape of the tip and cantilever, the tip-sample distance, and the strength of stray magnetic field of the tip are required. Thus, the interpretation of MFM images is not straightforward. In this thesis, we only use MFM to acquire the qualitative information about the magnetic properties of the samples without going into the quantitative analysis.

On the other hand, compared to other magnetic imaging techniques, the implementation of MFM is easy for the labs with existing SPM systems. The fabrication of magnetic tips is also relatively quick and inexpensive. One can even fabricate an MFM tip simply by depositing a magnetic coating on a commercially-available AFM tip using PVD or CVD. Therefore, MFM is selected as our first tool for studying the magnetic properties of magnetic TI films because it is well compatible with our home-made SPM system and does not require much modification of the instruments, allowing us to characterise the samples and obtain useful information in a reasonable time.

4.6 Scanning gate microscopy

The scanning gate microscopy (SGM) is a non-contact SPM technique that utilises a DC-biased tip as a mobile electric gate to locally change the electric potential in the area under the tip while simultaneously measuring the corresponding change in the sample's transport properties, such as the resistance [120, 121]. The basic setup for SGM experiments is shown in Fig. 4.7.

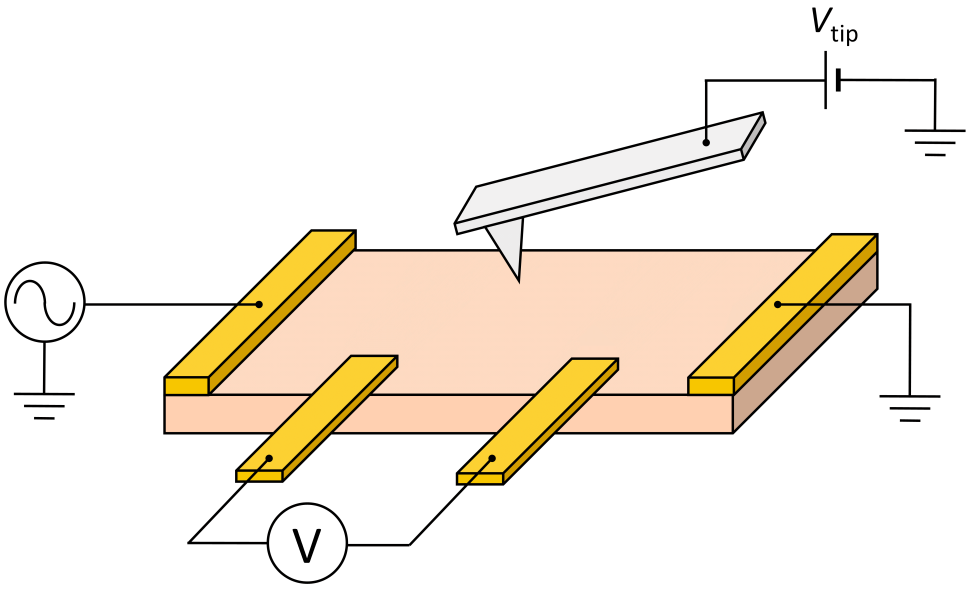

Figure 4.7: The basic measurement setup for SGM experiments. The current is passed from left to right and the voltage drop in between is measured by a voltmeter while a biased tip is scanning over the sample. The change of local carrier density due to the gating effect of the tip will be reflected in the transport properties, such as the resistance, and recorded by the voltmeter. By plotting the resistance as a function of the tip position, the spatial distribution of current on the sample can be mapped out.

During a SGM scan, the potential created by the biased tip can scatter the carriers in an area under the tip, and thus the local carrier density of the sample will be tuned by the scanning tip. Therefore, when the biased tip scans across an area in which an electric current flows, the conducting carriers will be scattered, leading to a change in the measured resistance, thereby creating a contrast in the SGM image. In contrast, when the tip scans over an area with lower current density (or no current), the change of contrast in the SGM image will be less. Thus, by plotting the resistance as a function of the tip position, the spatial distribution of current in the sample can be mapped out in SGM images.

The SGM can be performed using commercially-available conductive AFM tips and has been widely used to study the transport behaviour of carriers in low-dimensional systems [120], such as the ballistic transport in quantum point contacts [122, 123] and edge transport in two-dimensional systems [124–127]. In this thesis, the SGM technique is used to probe the edge transport in the QAHE, with the goal of visualising the QAH states propagating along the domain boundary in the magnetic TI films.

4.7 Scanning Hall probe microscopy

The scanning Hall probe microscopy (SHPM) is the only SPM technique used in this thesis that was not performed on our home-made SPM system. Due to the incompatibility with our SPM system, the SHPM experiments described in this thesis were carried out in a dedicated SHPM system in our collaborator's lab in the University of Bath.

The SHPM is a non-contact mode SPM that is also used for probing the magnetic properties of samples. The basic principle of the SHPM is illustrated in Fig. 4.8 [128].

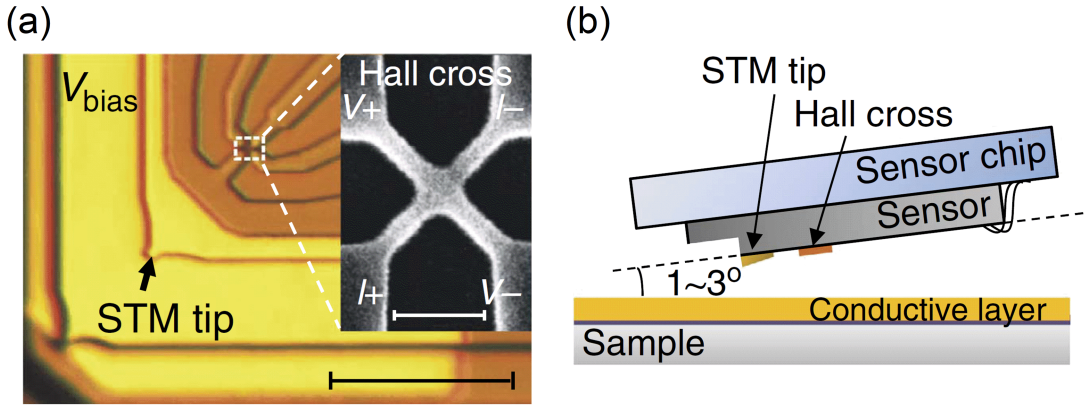

Figure 4.8: (a) The optical image of the Hall sensor used in the SHPM. The black scale bar corresponds to 20 µm. The inset shows a scanning electron microscopy (SEM) image of the Hall cross with a scale bar of 1 µm. (b) The basic measurement setup for SHPM experiments. The probe chip is usually mounted at a small angle of $\sim$ 1-3° to the sample surface so that the STM tip will be the lowest point of the probe chip. After applying a bias on the STM tip, the tunnelling current between the tip and the sample can be used to determine the tip-sample distance. A conductive layer on the surface is required for the STM to work if the sample itself is insulating. Adapted from [128].

As shown in Fig. 4.8(a), a 2DES (usually made of the GaAs/AlGaAs quantum well) is first shaped into a Hall cross. Two of the terminals are used as current leads and the other two are used as voltage probes, as shown in the inset of Fig. 4.8(a). A metal layer deposited at one corner of the probe chip forms the "STM tip". As shown schematically in Fig. 4.8(b), the probe chip is usually mounted with a small angle of $\sim$ 1-3 ° to the sample surface so that the STM tip will be the lowest point of the probe chip [128]. When the Hall probe approaches the surface, a bias is applied on the STM tip, and the tunnelling current between the tip and the sample surface can be used to determine the tip-sample distance. After parking the Hall probe at an appropriate height above the sample, the stray magnetic field emanating from the sample should induce the Hall effect in the 2DES, and hence a Hall voltage will be detected

by the voltage probes. Then, by Eq. 3.2, the magnitude of the stray magnetic field can be obtained accordingly.

Compared to the MFM, there are several advantages in using the SHPM to study the magnetism of samples. For instance, unlike the MFM, the SHPM is non-invasive and will not modify the magnetic states of the sample under test during the scan. Thus, in principle the magnetic features in a region can be repeatedly obtained in different SHPM scans if the external conditions are not changed. Moreover, the SHPM can provide direct quantitative information of the magnetic structures of a sample. In contrast to the MFM, which generates images in terms of the frequency shift of the PLL, the SHPM can directly map the magnetic structures in units of magnetic field, e.g. gauss or tesla, making the interpretation of scan images much more straightforward.

The SHPM has been reported to reach a sensitivity of ~ 0.1 G and a spatial resolution of ~ 0.35 μm [129], suggesting it is a superb tool for imaging weak magnetic features and can be useful for studying the magnetic properties of magnetic TI films.

Chapter 5

Transport and SPM study on vanadium-doped bismuth antimony telluride

5.1 Introduction

In the QAHE, the chiral edge states are predicted to propagate along the domain boundaries between opposite magnetisations [75], as discussed in Sec. 3.6. For a thin film of magnetic TI with a uniform magnetisation normal to the top and bottom surfaces, such domain boundaries will be pushed to the side surface, as illustrated in Fig. 3.26. Although the existence and behaviour of chiral edge states in the QAHE has been confirmed by transport measurements [93, 104–106], it would be more straightforward and reassuring if the spatial distribution of QAH states can be directly mapped out by SPM. Similar ideas have been carried out in the study of the QHE [124–127], in which edge states should give rise to a contrast at the edges of the 2DES. For the QAHE, there are two possible scenarios. When the film is fully magnetised with a uniform out-of-plane magnetisation, the contrast of the QAH states should appear at the edge of the device like the QHE. However, when the film is fully demagnetised, since the regions with up and down magnetisations on the top or bottom surface are randomly distributed, the contrast pattern should be consistent with the map of domain walls because the QAH states should only be allowed to travel along the domain boundaries. The difference between the fully-magnetised and fully-demagnetised states becomes the unique signature of the QAHE in SPM experiments. By taking the contrast maps under these two different conditions, the contributions from the QH and QAH states can be clearly distinguished. Furthermore, by combining transport measurements and SPM images, one can study the

evolution of QAH states during the magnetisation and demagnetisation process in magnetic TIs and probe the dissipation mechanism if the contrast from dissipative states is observed. Since the domain boundary does not have to be at the physical edges of the samples, the chiral edge states in domain walls can also be used to study the 1D quantum transport without edge effects [130–132]. Therefore, the motivation behind the experiments in this chapter is to test whether the combination of SPM and transport measurements can actually be used to examine the above ideas, and hopefully to establish a viable approach for probing the QAH states in domain walls.

5.2 Sample fabrication

The V-doped $(Bi,Sb)_2Te_3$ samples used in this chapter were prepared by Dr. Cui-Zu Chang and coworkers at the Massachusetts Institute of Technology and Pennsylvania State University. Here we only introduce the basic growth method of the samples. Detailed descriptions of the growth procedure and characterisation can be found in the papers of Dr. Chang *et al.* [106, 107].

The growth of the V-doped $(Bi,Sb)_2Te_3$ films was carried out in an ultrahigh vacuum MBE system with a base pressure of 2×10^{-10} Torr. Heat-treated insulating STO (111) substrates were degassed before the growth of TI films. High-purity Bi (99.999%), Sb (99.9999%), and Te (99.9999%) were evaporated from Knudsen effusion cells, while the transition metal dopants V (99.995%) were evaporated by an e-gun crucible. The flux ratio of Te to Bi and Sb was set to ~ 8 to minimise the Te deficiency in the films. The growth rate for the films was controlled at ~ 0.2 QL per minute, and the STO substrate was maintained at 230 °C during the sample growth. The growth process was monitored *in situ* by reflection high energy electron diffraction (RHEED). The sharp and streaky '1×1' diffraction patterns in RHEED images (as shown in the supplementary information of [106]) suggest high crystal quality and atomically flat surface of the films.

The concentrations of Sb, Bi, and V in the films were first determined by their ratio obtained *in situ* using separate quartz crystal monitors during the sample growth, and later verified *ex situ* by inductively coupled plasma atomic emission spectroscopy (ICP-AES). According to these measurements, the composition of the films was calculated to be $V_{0.11}(Bi_{0.29}Sb_{0.71})_{1.89}Te_3$ (henceforth referred to as V-BST).

After the growth of V-BST films, an additional capping layer was then deposited on the films as protection against further doping from the environment. Alumina or tellurium is usually used for the capping layer.

Contamination from the environment during fabrication and measurement can substantially change the properties of magnetic TIs [133, 92, 93], causing serious problems for the observation of the QAHE. For example, since the Fermi level of magnetic TIs can be significantly changed by doping, given the small size of the magnetic gap [101, 107–110], the environmental doping effect can easily shift the Fermi level out of the magnetic gap and quench the QAHE. So far, it is still not clear whether the key factor that destroys the QAHE is the temperature, oxidation, or doping from the atmosphere and fabrication process. Although some groups have successfully observed the QAHE on devices made by lithography [102, 105, 109, 110], currently there is still no reliable recipe that can be used to repeatedly fabricate magnetic TIs devices showing a good QAHE. Therefore, the magnetic TI devices studied in this thesis were scratched into Hall bars by metal tips or scalpels, following the methods in [93, 101, 106, 134].

The scratched Hall bar samples were first fixed on a leadless chip carrier (LCC) using silver conductive paste. Indium pieces were manually placed onto the terminals of the Hall bars as Ohmic contacts. The indium contacts were then connected to the bond pads of the LCC by gold wires. Finally, the inner base of the LCC, which is electrically contacted to the STO substrate by silver paste, can be connected to bond pads on the LCC to form backgates.

Two V-BST devices, VBST1 and VBST2, were used in the experiments in this chapter. Since VBST1 is the first magnetic TI film we received from the collaborators, a number of pilot studies were carried out on VBST1 to help us design later experiments. In the next section, we will introduce the experiments performed on VBST1 and discuss the results, as well as how it led to the measurements on VBST2.

5.3 Transport and MFM measurements on device VBST1

5.3.1 Characterisation of VBST1 and preparation for the MFM system

The layer structure and photograph of VBST1 are shown in Fig. 5.1. Prior to sending the VBST1, our collaborators have used the sample for their experiments and hence there is insufficient area with a good enough surface condition for us to make Hall bars. Therefore, two indium pieces were placed onto the film and bonded to an LCC as Ohmic contacts for two-terminal measurements. Transport measurements in this configuration will reflect the overall property of the effective area on the film.

To check whether the film is ferromagnetic, a series of magnetic field ($\mu_0 H$) sweeps were performed at different temperatures (T) in a cryostat, as shown in Fig. 5.2. At $T = 1.4$ K, a clear butterfly structure in the two-terminal resistance (R) can be observed by sweeping

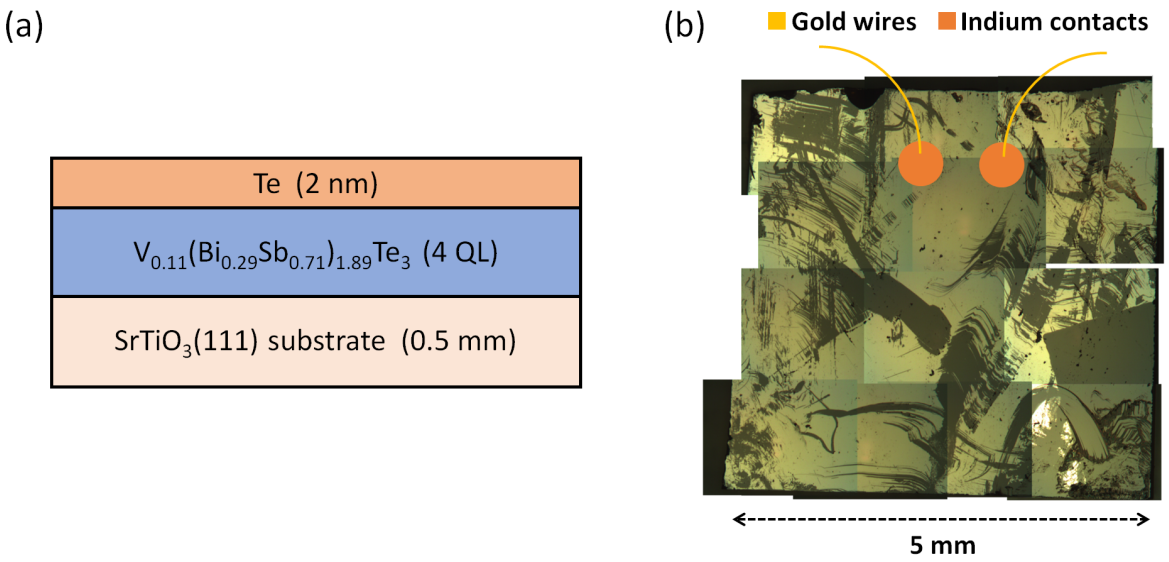

Figure 5.1: (a) The layer structure of VBST1. (b) An optical image of VBST1 (obtained by merging the high resolution photographs taken in different small areas on the film). The orange regions are indium Ohmic contacts, while the yellow curves are gold wires connecting the film to the bond pads of LCC. The distance between two indium contacts is $\sim$ 1 mm.

the magnetic field in opposite directions. As the temperature increases, the height of the two peaks at the coercive field (H_c) reduces while the value of coercive field moves toward $\mu_0 H = 0$ T. The butterfly structure completely disappears at $T = 21$ K and evolves into a weak localisation curve, implying that ferromagnetic order in the film is destroyed and the Curie temperature $T_C \sim 20$ K.

Having confirmed the magnetism of VBST1, our next goal is to check the size of the domains and domain walls in our film by directly imaging the magnetic domain structures using SPM. For this purpose, we mounted a magnetic probe (with the specifications shown in Appendix A) onto our SPM system to prepare for MFM measurements. By changing the external magnetic field, we expect to see the evolution of domain structures in VBST1.

Since our home-made SPM system has not previously been used for MFM experiments, it was necessary to first conduct some initial tests to ensure the MFM can work properly on our system. Thus, we made a sample with a small piece of a floppy disk on top as a testing device for the MFM. The magnetic medium of a commercial floppy disk possesses a strip-like magnetic pattern that can be used for data storage, which is highly-ordered and very suitable for the calibration of our MFM system.

As shown in Fig. 5.3(a) and (b), the strip pattern is clearly resolved in the MFM image, while the AFM image shows no features, indicating the contrast is not caused by surface topography but by magnetic force. We also changed the scan range and scan direction to

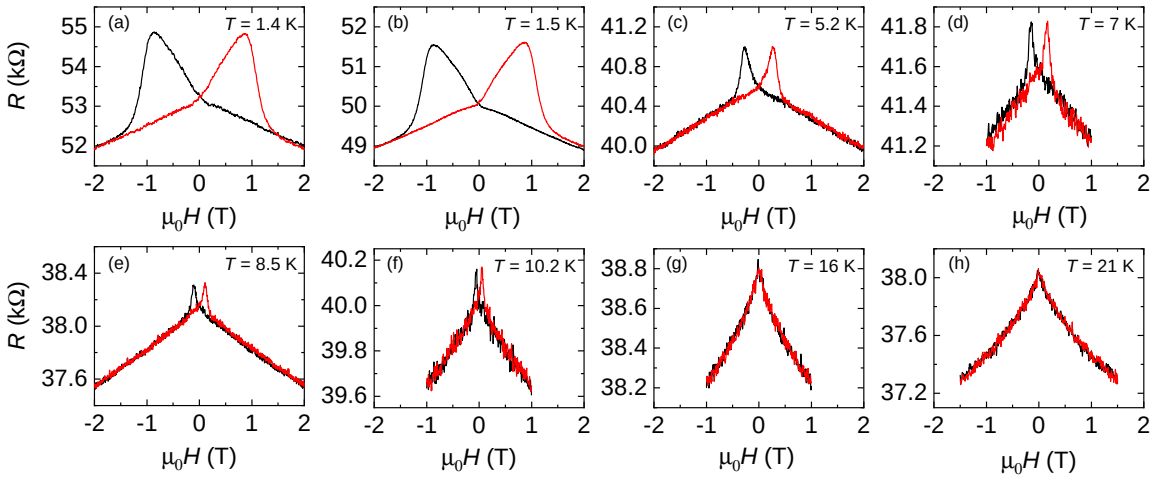

Figure 5.2: (a) to (f) The magnetic field dependence of the VBST1 film resistance at different temperatures. Red and black curves indicate the downward and upward magnetic field sweeps, respectively. The height of the peaks at H_c decreases with increasing temperature and completely disappears in the sweep at $T = 21$ K, implying that $T_C \sim 20$ K.

check that the strip pattern is not an artifact or a local feature, and confirmed it is a feature commonly existing over the entire floppy disk.

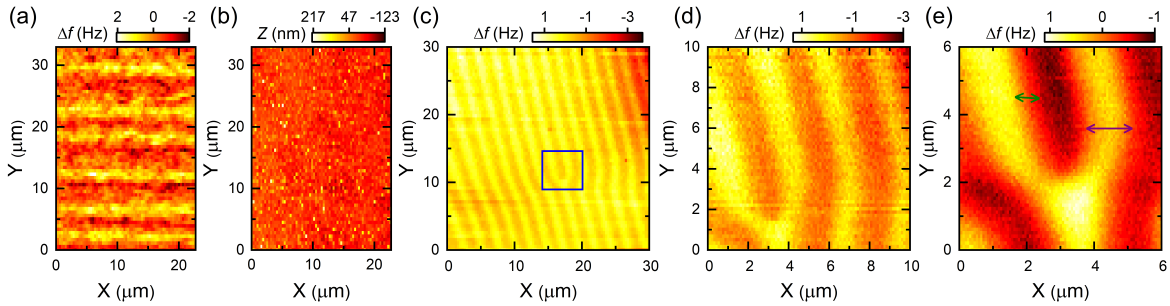

Figure 5.3: The measurements for testing the MFM performance on our home-made SPM system. (a) and (b) are the MFM and AFM image taken on the magnetic medium of a floppy disk, respectively. While the AFM image shows no features, a strip pattern can be observed in the MFM image, suggesting that the contrast in MFM image is not caused by surface topography but by magnetic force. (c) The MFM image of the domain structure observed on a 2 μm-thick YIG sample using our SPM system. The Y-shape domain indicated by the blue square is further examined with 3 times and 5 times higher resolution in (d) and (e), respectively. It can be seen in (e) that the domain size $\sim$ 1 μm (denoted by purple arrows) and the domain wall width $\sim$ 500 nm (denoted by green arrows). All images were taken at a tip height of 100 nm.

In addition, we further tested the MFM on a 2 μm-thick yttrium iron garnet (YIG) sample with out-of-plane magnetisation and successfully observed the magnetic domains, as shown

in Fig. 5.3(c)-(e). The Y-shape domain indicated by the blue square in Fig. 5.3(c) is further examined with 3 times and 5 times higher resolution in (d) and (e), respectively. It can be seen in (e) that the domain size $\sim$ 1 μm (denoted by purple arrows) and the domain wall width $\sim$ 500 nm (denoted by green arrows). These measurements demonstrate that the MFM technique can be achieved by our SPM system.

5.3.2 MFM measurements on VBST1

After the above tests, the device VBST1 was loaded onto the SPM system and lowered into a Oxford Instruments Kelvinox MX100 system to be cooled down to 4.2 K. A superconducting magnet inside the cryostat can be used to apply magnetic field and alter the magnetisation states of VBST1. To establish a standard for the response of VBST1 and the MFM tip under the conditions in this cryostat, an initial magnetic field sweep was performed before the tip was brought close to the surface of VBST1, as shown in Fig. 5.4. From the butterfly structure of film resistance in Fig. 5.4(a), one can obtain the coercive field $H_c \sim 0.4$ T and saturation field $H_s \sim 0.7$ T. In addition, to monitor the frequency shift signals of the tip during the magnetic field sweep, the SPM system was connected to a lock-in amplifier, and the frequency shift signals were converted into electrical signals, as shown in Fig. 5.4(b).

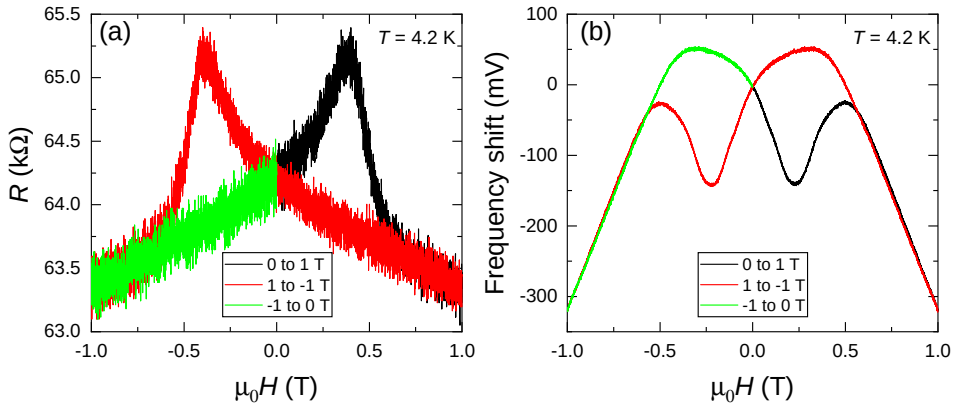

Figure 5.4: (a) The magnetic field dependence of the film resistance of VBST1 at $T = 4.2$ K. The black, red, and green curves represent the three stages of H sweeps between 1 T to -1 T, respectively. The butterfly structure is a manifestation of ferromagnetism in the film. (b) The magnetic field dependence of MFM tip response.

Our procedure of taking MFM images on VBST1 is as follows. We first managed to find a boundary between the V-BST film and STO substrate using either AFM or EFM. Once the boundary is found, we then move the tip toward the V-BST side to prepare for the MFM scan. At this stage, it is important to find an area which is flat enough, i.e. no

large debris or dust and no significant topographical variations, so that the tip can safely scan over the surface without crashing into obstructions and being damaged. However, since this sample is seriously scratched, it is hard to find a clean region, which limits the smallest tip-surface distance that we can use in the scans, and in turn affects the sensitivity of the SPM experiments. The scan range can also be affected by the topographical condition because it would be harder to find a debris-free region in a larger area. Taking into account these factors, the scan range was set to be 25×25 μm^2, and the tip height was 200 nm above the sample surface. The MFM images of one chosen region on VBST1 at different magnetic fields are shown in Fig. 5.5. Figure 5.5(a) and (b) show the magnetic field dependence of film resistance R of VBST1 and the frequency shift Δf of MFM tips at $T = 4.2$ K. Each MFM image in Fig. 5.5(c) is colour-coded in their titles and was taken at the end of the magnetic field sweep with corresponding colours in Fig. 5.5(a) and (b), except for the "0 T" image, which was taken before the H sweep from 0 T to 2 T.

In theory, one should expect to see the domains grow larger as the magnetic field increases from 0 T to $H_c \sim 0.4$ T, where equal population of up- and down-domains should form in VBST1. Beyond H_c, the domain size should shrink and the entire film should gradually change into a single domain state when the magnetic field reaches $H_s \sim 0.7$ T. However, from 0 T to 0.8 T, we cannot observe an obvious evolution of domain structure in the MFM pattern. Instead, the shape of features starts to change from 1.0 T to 1.4 T. This contradicts our prediction that the film should be in a fully-magnetised state and the MFM image should be basically featureless beyond 0.7 T. The same measurement was also conducted in the negative magnetic field regime, i.e. from $\mu_0 H = 0$ T to -1.4 T. Nevertheless, not only the evolution of MFM images but also the shape of features are similar to Fig. 5.5(c), which may suggest that the change of contrast observed is not due to domain movements. Furthermore, similar experiments were repeated with different scan ranges and tip heights (i.e. different spatial resolutions) as well as in different locations on the film, but none of the observations is consistent with the expected evolution of the domain structure.

As an alternative approach, we performed a magnetic field spectroscopy, which should allow us to probe the domain movements with less influence from the possible relaxation of magnetisation that occurs during the scan [101, 102]. Moreover, in this way, the change of contrast should be dominated by the change of magnetisation in the film under the MFM tip, and the unwanted signals caused by the debris on the surface should be diminished.

The spectroscopy was taken along the green dashed line in Fig. 5.6(a) at a tip height of 200 nm. The H field was swept from -1.4 T to 1.4 T and then back to -1.4 T, as indicated by the cyan arrow in Fig. 5.6(b). In principle, the left and right panels should have similar patterns with opposite colour contrast, if the patterns are caused by magnetic domain reversal.

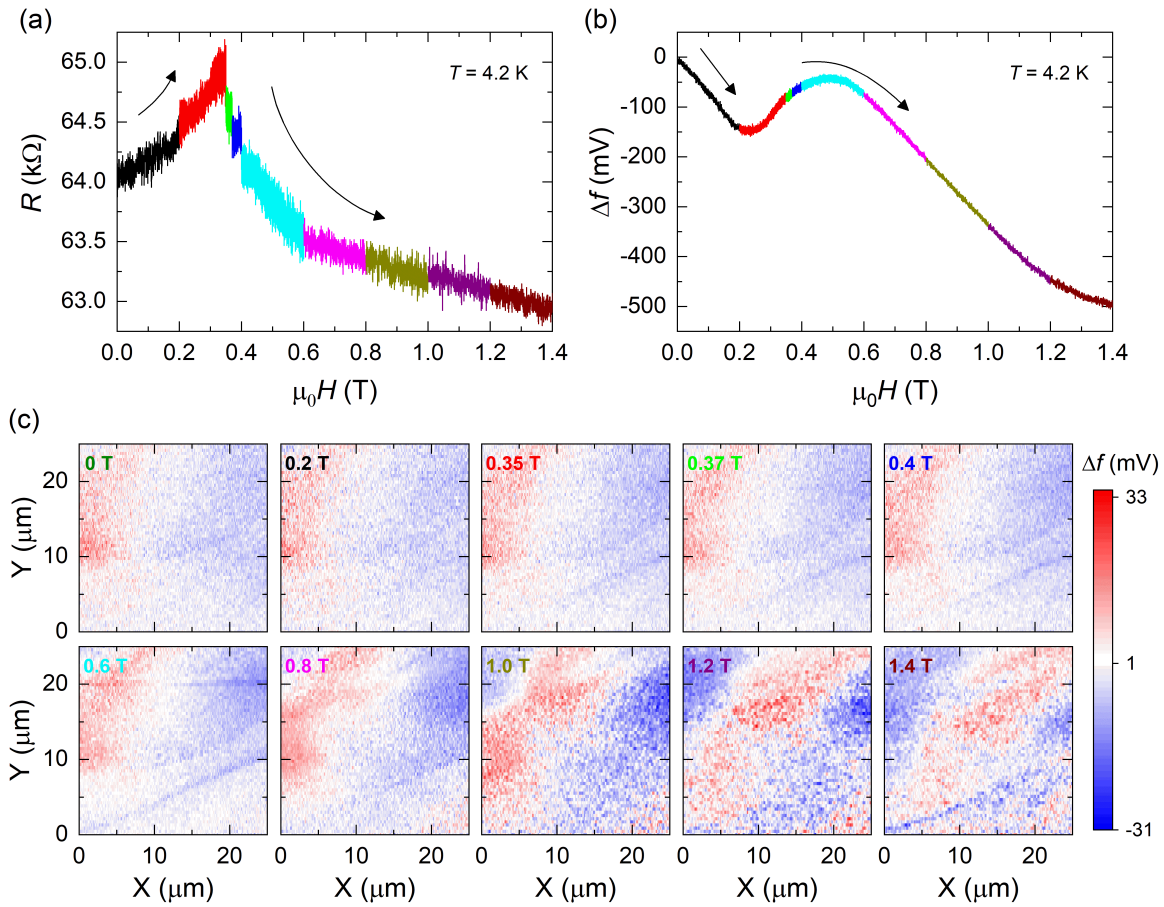

Figure 5.5: The magnetic field dependence of (a) the film resistance R of VBST1 and (b) the frequency shift Δf of MFM tips at $T = 4.2$ K. The arrows indicate the direction of magnetic field sweeps. Each of the MFM images in (c) is colour-coded in their titles and was taken at the end of the magnetic field sweep with corresponding colours in (a) and (b), except for the 0 T image, which was taken before the H sweep from 0 T to 2 T. It should be noted that, as can be seen in (b), because the average level of Δf changes substantially with the magnetic field, the MFM images in (c) are obtained after subtracting the background from their corresponding raw images. The scan range is 25×25 μm^2 and the tip height is 200 nm above the sample surface for this series of MFM scans.

Moreover, in each panel the left side and right side should have opposite colours because the magnetisation states near $\mu_0 H = -1.4$ T and $\mu_0 H = 1.4$ T should be exactly opposite. However, it turns out that a very similar symmetric pattern without opposite contrast on the left and right side shows in both panels. Again, the result does not support our prediction about the contrast variation with the change of magnetic field.

Therefore, we have to conclude that the patterns we observed in the MFM images do not simply arise from the magnetic domain structures, and we cannot claim to have observed the

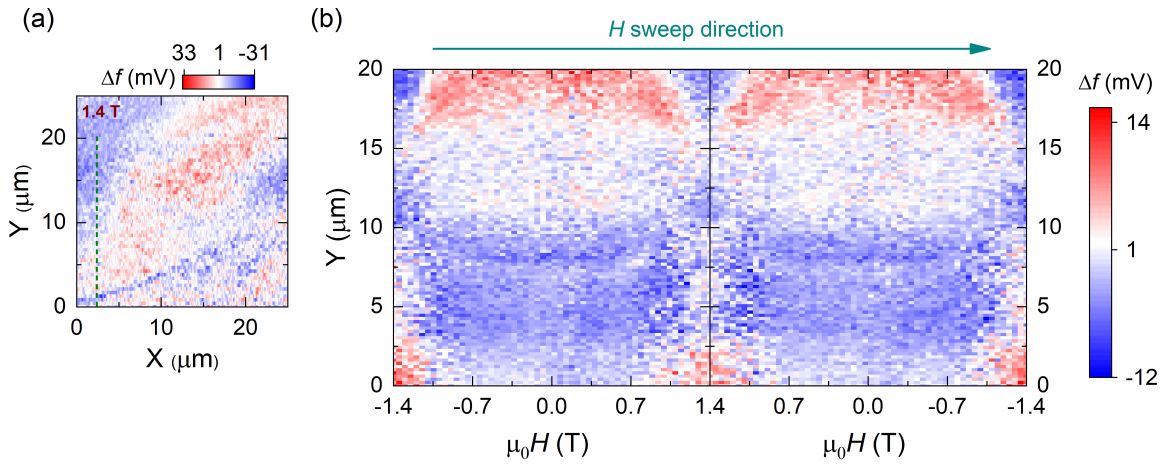

Figure 5.6: (a) The MFM image at the same location as Fig. 5.5(c). The green dashed line shows where the magnetic field spectroscopy was taken. (b) The magnetic field spectroscopy along the dashed line shown in (a). In this spectroscopy, the magnetic field was swept from $\mu_0 H = -1.4$ T $\rightarrow$ 1.4 T $\rightarrow -1.4$ T.

domain structures of the magnetic TIs. After our attempt, two groups successfully observed the domain structures in magnetic TIs using MFM [135–137]. Retrospectively, there are a couple of possible reasons why we could not observe the domain structures in VBST1. The first one is to do with the poor surface condition of our film. In addition to the debris and dust that can give rise to confusing signals, ripples in the film, the folded parts and material accumulation near the scratched traces are the same magnetic TI material and can contribute to the MFM signals too. The stray magnetic fields of these objects may affect the MFM tip from the sides and make the magnetic force sensed by the MFM tip very complicated, smearing out the contrast change purely caused by the domain movements in the film. Secondly, according to Kittel's law, the domain size in a thinner film will be smaller due to the size confinement effect, and the domain walls will also be narrower [138]. The groups who observed the domain structures of magnetic TIs used much thicker films (7-17 QL) than our sample [135–137]. The size of domains reported in their work is generally no more than 500 nm. It is possible that the domain size in our film is even smaller, which is not only close to the resolution limit of our SPM system, but may also be easily overshadowed by the interference signals from the aforementioned objects on the surface. Finally, although the nominal coercivity of the MFM tip is 300 Oe and the tip should be magnetised before the film in a magnetic field sweep, a better choice would be to use tips with much higher coercivity than the H_c of the magnetic TI film. The magnetisation and demagnetisation process of the tip itself can lead to additional contrast that does not originate from the film and increase the difficulty of interpreting the MFM images.

In summary, the poor surface condition of VBST1 and the potential complex behaviours of our MFM tips are the possible reasons for not being able to observe the domain structures on VBST1. Accordingly, for the next film, we tried to improve the surface condition and image the domain structures using different SPM techniques.

5.4 Transport and SPM measurements on device VBST2

5.4.1 Visualising magnetic domain structures in VBST2 by SHPM

To avoid the problems of poor surface conditions, for our second film - VBST2, we tried to minimise the fabrication processes before any SPM measurements to keep the surface as clean as possible. Therefore, we simply placed five indium pieces on the film as Ohmic contacts without scratching the surface, and bonded these contacts onto an LCC for basic characterisations. The layer structure and device layout of VBST2 are shown in Fig. 5.7.

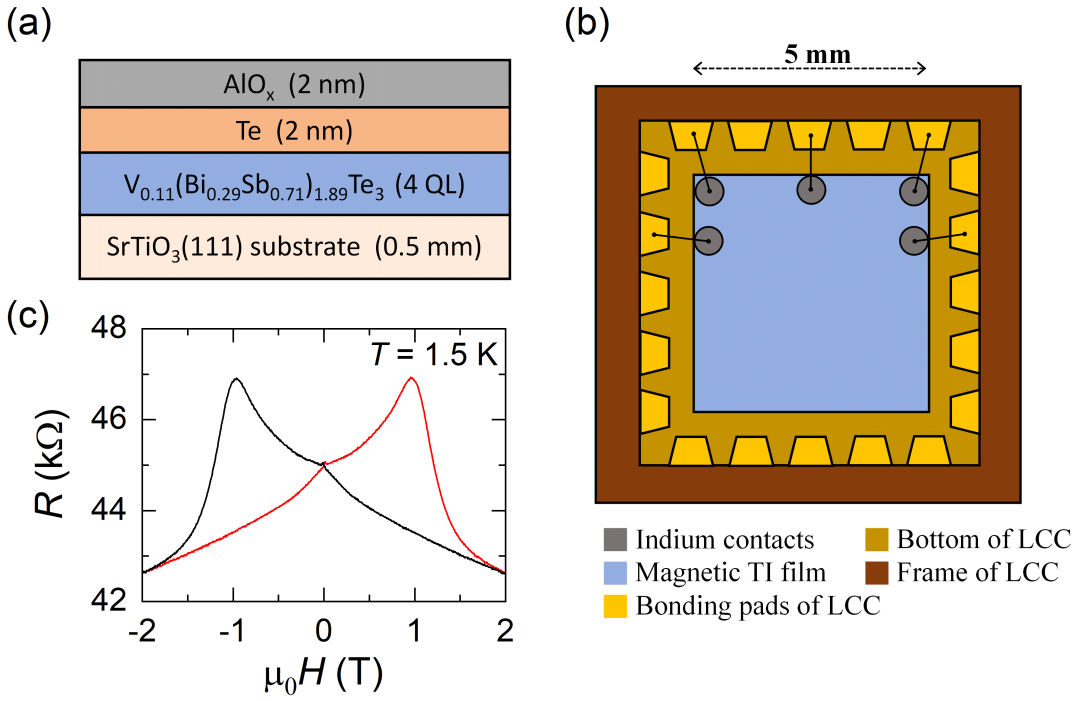

Figure 5.7: (a) The layer structure of VBST2. (b) The schematic diagram of the device VBST2. The 5×5 mm^2 magnetic TI film was mounted on the LCC and five indium contacts were made near the edge of the film. (c) The magnetic field dependence of the film resistance R shows a butterfly structure, verifying the ferromagnetism of VBST2. The black and red curves represent the downward and upward sweeps, respectively.

After confirming the ferromagnetism in VBST2 by two-terminal transport measurements, as shown in Fig. 5.7(c), the device was taken to Prof. Simon Bending's Lab at the University of Bath for further SPM measurements. Prof. Bending's lab specialises in the study of magnetic properties of superconducting and ferromagnetic materials using the SHPM system developed in his lab. The SHPM experiments described in this section were done in collaboration with Dr. Estefani Marchiori Pereira.

There are several advantages in using SHPM for imaging magnetic domain structures. First of all, unlike the MFM, the SHPM is non-invasive and does not modify the magnetic structures of the sample during the scan. Thus, in principle the domain pattern in a region can be repeatedly obtained in different SHPM scans if the external magnetic field is not changed. Secondly, SHPM can provide direct quantitative information of the magnetic structure. Compared to MFM, which generates images in terms of the frequency shift of the PLL, SHPM can directly map the magnetic structures in units of magnetic field, e.g. gauss or tesla, making the interpretation of scan images much more straightforward. Finally, the sensitivity of SHPM can be as high as ~ 0.1 G [129], which is excellent for imaging magnetic structures emanating weak magnetic fields, such as the domains of magnetically doped TI films. For these reasons, we decided to turn to the SHPM for pursuing the visualisation of domain structures in VBST2.

There are also some constraints for the SHPM system. First and foremost, the SHPM system is generally not designed for working under strong magnetic fields. In a high magnetic field, the QHE can be induced in the Hall probe and invalidate the working mechanism of SHPM. In fact, the Hall sensor electronics in the system we used saturate at fields ~ 100 mT, which occurs even earlier than the QHE. Therefore, unlike the MFM, which directly takes images at magnetic fields, to study the magnetic field dependence of domain patterns by the SHPM, we have to utilise the remanence images. The remanence field of a ferromagnet is defined as the residual magnetisation when the external magnetic field is withdrawn. Hence, we can obtain a remanence image by ramping the magnetic field to a target value and then back to zero, and the change of domain pattern should be observed in the remanence image.

Secondly, the cryostat system we used for the SHPM requires its sample space to be filled with ^{4}He gas to prevent the piezoelectric materials from being damaged due to plasma discharge under low temperature and high vacuum environment. As a result, the temperature for our SHPM experiments was always kept above the boiling point of ^{4}He, and most of the SHPM images were taken at 5-15 K. For this reason, we also characterised the film at 5 K and 10 K before the SHPM experiments and found the H_c to be 0.6 T and 0.4 T, respectively.

The SHPM images of VBST2 at 15 K are shown in Fig. 5.8. Figure 5.8(a) was taken at 0 T after zero-field cooling (ZFC) as a reference image. The external magnetic field was

then swept to 0.4 T and back to 0 T for taking the remanence image (Fig. 5.8(b)) because 0.4 T should be enough to fully-magnetise the film at 15 K. The same procedure was also performed for taking the remanence images of 0.6 T and −0.6 T. From the remanence images, no evident change in the pattern can be observed, which may imply that the two bright regions near the bottom-right corner as well as the dark region at the bottom-left corner are not associated with the domain structures of VBST2. To clearly compare the difference between images, we subtracted the SHPM image at 0 T from the remanence images and plotted the differential images, as shown in Fig. 5.8(e)-(g). The contrast map of the 0.4 T differential image (Fig. 5.8(e)) shows a distinct difference to that of the 0.6 T (Fig. 5.8(f)) and −0.6 T differential images (Fig. 5.8(g)), while the 0.6 T image and −0.6 T image manifest a similar pattern, suggesting that the pattern may originate from the domain structures of VBST2.

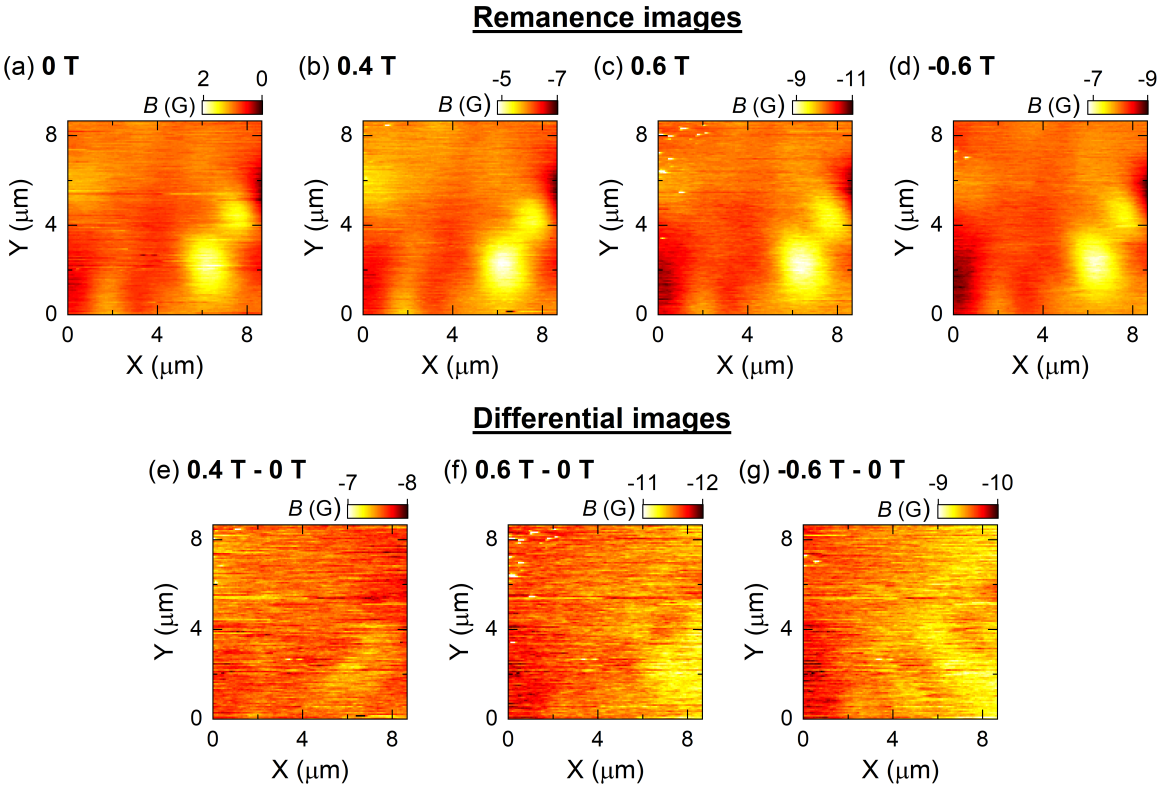

Figure 5.8: (a) The SHPM image taken at 0 T after ZFC. (b) The remanence image of 0.4 T taken after cycling the external magnetic field from 0 T to 0.4 T and back to 0 T. (c) and (d) are the remanence images of 0.6 T and −0.6 T taken in a similar manner as (b). (e), (f) and (g) are the differential images of 0.4 T, 0.6 T and −0.6 T, respectively, obtained by subtracting the 0 T image from the corresponding remanence image. All images were taken at a tip height of 300 nm at $T = 15$ K with a scan range of 8.66×8.66 μm^2.

To closely check the structure observed in the differential images, we decided to reduce the scan range for higher spatial resolution and reduce the temperature, which in theory should enlarge the size of magnetic domains.

Because the Curie temperature of the V-BST film reported was 23 K [106], we first heated the sample space to 25 K to eliminate the magnetisation of the film, and cooled it to 10 K to take another ZFC virgin state image, as shown in Fig. 5.9(a). Two bright regions exist at the bottom-right corner about the same position as in Fig. 5.8, suggesting that the Hall probe was still roughly in the same location. After checking the surface condition in this area, we chose the bottom-left quarter of the scan frame for our closeup SHPM scans, as shown in Fig. 5.9(b).

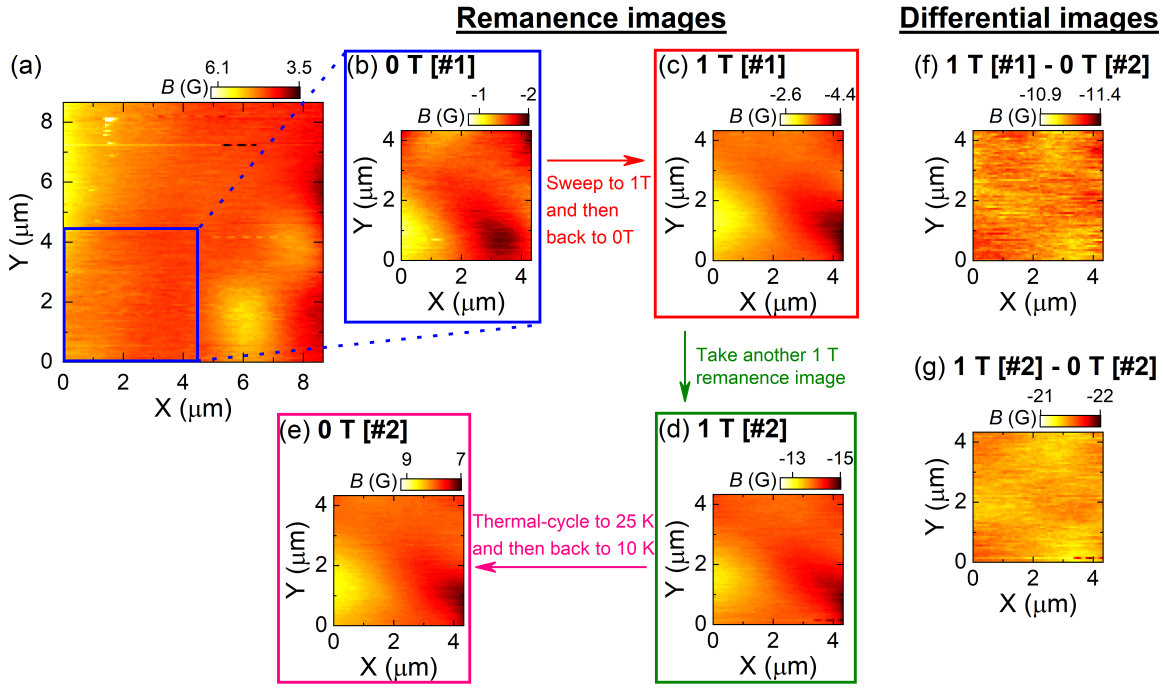

Figure 5.9: (a) The 8.66 × 8.66 μm^2 SHPM image taken at 0 T after ZFC. (b) The closeup SHPM image of the bottom-left quarter in (a). (c) The remanence image taken after sweeping the magnetic field to 1 T and then back to 0 T. (d) Because the Hall probe sometimes became slightly unstable in a period after the magnetic field sweep and even shifted in position after magnetic field sweeps, the remanence image of 1 T was measured again. (e) To avoid the possible position shift of the Hall probe, the film was thermal-cycled to 25 K and then back to 10 K for taking another virgin state image. All images were taken at a tip height of 182.5 nm at $T = 10$ K with a scan range of 4.33 × 4.33 μm^2, except (a), which was taken at a tip height of 300 nm at $T = 10$ K with a scan range of 8.66 × 8.66 μm^2.

Since we know $H_c \sim 0.4$ T at 10 K from earlier characterisations, the film should be fully-magnetised for a field of 1 T at 10 K. Hence, a differential image between 0 T and 1 T remanence images should explicitly show the change of domain patterns between the virgin state and the fully-magnetised state. In addition, during the experiments we noticed that the Hall probe was sensitive to high magnetic field sweeps and could become slightly unstable in a period after the sweep or even shift in position. Thus, the procedure for the measurements is shown in Fig. 5.9(b) to (e). Firstly, after confirming the scan area using the virgin state image (Fig. 5.9(b)), the remanence image of 1 T was taken twice (Fig. 5.9(c) and (d)) in case the magnetic field sweep had affected the first one. Then we thermal-cycled the film again to 25 K and back to 10 K for taking another virgin state image with no shift in the Hall probe's position (Fig. 5.9(e)). In this way, we can subtract the last virgin state image from the remanence images and extract weak signals. Also, the comparison between the two differential images from the two different remanence images will show whether the contrast pattern is caused by noise or domain movements. It can be seen from Fig. 5.9(f) and (g), both images show a similar pattern. The size of the patch-like structures ranges from several hundred nanometers to 2 μm, and the magnetic fields emanating from these structures are lower than 1 G. An MFM study conducted by Wang *et al.* at about the same period as our SHPM experiments reported the observation of domain structures in a 10 QL $V_{0.11}Sb_{1.89}Te_3$ film, in which single domains with a size up to ~ 2 μm were seen [137]. Although the material and thickness of their sample are slightly different from ours, their result is consistent in order of magnitude with our observation. Hence, despite the domain size being slightly bigger than we expected for our 4 QL film, both the field strength and size are within a reasonable order of magnitude of the properties of magnetic domains.

Therefore, we planned to further reduce the scan range and tip-sample distance to improve the spatial resolution of the structure and obtain images showing clearer domains and domain walls. Unfortunately, the Hall probe drifted in the process of a liquid helium fill before we could do this, and the Hall probe moved to a different location with many large-size particles on the surface. Moreover, the SHPM system we used did not have a mechanism for controlling the motions of Hall probe in *xy*-plane. The only way to make lateral movements was by knocking the insert with a hammer, which is very uncontrollable. After a couple of unsuccessful trials to find clean regions, the Hall probe crashed into the surface of the film because of the knock, leaving a lot of debris on the surface and damaging the z-positioner of the SHPM system. As a result, we had to stop the experiment and take VBST2 out from the cryostat.

Although the structures observed in Fig. 5.9(f) and (g) are likely to have a magnetic origin according to our analysis, there is no decisive evidence that they are indeed magnetic domains of VBST2.

In summary, some structures that may be associated with the magnetic domains were observed in the SHPM study of VBST2. However, further experiments are needed to confirm our results. The main obstacles to the SHPM experiments on VBST2 are the weak magnetic effect (< 1 G) as well as small size (~ 1 μm) of magnetic domain structures. To detect such weak magnetic signals, the key is probably to improve the surface condition of the film so that the noise and signals caused by the debris on the surface can be alleviated, and the Hall probe can get closer to the surface to increase the sensitivity.

5.4.2 Preparation for experiments at millikelvin temperatures

Although we did not obtain clear images of domain structures, our SHPM data and other papers that report observations of magnetic domain structures give us a rough idea about the size of domain structures in magnetic TI films. Since both the MFM and SHPM measurements are difficult to implement using the instruments we have access to, we decided to study different aspects of the V-BST films.

In theory, the chiral edge states of magnetic TI films in the QAHE should travel along the domain boundary. When a thin film of magnetic TI is uniformly magnetised, the domain wall should be pushed to the side surface of the film. In this condition, edge states should be observed by the SGM at the physical edges of the film. On the other hand, when the film is demagnetised at the coercive field and enters a multi-domain state, the chiral edge states should be observed in the network of domain walls existing on the entire sample surface. Thus, the contrast change in SGM between the fully-magnetised and demagnetised states should be the observational evidence of the QAH states. Moreover, in a multi-domain state the current path imaged by SGM should delineate the outline of magnetic domains. If the structures observed in SGM images are similar to the size and shape of the magnetic domains shown in the MFM and SHPM images, the observation of QAH states can be further confirmed.

In order to perform the SGM study of the QAHE, the VBST2 sample was scratched into a Hall bar geometry and rebonded, as shown in Fig. 5.10(a). The magnetic tip used in the MFM measurements described in Sec. 5.3 was replaced by a diamond tip, which has a higher endurance in AFM experiments and allows us to apply a bias on the tip for the SGM and EFM experiments.

Because the study of the QAHE requires millikelvin temperatures, the VBST2 Hall bar device and the SPM system were lowered into a dilution refrigerator. Pilot experiments show

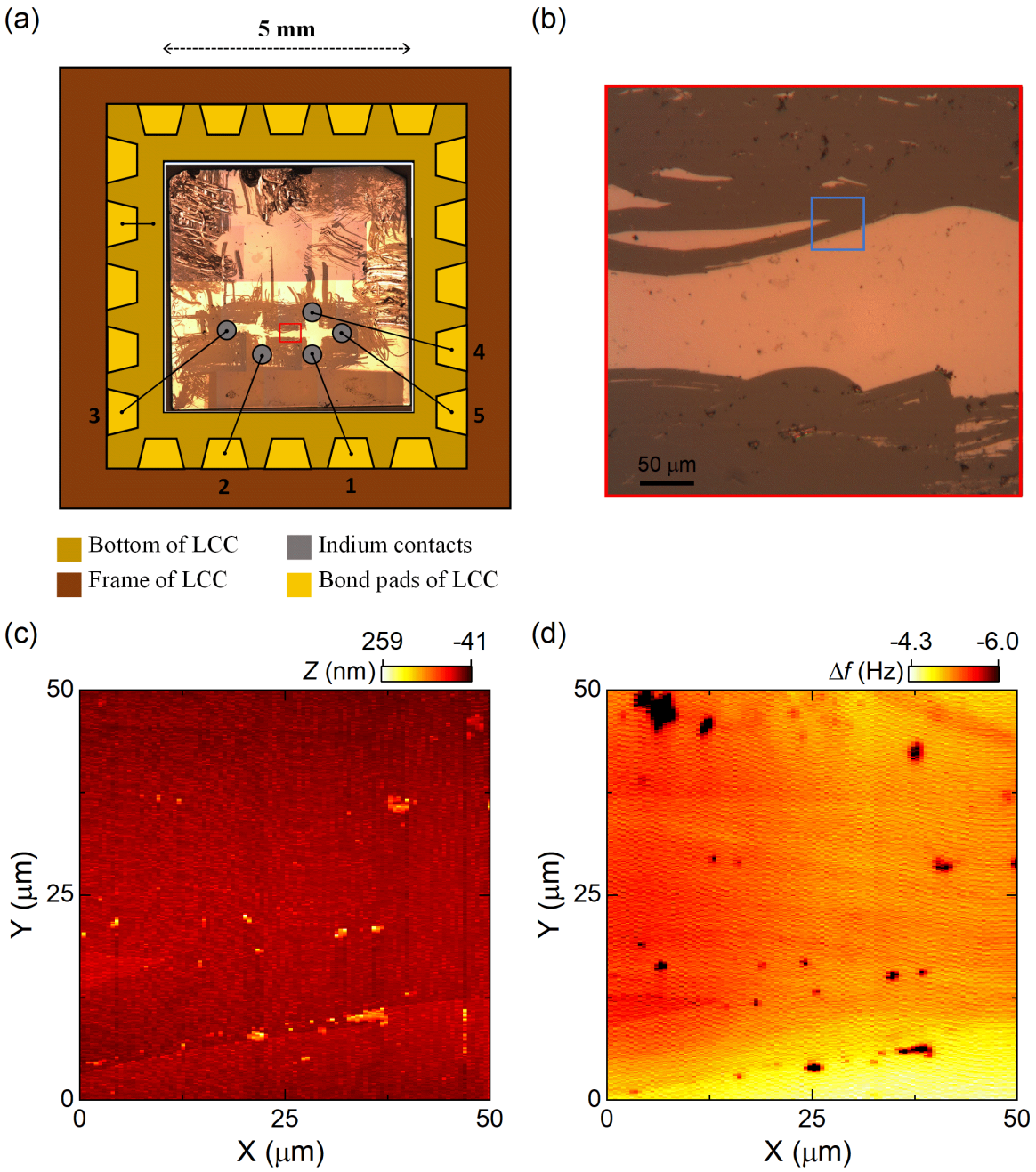

Figure 5.10: (a) The layout of the VBST2 Hall bar device. Numbers 1 to 5 correspond to the five contacts on the Hall bar. A zoomed-in image of the region enclosed in the red box is shown in (b). The area chosen for SPM study is indicated by a blue box in (b). (c) The AFM image of the area inside the blue box in (b). The edge of the Hall bar channel and a triangular feature of the part of an isolated film can be seen on the left side of the image. (d) The EFM image of the area inside the blue box in (b). The features shown in the AFM image can also be observed in the EFM image. These measurements were taken at $T = 300$ K.

that the piezo positioners of our SPM system may drift up to $\sim$ 100 µm in the *xy*-plane owing to the contraction of piezo materials during the cool-down procedure. Therefore, before the sample was sealed in the IVC can, we used the AFM to find a smooth edge in the scratched Hall bar to roughly position the tip in an area suitable for later SPM scans, as shown in Fig. 5.10(c).

After the SPM system was sealed in the IVC can and pumped to high vacuum ($\sim 10^{-6}$ mbar), the Q-factor of the tip usually becomes very high, and the tapping mode AFM is no longer viable because the PID loop cannot provide sufficiently quick feedback to the SPM system. Consequently, in the low-temperature measurements that normally are performed under high vacuum, we have to rely on EFM rather than AFM to distinguish the topographical features on the surface of the film. Hence, next we used the EFM to look for and return to the same scan area, as shown in Fig. 5.10(d). Remarkably, we observed that the main channel and triangular feature near the bottom-left corner showed opposite contrast despite both being V-BST film. This may be related to the grounding condition of the film. Since the film of the main channel was grounded through the contacts while the triangular feature is part of an isolated piece of film, the capacitance between the tip and these two types of films turned out to be different. This is something that should be kept in mind when interpreting the EFM images in later discussions.

The sample along with the SPM system were then lowered into a Kelvinox MX100 dilution refrigerator (henceforth referred to as "fridge") for low-temperature measurements.

5.4.3 Transport measurements on VBST2

At fridge temperatures, we first performed transport measurements to characterise the electric properties of VBST2 before proceeding to SPM experiments.

To begin with, the two-terminal resistance between different combinations of contacts was measured using a constant current of 10 nA to find the most appropriate pair of contacts for transport measurements. Due to the large aspect ratio of the middle channel of the scratched Hall bar, the resistance between most contacts were higher than 500 kΩ, except for between electrode 1 and electrode 4, which is $\sim$ 200 kΩ. Accordingly, we decided to perform most of our transport measurements using $R_{14,14}$, where $R_{ij,mn}$ means that the current is passed from electrode i to electrode j and the voltage drop is measured between electrode m and electrode n.

The DC current-voltage (I-V) curves between contact 1 and 4 of VBST2 at different temperatures are shown in Fig. 5.11(a). The I-V curve at the base temperature $T = 23$ mK shows a very small non-linearity, which becomes less prominent at 50 mK and completely disappears at 4.7 K. The small non-linearity is possibly caused by the Joule heating effect

that becomes pronounced at very low temperatures. As the temperature increases, this heating effect becomes less significant and even negligible at 4.7 K. The same effect has been observed by other groups and thus the source-drain (S-D) current used for fridge-temperature experiments on magnetic TIs is usually chosen to be less than 10 nA [101, 105, 106]. Based on our *I-V* curves, we decided to use 1 nA as excitation current for later transport measurements. Moreover, from the *I-V* curves in Fig. 5.11(a) we deduce that the film is not in the QAH regime at $V_g = 0$ because the resistance becomes smaller in high current regime where the Joule heating is more pronounced, suggesting that the film still has an insulating temperature-dependence. This is opposite to the observation of Bestwick *et al.*[101] and Chang *et al.*[106], in which the samples are tuned into the QAH regime and show a metallic temperature-dependence, as the example shown in Fig. 5.11(b).

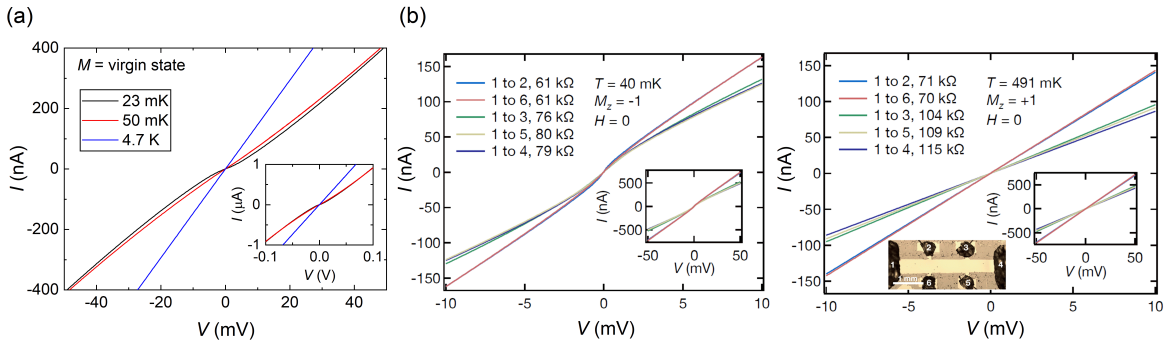

Figure 5.11: (a) The *I-V* curves of VBST2 Hall bar at 23 mK, 50 mK, and 4.7 K. The non-linearity observed in the *I-V* curve at 23 mK becomes smaller at 50 mK, and finally disappears at 4.7 K, suggesting that it may arise from the current heating effect that is more prominent at lower temperatures. These *I-V* curves imply that VBST2 has an insulating temperature-dependence and hence is not in the QAH regime at $V_g = 0$. The inset shows the *I-V* curve over a larger voltage range. (b) Similar non-linear *I-V* curves observed on magnetic TI films by Bestwick *et al.* [101]. The non-linearity observed at 40 mK (left panel) becomes negligible at 491 mK (right panel). The inset photograph in the right panel is the layout of their Hall bar. In contrast to our results, their *I-V* curves show a metallic temperature dependence, indicating that their sample is in the QAH regime. The graphs in (b) are adapted from [101].

The backgate voltage (V_g) dependence of transport properties was also tested. However, no V_g dependence was observed on VBST2. This is likely due to a bad connection between the STO substrate and the LCC. For example, if the silver paste is not uniformly distributed on the back of STO, or some debris and bubbles get stuck at the interface between the STO and the bottom of LCC during the device fabrication, the film will not be homogeneously gated. It is also possible that the STO and LCC are not held tight enough by the silver paste and a gap between them can substantially reduce the gating effect. Nevertheless, we decided

to continue the experiments without lifting the probe to check the backgate at this stage because taking the sample out of vacuum will inevitably introduce more contamination and degrade the quality of the TI film. Therefore, all the transport measurements on VBST2 were carried out at $V_g = 0$ V.

Magnetic field sweeps for $R_{14,14}$ are shown in Fig. 5.12. The conditions for each sweep are shown in the top-left corner of each plot, where T_{mc} is the temperature of the mixing chamber and M_0 is the magnetisation state before the sweep. All magnetic field sweeps start from 0 T and go through the black, red, green, blue curves and then finally returns to 0 T. Although the butterfly structure can still be observed, we found that the magnetoresistance of the film is extremely sensitive to temperature variations. Firstly, a significant drop in $R_{14,14}$ after the magnetic field sweep started can be observed in all plots in Fig. 5.12. This is likely due to eddy current heating from dH/dt on VBST2 and the mixing chamber, the magnetocaloric effect due to magnetic moment flipping in VBST2, and the vibration of cryogenic parts of the fridge under strong magnetic fields. As will be discussed later, the temperature of the sample (T_s) is actually decoupled from the temperature of the mixing chamber (T_{mc}) at such low temperatures. Secondly, magnetic field sweeps with different sweep rates can significantly affect the shape of the butterfly. For instance, the sweep rate of 10 T/hr (Fig. 5.12(a)) creates a heating power that is higher than the cooling power of the fridge at 22.9 mK, thus the background level of $R_{14,14}$ becomes increasingly lower due to the continuous heating. In contrast, the heating powers caused by the sweeps of 2 T/hr (Fig. 5.12(b)) and 1 T/hr (Fig. 5.12(c)) are smaller than the cooling power of the fridge at 30.2 mK and 24.5 mK, respectively, hence the background level of $R_{14,14}$ becomes increasingly higher. Thirdly, a sharp drop in $R_{14,14}$ when the magnetic field is swept across 0 T can be observed. Although the reason is not clear, this phenomenon has been observed in experiments using different materials (including GaAs/AlGaAs quantum well, non-magnetic TIs and graphene devices) in different dilution refrigerators in our group, suggesting that it is related to the instruments, perhaps some kind of heating mechanism originating from the reversal of polarity of the superconducting magnet. This effect has also been reported by other groups [101, 104, 109], but none of them identified the source of the heating. To double-check that this heating around the ZF near the polarity switching of superconducting magnet is not caused by the magnetic TI film itself, we further tried removing our device and lowering an empty sample holder into the cryostat. It turns out that this heating event around the ZF is still present in T_{mc}, which suggests that it should come from the instruments.

All the aforementioned thermal effects become negligible and no corresponding structures can be observed above 1.5 K, indicating these phenomena only can be explicitly detected at very low temperatures. These thermal effects considerably increase the difficulty of

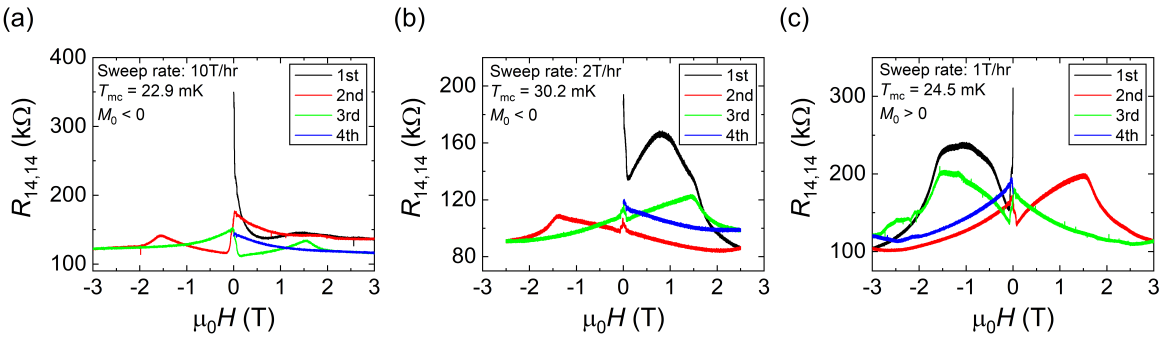

Figure 5.12: The magnetic field sweeps on VBST2 at fridge temperatures show strong sweep-rate dependence. All magnetic field sweeps start from 0 T and go through the black, red, green, blue curves and then finally returns to 0 T. T_{mc} is the temperature of mixing chamber and M_0 indicates the initial magnetisation state of the film before the sweeps. (a) The magnetic field sweep at 22.9 mK using a sweep rate of 10 T/hr. (b) The magnetic field sweep at 30.2 mK using a sweep rate of 2 T/hr. (c) The magnetic field sweep at 24.5 mK using a sweep rate of 1 T/hr.

interpreting the data associated with magnetic field sweeps, but it is still clear that VBST2 does not show the QAHE. Remarkably, these thermal effects seem to be less serious in magnetic TI films that show the QAHE. A possible explanation is because the QAH states are not sensitive to the change of temperatures, just like the QH states in the QHE. As long as the thermal energy generated by the heating effect is not larger than the size of magnetic gap/Landau gap in the QAHE/QHE, the carrier transport behaviour of the QAH/QH states are almost independent of the temperature. This speculation is also consistent with the fact that VBST2 is not in the QAH regime according to the *I*-*V* curves and should be dominated by dissipative 2D and 3D bulk transport that are much more temperature-dependent.

To simplify the complicated heating factors in magnetic field sweeps, we prepared a data acquisition program to record the T_{mc} change during a magnetic field sweep, aiming to find out the most appropriate sweep rate for measurements. As shown in Fig. 5.12, a fast sweep generates excessive heating power that keeps heating the system, while a slow sweep rate has less heating power than the cooling power of the fridge. Consequently, both show temperature fluctuations during the magnetic field sweeps. By many rounds of trial and error, we found that 5 T/hr seems to produce a heating power which is roughly equivalent to the cooling power of the fridge, as shown in Fig. 5.13. For the 10 T/hr sweep in Fig. 5.13(a) and (c), both the temperature of the sample and the mixing chamber kept increasing during the sweep. On the other hand, for the 5 T/hr sweep in Fig. 5.13(b) and (d), the temperature of the mixing chamber seems to fluctuate between 70 mK and 110 mK, and the background

level of $R_{14,14}$ became stable after the 1st trace (black), suggesting that the temperature of the film gradually reached thermal equilibrium in the process of the 1st sweep.

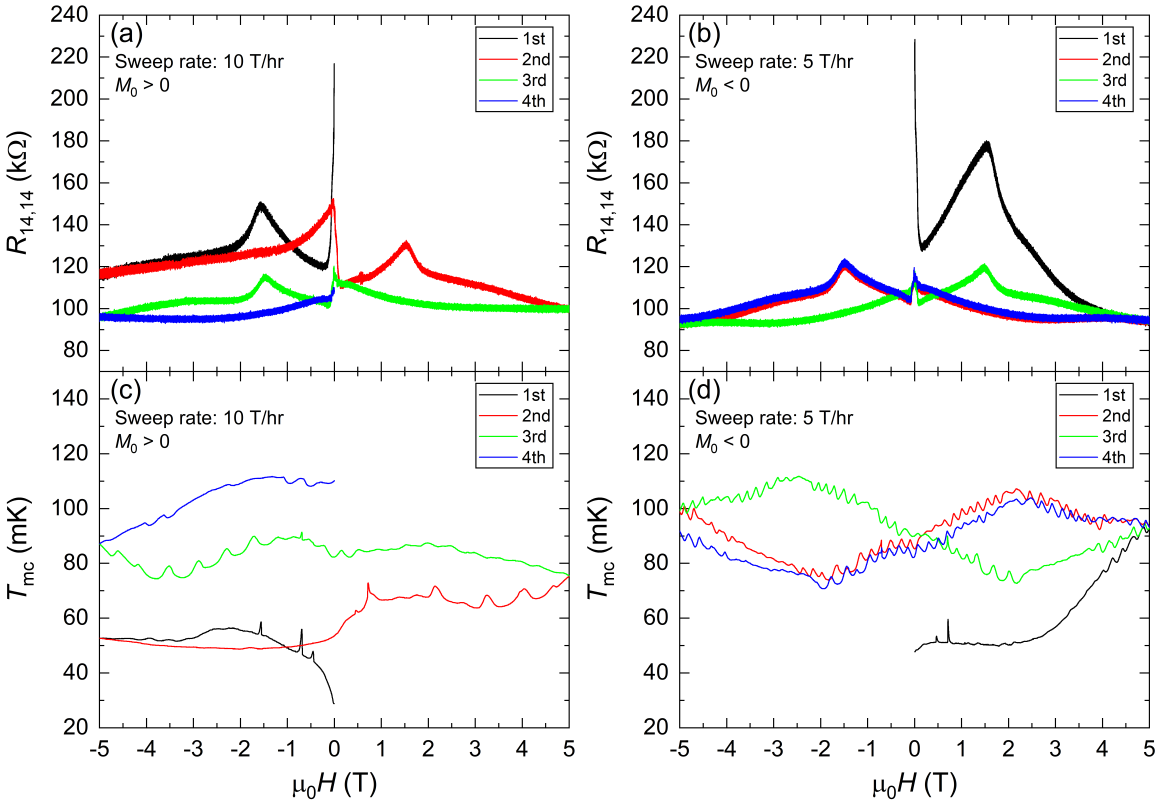

Figure 5.13: The magnetoresistance of VBST2 and the mixing chamber temperature of the fridge during the magnetic field sweeps at a sweep rate of (a) 10 T/hr and (b) 5 T/hr. Both sets of magnetic field sweeps start from 0 T and go through the black, red, green, and finally blue curves.

Several features are worth noting in Fig. 5.13. Firstly, although both T_{mc} and $R_{14,14}$ reflect the heating that occurs at the beginning of the magnetic field sweeps, it is much more pronounced in terms of the change of $R_{14,14}$. Comparing Fig. 5.13(c) and (d), the change of T_{mc} due to the onset of magnetic field sweep are different. However, the change of $R_{14,14}$ in Fig. 5.13(a) and (b) are similar in magnitude. This implies that T_{mc} no longer represents T_s, and the film is more sensitive to temperature changes caused by magnetic field sweeps. In later experiments, we repeatedly found that the change of film resistance cannot be directly deduced by the change of T_{mc}, supporting our speculation that T_{mc} is decoupled from T_s.

Secondly, the heating event around the ZF during the polarity reversal of external magnetic field does not always reflect in the change of T_{mc}. For instance, T_{mc} in Fig. 5.13(d) around the ZF does not show a sign of heating, whereas $R_{14,14}$ in Fig. 5.13(b) clearly shows a sharp drop around the polarity reversal of the external magnetic field. This may indicate that the

heating occurs closer to the sample holder than the mixing chamber, and may originate from some paramagnetic parts on the probe or cryostat. Since the heating mostly happens between $\mu_0 H = 0$ and ± 20 mT when the external magnetic field is swept toward zero, we carried out an experiment by stepping the H field between -100 mT and 100 mT to closely examine the magnetic field dependence of $R_{14,14}$ around the ZF. As shown in Fig. 5.14, the magnetic field was changed from 100 mT toward -100 mT in 10 mT intervals at a rate of 5 T/hr followed by a wait of 20-30 minutes. The waiting time is determined by monitoring the relaxation of $R_{14,14}$ after each sweep until it became saturated and stabilised. As can be seen in Fig. 5.14, $R_{14,14}$ rapidly drops every time when the H field sweep is initiated due to the heating caused by $\mathrm{d}H/\mathrm{d}t$. In the following waiting period, $R_{14,14}$ creeps back to a higher value. If we take the $R_{14,14}$ values after the waiting period as the thermodynamically equilibrium values and connect these points together (shown by the dashed line in Fig. 5.14), we found that the sharp drop of $R_{14,14}$ around the ZF can be greatly suppressed. Bestwick *et al.* has tried an ultra-slow magnetic field sweep using an average rate of 39.6 mT/hr to reduce the heating effect that comes with the sweep. However, this approach is not practical in our cryostat since our dilution refrigerator can rarely stay at a stable temperature for such a long time. Furthermore, the Cr-doped TI film they used has a coercive field less than 200 mT, while our VBST2 has a coercive field of ~ 1.5 T at millikelvin temperatures. It would take unrealistic long time to complete such an ultra-slow sweep.

Alternatively, we also tried using a slower sweep rate for the range where thermal effect is pronounced and a fast rate for the rest of the sweep. A result from these experiments is shown in Fig. 5.15. We used 5 T/hr for the sweep between $\mu_0 H = \pm 0.3$ T, and 10 T/hr for the sweep of $|\mu_0 H| > 0.3$ T, hoping to minimise the sweep-rate-dependent thermal effect but at the same time still obtain the result of magnetic field sweeps in a feasible time scale. Unfortunately, a prominent heating effect due to the change of $\mathrm{d}H/\mathrm{d}t$ can be observed as a sudden drop of the magnetoresistance when the sweep rate is increased, as indicated by the black arrows, leading to even more artificial features in the butterfly structure.

From the resistance-temperature (R-T) relation of $R_{14,14}$, as shown in Fig. 5.16, we can have a more quantitative idea about the various heating effects during the magnetic field sweeps. The R-T curve between 33 mK and 572 mK shown in Fig. 5.16(a) is taken during a cool-down process when the magnetisation state is upward ($M_0 > 0$) in the absence of external magnetic field ($H = 0$). The cool-down process is made slow enough with a cooling rate of 0.683 mK/min to make sure that the T_{mc} and T_s are always in good thermal equilibrium. Therefore, unlike the magnetic field sweep experiments, the T_{mc} in this measurement can be regarded as T_s. A similar R-T curve at $M_0 < 0$ taken at $H = 0$ between 36 mK and 840 mK is shown in Fig. 5.16(c). If we use these R-T curves to deduce the actual T_s in the magnetic field

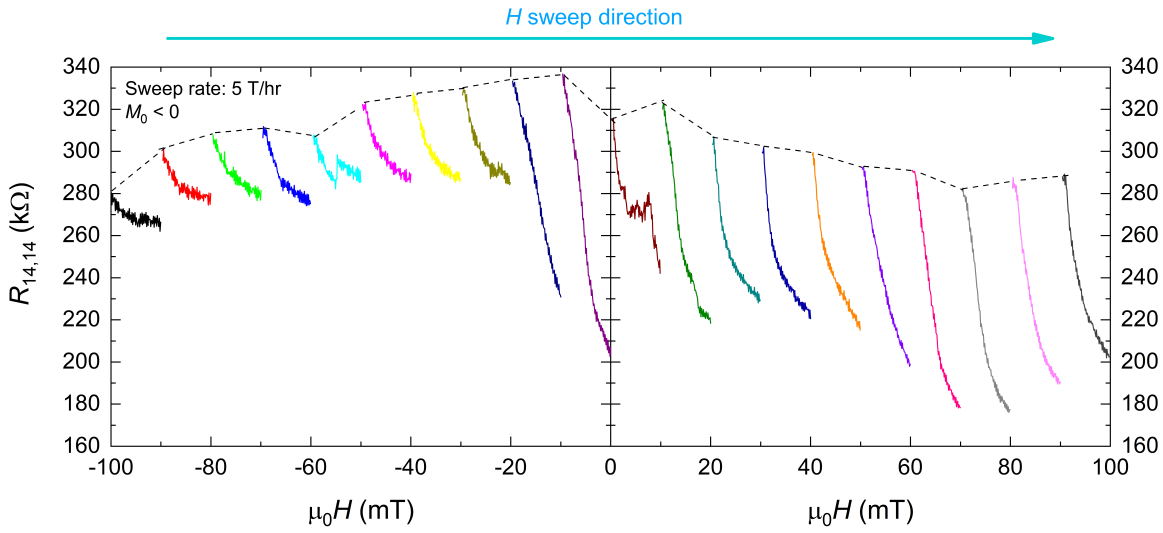

Figure 5.14: The magnetic field dependence of $R_{14,14}$ measured by a series of sweeps from 100 mT toward -100 mT in 10 mT intervals using a sweep rate of 5 T/hr followed by a wait of 20-30 minutes. The $R_{14,14}$ value after each waiting period is regarded as the thermodynamically equilibrium value. These points are connected by the dashed line to show the magnetic field dependence of $R_{14,14}$ around 0 T without the influence of heating effect that arises from the polarity reversal of the H field.

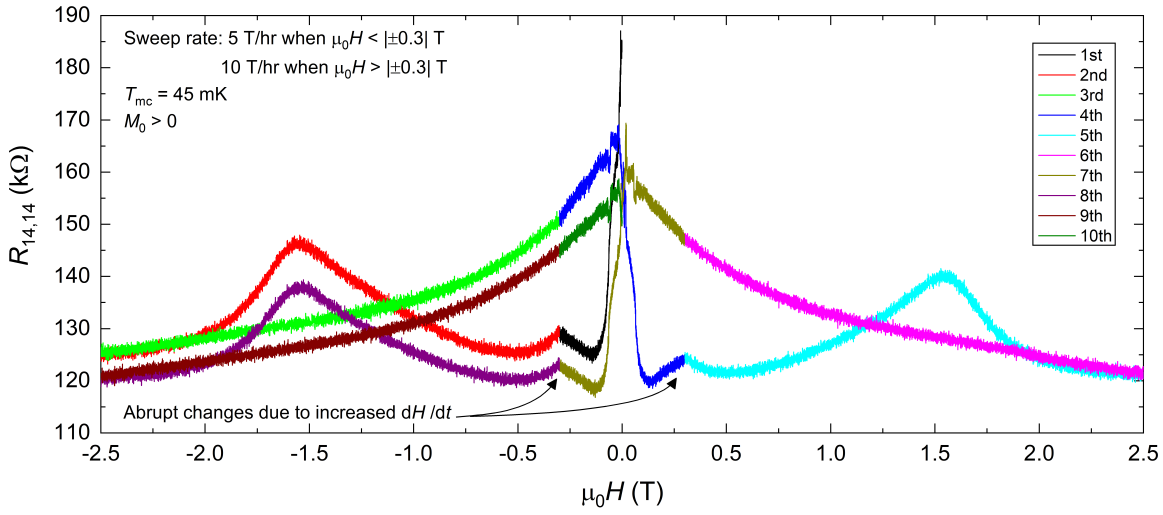

Figure 5.15: The magnetic field sweeps using a sweep rate of 5 T/hr and 10 T/hr for the sweeps between $\mu_0 H < |\pm 0.3|$ T and $\mu_0 H > |\pm 0.3|$ T, respectively. The magnetic field sweep starts from 0 T and go through the curves with different colours representing the sequence of sweeps. Abrupt changes due to the increase of dH/dt can be observed at the fields where the sweep rate is increased, as denoted by the black arrows.

sweeps shown in Fig. 5.13(a) and (b), we find that the VBST2 film possibly has been heated to above 100 mK shortly after the first sweep begins, while the T_{mc}, though it also shows an increase, still stays at less than 60 mK in this rapid heating period. This again supports our speculation that T_s and T_{mc} are decoupled in the magnetic field sweep measurements. However, we need to emphasise that the T_s deduced from the change of $R_{14,14}$ is not precise since the features in the magnetoresistance during a magnetic field sweep are not due to heating effects alone but are also affected by the ferromagnetic properties of the magnetic TI film. Especially for a sample like VBST2 that is not in the QAH regime (i.e. dominated by dissipative bulk transport), the features shown in the magnetoresistance during magnetic field sweeps should be ascribed to both thermal and magnetic effects. We can only analyse the weight of contribution from these two effects based on the conditions of the measurement, such as the starting temperature of the experiment, the sweep rates, the change in T_{mc} during the sweeps, and the field where a feature appears in the butterfly structure. Hence, the better way is to think of the magnetoresistance as a result of the butterfly structure that arises from ferromagnetism of the film being modified in shape and background level by various heating effects during the magnetic field sweeps.

Similarly, the temporal relaxation behaviour observed when a magnetic field sweep is paused can also be caused by both thermal and magnetic effects. For instance, in Fig. 5.14, $R_{14,14}$ always relaxes back to a higher value after every magnetic field step. Although we believe that it is mostly caused by the temperature variation, we cannot completely rule out the possible influence of superparamagnetism in magnetically doped TI films that was reported by some groups [136, 102]. In their study, the magnetisation reversal of magnetic TI films may occur via a series of random reversal of nanoscale isolated weakly-interacting domains instead of domain wall motion. These nanoscale domains are essentially each a single magnetic moment originating from the aggregation of magnetic dopants. The magnetic moments of this type are metastable and can render the TI film superparamagnetic. When such a magnetic moment flips its direction due to thermal fluctuations, it can affect adjacent magnetic moments and cause more magnetic moment reversal, resulting in a spontaneous magnetic relaxation. This phenomenon would be particularly obvious when the influence from the external magnetic field is weakened [102, 136], such as slowly reducing the magnitude of external magnetic field or suddenly pausing a magnetic field sweep, which usually leads to the observations of relaxation behaviour in the magnetoresistance.

In conclusion, because the lack of a working backgate and the poor quality of the magnetic TI material, we were unable to observe the QAHE on VBST2. The Arrhenius plots of the *R-T* curves shown in Fig. 5.16(b) and (d) suggest that the activation energy E_a is $\sim$ 3.93-4.22 μeV, which is about 45-49 mK. Such a small energy scale implies that the Fermi level is far

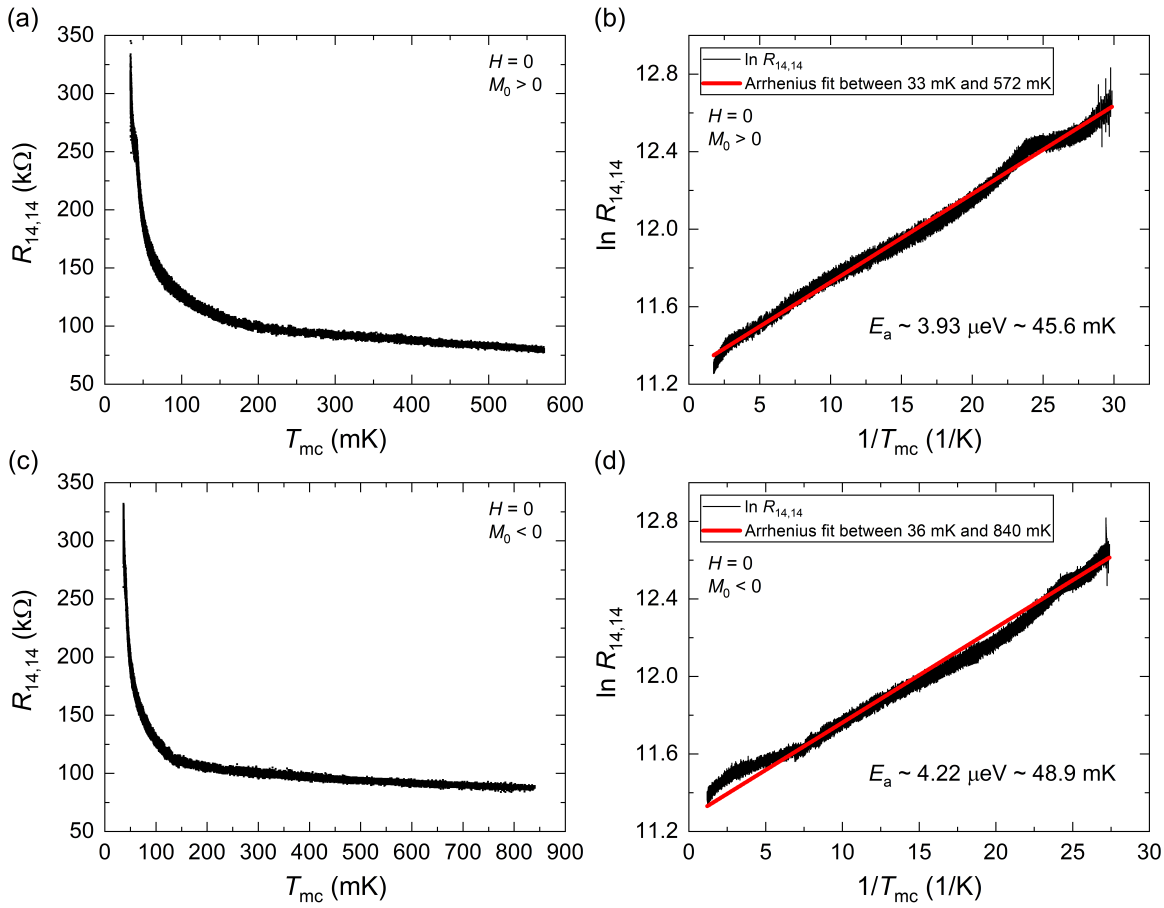

Figure 5.16: (a) The resistance-temperature (R-T) curve between 33 mK and 572 mK taken during a cool-down process when the initial magnetisation state is $M_0 > 0$ in the absence of an external magnetic field ($H = 0$). The cool-down process is made slow enough with a cooling rate of 0.683 mK/min to make sure T_{mc} and T_s are always in good thermal equilibrium, so that T_{mc} in this measurement can be regarded as T_s. (b) The Arrhenius fit of the R-T curve in (a). The activation energy is $\sim$ 3.93 μeV, which is about 45.6 mK. (c) The R-T curve between 36 mK and 840 mK taken at $H = 0$ during a cool-down process when the initial magnetisation state is $M_0 < 0$. The cooling rate of 0.946 mK/min is slow enough to make sure T_{mc} and T_s are always in good thermal equilibrium. (d) The Arrhenius fit of the R-T curve in (c). The activation energy is $\sim$ 4.22 μeV, which is about 48.9 mK.

away from the centre of the magnetic gap (if the gap is successfully induced by exchange coupling), and the bulk transport may be dominant in VBST2. The result is a magnetic TI film with complicated interplay between the electronic and spin systems, which in turn leads to complex thermal and magnetic effects that are hard to disentangle. Therefore, we decided to stop the transport measurements and investigate whether SPM experiments can offer some insight into the interactions between the electronic and spin systems.

5.4.4 SPM measurements on VBST2

The first step for the SPM experiments at fridge temperatures is to locate the edge of the film because the tip usually drifts due to thermal contraction of piezo positioners during the cooling process. A bias is applied on the scanning tip to perform the EFM and search for the edge. The edge of the film imaged by the EFM using a tip bias $V_{\text{tip}} = 3$ V at fridge temperatures is shown in Fig. 5.17(a). The lower brighter half is the magnetic TI film while the upper darker half is the STO substrate. Due to the debris on the sample surface, the minimum tip-sample distance was limited to ~ 200 nm. We then attempted to image the electric current on the film by SGM at this tip height.

To prepare for the SGM measurements, a S-D current of 1 nA was passed between electrode 2 and electrode 4. The transport behaviour of $R_{24,24}$ is characterised by the magnetic field sweeps shown in Fig. 5.17(b). $R_{24,24}$ is much more resistive than the $R_{14,14}$ used in the previous transport measurements. The dip in the black trace of $R_{24,24}$ between -1 T and -2 T is caused by a sudden heating event that can be observed at corresponding magnetic field in the T_{mc} curve. The shape of the butterfly structure is similar to that of $R_{14,14}$.

We first applied a tip bias $V_{\text{tip}} = 3$ V with a S-D current of 1 nA to perform the SGM measurement in the same scan range as the EFM image (Fig. 5.17(a)) under the condition of $M_0 < 0$ and $H = 0$. The SGM image cannot resolve any features related to the current distribution. We then varied the tip bias up to ± 10 V to enhance the scattering potential under the tip, and increased the S-D current up to 100 nA to raise the signal-to-noise ratio. The measurements were also carried out in the conditions of $M_0 > 0$ and $H \neq 0$ as well as smaller tip-sample distance in reduced scan ranges. Nevertheless, no distinguishable features related to the current can be seen in the SGM images of these experiments. A typical image from these SGM measurements is shown in Fig. 5.17(c), which was taken at a tip height of 200 nm with a S-D current of 100 nA and $V_{\text{tip}} = 5$ V. No features related to the current distribution can be observed. The scan direction is along the y-direction, which results in the vertical lines in the image owing to the fluctuations of $R_{24,24}$ during the scan.

There are several possible reasons why the SGM could not observe the current distribution on VBST2. Firstly, since VBST2 is not in the QAH regime, the transport should be dominated by 2D and 3D bulk states. Thus, it is possible that the signals from edge conduction are too weak to be resolved from the huge background of bulk conduction. Moreover, even if the edge transport does exist in VBST2, the width of the edge states may fall below the resolution limit of our SGM system. In one of our previous experiments studying the edge transport in a graphene Moiré superlattice using the same SGM system, the contrast arising from the edge current was found to have a width ~ 500 nm [139]. Since the Hall bar of

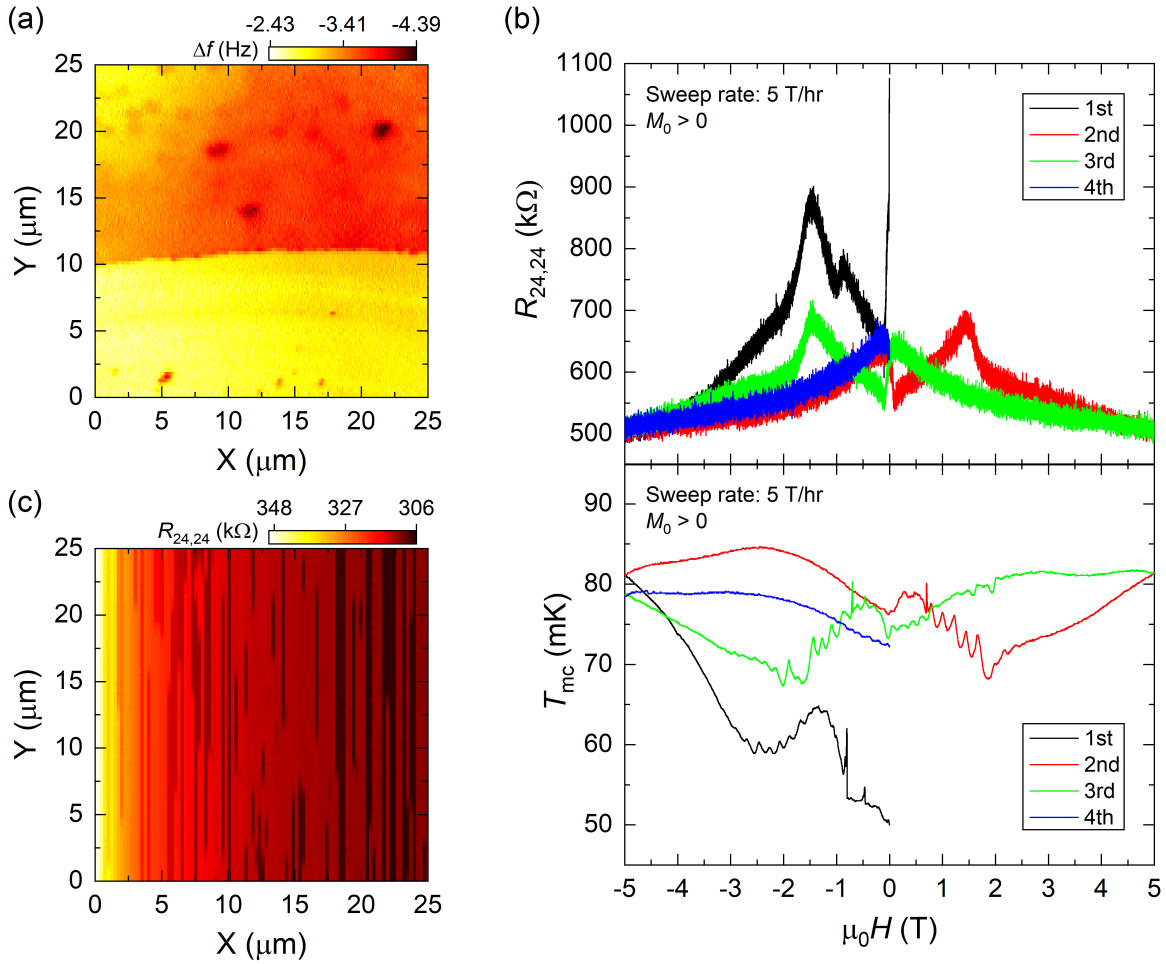

Figure 5.17: (a) The EFM image of the film edge found at fridge temperatures. The tip was kept at a distance of 200 nm from the surface with a bias $V_{\text{tip}} = 3$ V. (b) The magnetic field dependence of $R_{24,24}$ and T_{mc}. The magnetic field sweeps start from 0 T and go through the black, red, green, blue curves and then finally returns to 0 T. A sudden heating event can be seen in the black trace of T_{mc} between -1 T and -2 T, which leads to a dip in the balck trace of $R_{24,24}$ at corresponding magnetic field. (c) The SGM image taken at a tip height of 200 nm with a S-D current of 100 nA and $V_{\text{tip}} = 5$ V in the same scan range as the EFM image in (a). No features related to the current distribution can be observed. The scan direction is along the y-direction, which results in the vertical lines in the image owing to the fluctuations of $R_{24,24}$ during the scan. It can also be observed that $R_{24,24}$ slowly decreased during the scan from ~ 350 kΩ (left side) to 306 kΩ (right side) because of the heating effect from the scanning motions. At the end of this SGM measurement, T_{mc} has become higher than 380 mk.

VBST2 was manually scratched by a scalpel, many cracks and indentations appear in the regions close to scratched traces due to the collapse of underlying STO substrate during

the scratching process. These structures appear as light, nearly-horizontal curves between Y = 10 μm to 40 μm in Fig. 5.10(d). Such topographical features near the film edge have a scale that is comparable to the possible width of contrast from the edge current in SGM images and could easily obscure the SGM signal, which is already very small. Finally, we found that the temperature of the system (including the film and mixing chamber) could substantially increase during scanning experiments at fridge temperatures because of the heat generated by the vibration of the tip, and the scanning and stepping motions of the piezo scanners and positioners. In addition, the laser used for detecting the tip oscillation was also constantly heating the entire sample space. During the scanning experiments, a rise of T_{mc} and a drop of $R_{24,24}$ (i.e. rise of T_s) were always observed, meaning that T_s and T_{mc} were not constant throughout one SPM scan at fridge temperatures. Although the laser can be switched off during the SGM experiments, the scanning motions still creates considerable heat energy, and T_{mc} typically reached 200-500 mK after an SGM experiment. For instance, in Fig. 5.17(c) $R_{24,24}$ slowly decreases during the scan from $\sim$ 350 kΩ (left side) to 306 kΩ (right side) because of the heating effect from the scanning motions. At the end of this SGM measurement, T_{mc} was found to become higher than 380 mk. Since the sample has a much smaller heat capacity and is much closer to the piezo scanners and positioners than the mixing chamber, it can be expected that T_s might have risen to an even higher temperature than the T_{mc} at the end of the SGM experiments. Even if the QAHE does exist in VBST2, it may well be quenched at such high temperatures and no edge conduction should be observed.

As a final attempt, we tried the KPM on VBST2 to detect the variation in surface potential caused by the current distribution on the surface of VBST2. The regions with higher current density should show a different contact potential difference to the tip, and thus produce contrast in a KPM image. In order to move the tip closer to the surface, the KPM measurements were mostly performed in the small area (8×8 μm^2) in the centre of Fig. 5.17(a) across the film edge to avoid hitting debris on the surface. The EFM image of this area taken at a tip height of 70 nm with $V_{\text{tip}} = 3$ V is shown in Fig. 5.18(a), in which the edge can still be clearly seen. The KPM image taken in the same area using an AC modulation voltage of 1 V at the frequency of 1 kHz is shown in Fig. 5.18(b). A potential difference of about 100-200 mV can be observed across the film edge. However, although the KPM was able to image the surface potential difference between the STO substrate and the magnetic TI film, no further features related to the edge conduction or current distribution can be observed.

We also tried changing the magnitude and frequency of the AC modulation voltage, biasing the device with different voltages, and applying strong magnetic field during the

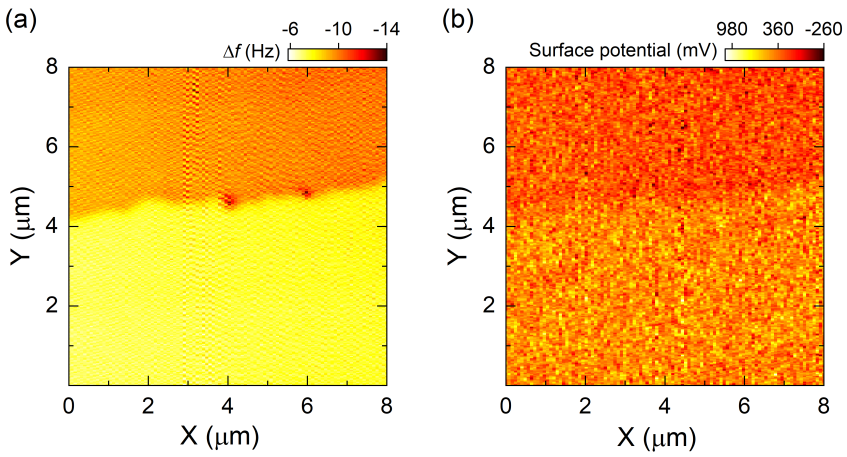

Figure 5.18: (a) The EFM image taken at a tip height of 70 nm with $V_{\text{tip}} = 3$ V in a 8×8 μm^2 area in the centre of Fig. 5.17(a) across the film edge. The film edge can be clearly seen. (b) The KPM image taken in the same area as (a) using an AC modulation voltage of 1 V at 1 kHz. A potential difference $\sim$ 100-200 mV can be observed across the film edge.

KPM measurements to enhance the contrast. Nevertheless, the KPM images all look quite similar and no more features were resolved.

In summary, due to the intrinsically poor sample quality and the lack of a working backgate, the magnetic gap could be very small and the Fermi level may be far away from the Dirac point. We were unable to tune the Fermi level into the magnetic gap and therefore could not observe a good QAHE on VBST2. The transport might be dominated by dissipative bulk conduction, which could smear out the signals from edge conduction in the SGM and KPM measurements.

It will be key to improve the quality of the magnetic TI film so that the sample can have a larger magnetic gap with its Fermi level intrinsically close to the Dirac point. The fabrication of a working backgate that allows the adjustment of chemical potential is also crucial for future devices.

5.5 Summary

In this chapter, we combine transport measurements with SPM measurements to investigate both the magnetic and electrical properties of V-BST films. The goal is to study the evolution of the QAH states and magnetic domain structures during the magnetisation and demagnetisation process of magnetic TI films by directly imaging the spatial distribution of QAH states and domain structures. When the film is fully magnetised with a uniform out-of-plane magnetisation, the contrast of QAH states should appear at the edge of the device, whereas

when the film is fully demagnetised, the contrast pattern should be consistent with the map of domain walls. The difference between the fully-magnetised and fully-demagnetised states thus is the unique signature of the QAHE in SPM experiments.

As the first step, we tried to map out the domain structures of VBST1 by MFM using our home-made SPM system. The ferromagnetism of VBST1 is confirmed by the butterfly structure observed in transport measurements when the film is cooled below $T_C \sim 20$ K. The MFM scans were then performed at 4.2 K, where the coercive field $H_c \sim 0.4$ T and the saturation field $H_s \sim 0.7$ T. In theory, the film should gradually evolve into a multi-domain state as the magnetic field increases from 0 T to $H_c \sim 0.4$ T due to demagnetisation, and then enter a singe domain state beyond $H_s \sim 0.7$ T. However, we could not observe the predicted evolution of domain structures by either MFM scans or magnetic field spectroscopy.

The poor surface condition of VBST1 and the potential complex behaviours of our MFM tips are the possible reasons for not being able to observe the domain structures on VBST1. In addition, the domain structures in VBST1 may be smaller than 500 nm [138], which is not only close to the limit of our MFM resolution, but may also be easily overshadowed by the signals from the artefacts on the surface.

Therefore, for our second film - VBST2, we minimised the fabrication process before any SPM measurements to keep the surface as clean as possible, and used a dedicated SHPM system to probe the domain structures. In the SHPM images, we observed patch-like structures that ranges from several hundred nanometers to 2 μm, and the magnetic fields emanating from these structures are lower than 1 G. Both the field strength and size of the magnetic structures are consistent in order of magnitude with the observations of other groups [135]. Unfortunately, we were unable to confirm our results by further measurements due to some deficiencies in the SHPM experiments. Therefore, although the structures observed are likely to have a magnetic origin according to our analysis, we cannot claim that they are indeed magnetic domains of VBST2. More experiments are needed to verify our results.

Subsequently, we decided to study the QAHE from the electrical perspective, i.e. mapping the current distribution of QAH states in VBST2. Thus, the film was scratched into a Hall bar for transport characterisation. However, the QAHE is not observed and VBST2 does not seem to be in the QAH regime. As a result, VBST2 is extremely sensitive to thermal effects, such as eddy current heating caused by $\mathrm{d}H/\mathrm{d}t$ on the film and the mixing chamber, the magnetocaloric effect due to magnetic moment flipping in the film, and the vibration of cryogenic parts of the fridge under strong magnetic fields. In addition, a rapid heating event is found when the external magnetic field is swept across 0 T, which has also been reported by other groups [101, 104, 109]. Our subsequent experiments suggest that this heating event originates from the instruments but not the sample itself.

All the aforementioned thermal effects become negligible and no corresponding structures can be observed above 1.5 K, indicating that these phenomena only can be detected at very low temperatures. These thermal effects also seem to be less serious in magnetic TI films that exhibit the QAHE. A possible explanation is because the QAH states are not sensitive to the change of temperature, just like the QH states in the QHE. This speculation agrees with the fact that VBST2 is not in the QAH regime and should be dominated by dissipative 2D and 3D bulk transport that are much more temperature-dependent.

The Arrhenius plots suggest that the activation energy $E_a \sim 3.93$-4.22 μeV (i.e. ~ 45-49 mK). Such a small energy scale implies that the Fermi level is far away from the centre of the magnetic gap and VBST2 may be dominated by bulk transport, resulting in a magnetic TI film with complicated interplay between the electronic and spin systems, which in turn leads to complex thermal and magnetic effects that are hard to disentangle.

Finally, the SGM and KPM were used to detect the QAH states at fridge temperatures, but no features related to the current distribution can be resolved. Again, this is probably due to the intrinsically poor sample quality and surface condition, as well as the lack of a working backgate. The heat generated by the SPM system also increases the difficulty for the observation of QAHE at fridge temperatures.

Therefore, we believe that the key is to improve the quality of magnetic TI films so that the critical temperature of the QAHE can be boosted and bulk states can be reduced. Moreover, a better fabrication process is desired to improve the surface condition of the Hall bar device and minimise the influence of artificial structures for SPM measurements. A working backgate that allows the adjustment of chemical potential is also crucial for future devices.

Chapter 6

Transport in chromium-doped bismuth antimony telluride heterostructures

6.1 Introduction

One of the major difficulties in the research of the QAHE is the ultralow critical temperature. Although the critical temperature was boosted to 120 mK with the realisation of QAHE in vanadium-doped bismuth antimony telluride [106], a dilution refrigerator is still required for the measurements of the QAHE. Since the Hall plateau transition in the QAHE is driven by the magnetic phase transition, it is surprising to see that the critical temperature of the QAHE is two orders of magnitude lower than the Curie temperature of the magnetic TI films, which is usually on the order of tens of kelvins. Much work has investigated the origin of this discrepancy [101, 107, 109, 140, 141], but there is still no clear conclusion so far. In 2017, Mogi *et al.* reported a new type of magnetic TI structure which consists of a layer of $(Bi,Sb)_2Te_3$ sandwiched by two layers of Cr-doped $(Bi,Sb)_2Te_3$ that manifested a quantised Hall conductivity at 500 mK [142]. After that, more groups began to grow similar magnetic TI heterostructures with different doping and thicknesses in pursuit of higher critical temperatures for the QAHE.

Because we were unable to observe the QAHE from all the previous V-BST samples, we decided to turn our attention to the magnetic TI heterostructure as well. As discussed in Chapter 3 and Chapter 5, the non-zero longitudinal resistance and ultralow critical temperatures of the QAHE have always been an issue of discussion in this field. Some experiments have been carried out to probe the source of dissipation in the QAHE in V-doped and Cr-doped $(Bi,Sb)_2Te_3$ films [101, 104, 107, 109, 110], but no careful study has been made for the newly-emerging magnetic TI heterostructures yet. Therefore, we hope that by performing

comprehensive transport measurements on magnetic TI heterostructure devices, we will gain insight into the dissipation mechanism and the cause of ultralow critical temperatures of the QAHE.

6.2 Experimental details

6.2.1 Sample fabrication

The Cr-doped $(Bi,Sb)_2Te_3$ heterostructures used for the experiments in this chapter were prepared by Dr. Cui-Zu Chang and coworkers at the Pennsylvania State University. The details of the sample growth procedure and characterisation are given in the articles from Dr. Chang's group [143, 144]. Here we only briefly introduce the basic growth method described in their papers.

The growth of the Cr-doped $(Bi,Sb)_2Te_3$ sandwich heterostructures was carried out in a commercial EPI-620 MBE system with a base pressure lower than 2×10^{-10} mbar. The insulating STO (111) substrates used for the growth of all the sandwich heterostructures were first soaked in 90°C deionized water for 1.5 hours, and then annealed at 985 °C for 3 hours in a tube furnace with pure oxygen flow. Through the above steps, the surface of STO substrates were passivated and became atomically flat. These heat-treated insulating STO substrates were then outgassed at $\sim 530\,^{\circ}$C for 1 hour before the growth of TI heterostructures. High-purity Bi (99.999%), Sb (99.9999%), Te (99.9999%), and Cr (99.999%) were evaporated from Knudsen effusion cells. The flux ratio of Te to Bi and Sb was set to be > 10 to minimise the Te deficiency in the TI films. Each layer of the sandwich heterostructure was grown with a different Bi/Sb ratio by adjusting the temperatures of Knudsen cells to tune the chemical potential close to its charge neutral point. The growth rate for the films was controlled at $\sim$ 0.25 QL per minute, and the STO substrates were maintained at 240 °C during the sample growth. After the growth, the TI films were annealed at ~ 240 °C for 30 minutes to improve the crystal quality before being cooled down to room temperature. The sharp and streaky '1×1' diffraction patterns in RHEED images (as shown in the supplementary information of [143]) indicate high crystal quality and atomically flat surface of the TI films.

Due to the same concern about the doping effect and contamination as described in Sec. 5.2, the device studied in this chapter was scratched into Hall bars by a metal tip to avoid introducing doping and contamination from the environment and lithographic processes. The scratched Hall bar sample was then fixed onto an LCC using silver conductive paste. Indium pieces were manually placed onto the terminals of the Hall bars as Ohmic contacts, and these indium contacts were later connected to the bond pads of the LCC by gold wires. Finally, the

inner base of the LCC, which is electrically contacted with the STO substrate by silver paste, was connected to some of the bond pads on the LCC to enable the manipulation of backgate voltage.

The magnetic TI heterostructure device (henceforth referred to as CBST1) used in this chapter is not capped because our sample supplier noticed that a charge transfer effect sometimes occurs between the magnetic TI film and the capping layer, which is detrimental to the QAHE. Therefore, we decided not to make a capping layer for CBST1 to see if it will be more likely to show the QAHE.

The stack structure of CBST1 is schematically shown in Fig. 6.1(a). A 5 QL undoped $(Bi,Sb)_2Te_3$ is sandwiched by two 3 QL Cr-doped $(Bi,Sb)_2Te_3$, forming a 3-5-3 TI heterostructure on the STO substrate.

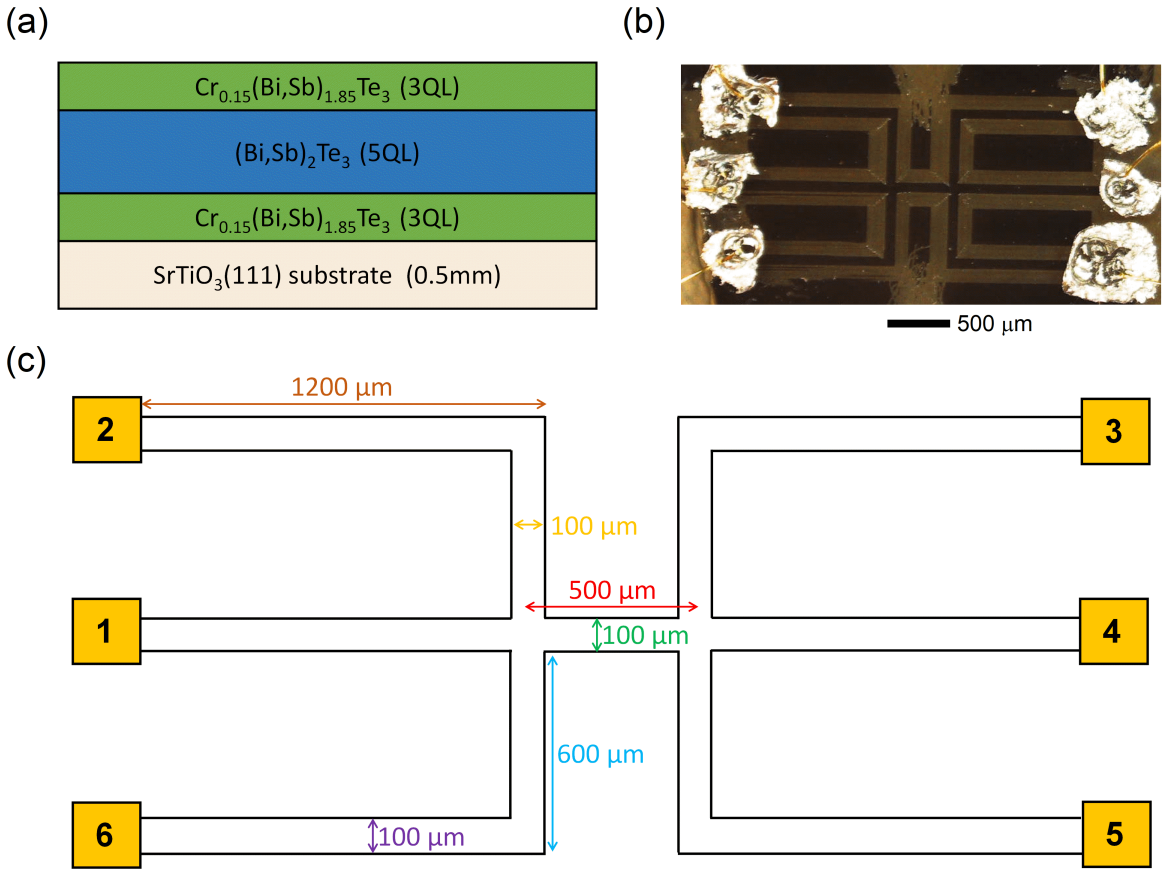

Figure 6.1: (a) The layer structure of CBST1. (b) An optical photograph of the scratched Hall bar. (c) The device layout and dimensions of the Hall bar. Although the nominal aspect ratio of the middle channel is 5, the scratched traces actually have a finite width. Thus, the accurate aspect ratio is found to be ~ 6.5 by directly measuring the optical image in (b).

Figure 6.1(b) shows the optical photograph of the Hall bar. The dark part is the magnetic TI film and the six silver regions are the indium contacts. The light area is the transparent STO substrate. The Hall bar was made with elongated leads to prepare for possible future SPM experiments. The dimension of all the channels of the Hall bar is shown in Fig. 6.1(c). It is worth noting that although the nominal aspect ratio of the middle channel of the Hall bar is 5, every scratched trace actually has a certain width. Therefore, by directly measuring the length and width of the Hall bar in the optical image, the accurate aspect ratio of the middle channel is found to be ~ 6.5.

6.2.2 Correction of the mixing between R_{xx} and R_{xy}

Because the Hall bar of CBST1 was not lithographically defined, a certain level of misalignment between the probes measuring the longitudinal and Hall voltage difference is present, which leads to the mixing between the longitudinal resistance R_{xx} and Hall resistance R_{xy} signals. This effect is particularly serious for the R_{xy} signals around the plateau-plateau transition regimes near the coercive field where the measured R_{xy} will inevitably pick up the extremely large electrical signals from R_{xx} in such an imperfect Hall bar geometry. Thus, a correction for the measured R_{xy} is necessary. The principle behind this correction is described as follows.

Considering the ideal butterfly structure in R_{xx} and square loop in R_{xy}, as shown in Fig. 6.2, the hysteresis for R_{xx} and R_{xy} in a magnetic field sweep should have the relations:

$$R_{xy\uparrow}(H) + R_{xy\downarrow}(-H) = 0 \tag{6.1}$$

and

$$R_{xx\uparrow}(H) = R_{xx\downarrow}(-H), \tag{6.2}$$

where the $\uparrow$ and $\downarrow$ in the subscripts denote the upward and downward magnetic field sweeps, respectively. However, for a real measurement with misaligned voltage probes, the R_{xy} signal actually has a component of the R_{xx} signal, and the relation becomes

$$R_{xy\uparrow}(H)_{\text{measured}} + R_{xy\downarrow}(-H)_{\text{measured}} = R_{xy\uparrow}(H) + R_{xy\downarrow}(-H) + R_{xx\uparrow}(H) + R_{xx\downarrow}(-H), \tag{6.3}$$

where the "measured" in the subscripts means the actual measured signal.

Since $R_{xy\uparrow}(H)$ + $R_{xy\downarrow}(-H)$ should equal to zero according to Eq. 6.1, the remaining part of Eq. 6.3 should be $R_{xx\uparrow}(H)$ + $R_{xx\downarrow}(-H)$. Moreover, because $R_{xx\uparrow}(H)$ should equal to $R_{xx\downarrow}(-H)$ according to Eq. 6.2, the R_{xx} components mixed in $R_{xy\uparrow}(H)_{\text{measured}}$ and

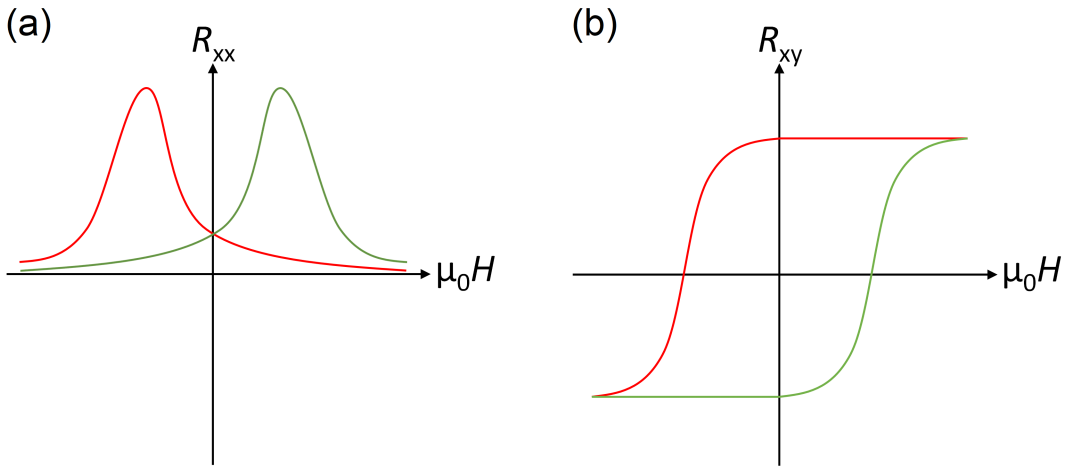

Figure 6.2: The ideal (a) butterfly structure of R_{xx} and (b) square loop of R_{xy} in magnetic field sweeps.

$R_{xy\downarrow}(-H)_{\text{measured}}$ should be

$$(R_{xy\uparrow}(H)_{\text{measured}} + R_{xy\downarrow}(-H)_{\text{measured}})/2. \tag{6.4}$$

Therefore, the correction term given by Eq. 6.4 should be subtracted from both the R_{xy} signals of the upward and downward magnetic field sweeps to correct the mixing of R_{xy} and R_{xx}. It should be noted that all the R_{xy} or ρ_{xy} data shown in the following sections are corrected, unless otherwise specified.

6.3 Probing the QAH phase transition

The CBST1 device was loaded into a Bluefors cryogen-free dilution refrigerator for transport measurements at millikelven temperatures. In some of our previous unsuccessful measurements of the QAHE on other magnetic TI devices, we noticed that the gating effect saturates at high backgate voltage (V_g), and the gate sweep curves are usually hysteretic between the forward and backward V_g sweeps. These two effects are possibly associated with the electric properties of STO substrates at low temperatures. Since STO has a very high dielectric constant ($\varepsilon \sim 30000$) at low temperatures [98, 145, 146], it is commonly used as the substrate of magnetic TI devices for applying a large electric field to fine-tune the carrier density. However, after ramping V_g at fridge temperatures, the STO substrate tends to be gradually charged, making the gating effect become increasingly weak. As a result, the carrier density becomes less tunable and the resistance curve in V_g sweeps plateaus off at high V_g. In addition,

due to the ferroelectricity of STO [147], the forward and backward V_g sweep curves always show hysteresis, which affects the judgement regarding the energy of the Dirac point and QAH regime. The only way we know to thoroughly discharge the STO substrate and reset the electric hysteresis of the device is to ground the device and warm it up to about room temperature (> 250 K). Obviously, it is not practical in real experiments to thermal-cycle the sample between room temperature and fridge temperatures after every V_g sweep. A way to lessen the inconvenience is to sweep only a small range of V_g each time, and then take the magnetic field sweeps to record the lowest longitudinal resistivity (ρ_{xx}) and highest Hall resistance (ρ_{xy}). By plotting the trace connected by these minimum ρ_{xx} and maximum ρ_{xy}, we are still able to tell the position of the Dirac point and the energy where the film enters the QAH regime. Then we simply have to thermal-cycle the sample once and directly go to the desired V_g next time for further measurements.

The magnetic field dependence of ρ_{xx} and ρ_{xy} of CBST1 at different V_g taken in such manner is shown in Fig. 6.3, in which the ρ_{xy} and ρ_{xx} are obtained by measuring the $R_{14,53}$ and $R_{14,23}$ of CBST1, respectively, using a S-D current of 1 nA with an excitation frequency of 15 Hz at $T_s = 16$ mK. (Note that $R_{ij,mn}$ means the current is passed from electrode i to electrode j and the voltage drop is measured between electrode m and electrode n.)

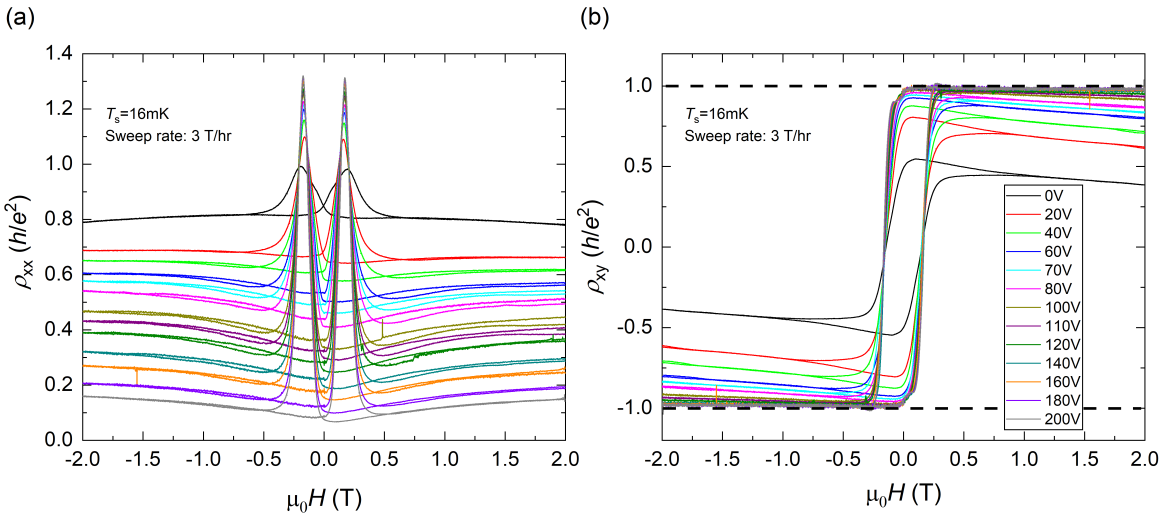

Figure 6.3: The magnetic field dependence of (a) ρ_{xx} and (b) ρ_{xy} of CBST1 taken at different V_g using the sweep rate of 3 T/hr. The ρ_{xy} and ρ_{xx} are obtained by measuring the $R_{14,53}$ and $R_{14,23}$ of CBST1, respectively, using a S-D current of 1 nA with an excitation frequency of 15 Hz at $T_s = 16$ mK. The dashed lines in (b) denote the quantised value h/e^2.

It can be observed in Fig. 6.3(a) that the background level of ρ_{xx} decreases with increasing V_g and becomes lowest at $V_g = 200$ V, while $\rho_{xx}(H_c)$ grows higher with increasing V_g. The different V_g dependence implies that the conduction at H_c is governed by a different transport

mechanism to the rest of the magnetic field sweep. This is consistent with expectations because in the single domain state (i.e. when the film is fully-magnetised) the transport should be dominated by edge states, whereas in the multi-domain state at H_c the transport is allowed to occur through the surface. On the other hand, the two plateaux in the hysteresis loop of ρ_{xy} slowly move toward the quantised value h/e^2 with the increasing V_g, as shown in Fig. 6.3(b), suggesting a more developed QAHE at higher V_g.

To clearly see the evolution of the V_g dependence of the magnetoresistance of CBST1, we plot the minimum ρ_{xx} and maximum ρ_{xy} as a function of V_g in Fig. 6.4(a). It can be seen that ρ_{xy} is already increasing with decreasing ρ_{xx} between 0 V and 20 V, which suggests that CBST1 has entered the QAH regime from at least $V_g = 20$ V [93, 148]. This is further supported by the evolution of H_c with V_g in Fig. 6.4(b), in which an abrupt drop in H_c occurs between $V_g = 0$ V and 20 V, and then H_c starts to obey an ascending trend from $V_g = 20$ V to 200 V, indicating the onset of insulator-QAH transition between 0 and 20 V.

As shown in Fig. 6.4(a), although both the lowest $\rho_{xx} \sim 0.0667\ h/e^2$ and the highest $\rho_{xy} \sim 0.998\ h/e^2$ appear at $V_g = 200$ V, the trend shows that ρ_{xx} is still descending and ρ_{xy} is still ascending even at 200 V, indicating that the Dirac point may be somewhere beyond $V_g =$ 200 V. Due to the constraint of instruments, we could not go to higher V_g. However, even if we can further increase V_g, we believe it is still unlikely that we will reach the Dirac point. As explained in the beginning of this section, the gating effect through STO substrate tends to become weaker with the increasingly higher V_g owing to the charging effect. Because the ρ_{xy} has started to show a sign of saturation above $V_g = 120$ V, we speculate that ρ_{xy} should not change much beyond 200 V.

The ρ_{xx} slope and ρ_{xy} slope shown in Fig. 6.4(c) are calculated from the data between $\mu_0 H = -1.5$ T and -2 T, where the magnetisation of the film is almost saturated and the magnetoresistance in the downward sweep starts to retrace that in the upward sweep. In some studies, the slope of ρ_{xy} in this regime is treated as an analogue of the Hall coefficient in an ordinary Hall effect [149, 150]. Although it cannot be used to quantitatively compute the carrier concentration as a true Hall effect, it still provides some qualitative information about the carrier concentration. It can be seen that, after entering the QAH regime at $V_g = 20$ V, the absolute value of the ρ_{xy} slope generally decreases with increasing V_g, implying that the 2D surface and 3D bulk states are being slowly depleted in this process. The ρ_{xx} slope, on the other hand, does not have this layer of meaning, but we notice that it shows a sign change at $V_g = 20$ V, which can be the signal of the QAH phase transition and is consistent with our observations in Fig. 6.4(a) and (b).

Finally, we observe that the longitudinal resistivity at the coercive field, $\rho_{xx}(H_c)$, increases with increasing V_g. The origin of this dependence can be explained by the different scattering

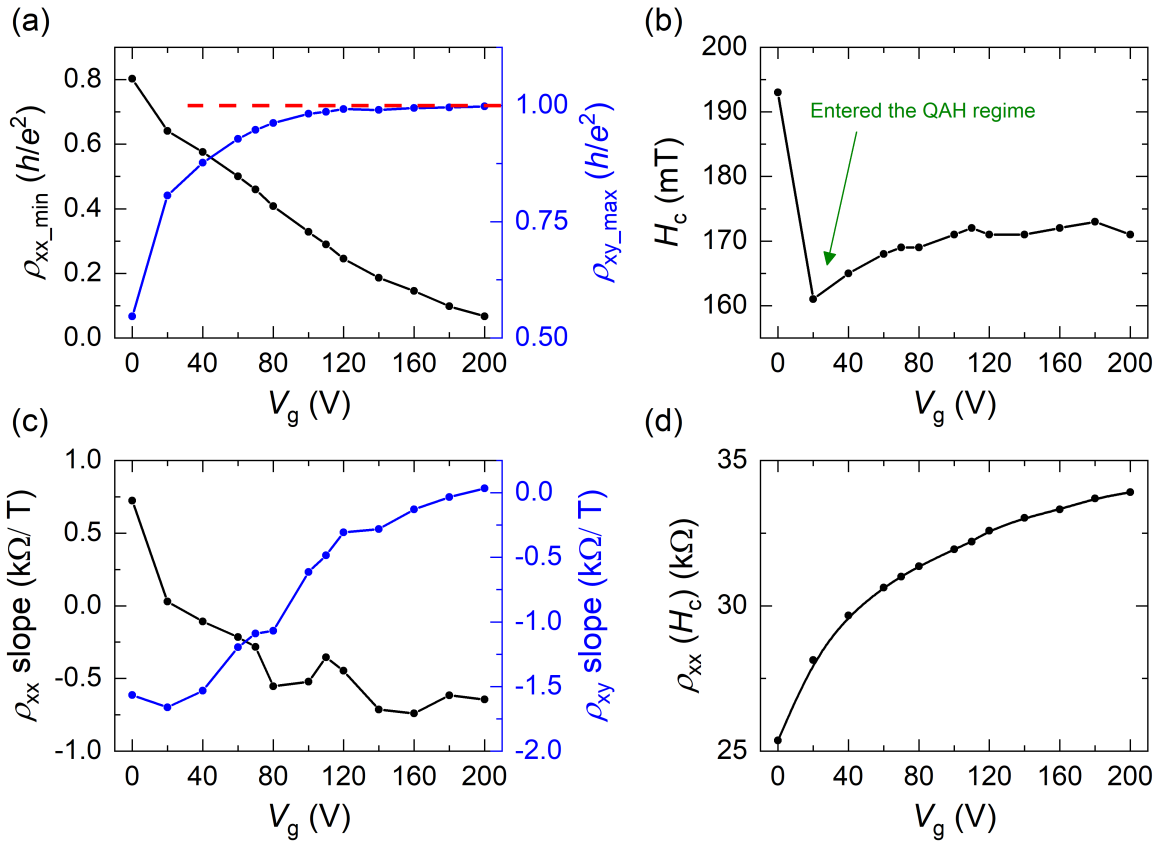

Figure 6.4: The V_g dependence of the magnetoresistance of CBST1 extracted from Fig. 6.3. (a) The V_g dependence of the minimum ρ_{xx} and maximum ρ_{xy}. The red dashed line denotes the quantised value h/e^2. (b) The V_g dependence of H_c. (c) The slope of ρ_{xx} and ρ_{xy} calculated from the data between $\mu_0 H = -1.5$ T and -2 T in the magnetic field sweeps. (d) The ρ_{xx} at H_c as a function of V_g.

mechanisms inside and outside the QAH regime. When the film is not in the QAH regime, 2D surface states or even some 3D residual bulk states can travel between the source and drain. The two peaks at the coercive field are caused by the scattering between these states and the magnetic domains during the propagation process [135, 151]. However, when the Fermi level is tuned into the magnetic gap and the film enters the QAH regime, the 2D and 3D states are mostly depleted and the two peaks in longitudinal resistance at the coercive field occur mainly via the backscattering of chiral edge states meandering through the network of domain walls, resulting in a significantly lower electric conductivity and thus higher resistivity at the coercive field. Hence, the V_g dependence of $\rho_{xx}(H_c)$ also agrees with the previous observations about the QAH phase transition.

Therefore, although the Fermi level of CBST1 cannot be tuned to the Dirac point, a variety of evidence has verified the insulator-QAH transition between $V_g = 0$ V and 20 V,

and the quantised ρ_{xy} is also observed. Nevertheless, there is still a non-vanishing $\rho_{xx} \sim 0.0667\ h/e^2$, indicating the presence of dissipative states at $V_g = 200$ V. In the following sections, we will explore the source of dissipation and discuss the interactions between different dissipative states.

6.4 Non-chiral edge transport in device CBST1

We begin with the local transport measurements for different measurement configurations. (All the measurements were taken using a S-D current of 1 nA with an excitation frequency of 15 Hz unless otherwise stated.) The magnetic field dependence of the two-terminal resistance of different contact combinations at $T_s = 16$ mK with $V_g = 200$ V is shown in Fig. 6.5. As can be seen in Fig. 6.5(a), the two-terminal resistance of all configurations has a similar butterfly structure with minimum values approaching h/e^2 (denoted by the dashed line) when the magnetisation is well-defined. This result of two-terminal measurement agrees with the fact that the voltage drop (i.e. energy loss) for a ballistic transport process should only occur when the QAH states enter the drain electrode.

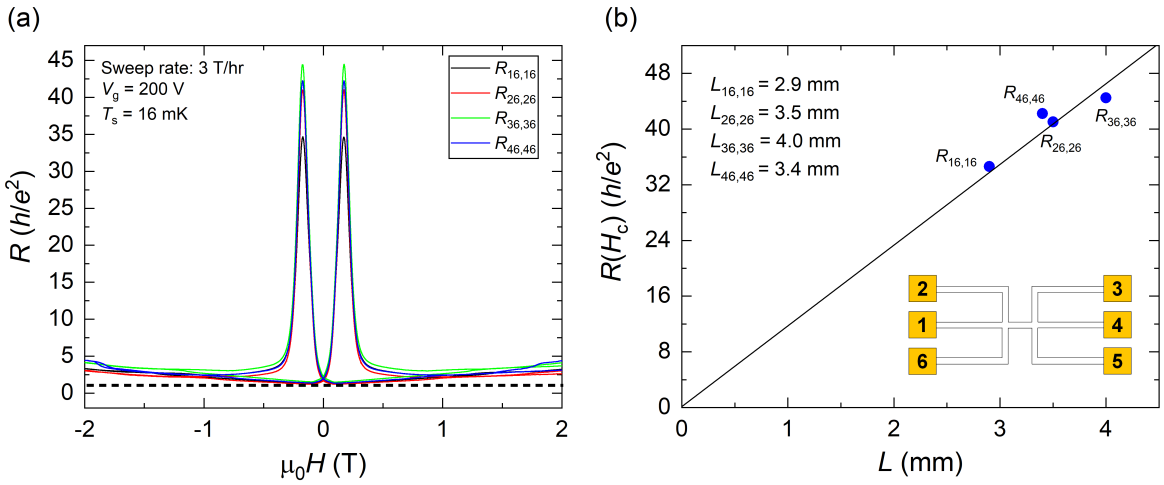

Figure 6.5: (a) The magnetic field dependence of the two-terminal resistance of different contact combinations at $T_s = 16$ mK with $V_g = 200$ V. The dashed line denotes the quantised value h/e^2. (b) The resistance at H_c ($R(H_c)$) plotted as a function of the channel length (L) for different contact combinations. The inset shows a schematic of the CBST1 Hall bar.

The resistance at H_c ($R(H_c)$) is extracted and plotted as a function of the channel length (L) for different contact combinations, as shown in Fig. 6.5(b). The $R(H_c)$ is roughly proportional to the channel length, suggesting that the transport at H_c is dominated by length-dependent bulk-like conduction rather than the scale-invariant edge-like conduction. The

slight deviation from linearity may arise from the inhomogeneity in the long leads of the Hall bar. In addition, the sweep rates can also affect the resistance at H_c, probably due to thermal effects. Thus, in an ultra-slow magnetic field sweep the deviation should be smaller.

Nevertheless, the local two-terminal measurement itself does not allow us to probe the properties of chiral edge states. To determine the chirality of edge states, we further performed three-terminal measurements on CBST1, as shown in Fig. 6.6(a). The current is passed from electrode 4 to electrode 6, and the magnetic field is swept between $\mu_0 H = -2$ T and 2 T with a sweep rate of 3 T/hr at $T_s = 16$ mK and $V_g = 200$ V. The four different configurations all exhibit a hysteresis loop in the magnetic field sweeps, which is actually a manifestation of the chirality of edge states in CBST1. As illustrated in Fig. 6.6(b), when the magnetisation is in the $M < 0$ state, the chiral edge states will travel along the direction of the green arrows, whereas in the $M > 0$ state the chiral edge states will travel along the direction of the orange arrows. When the conduction is via the green path (i.e. $M < 0$), ideally, no dissipation should occur before the chiral edge states reach electrode 6. Thus, electrode 3 ,2, and 1 should be at the same potential as electrode 4, while electrode 5 and 6 should be at ground. In this case, $R_{46,41}$, $R_{46,42}$, and $R_{46,43}$ should be close to zero, and $R_{46,45}$ should be around h/e^2. On the other hand, when the conduction is via the orange path (i.e. $M > 0$), electrode 5 should be at the same potential as electrode 4, while electrode 1, 2, and 3 should be at the same potential as electrode 6 (ground), leading to $R_{46,41}$, $R_{46,42}$, and $R_{46,43} \sim h/e^2$ while $R_{46,45} \sim 0$. This behaviour can be clearly observed in all four hysteresis loops in Fig. 6.6(a), in which the traces in the $M > 0$ regime always differ from the traces in the $M < 0$ regime by h/e^2.

These three-terminal measurements reveal the chirality of the edge states. However, the three-terminal resistance in Fig. 6.6(a) does not completely vanish throughout the entire fully-magnetised regime and only becomes close to zero around $\mu_0 H = 0$ T. Furthermore, some deviation from $\rho_{xx} = 0$ and $\rho_{xy} = h/e^2$ in the high magnetic field regime can be seen. Both situations suggest the presence of dissipative states other than the chiral edge states in CBST1, even in the QAH regime.

To investigate the origin of dissipation, we carried out non-local measurements in an attempt to distinguish between the contributions from bulk and edge conduction. The classical bulk contribution to the non-local signal can be estimated by the van der Pauw equation $R_{\mathrm{NL}}^{\mathrm{classical}}/\rho_{xx} \approx \exp(-\pi L/W)$, where L is the distance between voltage probes and W is the channel width [103, 152]. For CBST1, the aspect ratio $L/W \sim 6.5$ and hence $\exp(-\pi L/W) \approx 3 \times 10^{-9}$. However, the ratio between the non-local resistance and local resistance in our experiment is found to be $R_{16,43}/\rho_{14,23} \approx 3 \times 10^{-2}$, which is too high to be merely ascribed to the classical bulk contribution. This implies that the dissipation is not

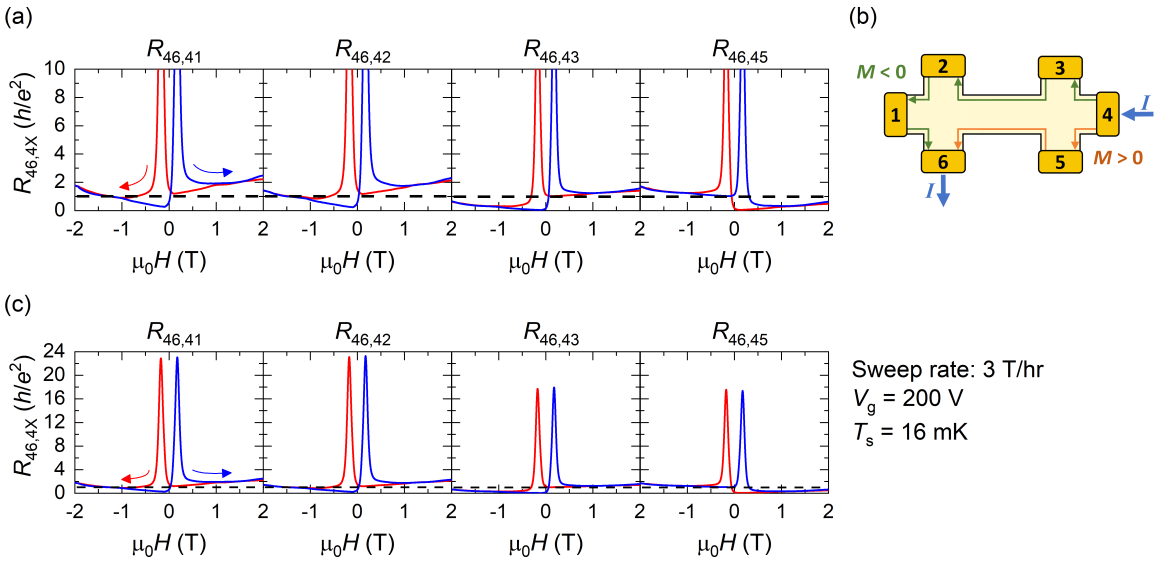

Figure 6.6: (a) The magnetic field dependence of the three-terminal resistance taken at $T_s =$ 16 mK and $V_g = 200$ V using a sweep rate of 3 T/hr. The blue and red curves represent the upward and downward magnetic field sweep, respectively. The dashed lines denote the quantised value h/e^2. (b) The schematic diagram illustrating the chirality of edge states in the $M > 0$ and $M < 0$ states. (c) The full-scale plots of (a) with the dashed lines denoting the quantised value h/e^2.

solely caused by the residual 2D and 3D bulk states, and may originate from some kind of dissipative edge states.

Thus, we then examine the magnetic field dependence of non-local signals using two different configurations: $R_{16,43}$ and $R_{26,35}$. As can be seen in Fig. 6.7(a) and (b), even in these non-local configurations, both $R_{16,43}$ and $R_{26,35}$ show hysteresis in the magnetic field sweeps, indicating the existence of dissipative edge states in CBST1. A possible candidate of these non-chiral edge states is the topological surface states on the side surface of the film [103, 104]. The side surface of a TI originally should host the topological surface states, and these states should be confined into quasi-1D channels and be gapped due to quantum confinement effect if the film is thin enough. Therefore, in a sufficiently thin magnetic TI film, the transport should be dominated by the chiral edge conduction. However, for a thicker film (> 5 QL), the quantum confinement effect on the side surface is not strong enough and the side surface states may not be gapped [103]. Thus, the helical nature of the topological surface states will become prominent in transport measurements. Furthermore, for the side surface the magnetisation is in-plane, which can shift the position of the Dirac point in k-space, and the Dirac cone will no longer be protected by the time-reversal symmetry [104, 134]. As a result, the helical states on the side surface will no longer be immune to

backscattering and hence become dissipative "quasi-helical" edge states. Since CBST1 is a heterostructure with 11 QL in total, the existence of such quasi-helical edge states is plausible. It is likely that the slope of the magnetoresistance in the fully-magnetised regime in Fig. 6.7 as well as in Fig. 6.6(a) also arise from the H-field dependent behaviour of these non-chiral edge states.

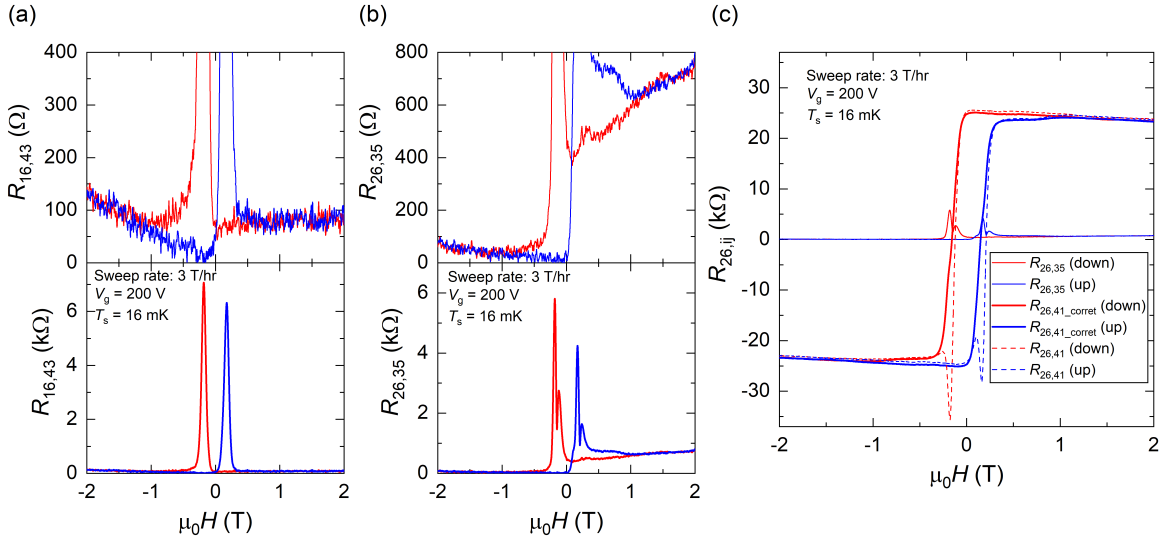

Figure 6.7: The magnetic field dependence of the non-local resistance $R_{16,43}$ and $R_{26,35}$ taken at $T_s = 16$ mK with $V_g = 200$ V using a sweep rate of 3 T/hr. (a) The upper panel shows the hysteresis of $R_{16,43}$ in the magnetic field sweeps. The lower panel is the full-scale plot of the upper panel. (b) The upper panel shows the hysteresis of $R_{26,35}$ in the magnetic field sweeps. The lower panel is the full-scale plot of the upper panel. A double peak structure can be observed at H_c, which is caused by the mixing with the Hall resistance signal. (c) The magnetic field dependence of $R_{26,35}$ and $R_{26,41}$. $R_{26,41}$ in this configuration is equivalent to the Hall resistance. The thin curves are $R_{26,35}$ as shown in the lower panel of (b). The thick curves and dashed curves represent the corrected and raw signals of $R_{26,41}$, respectively. It can be seen that the double peak structure in $R_{26,35}$ overlaps with the plateau-plateau transition regime in $R_{26,41}$ and creates two dips in the raw signal of $R_{26,41}$, indicating the mixing between $R_{26,35}$ and $R_{26,41}$. In the corrected $R_{26,41}$ signal, the component of $R_{26,35}$ is removed and $R_{26,41}$ becomes a typical square-shaped hysteresis loop commonly seen in the Hall resistance in the QAHE.

The non-adiabatic transport in QAHE caused by these quasi-helical edge states has been theoretically predicted and proposed as the possible source of dissipation observed in experiments [103, 104, 107]. Nevertheless, there have not been systematic study of the properties of these non-chiral edge states. Thus, probing the behaviour of the non-chiral edge states in QAHE will be one of the major topics in later discussions.

Finally, as can be seen in the lower panel of Fig. 6.7(b), the butterfly-shaped hysteresis displays a double-peak structure at H_c, which should be attributed to the mixing between $R_{26,35}$ and the Hall resistance in this measurement configuration. The magnetic field dependence of $R_{26,35}$ and $R_{26,41}$ are plotted together in Fig. 6.7(c), where $R_{26,41}$ in this configuration is equivalent to the Hall resistance. The thin curves are $R_{26,35}$, which is the same as the lower panel of Fig. 6.7(b). The thick curves and dashed curves represent the corrected and raw signals of $R_{26,41}$, respectively. The double peak structure in $R_{26,35}$ overlaps with the plateau-plateau transition regime in $R_{26,41}$ and creates two dips in the raw signal of $R_{26,41}$, indicating the mixing between $R_{26,35}$ and $R_{26,41}$. In the corrected $R_{26,41}$ signal, the component of $R_{26,35}$ is removed and $R_{26,41}$ becomes a typical square-shaped hysteresis loop commonly seen in the Hall resistance in the QAHE.

In summary, we established the chirality of chiral edge states by three-terminal measurements and confirmed the presence of non-chiral edge states in the QAH regime. Next, we will investigate the behaviour of these dissipative states.

6.5 Electrical transport in device CBST1 in the high magnetic field regime

In Fig. 6.6 and Fig. 6.7, the magnetoresistance always has a slope in the fully-magnetised regime, which we believe is associated with the H-field dependent behaviour of the non-chiral edge states. To further explore this phenomenon, high magnetic field sweeps up to $\mu_0 H = 10$ T were performed, as shown in Fig. 6.8. (Note that the ρ_{xx} and ρ_{xy} in later discussions are obtained by $R_{46,32}$ and $R_{46,53}$, respectively.)

Although the slope of magnetoresistance in all the measurements in Fig. 6.6 and Fig. 6.7 suggests a higher resistance in a stronger magnetic field, we found that a change in slope actually occurs between $\mu_0 H = 2.5$ T and 3 T in the high magnetic field sweeps, as shown in Fig. 6.8. The transition field is denoted by H^* in the insets of Fig. 6.8(a) and (b). Remarkably, a similar behaviour was previously observed by Kou *et al.* on a 10 QL magnetic TI film [104], which is comparable to the thickness of our magnetic TI sample. In contrast, this phenomenon is absent in all the studies on thinner magnetic TI films so far. This supports our hypothesis regarding the dissipative quasi-helical states on the side surface. Based on this observation, we speculate that the most likely reason for this slope change is a transition between different dominant dissipation mechanisms. To understand the transport properties of magnetic TI systems with both chiral and non-chiral edge states, we employ a theoretical model constructed by Wang *et al.* using the Landauer-Büttiker formalism [103], as described

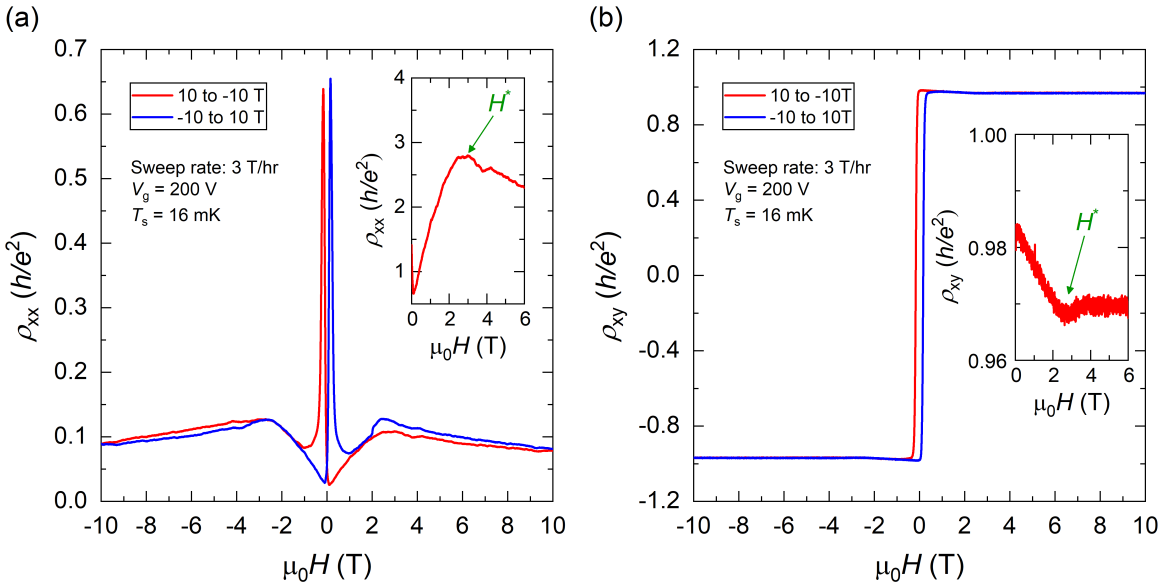

Figure 6.8: The magnetic field dependence of (a) ρ_{xx} and (b) ρ_{xy} up to ± 10 T taken at $T_s =$ 16 mK with $V_g = 200$ V using a sweep rate of 3 T/hr. Red and blue curves represent the downward and upward sweeps, respectively. The insets in (a) and (b) show the closeup images of the downward sweeps of ρ_{xx} and ρ_{xy} around the point of slope change, respectively. The field at which the slope change occurs is denoted by H^*.

in Fig. 6.9. With the same naming convention used in Chapter 3, the transmission probability for a state propagating from electrode i to electrode j is T_{ij}. For a standard Hall bar with N terminals, we identify $i = N+1$ as $i = 1$. For instance, the Hall bar shown in Fig. 6.9 is $N = 6$ and hence $i = 7$ is equivalent to $i = 1$.

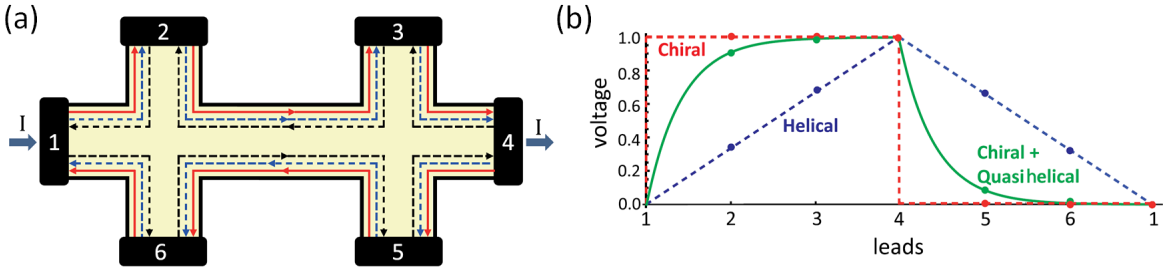

Figure 6.9: The theoretical model constructed by Wang *et al.* for the transport in magnetic TI systems with both chiral and non-chiral edge state using the Landauer-Büttiker formalism. (a) A six-terminal magnetic TI Hall bar device with both chiral edge states (solid lines) and counterpropagating quasi-helical edge states (black and blue dashed lines). The current is passed from electrode 1 to electrode 4, while electrode 2, 3, 5, and 6 are voltage leads. (b) The voltage of each lead calculated by the model. Adapted from [103].

Therefore, for chiral edge states in the QHE or QAHE we have $T_{i,i+1} = 1$ for $i = 1$ to N, and all other $T_{ij} = 0$. For helical edge states in the QSHE we have $T_{i,i+1} = 1$ and $T_{i+1,i} = 1$ for $i = 1$ to N, and all other $T_{ij} = 0$. For the quasi-helical edge states, however, the transmission probability between neighbouring electrodes is not perfect, hence we have $T_{i,i+1} = k_1$ and $T_{i+1,i} = k_2$ with k_1, $k_2 < 1$ and all other $T_{ij} = 0$. Consequently, the total transmission probability for a system with quasi-helical states coexisting with chiral edge states should be given by $T_{i,i+1} = 1 + k_1$ and $T_{i+1,i} = k_2$, and all the others zero.

In theory, k_1 and k_2 should approach zero for an infinitely large device either due to the dissipation arising from the phase decoherence of quasi-helical states in metallic electrodes, or the momentum relaxation when the sample size L is much lager than the mean free path l_{mfp}. Thus, when $L \gg l_{\mathrm{mfp}}$, k_1 and k_2 can be approximated by

$$k_1, k_2 \sim \frac{l_{\mathrm{mfp}}}{l_{\mathrm{mfp}} + L}. \tag{6.5}$$

In the presence of an external magnetic field, the backscattering of quasi-helical edge states will be enhanced due to breaking of the time-reversal symmetry, while the chiral edge states remain robust against backscattering. When the magnetic length l_B becomes smaller than the mean free path l_{mfp} in an increasingly stronger magnetic field, k_1 and k_2 will start to approach zero. As a result, the influence of quasi-helical states at high magnetic field becomes weaker and ρ_{xx} will begin to decrease with increasing magnetic field after $l_B < l_{\mathrm{mfp}}$ [103]. We believe this is the reason behind the slope change of the magnetoresistance in the high magnetic field regime. In Fig. 6.8, this transition occurs at around $\mu_0 H = 2.5$ T, where $l_B \sim 15.8$ nm, suggesting that the mean free path in our system can be $l_{\mathrm{mfp}} \sim 20$ nm.

Considering the elongated leads of the Hall bar of CBST1, the channel length between the two voltage probes (electrode 2 and electrode 3) is 4000 μm, which is 200000 times longer than the l_{mfp}. Hence, the approximation given by Eq. 6.5 should be valid for our device and we estimate k_1, $k_2 \sim 5 \times 10^{-6}$.

The voltage of each electrode of the Hall bar then can be computed using the Landauer-Büttiker formalism. In our measurement setup, as shown in Fig. 6.10(a), electrode 4 and 6 are used as source and drain, respectively. Thus, we can define $V_4 \equiv V$ and $V_6 \equiv 0$, and choose $I_4 = -I_6 \equiv I$. Similar to [103], the travelling directions of different edge states in the case of $M > 0$ are denoted by lines with different colours in Fig. 6.10(a). The red solid line indicates the direction of chiral edge states, while the light blue and dark blue dashed lines represent the directions of the counterpropagating quasi-helical states in CBST1.

The voltage of each electrode of CBST1 calculated by the Landauer-Büttiker formalism is shown in Fig. 6.10(b). The edge states start from Lead4 and then go through Lead5, Lead6, Lead1, Lead2, Lead3, and then finally back to Lead4 (labelled as Lead4'). The red and

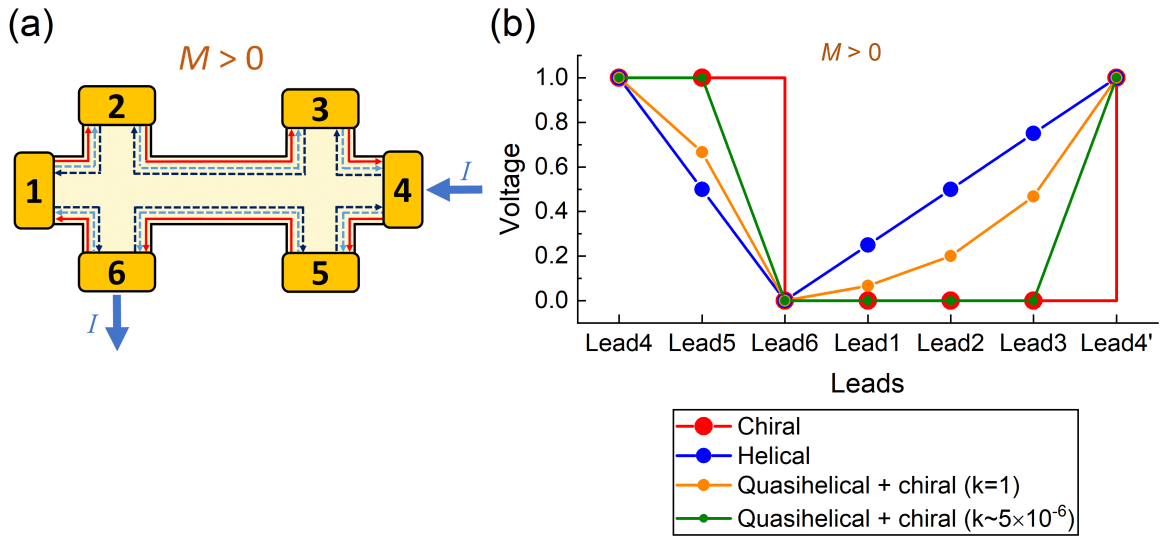

Figure 6.10: (a) The schematic diagram showing the measurement setup and the travelling directions of edge states in CBST1. The current is passed between electrode 4 and electrode 6, and the voltage probes are on electrode 1, 2, 3, and 5. The travelling directions of different edge states for the case of $M > 0$ are denoted by lines with different colours. The red solid line indicates the direction of chiral edge states, while the light blue and dark blue dashed lines represent the directions of the counterpropagating quasi-helical states. (b) The voltage of each electrode calculated by the Landauer-Büttiker formalism.

blue dots represent the voltages of the six electrodes when the transport is purely chiral or helical, respectively. When there are quasi-helical states coexisting with chiral edge states, the values of k_1 and k_2 need to be taken into account. The orange dots show the extreme case of $k_1 = k_2 = 1$. It can be seen that the voltage first deceases exponentially from source to drain, and then increases exponentially from drain to source. As k_1 and k_2 approach zero, we found that the voltage drop before entering the drain (Lead6) and the rise before re-entering the source (Lead4') both become sharper. The green dots show the case of our device, in which k_1 and k_2 are estimated to be $\sim 5 \times 10^{-6}$. The voltage difference between the two longitudinal voltage probes (Lead2 and Lead3) seems to be much smaller than the experimental observation. Given that the Fermi level of CBST1 is not at the Dirac point, we suspect that this discrepancy may originate from the residual bulk states which assist the backscattering of quasi-helical states by providing more backscattering paths. However, the quantitative explanation is still unclear at the moment. We must emphasise that our calculation is based on a toy model, in which k_1 and k_2 are assumed to be equivalent and can be approximated by $k_1, k_2 \sim l_{\mathrm{mfp}}/(l_{\mathrm{mfp}} + L)$. But these two assumptions may not be accurate enough for CBST1.

Due to the discovery of the slope change in magnetoresistance in the high magnetic field regime, we then decided to conduct a more comprehensive study about this transition behaviour.

To begin with, we took a series of magnetic field sweeps up to $\mu_0 H = \pm$ 5 T at different T_s to see how this transition varies with the temperature. As shown in Fig. 6.11, the kink initially appears at $\mu_0 H \sim 2.5$ T and its position does not change when $T_s \leq 50$ mK. After reaching 100 mK, the position of the kink moves slightly inward. As T_s increases, the kink continues to shift toward 0 T, but the position becomes harder to define above 400 mk because its amplitude gradually shrinks.

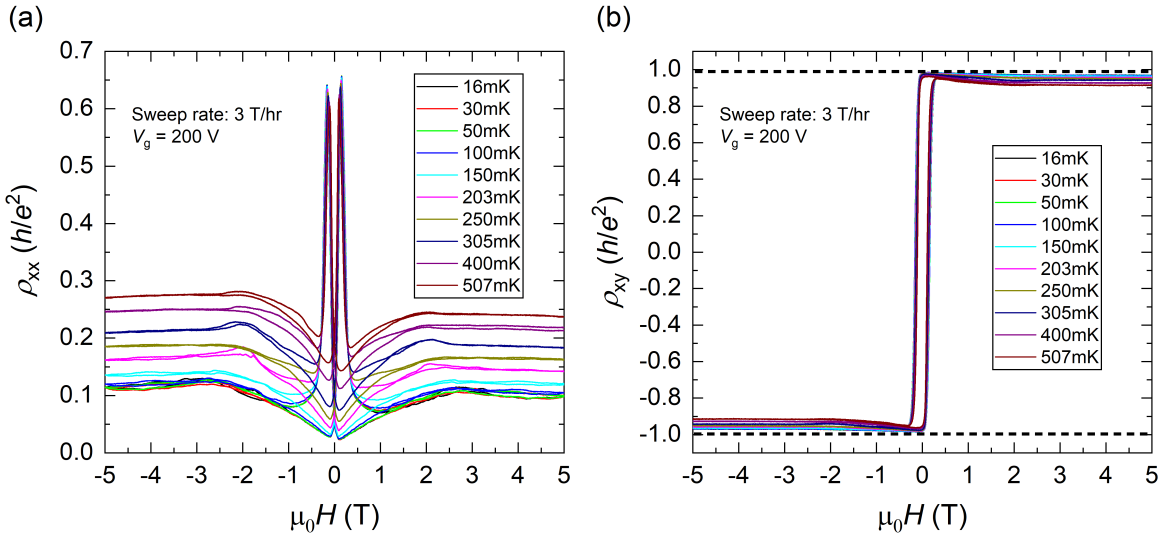

Figure 6.11: The magnetic field dependence of (a) ρ_{xx} and (b) ρ_{xy} taken at different T_s with $V_g = 200$ V using a sweep rate of 3 T/hr. The kink indicating the transition between different dissipation mechanisms initially appears at $\mu_0 H \sim 2.5$ T and its position does not change much below 50 mK. After reaching 100 mK, the position of the kink slightly moves inward. As T_s increases, the kink continues to shift toward 0 T.

To closely check the T_s dependence of the kink, the zoomed-in images of the downward magnetic field sweeps in Fig. 6.11 around H^* are shown in Fig. 6.12. It can be seen that this "kink" feature actually occurs in both ρ_{xx} and ρ_{xy} signals, and, though less obvious in the ρ_{xy}, the position of H^* shifts toward $\mu_0 H = 0$ T as T_s increases. At first glance, it seems inconsistent with our hypothesis since l_{mfp} should decrease with increasing T_s, and thus H^* should shift away from 0 T because a stronger magnetic field is required to satisfy the condition of $l_B < l_{\mathrm{mfp}}$. However, it is important to keep in mind that the quasi-helical edge state is not the only channel affected by the temperature. As we increase T_s, more 2D and 3D bulk states as well as mid-gap states will be thermally-activated, which can lead to enhanced

diffusive transport and, to some extent, short the edge conduction. This argument is further supported by the evolution of $\rho_{xx}(H_c)$ and the "Hall coefficient" (i.e. the slope of ρ_{xy}-B). Figure 6.13(a) shows the slope of magnetoresistance between $\mu_0 H = 0.5$ T and 1 T extracted from Fig. 6.12, in which the absolute value of the slope of ρ_{xy} increases with T_s. This is similar to the analysis in Fig. 6.4(c) and suggests that the carrier concentration of 2D and 3D bulk states increases with increasing T_s. In addition, Fig. 6.13(b) shows the T_s dependence of $\rho_{xx}(H_c)$, in which $\rho_{xx}(H_c)$ drops with the increasing temperature. Similar to Fig. 6.4(d), such behaviour also implies an increase of bulk states at higher temperatures. Consequently, when the weight of edge transport slowly decreases in conduction, the resistance at H_c becomes smaller due to increasing diffusive transport.

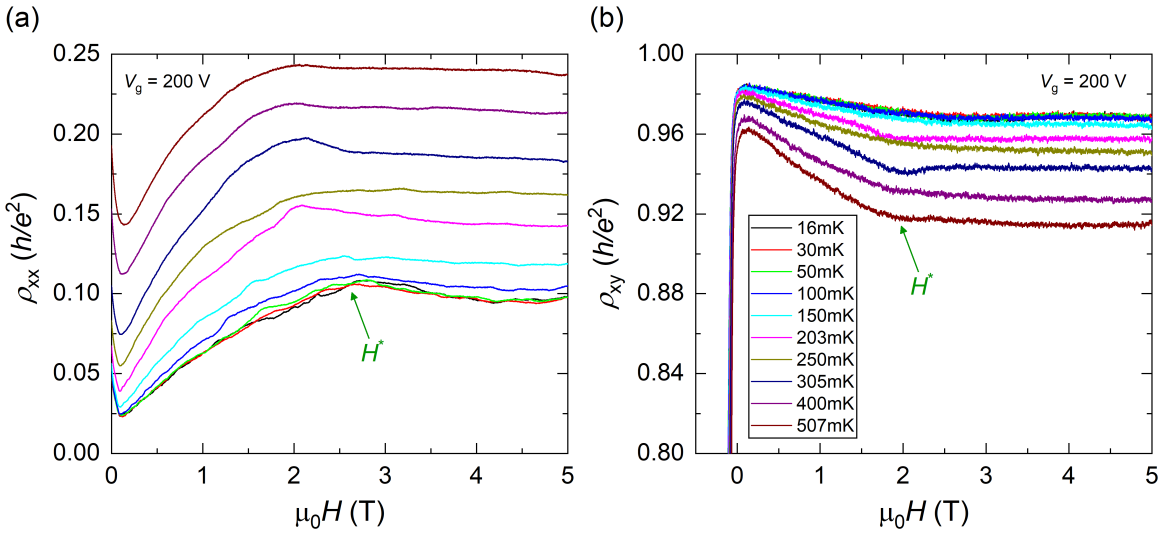

Figure 6.12: The zoomed-in images of the magnetic field dependence of (a) ρ_{xx} and (b) ρ_{xy} around H^* in the downward sweep in Fig. 6.11. The "kink" feature appears in both ρ_{xx} and ρ_{xy} signals, and the position of H^* shifts toward $\mu_0 H = 0$ T as T_s increases.

Therefore, our data show that the entire magnetic field dependence of ρ_{xx} and ρ_{xy} should always be considered as an outcome of the mixed dissipative edge and bulk conduction on top of the chiral edge transport. Beyond H^*, the residual dissipation mostly comes from bulk states, which can be localised by strong magnetic fields and lead to decreasing ρ_{xx} with increasing $\mu_0 H$ in the high field regime. On the other hand, below H^* (except for the coercive-peak regime), the residual dissipation is dominated by quasi-helical edge states, which also have a magnetic-field-dependent backscattering behaviour but will start to be suppressed after $l_B < l_{\mathrm{mfp}}$ [103]. The transition between these two dissipation scenarios may occur near H^* and result in the kink structure in magnetic field sweeps.

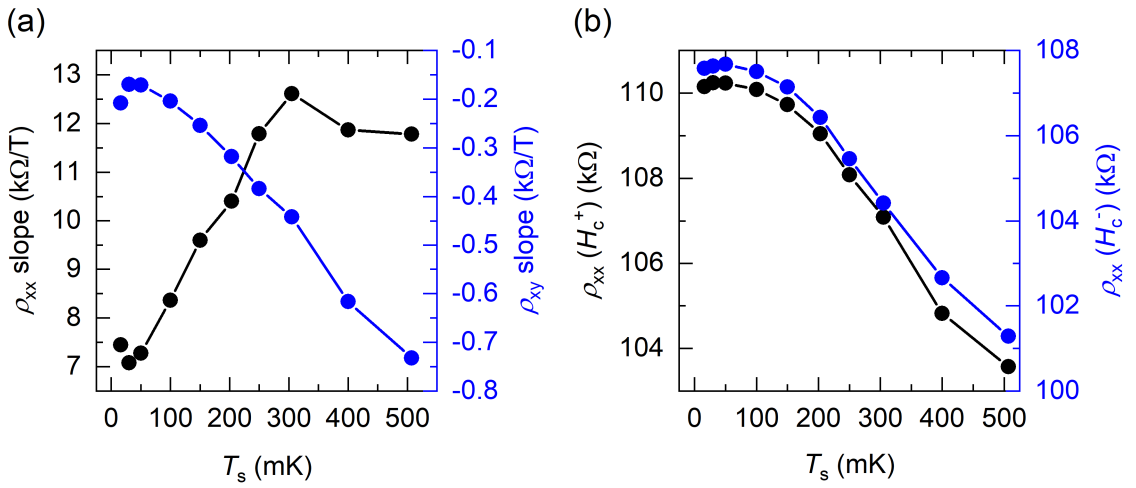

Figure 6.13: (a) The T_s dependence of the slope of ρ_{xx} and ρ_{xy} between $\mu_0 H = 0.5$ T and 1 T extracted from Fig. 6.12. (b) The T_s dependence of $\rho_{xx}(H_c)$ extracted from Fig. 6.11. The H_c^+ (black) and H_c^- (blue) represent the coercive field values in the positive and negative magnetic field regime, respectively.

Interestingly, in Fig. 6.4(c), the sign of the ρ_{xx} slope changes after $V_g > 20$ V, which is regarded as a signal of crossover into the QAH regime. However, in Fig. 6.13(a), the slope of ρ_{xx} between $\mu_0 H = \pm 2$ T does not change sign even when the film is heated to 507 mK, which suggests that CBST1 is still in the QAH regime at $T_s = 507$ mK and the size of magnetic gap of CBST1 should be larger than 507 mK (~ 43.7 μeV).

In Fig. 6.12, we see that the curves of ρ_{xx} and ρ_{xy} below $T_s = 50$ mK almost overlap and the position of H^* is similar. Likewise, in Fig. 6.13 we observe that the slopes and $\rho_{xx}(H_c)$ do not have a clear T_s dependence below $T_s = 50$ mK. Therefore, we suspect that the electron temperature is always higher than 50 mK, and the sample temperature T_s read by the sample thermometer can no longer represent the actual electron temperature in our measurements.

To further investigate this, we extract the T_s dependence of H_c from Fig. 6.11, as shown in Fig. 6.14(a). The H_c^+ and H_c^- are the coercive field values in the positive and negative magnetic field regime, respectively. Basically, both H_c^+ and H_c^- shift toward $\mu_0 H = 0$ T as T_s increases, which is consistent with our observations on all the other magnetic TI films we have measured, such as the results shown in Fig. 5.2. Nevertheless, it can be seen that H_c remains at roughly the same value from $T_s = 16$ mK to 50 mK, implying that the electron temperature may not actually fall below 50 mK.

This is further supported by Fig. 6.14(b), in which the T_s and ρ_{xx} values extracted from the curves in Fig. 6.11(a) are plotted for $\mu_0 H = 0$ T, 5 T, and -5 T. It can be seen that all ρ_{xx}-T_s curves show a similar behaviour, in which ρ_{xx} barely changes below $T_s = 50$ mK, but becomes proportional to T_s for $T_s > 50$ mK.

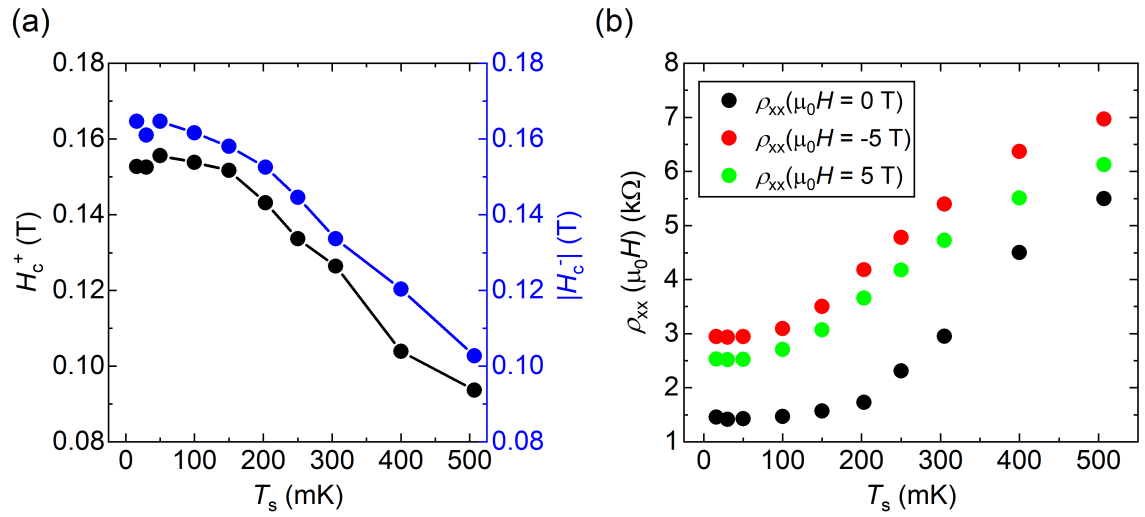

Figure 6.14: (a) The T_s dependence of H_c extracted from Fig. 6.11. The H_c^+ and H_c^- are the coercive field values in the positive and negative magnetic field regime, respectively. (b) The T_s dependence of $\rho_{xx}(\mu_0 H)$ extracted from Fig. 6.11(a). The black, red, and green dots indicate ρ_{xx} at $\mu_0 H = 0$ T, -5 T, and 5 T, respectively.

Accordingly, from Fig. 6.13 and Fig. 6.14 we speculate that the electron temperature T_e may differ from the sample temperature T_s when $T_s < 50$ mK in the experiments. The lowest temperature that T_e reached is possibly 50 mK.

Finally, similar $\rho_{xx}(\mu_0 H)$-T_s curves at other H values can be extracted from Fig. 6.11, and the activation energy E_a can be obtained by Arrhenius plots. It should be noted that due to the presence of the coercive peak between -1 T $< \mu_0 H < 0$ T in the downward sweep (0 T $< \mu_0 H < 1$ T in the upward sweep) and the heating around 0 T from the reversal of polarity of superconducting magnet, the data between -1 T $< \mu_0 H < 1$ T is not used for the Arrhenius fit. Apart from this range, E_a at different magnetic fields are calculated and shown in Fig. 6.15(a). Clearly, the E_a-H relation is symmetric about $\mu_0 H = 0$ T, and the highest E_a occurs at the ZF. As $|\mu_0 H|$ increases from 0 T, E_a drops rapidly until 2 T and then appears to saturate after 3 T. Although we currently do not have a quantitative explanation, this E_a-H relation is consistent with our hypothesis about the shift between different dominant dissipation mechanisms in the QAH regime. Namely, the residual dissipation and non-vanishing ρ_{xx} in the QAHE can be ascribed to the quasi-helical states and bulk states that coexist with the dissipationless chiral edge states (which play the main role in the conduction) in the QAH regime. In the lower magnetic field regime ($< H^* \sim 2.5$ T), quasi-helical states are the most important source of dissipation and dominate the ρ_{xx} slope in magnetic field sweeps, leading to an increasing ρ_{xx} with the increasing H; whereas in the higher magnetic field regime ($> H^* \sim 2.5$ T), bulk states become the major source of dissipation and result in an

decreasing ρ_{xx} with the increasing H. When $|\mu_0 H| > 2.5$ T, the bulk states have a stable activation energy $E_a \sim 16.2$ μeV (~ 188 mK), while when $|\mu_0 H| < 2.5$ T, the activation energy of bulk states can be affected by the quasi-helical states conducting in parallel and hence E_a becomes magnetic-field-dependent.

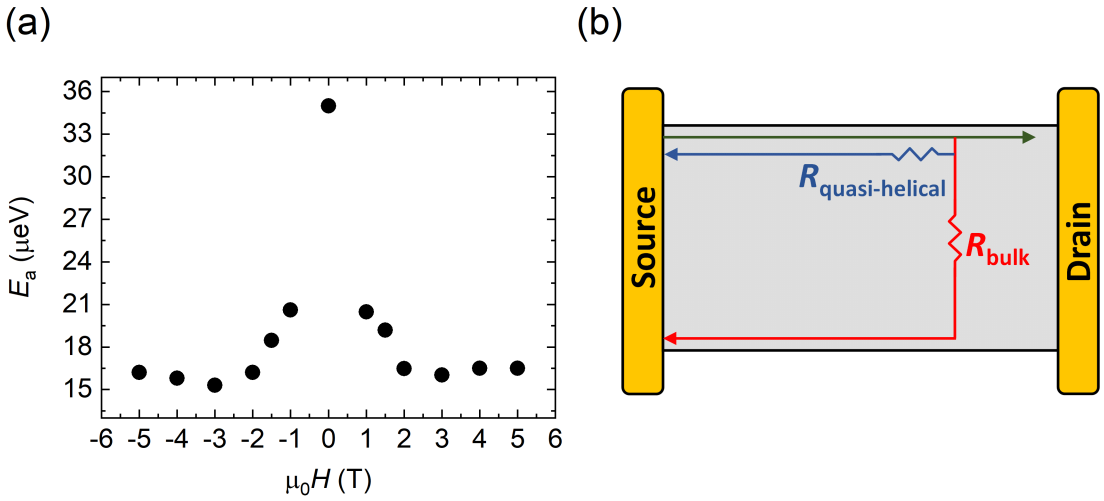

Figure 6.15: (a) The magnetic field dependence of E_a extracted from the downward sweep in Fig. 6.11. (b) The possible scattering paths in the QAH regime. The device is a simplified version of the CBST1 device. The green arrow indicates the quasi-helical channel travelling from source to drain electrode. The blue arrow is the case when the forward-propagating quasi-helical channel is backscattered into the backward-propagating quasi-helical channel at the same edge. The red arrow is the case when the forward-propagating quasi-helical channel is backscattered into the backward-propagating quasi-helical channel at the opposite edge with the assistance of residual bulk states. The resistance of these two backscattering paths are denoted by $R_{\text{quasihelical}}$ and R_{bulk}, respectively.

A simplified version describing the interplay between quasi-helical states and bulk states is shown in Fig. 6.15(b), in which the backscattering paths via the same edge and across the bulk can be represented by two resistors in parallel. The dominant dissipation mechanism in the QAH regime then can be determined by the ratio between $R_{\text{quasihelical}}$ and R_{bulk}. When $R_{\text{quasihelical}}/R_{\text{bulk}} < 1$, backscattering may tend to occur at the same edge. In this case (blue arrow), dissipation is generated because the forward-propagating quasi-helical channel is backscattered into the backward-propagating quasi-helical channel at the same edge. On the other hand, when $R_{\text{quasihelical}}/R_{\text{bulk}} > 1$, backscattering may tend to occur through the bulk. In this case (the red arrow), dissipation is generated because the forward-propagating quasi-helical channel is backscattered into the backward-propagating quasi-helical channel at the opposite edge. Changing the temperature, gate voltage, or external magnetic field

can alter the ratio between $R_{\text{quasihelical}}$ and R_{bulk}, and hence lead to the transition between dissipation mechanisms dominated by different backscattering paths.

In summary, in this section we have observed a "kink" structure at H^* in magnetoresistance and speculate that it may arise from the transition between different dissipation mechanisms governed by different conducting channels. From the theoretical model [103], this transition should be affected by the temperature or the applied magnetic field in transport measurements. Our experiments show that the transition does have a T_s dependence, probably due to the increase of carrier concentration at higher temperatures that fosters the shift between dominant dissipation mechanisms. The possible l_{mfp} of quasi-helical states at base temperature can be around 20 nm according to the position of H^*. The E_a extracted from the magnetic field sweeps at different T_s exhibits a magnetic field dependence as well, ranging from 35.0 μeV ($\sim$ 405 mK) at $\mu_0 H = 0$ T to 16.2 μeV ($\sim$ 188 mK) at $\mu_0 H = \pm$ 5 T. The fact that CBST1 does not leave the QAH regime even at $T_s = 507$ mK implies that the magnetic gap is at least larger than 43.7 μeV. Finally, our analysis of the T_s dependence suggests that the electron temperature is not actually cooled below 50 mK. In the next section, we will investigate the current dependence of ρ_{xx} and ρ_{xy}, and discuss the relation between the S-D current, sample temperature T_s, and electron temperature T_e.

6.6 Current dependence of electrical transport in device CBST1

In the previous section, we found a discrepancy between T_e and T_s. Therefore, in this section we study how the energy of electrons can affect the manifestation of the QAHE.

We start from the current-voltage (I-V) relations of CBST1 under various conditions. The I-V measurements in this section were performed by adding an AC excitation current of 1 nA at 15 Hz onto a DC current (I_{DC}) as the S-D current. The longitudinal voltage drop V_{xx} is obtained using electrode 4 and 6 as current leads and electrode 3 and 2 as voltage probes, while the Hall voltage is measured between electrode 5 and 3. To distinguish it from a pure AC lock-in measurement, we use $\mathrm{d}V_{xx}/\mathrm{d}I$ and $\mathrm{d}V_{xy}/\mathrm{d}I$ to represent the resistance measured in this AC + DC setup in this section,

As discussed in Sec. 6.3, the crossover to the QAH regime occurs at $V_g = 20$ V. Thus, we first compare the DC I-V curves inside and outside the QAH regime, as shown in Fig. 6.16. The relation between $\mathrm{d}V_{xx}/\mathrm{d}I$, $\mathrm{d}V_{xy}/\mathrm{d}I$ and I_{DC} at $T_s = 16$ mK, $M > 0$, and $V_g = 0$ V is shown in Fig. 6.16(a). It can be seen that both $\mathrm{d}V_{xx}/\mathrm{d}I$ and $\mathrm{d}V_{xy}/\mathrm{d}I$ decrease with increasing I_{DC}. By integrating the data points in Fig. 6.16(a), we obtain the DC I-V curve at $V_g = 0$ V

between $I_{DC} = \pm$ 2 μA, as shown in Fig. 6.16(b), which is slightly non-linear with higher resistance in the low I_{DC} regime. This phenomenon has the same explanation as discussed in Fig. 5.11. At such a low temperature, the Joule heating effect is more prominent and CBST1 can become warmer when I_{DC} is high [101]. Since magnetic TI systems have an insulating temperature-dependence outside the QAH regime, the resistance becomes smaller when I_{DC} is higher. With this interpretation, it is easy to understand why the relation between dV_{xx}/dI, dV_{xy}/dI and I_{DC} at $T_s = 16$ mK, $M > 0$, and $V_g = 200$ V exhibits a completely different behaviour, as shown in Fig. 6.16(c) and (d). In Fig. 6.16(c), dV_{xx}/dI increases with increasing I_{DC}, whereas dV_{xy}/dI decreases with increasing I_{DC}. This is probably because the QAHE is undermined by higher temperatures resulting from the high I_{DC}, leading to higher residual longitudinal resistance and larger deviation of Hall resistance from the quantised value. Likewise, we obtain the DC I-V curve at $V_g = 200$ V between $I_{DC} = \pm$ 2 μA by integrating the data points in Fig. 6.16(c), as shown in Fig. 6.16(d). It displays a clear non-linearity with lower resistance in the low I_{DC} regime, exactly opposite to Fig. 6.16(b).

Therefore, the I-V relations agree with change from insulating to metallic temperature-dependence after the crossover to the QAH regime, and also are consistent with our argument regarding the Joule heating effect on I-V curves at ultralow temperatures in Sec. 5.4.3.

In addition, we further examine the I-V curves in the presence of external magnetic fields to check whether the non-linearity arose from superconducting phase transition of the indium contacts. Indium has a superconducting critical temperature and critical field of 3.4 K and 30 mT, respectively [153, 154]. Thus, at fridge temperatures the superconductivity of indium contacts should be destroyed by a magnetic field stronger than 30 mT. If the non-linearity disappears when $\mu_0 H > 30$ mT, its origin may be attributed to the superconducting phase transition of indium contacts rather than the Joule heating effect.

Figure 6.17(a) and (b) show the current dependence of dV_{xx}/dI below $I_{DC} = 2$ μA taken at $\mu_0 H = 2$ T and 0.156 T ($\sim H_c$), respectively. The dV_{xx}/dI-I_{DC} curve without external magnetic field is shown in Fig. 6.17(c) for comparison. Evidently, the relation between dV_{xx}/dI and I_{DC} is still non-linear for both $\mu_0 H = 2$ T and 0.156 T, suggesting that the non-linearity does not come from the superconductivity of the indium contacts. Remarkably, the curve at 0.156 T shows an opposite slope change to the data at 0 T and 2 T. This is probably because the transport near H_c is no longer dominated by edge conduction, and hence loses the metallic temperature-dependence. However, it should also be noted that the transport near H_c is complicated, with not only 2D and 3D bulk states but also quasi-1D edge states meandering in the network of domain walls. The interplay between them may lead to the rise of dV_{xx}/dI in the high current regime in Fig. 6.17(b). But we have not found a clear explanation for this behaviour so far.

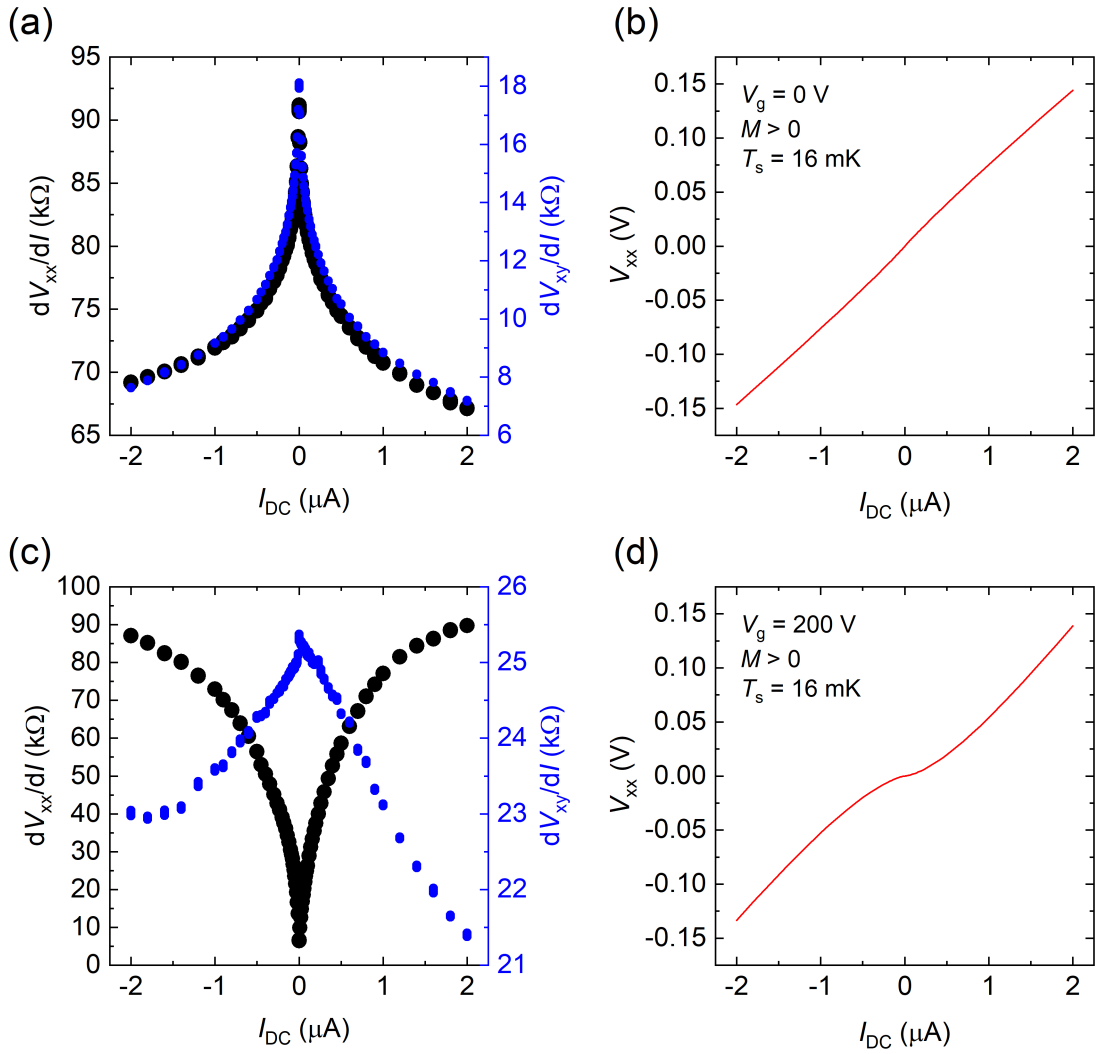

Figure 6.16: The *I*-*V* relations of CBST1 at $T_s = 16$ mK taken by using electrode 4 and 6 as current leads and electrode 3 and 2 as voltage probes, while the Hall voltage is measured between electrode 5 and 3. dV_{xx}/dI and dV_{xy}/dI are used to represent the resistance measured in this AC + DC setup. (a) The relation between dV_{xx}/dI, dV_{xy}/dI and I_{DC} at $T_s = 16$ mK, $M > 0$, and $V_g = 0$ V. (b) The *I*-*V* curve obtained by integrating the dV_{xx}/dI over I_{DC} in (a). (c) The relation between dV_{xx}/dI, dV_{xy}/dI and I_{DC} at $T_s = 16$ mK, $M > 0$, and $V_g = 200$ V. (d) The *I*-*V* curve obtained by integrating the dV_{xx}/dI over I_{DC} in (c).

Up to this point, we have shown that the non-linearity in the *I*-*V* relations is caused by Joule heating but not other effects. Nevertheless, it is crucial to bear in mind that the resistance calculated from the *I*-*V* curves in the above AC + DC measurements cannot be directly used to interpolate the ρ_{xx}-T curve in Fig. 6.14 and deduce the temperature of CBST1 because both the *I*-*V* curves in Fig. 6.16 and Fig. 6.17 are obtained by four-terminal measurements, which does not take into account the Joule heating effect on the indium

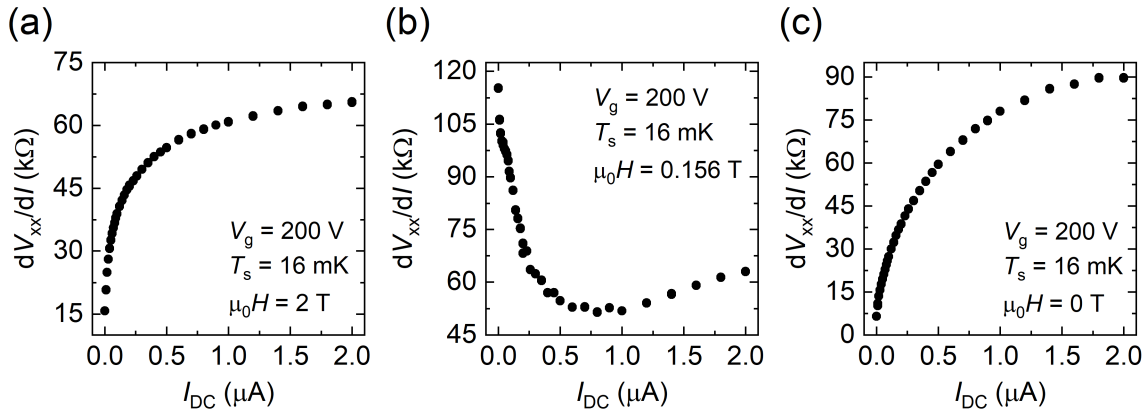

Figure 6.17: The current dependence of the longitudinal resistance at $T_s = 16$ mK with $V_g = 200$ V for external magnetic fields of (a) 2 T, (b) 0.156 T and (c) 0 T. At $\mu_0 H = 2$ T and 0.156 T ($\sim H_c$), the superconductivity of indium contacts should be broken. The relation at 0 T is shown in (c) for comparison.

contacts. Hence, we cannot simply compare a resistance calculated from the slope of these *I-V* curves to a corresponding point on a *R-T* curve to speculate the "real" temperature of the magnetic TI heterostructure.

Alternatively, we study the temperature dependence of *I-V* curves to gain more information about the actual temperature of CBST1. As shown in Fig. 6.18, the relations between dV_{xx}/dI and I_{DC} at $T_s = 16$ mK, 300 mK, and 500 mK are plotted together for comparison. It can be seen that the curve of 16 mK (black dots) first overlaps with the curve of 300 mK (blue dots) from $I_{DC} \sim 230$ nA, and later the curve of 500 mK (red dots) also overlaps with these two curves after $I_{DC} \sim 600$ nA. This seems to imply that T_e may have exceeded 300 mK when $I_{DC} = 230$ nA because the black and blue curves have almost no difference beyond that (indicated by the green dashed line). Similarly, T_e may have exceeded 500 mK when $I_{DC} = 600$ nA and all curves just show the same behaviour beyond that (indicated by the orange dashed line).

Moreover, in Fig. 6.18 the non-linearity becomes much smaller at higher T_s, which is consistent with our theory since the Joule heating effect is expected to be less pronounced at elevated temperatures, and the non-linear *I-V* relation should become negligible at sufficiently high temperatures. These behaviours strengthen our argument about the Joule heating effect on CBST1 and also provide us with a quantitative idea for the possible electron temperature corresponding to a certain I_{DC}.

For comparison, we use a different approach to investigate the effect of high S-D current on the resistance. With I_{DC} fixed, we measure the T_s dependence of dV_{xx}/dI at different I_{DC} and study how the *R-T* relation changes with I_{DC}. Figure 6.19(a) shows the *R-T* relations

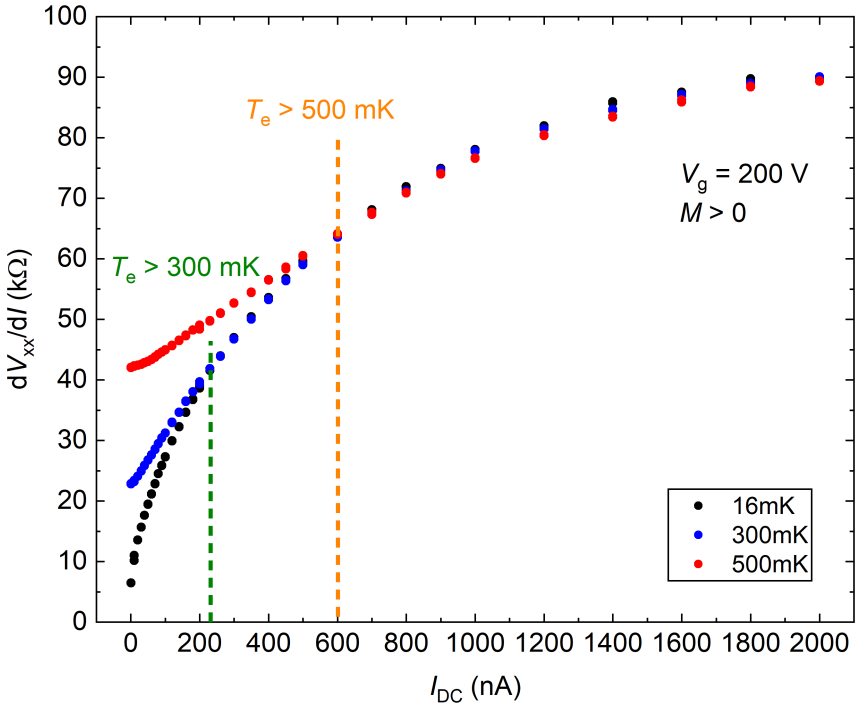

Figure 6.18: The current dependence of the longitudinal resistance at $V_g = 200$ V in the $M > 0$ state taken at $T_s = 16$ mK (black dots), 300 mK (blue dots), and 500 mK (red dots). The black and blue curves start to overlap with each other since $I_{DC} = 230$ nA, and the red curve also joins them when $I_{DC} = 600$ nA.

at $V_g = 200$ V in the $M > 0$ state with $I_{DC} = 1$ nA, 100 nA, 200 nA, and 1 μA. First of all, we notice that the R-T curve of 1 nA (black) exhibits a similar behaviour to the R-T curves observed in Fig. 6.14(b), i.e. the resistance almost does not change with T_s below 50 mK. This again confirms our hypothesis that the electron temperature T_e may differ from the sample temperature T_s for $T_s < 50$ mK. Secondly, it can be seen that both the R-T curves of 100 nA (red) and 200 nA (green) in Fig. 6.19(a) have a "saturation zone" as well. For the curve of 100 nA, the resistance barely changes with T_s below 200 mK. For the curve of 200 nA, this saturation zone extends to $\sim$ 280 mK. From these observations, we speculate that the lowest T_e when using $I_{DC} = 100$ nA is possibly $\sim$ 200 mK, while the lowest T_e when using $I_{DC} = 200$ nA may be $\sim$ 280 mK. Finally, the most extreme case is the curve of 1 μA (blue), which stays almost the same throughout the entire T_s range, implying that the T_e may have exceeded 500 mK at $I_{DC} = 1$ μA.

Since the R-T relations of 1 nA, 100 nA, and 200 nA in Fig. 6.19(a) are linear in the high temperature regime, we can calculate the activation energy E_a of them using Arrhenius plots. As shown in Fig. 6.19(b), the black, red, and green dots are the lnσ_{xx} values calculated from the dV_{xx}/dI data of the 1 nA, 100 nA, and 200 nA curves in Fig. 6.19(a), respectively.

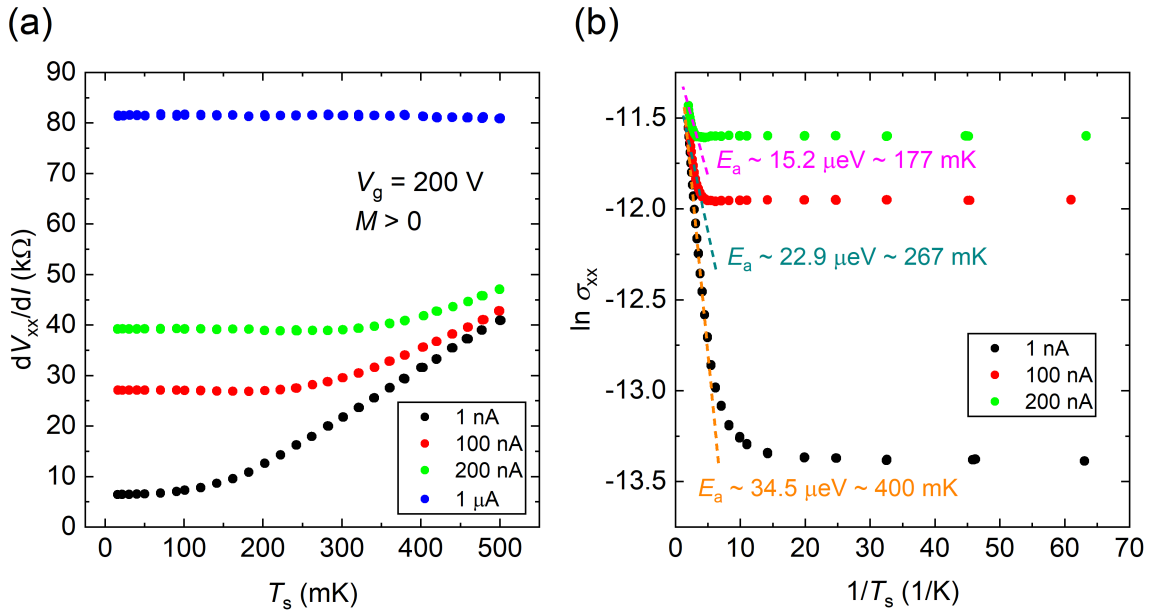

Figure 6.19: (a) The temperature dependence of the longitudinal resistance at $V_g = 200$ V in the $M > 0$ state taken using $I_{DC} = 1$ nA (black dots), 100 nA (red dots), 200 nA (green dots) and 1 μA (blue dots). (b) The Arrhenius plot of the R-T relations in (a) (except the curve of $I_{DC} = 1$ μA). The black, red, and green dots are the $\ln\sigma_{xx}$ values calculated from the dV_{xx}/dI data of the 1 nA, 100 nA, and 200 nA curves in (a), respectively. The activation energy E_a is obtained by the fitting of the black, red, and green dots in the high temperature linear regime. The orange, cyan, and pink dashed lines indicate the fitting lines for the black, red, and green dots, respectively. The fitting ranges are 180-500 mK, 300-500 mK, and 360-500 mK for the orange, cyan, and pink fitting lines, respectively.

The activation energies of the black, red, and green dots are obtained by the orange, cyan, and pink fitting lines, respectively. The fitting ranges are 180-500 mK, 300-500 mK, and 360-500 mK for the orange, cyan, and pink fitting lines, respectively. The activation energies for the 1 nA, 100 nA, and 200 nA cases are 34.5 μeV (∼ 400 mK), 22.9 μeV (∼ 267 mK), and 15.2 μeV (∼ 177 mK), respectively. Apparently, E_a seems to be smaller when I_{DC} is higher. A possible explanation is that the Joule heating effect arising from high I_{DC} has actually rendered an extra amount of thermal energy to the impurity states at $T_s = 16$ mK, but this effect is not reflected in the change of T_s read by the thermometer. Therefore, when we change T_s and observe the thermal activation behaviour, the thermal energy required for impurity states to transit from their original energy levels to the closest band edge seemingly becomes smaller, and the E_a calculated from Arrhenius fit turns out to reduce with increasing I_{DC}.

It is worth mentioning that the lowest T_e values speculated from Fig. 6.19(a) agree quite well with our analysis of the current-dependence data in Fig. 6.18, in which the

speculated lowest T_e values are $\sim$ 300 mK and $\sim$ 500 mK for $I_{\mathrm{DC}} = 230$ nA and 600 nA, respectively. The relation between the speculated lowest T_e and I_{DC} from these two experiments is summarised in Fig. 6.20.

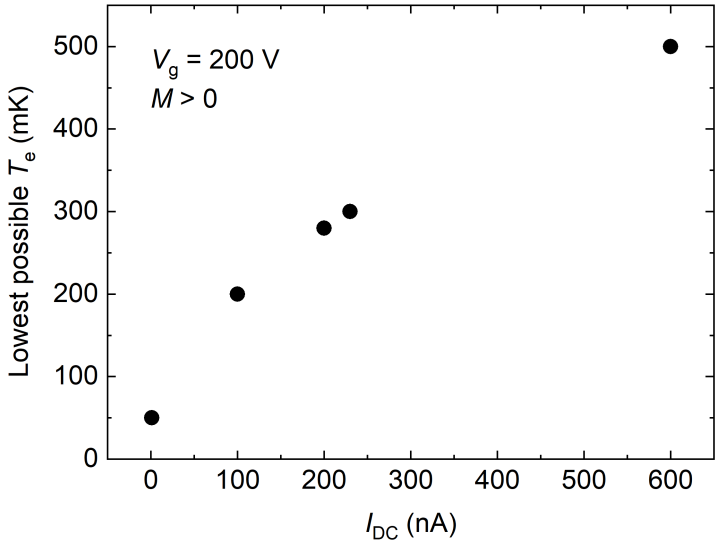

Figure 6.20: The speculated lowest electron temperatures (T_e) at different S-D currents (I_{DC}) for CBST1 with $V_g = 200$ V in the $M > 0$ state. The data points are obtained from Fig. 6.18 and Fig. 6.19(a).

6.7 Summary

In this chapter, we performed a variety of experiments to study the carrier transport behaviour in the Cr-doped $(Bi,Sb)_2Te_3$ heterostructure at fridge temperatures.

From the V_g dependence of ρ_{xx} and ρ_{xy}, we verify that CBST1 was tuned into the QAH regime between $V_g = 0$ V and 20 V. The V_g dependence of the ρ_{xy} slope, H_c, as well as $\rho_{xx}(H_c)$ all support the observation of the QAH phase transition. However, it is also found that ρ_{xx} is still descending and ρ_{xy} is still ascending even at $V_g = 200$ V, indicating that the Dirac point may be somewhere beyond $V_g = 200$ V. Due to the constraint of instruments and the charging effect of the STO substrate, we could not actually reach the Dirac point. The lowest $\rho_{xx} \sim 0.0667\ h/e^2$ and highest $\rho_{xy} \sim 0.998\ h/e^2$ are achieved at $V_g = 200$ V. The non-vanishing ρ_{xx} implies the presence of dissipative states at $V_g = 200$ V.

By the three-terminal measurements, we revealed the chirality of the QAH states. Nevertheless, the three-terminal resistance does not completely vanish throughout the entire fully-magnetised regime, and some deviation from $\rho_{xx} = 0$ and $\rho_{xy} = h/e^2$ can be seen in the high magnetic field regime. To investigate the origin of the dissipation, non-local

measurements were carried out and the results suggest the existence of dissipative edge states in CBST1. A possible candidate of these non-chiral edge states is the topological surface states on the side surface of the film that are no longer protected by the time-reversal symmetry due to the in-plane magnetisation and thus become dissipative [103, 104]. These "quasi-helical" edge states have been theoretically predicted and are highly likely to survive in our 11-QL-thick CBST1 device. We suspect that the slope of the magnetoresistance in the fully-magnetised regime may arise from the H-field dependent behaviour of these quasi-helical edge states.

To test our hypothesis, we performed high magnetic field sweeps up to $\mu_0 H = 10$ T, and observed a slope change in the magnetoresistance between $\mu_0 H = 2.5$ T and 3 T, denoted by the transition magnetic field H^*. A similar behaviour was previously observed by Kou *et al.* on a 10 QL magnetic TI film [104], but was absent in all the measurements on thinner magnetic TI films reported so far. This reinforces our argument about the dissipative quasi-helical states on the side surface. Based on this observation, we speculate that the most likely reason of this slope change is a transition between different dominant dissipation mechanisms. We employ a theoretical model constructed by Wang *et al.* to explain this phenomenon [103] and calculate the possible mean free path in our system to be $l_{\mathrm{mfp}} \sim 20$ nm.

Due to the discovery of the slope change in magnetoresistance in the high magnetic field regime, we took a series of magnetic field sweeps up to $\mu_0 H = \pm 5$ T at different T_s. We observed that H^* initially appears at $\mu_0 H \sim 2.5$ T and its position does not change when $T_s \leq 50$ mK, but starts to shift toward $\mu_0 H = 0$ T after $T_s \geq 100$ mK. According to our analysis, this is mainly due to the increasing number of diffusive conducting channels at higher temperatures that can short the quasi-helical states.

Therefore, the magnetic field dependence of ρ_{xx} and ρ_{xy} should be always treated as an outcome of the mixed dissipative edge and bulk conduction on top of the chiral edge transport. Beyond H^*, the residual dissipation mostly comes from bulk states, which can be localised by a strong magnetic field and lead to the decreasing ρ_{xx} with increasing $\mu_0 H$ in the high field regime. On the other hand, below H^* (except for the coercive-peak regime), the residual dissipation is dominated by quasi-helical edge states which also have a magnetic-field dependent backscattering behaviour but will start to be suppressed after $l_B < l_{\mathrm{mfp}}$. The transition between these two dissipation scenarios then results in the kink structure at H^* in the magnetic field sweeps.

The E_a extracted from the magnetic field sweeps at different T_s exhibits a magnetic field dependence as well, ranging from 35.0 μeV ($\sim$ 405 mK) at $\mu_0 H = 0$ T to 16.2 μeV ($\sim$ 188 mK) at $\mu_0 H = \pm 5$ T. This change of magnetic field dependence of E_a agrees with the

position of H^*, implying that it may also result from the shift between different dominant dissipation mechanisms in the QAH regime. Moreover, the fact that CBST1 does not leave the QAH regime even at $T_s = 507$ mK implies that the magnetic gap should be at least larger than 43.7 μeV.

In addition, our analysis of the T_s dependence suggests that the electron temperature T_e differs from the sample temperature T_s. By further measurements focused on the current-dependence of transport properties, we confirm the influence of Joule heating to the measured resistance of CBST1, which is more prominent in the experiments with low T_s and high I_{DC} conditions. The lowest possible T_e inferred from our measurements is found to be proportional to I_{DC}.

In conclusion, although the quality of CBST1 is not ideal and the Fermi level cannot be tuned to the Dirac point, we show that such an imperfect system can still be useful for studying the interplay between chiral edge states and residual bulk states, mid-gap states as well as non-chiral edge states in magnetic TI samples. Since the source of dissipation in the QAHE has always been an issue of discussion, we hope our experiments can provide useful information for further studies investigating the dissipation mechanism in the QAHE and raising the observable temperature of the QAHE in the future.

Chapter 7

Conclusions

In this thesis, we study the carrier transport behaviour in two different magnetic TI materials, V-BST and Cr-BST. We were unable to observe the QAH states in the V-BST samples by either transport or SPM measurements. The complex interactions between the spin and electronic systems immensely increase the difficulty of quantitative analysis. At about the same time as our experiments, successful observations of domain structures in magnetic TI samples were reported by other groups [135–137]. However, these observations were made on thicker samples that did not show the QAHE. Hence, imaging the domain distribution and motion in the QAH regime remains to be a challenge. In addition, our another goal, the visualisation of the QAH states using SPM techniques, has not been reported by any groups thus far. The poor surface condition of the scratched devices and heating caused by the scanning motion seriously obstructed our SPM experiments at fridge temperatures. These problems are probably also faced by other groups.

For the Cr-BST sample, we observe a QAHE with a non-vanishing longitudinal resistance $\sim 0.0667\ h/e^2$, suggesting the presence of many dissipative conducting channels. While most of the works about the QAHE focus on the properties of chiral edge states, only a small number of studies are dedicated to the research of dissipative states in the QAHE. We believe that the understanding towards the behaviour of dissipative states is essential for achieving a better QAHE and increasing its critical temperature.

The core of these problems is the quality of magnetic TI materials. Only by improving the quality of magnetic TI samples can a system with larger magnetic gap and less bulk and impurity states be attained. A film like this will exhibit the QAHE at higher temperatures and be more robust to the contamination and doping from the environment and lithographic processes, making the experimental conditions for observing the QAHE less demanding.

There are several future directions for our experiments. Firstly, the development of a lithographic fabrication recipe can significantly improve the surface condition of the devices,

which will be extremely helpful to all kinds of SPM techniques that have been used in this thesis. Secondly, our magnetic TI samples are prepared by collaborators in the Pennsylvania State University. We always found that the property of samples changed considerably after being sent to our lab. The QAHE was observed right after the sample growth, but could not be observed by the time the samples arrived at the Cavendish Laboratory. Thus, a better protection to prevent the magnetic TI samples from degradation during the shipping process is absolutely necessary.

In terms of other possible experiments, it has recently been reported that the "axion insulator" can be realised in magnetic TI heterostructures [142, 143]. The axion insulator phase is expected to serve as a platform for studying the topological magnetoelectric (TME) effect caused by the coupling between the magnetisation and electric polarisation in materials [82, 148, 155–157]. The axion insulator is a new topological phase in which the 2D surface states are gapped while the 3D bulk remains to be topologically non-trivial. This condition can be satisfied when an un-doped TI layer is sandwiched by two compositionally different magnetic TI layers with different coercive field values under magnetic fields. Remarkably, the magnetic TI heterostructure used in the measurements in Chapter 6 has a similar stack structure, except that the top and bottom magnetic TI layers are both Cr-BST. If one of the magnetic TI layers is replaced by V-BST, then the difference in the coercive field between them should be large enough to allow the axion insulator phase to exist, and provide us with a system for exploring the physics related to the TME effect.

Finally, it has been predicted that a chiral topological superconductor can be realised in a hybrid device of a QAH insulator and a superconductor [39, 158, 159]. The chiral topological superconductor can accommodate the Majorana zero mode at the vortex core or the sample edge [160, 161], and can be used for fault-tolerant topological quantum computing. Majorana fermions are exotic particles that are their own antiparticles [162], and have been studied for decades in high-energy physics but have not yet been definitely observed [163]. Therefore, the realisation of Majorana fermions as composite particles in condensed matter physics will allow physicists to study their behaviour and engineer the non-Abelian braiding, paving the way for the future application in topological quantum computation [164]. The study of QAH insulator/topological superconductor hybrid devices thus is not only important for fundamental research but also useful for developing quantum computing applications.

References

[1] K. v. Klitzing, G. Dorda, and M. Pepper. New method for high-accuracy determination of the fine-structure constant based on quantized Hall resistance. *Physical Review Letters*, 45:494–497, 1980.

[2] K. S. Novoselov, Z. Jiang, Y. Zhang, S. V. Morozov, H. L. Stormer, U. Zeitler, J. C. Maan, G. S. Boebinger, P. Kim, and A. K. Geim. Room-temperature quantum Hall effect in graphene. *Science*, 315(5817):1379–1379, 2007.

[3] C. C. Finlay, S. Maus, C. D. Beggan, T. N. Bondar, A. Chambodut, T. A. Chernova, A. Chulliat, V. P. Golovkov, B. Hamilton, M. Hamoudi, R. Holme, G. Hulot, W. Kuang, B. Langlais, V. Lesur, F. J. Lowes, H. Lühr, S. Macmillan, M. Mandea, S. McLean, C. Manoj, M. Menvielle, I. Michaelis, N. Olsen, J. Rauberg, M. Rother, T. J. Sabaka, A. Tangborn, L. Tøffner-Clausen, E. Thébault, A. W. P. Thomson, I. Wardinski, Z. Wei, and T. I. Zvereva. International geomagnetic reference field: the eleventh generation. *Geophysical Journal International*, 183(3):1216–1230, 2010.

[4] M. König, S. Wiedmann, C. Brüne, A. Roth, H. Buhmann, L. W. Molenkamp, X.-L. Qi, and S.-C. Zhang. Quantum spin Hall insulator state in HgTe quantum wells. *Science*, 318(5851):766–770, 2007.

[5] N. W. Ashcroft and N. D. Mermin. *Solid State Physics*. Brooks/Cole, Cengage Learning, 1976.

[6] R. Landauer. Spatial variation of currents and fields due to localized scatterers in metallic conduction. *IBM Journal of Research and Development*, 1(3):223–231, 1957.

[7] M. Büttiker. Four-terminal phase-coherent conductance. *Physical Review Letters*, 57:1761–1764, 1986.

[8] M. Büttiker. Absence of backscattering in the quantum Hall effect in multiprobe conductors. *Physical Review B*, 38(14):9375, 1988.

[9] L. D. Landau. Zur theorie der phasenumwandlungen II. *Physikalische Zeitschrift der Sowjetunion*, 11(545):26–35, 1937.

[10] R. E. Peierls. Quelques propriétés typiques des corps solides. *Annales de l'institut Henri Poincaré*, 5:177–222, 1935.

[11] J. M. Kosterlitz and D. J. Thouless. Ordering, metastability and phase transitions in two-dimensional systems. *Journal of Physics C: Solid State Physics*, 6(7):1181–1203, 1973.

[12] D. J. Thouless, M. Kohmoto, M. P. Nightingale, and M. den Nijs. Quantized Hall conductance in a two-dimensional periodic potential. *Physical Review Letters*, 49:405–408, 1982.

[13] F. D. M. Haldane. Model for a quantum Hall effect without Landau levels: condensed-matter realization of the "parity anomaly". *Physical Review Letters*, 61:2015–2018, 1988.

[14] C. L. Kane and E. J. Mele. Z_2 topological order and the quantum spin Hall effect. *Physical Review Letters*, 95:146802, 2005.

[15] C. L. Kane and E. J. Mele. Quantum spin Hall effect in graphene. *Physical Review Letters*, 95:226801, 2005.

[16] Liang Fu, C. L. Kane, and E. J. Mele. Topological insulators in three dimensions. *Physical Review Letters*, 98:106803, 2007.

[17] J. E. Moore and L. Balents. Topological invariants of time-reversal-invariant band structures. *Physical Review B*, 75:121306, 2007.

[18] Rahul Roy. Z_2 classification of quantum spin Hall systems: An approach using time-reversal invariance. *Physical Review B*, 79:195321, 2009.

[19] Rahul Roy. Topological phases and the quantum spin Hall effect in three dimensions. *Physical Review B*, 79:195322, 2009.

[20] D. Hsieh, D. Qian, L. Wray, Y. Xia, Y. S. Hor, R. J. Cava, and M. Z. Hasan. A topological Dirac insulator in a quantum spin Hall phase. *Nature*, 452:970–974, 2008.

[21] E. H. Hall. On a new action of the magnet on electric currents. *American Journal of Mathematics*, 2(3):287–292, 1879.

[22] R. Landauer. Conductance from transmission: common sense points. *Physica Scripta*, 1992(T42):110, 1992.

[23] Klaus von Klitzing. Developments in the quantum Hall effect. *Philosophical Transactions of the Royal Society A*, 363(1834):2203–2219, 2005.

[24] R. B. Laughlin. Quantized Hall conductivity in two dimensions. *Physical Review B*, 23:5632–5633, 1981.

[25] Y. Aharonov and D. Bohm. Significance of electromagnetic potentials in the quantum theory. *Physical Review*, 115:485–491, 1959.

[26] Daijiro Yoshioka. *The Quantum Hall Effect*. Springer, 1998.

[27] Ryogo Kubo. Statistical-mechanical theory of irreversible processes. I. general theory and simple applications to magnetic and conduction problems. *Journal of the Physical Society of Japan*, 12(6):570–586, 1957.

[28] R. Kubo. The fluctuation-dissipation theorem. *Reports on Progress in Physics*, 29(1):255, 1966.

[29] Joseph E. Avron and Ruedi Seiler. Quantization of the Hall conductance for general, multiparticle Schrödinger Hamiltonians. *Physical Review Letters*, 54:259–262, 1985.

[30] Qian Niu, D. J. Thouless, and Yong-Shi Wu. Quantized Hall conductance as a topological invariant. *Physical Review B*, 31:3372–3377, 1985.

[31] Qian Niu and D. J. Thouless. Quantum Hall effect with realistic boundary conditions. *Physical Review B*, 35:2188–2197, 1987.

[32] David J. Thouless. *The Topological Quantum Numbers in Nonrelativistic Physics*. World Scientific Publishing Company, 1998.

[33] Michael Victor Berry. Quantal phase factors accompanying adiabatic changes. *Proceedings of the Royal Society of London. Series A*, 392(1802):45–57, 1984.

[34] K. S. Novoselov, A. K. Geim, S. V. Morozov, D. Jiang, Y. Zhang, S. V. Dubonos, I. V. Grigorieva, and A. A. Firsov. Electric field effect in atomically thin carbon films. *Science*, 306(5696):666–669, 2004.

[35] Hans Peter Boehm, Ralph Setton, and Eberhard Stumpp. Nomenclature and terminology of graphite intercalation compounds. *Pure and Applied Chemistry*, 66(9):1893–1901, 1994.

[36] A. H. Castro Neto, F. Guinea, N. M. R. Peres, K. S. Novoselov, and A. K. Geim. The electronic properties of graphene. *Reviews of Modern Physics*, 81:109–162, 2009.

[37] Edward McCann. Electronic properties of monolayer and bilayer graphene. In *Graphene Nanoelectronics*, NanoScience and Technology, pages 237–275. Springer Verlag, 2012.

[38] C. W. J. Beenakker. Colloquium: Andreev reflection and Klein tunneling in graphene. *Reviews of Modern Physics*, 80:1337–1354, 2008.

[39] M. Z. Hasan and C. L. Kane. Colloquium: Topological insulators. *Reviews of Modern Physics*, 82:3045–3067, 2010.

[40] Congjun Wu, B. Andrei Bernevig, and Shou-Cheng Zhang. Helical liquid and the edge of quantum spin Hall systems. *Physical Review Letters*, 96:106401, 2006.

[41] Xiao-Liang Qi and Shou-Cheng Zhang. The quantum spin Hall effect and topological insulators. *Physics Today*, 63:33–38, 2010.

[42] Joseph Maciejko, Taylor L. Hughes, and Shou-Cheng Zhang. The quantum spin Hall effect. *Annual Review of Condensed Matter Physics*, 2(1):31–53, 2011.

[43] Hongki Min, J. E. Hill, N. A. Sinitsyn, B. R. Sahu, Leonard Kleinman, and A. H. MacDonald. Intrinsic and Rashba spin-orbit interactions in graphene sheets. *Physical Review B*, 74:165310, 2006.

[44] Yugui Yao, Fei Ye, Xiao-Liang Qi, Shou-Cheng Zhang, and Zhong Fang. Spin-orbit gap of graphene: First-principles calculations. *Physical Review B*, 75:041401, 2007.

[45] B. Andrei Bernevig and Shou-Cheng Zhang. Quantum spin Hall effect. *Physical Review Letters*, 96:106802, 2006.

[46] B. Andrei Bernevig, Taylor L. Hughes, and Shou-Cheng Zhang. Quantum spin Hall effect and topological phase transition in HgTe quantum wells. *Science*, 314(5806):1757–1761, 2006.

[47] Markus König, Hartmut Buhmann, Laurens W. Molenkamp, Taylor Hughes, Chao-Xing Liu, Xiao-Liang Qi, and Shou-Cheng Zhang. The quantum spin Hall effect: Theory and experiment. *Journal of the Physical Society of Japan*, 77(3):031007, 2008.

[48] Andreas Roth, Christoph Brüne, Hartmut Buhmann, Laurens W. Molenkamp, Joseph Maciejko, Xiao-Liang Qi, and Shou-Cheng Zhang. Nonlocal transport in the quantum spin Hall state. *Science*, 325(5938):294–297, 2009.

[49] Bertrand I. Halperin. Possible states for a three-dimensional electron gas in a strong magnetic field. *Japanese Journal of Applied Physics*, 26(S3-3):1913, 1987.

[50] Mahito Kohmoto, Bertrand I. Halperin, and Yong-Shi Wu. Diophantine equation for the three-dimensional quantum Hall effect. *Physical Review B*, 45:13488–13493, 1992.

[51] A.-Z. Ezzine de Blas and F. Axel. Diophantine equation for the 3D transport coefficients of Bloch electrons in a strong tilted magnetic field with quantum Hall effect. *Journal of Physics: Condensed Matter*, 16(43):7673–7708, 2004.

[52] Liang Fu and C. L. Kane. Topological insulators with inversion symmetry. *Physical Review B*, 76:045302, 2007.

[53] D. Hsieh, Y. Xia, L. Wray, D. Qian, A. Pal, J. H. Dil, J. Osterwalder, F. Meier, G. Bihlmayer, C. L. Kane, Y. S. Hor, R. J. Cava, and M. Z. Hasan. Observation of unconventional quantum spin textures in topological insulators. *Science*, 323(5916):919–922, 2009.

[54] Pedram Roushan, Jungpil Seo, Colin V. Parker, Y. S. Hor, D. Hsieh, Dong Qian, Anthony Richardella, M. Z. Hasan, R. J. Cava, and Ali Yazdani. Topological surface states protected from backscattering by chiral spin texture. *Nature*, 460:1106, 2009.

[55] Haijun Zhang, Chao-Xing Liu, Xiao-Liang Qi, Xi Dai, Zhong Fang, and Shou-Cheng Zhang. Topological insulators in Bi_2Se_3, Bi_2Te_3 and Sb_2Te_3 with a single Dirac cone on the surface. *Nature Physics*, 5:438, 2009.

[56] Y. Xia, D. Qian, D. Hsieh, L. Wray, A. Pal, H. Lin, A. Bansil, D. Grauer, Y. S. Hor, R. J. Cava, and M. Z. Hasan. Observation of a large-gap topological-insulator class with a single Dirac cone on the surface. *Nature Physics*, 5:398, 2009.

[57] Y. S. Hor, A. Richardella, P. Roushan, Y. Xia, J. G. Checkelsky, A. Yazdani, M. Z. Hasan, N. P. Ong, and R. J. Cava. *p*-type Bi_2Se_3 for topological insulator and low-temperature thermoelectric applications. *Physical Review B*, 79:195208, 2009.

[58] D. Hsieh, Y. Xia, D. Qian, L. Wray, J. H. Dil, F. Meier, J. Osterwalder, L. Patthey, J. G. Checkelsky, N. P. Ong, A. V. Fedorov, H. Lin, A. Bansil, D. Grauer, Y. S. Hor, R. J. Cava, and M. Z. Hasan. A tunable topological insulator in the spin helical Dirac transport regime. *Nature*, 460:1101, 2009.

[59] S. R. Park, W. S. Jung, Chul Kim, D. J. Song, C. Kim, S. Kimura, K. D. Lee, and N. Hur. Quasiparticle scattering and the protected nature of the topological states in a parent topological insulator Bi_2Se_3. *Physical Review B*, 81:041405, 2010.

[60] D. Hsieh, Y. Xia, D. Qian, L. Wray, F. Meier, J. H. Dil, J. Osterwalder, L. Patthey, A. V. Fedorov, H. Lin, A. Bansil, D. Grauer, Y. S. Hor, R. J. Cava, and M. Z. Hasan. Observation of time-reversal-protected single-Dirac-cone topological-insulator states in Bi_2Te_3 and Sb_2Te_3. *Physical Review Letters*, 103:146401, 2009.

[61] Y. L. Chen, J. G. Analytis, J.-H. Chu, Z. K. Liu, S.-K. Mo, X. L. Qi, H. J. Zhang, D. H. Lu, X. Dai, Z. Fang, S. C. Zhang, I. R. Fisher, Z. Hussain, and Z.-X. Shen. Experimental realization of a three-dimensional topological insulator, Bi_2Te_3. *Science*, 325(5937):178–181, 2009.

[62] Y. L. Chen, J.-H. Chu, J. G. Analytis, Z. K. Liu, K. Igarashi, H.-H. Kuo, X. L. Qi, S. K. Mo, R. G. Moore, D. H. Lu, M. Hashimoto, T. Sasagawa, S. C. Zhang, I. R. Fisher, Z. Hussain, and Z. X. Shen. Massive Dirac fermion on the surface of a magnetically doped topological insulator. *Science*, 329(5992):659–662, 2010.

[63] Hailin Peng, Keji Lai, Desheng Kong, Stefan Meister, Yulin Chen, Xiao-Liang Qi, Shou-Cheng Zhang, Zhi-Xun Shen, and Yi Cui. Aharonov-Bohm interference in topological insulator nanoribbons. *Nature Materials*, 9:225, 2009.

[64] Dong-Xia Qu, Y. S. Hor, Jun Xiong, R. J. Cava, and N. P. Ong. Quantum oscillations and Hall anomaly of surface states in the topological insulator Bi_2Te_3. *Science*, 329(5993):821–824, 2010.

[65] James G. Analytis, Ross D. McDonald, Scott C. Riggs, Jiun-Haw Chu, G. S. Boebinger, and Ian R. Fisher. Two-dimensional surface state in the quantum limit of a topological insulator. *Nature Physics*, 6:960, 2010.

[66] Faxian Xiu, Nicholas Meyer, Xufeng Kou, Liang He, Murong Lang, Yong Wang, Xinxin Yu, Alexei V. Fedorov, Jin Zou, and Kang L. Wang. Quantum capacitance in topological insulators. *Scientific Reports*, 2:669, 2012.

[67] Benjamin Sacépé, Jeroen B. Oostinga, Jian Li, Alberto Ubaldini, Nuno J. G. Couto, Enrico Giannini, and Alberto F. Morpurgo. Gate-tuned normal and superconducting transport at the surface of a topological insulator. *Nature Communications*, 2:575, 2011.

[68] J. G. Checkelsky, Y. S. Hor, R. J. Cava, and N. P. Ong. Bulk band gap and surface state conduction observed in voltage-tuned crystals of the topological insulator Bi_2Se_3. *Physical Review Letters*, 106:196801, 2011.

[69] Bin Xia, Peng Ren, Azat Sulaev, Peng Liu, Shun-Qing Shen, and Lan Wang. Indications of surface-dominated transport in single crystalline nanoflake devices of topological insulator $Bi_{1.5}Sb_{0.5}Te_{1.8}Se_{1.2}$. *Physical Review B*, 87:085442, 2013.

[70] E. H. Hall. On the "rotational coefficient" in nickel and cobalt. *The London, Edinburgh, and Dublin Philosophical Magazine and Journal of Science*, 12(74):157–172, 1881.

[71] Y. K. Kato, R. C. Myers, A. C. Gossard, and D. D. Awschalom. Observation of the spin Hall effect in semiconductors. *Science*, 306(5703):1910–1913, 2004.

[72] J. Wunderlich, B. Kaestner, J. Sinova, and T. Jungwirth. Experimental observation of the spin-Hall effect in a two-dimensional spin-orbit coupled semiconductor system. *Physical Review Letters*, 94:047204, 2005.

[73] Chao-Xing Liu, Xiao-Liang Qi, Xi Dai, Zhong Fang, and Shou-Cheng Zhang. Quantum anomalous Hall effect in $Hg_{1-y}Mn_yTe$ quantum wells. *Physical Review Letters*, 101:146802, 2008.

[74] Chao-Xing Liu, Shou-Cheng Zhang, and Xiao-Liang Qi. The quantum anomalous Hall effect: Theory and experiment. *Annual Review of Condensed Matter Physics*, 7(1):301–321, 2016.

[75] Rui Yu, Wei Zhang, Hai-Jun Zhang, Shou-Cheng Zhang, Xi Dai, and Zhong Fang. Quantized anomalous Hall effect in magnetic topological insulators. *Science*, 329(5987):61–64, 2010.

[76] Joseph G. Checkelsky, Jianting Ye, Yoshinori Onose, Yoshihiro Iwasa, and Yoshinori Tokura. Dirac-fermion-mediated ferromagnetism in a topological insulator. *Nature Physics*, 8:729, 2012.

[77] Xufeng Kou, Yabin Fan, Murong Lang, Pramey Upadhyaya, and Kang L. Wang. Magnetic topological insulators and quantum anomalous Hall effect. *Solid State Communications*, 215-216:34 – 53, 2015.

[78] Jing Wang, Biao Lian, Haijun Zhang, Yong Xu, and Shou-Cheng Zhang. Quantum anomalous Hall effect with higher plateaus. *Physical Review Letters*, 111:136801, 2013.

[79] Jacob Linder, Takehito Yokoyama, and Asle Sudbø. Anomalous finite size effects on surface states in the topological insulator Bi_2Se_3. *Physical Review B*, 80:205401, 2009.

[80] Chao-Xing Liu, HaiJun Zhang, Binghai Yan, Xiao-Liang Qi, Thomas Frauenheim, Xi Dai, Zhong Fang, and Shou-Cheng Zhang. Oscillatory crossover from two-dimensional to three-dimensional topological insulators. *Physical Review B*, 81:041307, 2010.

[81] Hai-Zhou Lu, Wen-Yu Shan, Wang Yao, Qian Niu, and Shun-Qing Shen. Massive Dirac fermions and spin physics in an ultrathin film of topological insulator. *Physical Review B*, 81:115407, 2010.

[82] Xiao-Liang Qi, Taylor L. Hughes, and Shou-Cheng Zhang. Topological field theory of time-reversal invariant insulators. *Physical Review B*, 78:195424, 2008.

[83] Yang Xu, Ireneusz Miotkowski, Chang Liu, Jifa Tian, Hyoungdo Nam, Nasser Alidoust, Jiuning Hu, Chih-Kang Shih, M. Zahid Hasan, and Yong P. Chen. Observation of topological surface state quantum Hall effect in an intrinsic three-dimensional topological insulator. *Nature Physics*, 10:956, 2014.

[84] K. S. Novoselov, A. K. Geim, S. V. Morozov, D. Jiang, M. I. Katsnelson, I. V. Grigorieva, S. V. Dubonos, and A. A. Firsov. Two-dimensional gas of massless Dirac fermions in graphene. *Nature*, 438(7065):197–200, 2005.

[85] Yuanbo Zhang, Yan-Wen Tan, Horst L. Stormer, and Philip Kim. Experimental observation of the quantum Hall effect and Berry's phase in graphene. *Nature*, 438(7065):201–204, 2005.

[86] Peng Wei, Ferhat Katmis, Badih A. Assaf, Hadar Steinberg, Pablo Jarillo-Herrero, Donald Heiman, and Jagadeesh S. Moodera. Exchange-coupling-induced symmetry breaking in topological insulators. *Physical Review Letters*, 110:186807, 2013.

[87] Qi I. Yang, Merav Dolev, Li Zhang, Jinfeng Zhao, Alexander D. Fried, Elizabeth Schemm, Min Liu, Alexander Palevski, Ann F. Marshall, Subhash H. Risbud, and Aharon Kapitulnik. Emerging weak localization effects on a topological insulator–insulating ferromagnet (Bi_2Se_3-EuS) interface. *Physical Review B*, 88:081407, 2013.

[88] Murong Lang, Mohammad Montazeri, Mehmet C. Onbasli, Xufeng Kou, Yabin Fan, Pramey Upadhyaya, Kaiyuan Yao, Frank Liu, Ying Jiang, Wanjun Jiang, Kin L. Wong, Guoqiang Yu, Jianshi Tang, Tianxiao Nie, Liang He, Robert N. Schwartz, Yong Wang, Caroline A. Ross, and Kang L. Wang. Proximity induced high-temperature magnetic order in topological insulator - ferrimagnetic insulator heterostructure. *Nano Letters*, 14(6):3459–3465, 2014.

[89] Zilong Jiang, Cui-Zu Chang, Chi Tang, Peng Wei, Jagadeesh S. Moodera, and Jing Shi. Independent tuning of electronic properties and induced ferromagnetism in topological insulators with heterostructure approach. *Nano Letters*, 15(9):5835–5840, 2015.

[90] Jinsong Zhang, Cui-Zu Chang, Zuocheng Zhang, Jing Wen, Xiao Feng, Kang Li, Minhao Liu, Ke He, Lili Wang, Xi Chen, Qi-Kun Xue, Xucun Ma, and Yayu Wang. Band structure engineering in $(Bi_{1-x}Sb_x)_2Te_3$ ternary topological insulators. *Nature Communications*, 2:574, 2011.

[91] Jinsong Zhang, Cui-Zu Chang, Peizhe Tang, Zuocheng Zhang, Xiao Feng, Kang Li, Li-li Wang, Xi Chen, Chaoxing Liu, Wenhui Duan, Ke He, Qi-Kun Xue, Xucun Ma, and Yayu Wang. Topology-driven magnetic quantum phase transition in topological insulators. *Science*, 339(6127):1582–1586, 2013.

[92] Cui-Zu Chang, Jinsong Zhang, Minhao Liu, Zuocheng Zhang, Xiao Feng, Kang Li, Li-Li Wang, Xi Chen, Xi Dai, Zhong Fang, Xiao-Liang Qi, Shou-Cheng Zhang, Yayu Wang, Ke He, Xu-Cun Ma, and Qi-Kun Xue. Thin films of magnetically doped topological insulator with carrier-independent long-range ferromagnetic order. *Advanced Materials*, 25(7):1065–1070, 2013.

[93] Cui-Zu Chang, Jinsong Zhang, Xiao Feng, Jie Shen, Zuocheng Zhang, Minghua Guo, Kang Li, Yunbo Ou, Pang Wei, Li-Li Wang, Zhong-Qing Ji, Yang Feng, Shuaihua Ji, Xi Chen, Jinfeng Jia, Xi Dai, Zhong Fang, Shou-Cheng Zhang, Ke He, Yayu Wang, Li Lu, Xu-Cun Ma, and Qi-Kun Xue. Experimental observation of the quantum anomalous Hall effect in a magnetic topological insulator. *Science*, 340(6129):167–170, 2013.

[94] Xufeng Kou, Murong Lang, Yabin Fan, Ying Jiang, Tianxiao Nie, Jianmin Zhang, Wanjun Jiang, Yong Wang, Yugui Yao, Liang He, and Kang L. Wang. Interplay between different magnetisms in Cr-doped topological insulators. *ACS Nano*, 7(10):9205–9212, 2013.

[95] Cui-Zu Chang, Peizhe Tang, Yi-Lin Wang, Xiao Feng, Kang Li, Zuocheng Zhang, Yayu Wang, Li-Li Wang, Xi Chen, Chaoxing Liu, Wenhui Duan, Ke He, Xu-Cun Ma, and Qi-Kun Xue. Chemical-potential-dependent gap opening at the Dirac surface states of Bi_2Se_3 induced by aggregated substitutional Cr atoms. *Physical Review Letters*, 112:056801, 2014.

[96] Yi Zhang, Ke He, Cui-Zu Chang, Can-Li Song, Li-Li Wang, Xi Chen, Jin-Feng Jia, Zhong Fang, Xi Dai, Wen-Yu Shan, Shun-Qing Shen, Qian Niu, Xiao-Liang Qi, Shou-Cheng Zhang, Xu-Cun Ma, and Qi-Kun Xue. Crossover of the three-dimensional topological insulator Bi_2Se_3 to the two-dimensional limit. *Nature Physics*, 6:584, 2010.

[97] Cui-Zu Chang, Ke He, Li-Li Wang, Xu-Cun Ma, Min-Hao Liu, Zuo-Cheng Zhang, Xi Chen, Ya-Yu Wang, and Qi-Kun Xue. Growth of quantum well films of topological insulator Bi_2Se_3 on insulating substrate. *Spin*, 01(01):21–25, 2011.

[98] J. Chen, H. J. Qin, F. Yang, J. Liu, T. Guan, F. M. Qu, G. H. Zhang, J. R. Shi, X. C. Xie, C. L. Yang, K. H. Wu, Y. Q. Li, and L. Lu. Gate-voltage control of chemical potential and weak antilocalization in Bi_2Se_3. *Physical Review Letters*, 105:176602, 2010.

[99] Yao-Yi Li, Guang Wang, Xie-Gang Zhu, Min-Hao Liu, Cun Ye, Xi Chen, Ya-Yu Wang, Ke He, Li-Li Wang, Xu-Cun Ma, Hai-Jun Zhang, Xi Dai, Zhong Fang, Xin-Cheng Xie, Ying Liu, Xiao-Liang Qi, Jin-Feng Jia, Shou-Cheng Zhang, and Qi-Kun Xue. Intrinsic topological insulator Bi_2Te_3 thin films on Si and their thickness limit. *Advanced Materials*, 22(36):4002–4007, 2010.

[100] Yeping Jiang, Yilin Wang, Mu Chen, Zhi Li, Canli Song, Ke He, Lili Wang, Xi Chen, Xucun Ma, and Qi-Kun Xue. Landau quantization and the thickness limit of topological insulator thin films of Sb_2Te_3. *Physical Review Letters*, 108:016401, 2012.

[101] A. J. Bestwick, E. J. Fox, Xufeng Kou, Lei Pan, Kang L. Wang, and D. Goldhaber-Gordon. Precise quantization of the anomalous Hall effect near zero magnetic field. *Physical Review Letters*, 114:187201, 2015.

[102] S. Grauer, S. Schreyeck, M. Winnerlein, K. Brunner, C. Gould, and L. W. Molenkamp. Coincidence of superparamagnetism and perfect quantization in the quantum anomalous Hall state. *Physical Review B*, 92:201304, 2015.

[103] Jing Wang, Biao Lian, Haijun Zhang, and Shou-Cheng Zhang. Anomalous edge transport in the quantum anomalous Hall state. *Physical Review Letters*, 111:086803, 2013.

[104] Xufeng Kou, Shih-Ting Guo, Yabin Fan, Lei Pan, Murong Lang, Ying Jiang, Qiming Shao, Tianxiao Nie, Koichi Murata, Jianshi Tang, Yong Wang, Liang He, Ting-Kuo Lee, Wei-Li Lee, and Kang L. Wang. Scale-invariant quantum anomalous Hall effect in magnetic topological insulators beyond the two-dimensional limit. *Physical Review Letters*, 113:137201, 2014.

[105] J. G. Checkelsky, R. Yoshimi, A. Tsukazaki, K. S. Takahashi, Y. Kozuka, J. Falson, M. Kawasaki, and Y. Tokura. Trajectory of the anomalous Hall effect towards the quantized state in a ferromagnetic topological insulator. *Nature Physics*, 10:731, 2014.

[106] Cui-Zu Chang, Weiwei Zhao, Duk Y. Kim, Haijun Zhang, Badih A. Assaf, Don Heiman, Shou-Cheng Zhang, Chaoxing Liu, Moses H. W. Chan, and Jagadeesh S. Moodera. High-precision realization of robust quantum anomalous Hall state in a hard ferromagnetic topological insulator. *Nature Materials*, 14:473, 2015.

[107] Cui-Zu Chang, Weiwei Zhao, Duk Y. Kim, Peng Wei, J. K. Jain, Chaoxing Liu, Moses H. W. Chan, and Jagadeesh S. Moodera. Zero-field dissipationless chiral edge transport and the nature of dissipation in the quantum anomalous Hall state. *Physical Review Letters*, 115:057206, 2015.

[108] Minhao Liu, Wudi Wang, Anthony R. Richardella, Abhinav Kandala, Jian Li, Ali Yazdani, Nitin Samarth, and N. Phuan Ong. Large discrete jumps observed in the transition between Chern states in a ferromagnetic topological insulator. *Science Advances*, 2(7), 2016.

[109] Minoru Kawamura, Ryutaro Yoshimi, Atsushi Tsukazaki, Kei S. Takahashi, Masashi Kawasaki, and Yoshinori Tokura. Current-driven instability of the quantum anomalous Hall effect in ferromagnetic topological insulators. *Physical Review Letters*, 119:016803, 2017.

[110] E. J. Fox, I. T. Rosen, Yanfei Yang, George R. Jones, Randolph E. Elmquist, Xufeng Kou, Lei Pan, Kang L. Wang, and D. Goldhaber-Gordon. Part-per-million quantization and current-induced breakdown of the quantum anomalous Hall effect. *Physical Review B*, 98:075145, 2018.

[111] B. Jeckelmann and B. Jeanneret. The quantum Hall effect as an electrical resistance standard. *Reports on Progress in Physics*, 64(12):1603–1655, 2001.

[112] G. Binnig, H. Rohrer, Ch. Gerber, and E. Weibel. Surface studies by scanning tunneling microscopy. *Physical Review Letters*, 49:57–61, 1982.

[113] G. Binnig, C. F. Quate, and Ch. Gerber. Atomic force microscope. *Physical Review Letters*, 56:930–933, 1986.

[114] R. Wiesendanger. *Scanning Probe Microscopy and Spectroscopy: Methods and Applications*. Cambridge University Press, 1994.

[115] J. E. Lennard-Jones and S. Chapman. On the determination of molecular fields. –II. from the equation of state of a gas. *Proceedings of the Royal Society of London. Series A*, 106(738):463–477, 1924.

[116] J. E. Lennard-Jones. Cohesion. *Proceedings of the Physical Society*, 43(5):461–482, 1931.

[117] Laura Fumagalli, Daniel Esteban-Ferrer, Ana Cuervo, Jose L. Carrascosa, and Gabriel Gomila. Label-free identification of single dielectric nanoparticles and viruses with ultraweak polarization forces. *Nature Materials*, 11:808, 2012.

[118] Theodore G. Goodson. *Solar fuels : materials, physics, and applications*. CRC Press, 2017.

[119] Wilhelm Melitz, Jian Shen, Andrew C. Kummel, and Sangyeob Lee. Kelvin probe force microscopy and its application. *Surface Science Reports*, 66(1):1 – 27, 2011.

[120] H. Sellier, B. Hackens, M. G. Pala, F. Martins, S. Baltazar, X. Wallart, L. Desplanque, V. Bayot, and S. Huant. On the imaging of electron transport in semiconductor quantum structures by scanning-gate microscopy: successes and limitations. *Semiconductor Science and Technology*, 26(6):064008, 2011.

[121] Ziwei Dou. *Investigation on High-Mobility Graphene Hexagon Boron Nitride Heterostructure Nano-devices Using Low Temperature Scanning Probe Microscopy*. PhD thesis, University of Cambridge, Department of Physics, 2018.

[122] M. A. Topinka, B. J. LeRoy, R. M. Westervelt, S. E. J. Shaw, R. Fleischmann, E. J. Heller, K. D. Maranowski, and A. C. Gossard. Coherent branched flow in a two-dimensional electron gas. *Nature*, 410(6825):183–186, 2001.

[123] N. Paradiso, S. Heun, S. Roddaro, L.N. Pfeiffer, K.W. West, L. Sorba, G. Biasiol, and F. Beltram. Selective control of edge-channel trajectories by scanning gate microscopy. *Physica E: Low-dimensional Systems and Nanostructures*, 42(4):1038 – 1041, 2010.

[124] S. H. Tessmer, P. I. Glicofridis, R. C. Ashoori, L. S. Levitov, and M. R. Melloch. Subsurface charge accumulation imaging of a quantum Hall liquid. *Nature*, 392(6671):51–54, 1998.

[125] A. Yacoby, H. F. Hess, T. A. Fulton, L. N. Pfeiffer, and K. W. West. Electrical imaging of the quantum Hall state. *Solid State Communications*, 111(1):1–13, 1999.

[126] Kent L. McCormick, Michael T. Woodside, Mike Huang, Mingshaw Wu, Paul L. McEuen, Cem Duruoz, and J. S. Harris. Scanned potential microscopy of edge and bulk currents in the quantum Hall regime. *Physical Review B*, 59:4654–4657, 1999.

[127] A. Baumgartner, T. Ihn, K. Ensslin, K. Maranowski, and A. C. Gossard. Quantum Hall effect transition in scanning gate experiments. *Physical Review B*, 76:085316, 2007.

[128] Jun-Yi Ge, Vladimir N. Gladilin, Jacques Tempere, Cun Xue, Jozef T. Devreese, Joris Van de Vondel, Youhe Zhou, and Victor V. Moshchalkov. Nanoscale assembly of superconducting vortices with scanning tunnelling microscope tip. *Nature Communications*, 7:13880, 2016.

[129] A. M. Chang, H. D. Hallen, L. Harriott, H. F. Hess, H. L. Kao, J. Kwo, R. E. Miller, R. Wolfe, J. van der Ziel, and T. Y. Chang. Scanning Hall probe microscopy. *Applied Physics Letters*, 61(16):1974–1976, 1992.

[130] Christian Wickles and Wolfgang Belzig. Reflectionless transport of surface Dirac fermions on topological insulators with induced ferromagnetic domain walls. *Physical Review B*, 86:035151, 2012.

[131] Qinglei Meng, Smitha Vishveshwara, and Taylor L. Hughes. Topological insulator magnetic tunnel junctions: Quantum Hall effect and fractional charge via folding. *Physical Review Letters*, 109:176803, 2012.

[132] Takehito Yokoyama and Shuichi Murakami. Spintronics and spincaloritronics in topological insulators. *Physica E: Low-Dimensional Systems and Nanostructures*, 55, 2013.

[133] Murong Lang, Liang He, Faxian Xiu, Xinxin Yu, Jianshi Tang, Yong Wang, Xufeng Kou, Wanjun Jiang, Alexei V. Fedorov, and Kang L. Wang. Revelation of topological surface states in Bi_2Se_3 thin films by in situ Al passivation. *ACS Nano*, 6(1):295–302, 2012.

[134] Abhinav Kandala, Anthony Richardella, Susan Kempinger, Chao-Xing Liu, and Nitin Samarth. Giant anisotropic magnetoresistance in a quantum anomalous Hall insulator. *Nature Communications*, 6:7434, 2015.

[135] Wenbo Wang, Fang Yang, Chunlei Gao, Jinfeng Jia, G. D. Gu, and Weida Wu. Visualizing ferromagnetic domains in magnetic topological insulators. *APL Materials*, 3(8):083301, 2015.

[136] Ella O. Lachman, Andrea F. Young, Anthony Richardella, Jo Cuppens, H. R. Naren, Yonathan Anahory, Alexander Y. Meltzer, Abhinav Kandala, Susan Kempinger, Yuri Myasoedov, Martin E. Huber, Nitin Samarth, and Eli Zeldov. Visualization of superparamagnetic dynamics in magnetic topological insulators. *Science Advances*, 1(10), 2015.

[137] Wenbo Wang, Cui-Zu Chang, Jagadeesh S. Moodera, and Weida Wu. Visualizing ferromagnetic domain behavior of magnetic topological insulator thin films. *Npj Quantum Materials*, 1:16023, 2016.

[138] Charles Kittel. Physical theory of ferromagnetic domains. *Reviews of Modern Physics*, 21:541–583, 1949.

[139] Ziwei Dou, Sei Morikawa, Alessandro Cresti, Shu-Wei Wang, Charles G. Smith, Christos Melios, Olga Kazakova, Kenji Watanabe, Takashi Taniguchi, Satoru Masubuchi, Tomoki Machida, and Malcolm R. Connolly. Imaging bulk and edge transport near the Dirac point in graphene Moiré superlattices. *Nano Letters*, 18(4):2530–2537, 2018.

[140] M. Mogi, R. Yoshimi, A. Tsukazaki, K. Yasuda, Y. Kozuka, K. S. Takahashi, M. Kawasaki, and Y. Tokura. Magnetic modulation doping in topological insulators toward higher-temperature quantum anomalous Hall effect. *Applied Physics Letters*, 107(18):182401, 2015.

[141] W. Li, M. Claassen, Cui-Zu Chang, B. Moritz, T. Jia, C. Zhang, S. Rebec, J. J. Lee, M. Hashimoto, D.-H. Lu, R. G. Moore, J. S. Moodera, T. P. Devereaux, and Z.-X. Shen. Origin of the low critical observing temperature of the quantum anomalous Hall effect in V-doped $(Bi, Sb)_2Te_3$ film. *Scientific Reports*, 6:32732, 2016.

[142] Masataka Mogi, Minoru Kawamura, Atsushi Tsukazaki, Ryutaro Yoshimi, Kei S. Takahashi, Masashi Kawasaki, and Yoshinori Tokura. Tailoring tricolor structure of magnetic topological insulator for robust axion insulator. *Science Advances*, 3(10), 2017.

[143] Di Xiao, Jue Jiang, Jae-Ho Shin, Wenbo Wang, Fei Wang, Yi-Fan Zhao, Chaoxing Liu, Weida Wu, Moses H. W. Chan, Nitin Samarth, and Cui-Zu Chang. Realization of the axion insulator state in quantum anomalous Hall sandwich heterostructures. *Physical Review Letters*, 120:056801, 2018.

[144] Jue Jiang, Di Xiao, Fei Wang, Jae-Ho Shin, Domenico Andreoli, Jianxiao Zhang, Run Xiao, Yi-Fan Zhao, Morteza Kayyalha, Ling Zhang, et al. Crossover of quantum anomalous Hall to topological Hall effect in magnetic topological insulator sandwich heterostructures. *arXiv preprint: 1901.07611*, 2019.

[145] T. Sakudo and H. Unoki. Dielectric properties of $SrTiO_3$ at low temperatures. *Physical Review Letters*, 26:851–853, 1971.

[146] H.-M. Christen, J. Mannhart, E. J. Williams, and Ch. Gerber. Dielectric properties of sputtered $SrTiO_3$ films. *Physical Review B*, 49:12095–12104, 1994.

[147] M. Itoh, R. Wang, Y. Inaguma, T. Yamaguchi, Y-J. Shan, and T. Nakamura. Ferroelectricity induced by oxygen isotope exchange in strontium titanate perovskite. *Physical Review Letters*, 82:3540–3543, 1999.

[148] Naoto Nagaosa, Jairo Sinova, Shigeki Onoda, A. H. MacDonald, and N. P. Ong. Anomalous Hall effect. *Reviews of Modern Physics*, 82:1539–1592, 2010.

[149] CuiZu Chang, MinHao Liu, ZuoCheng Zhang, YaYu Wang, Ke He, and QiKun Xue. Field-effect modulation of anomalous Hall effect in diluted ferromagnetic topological insulator epitaxial films. *Science China Physics, Mechanics & Astronomy*, 59(3):637501, 2016.

[150] Cui-Zu Chang and Mingda Li. Quantum anomalous Hall effect in time-reversal-symmetry breaking topological insulators. *Journal of Physics: Condensed Matter*, 28(12):123002, 2016.

[151] A. D. Kent, J. Yu, U. Rüdiger, and S. S. P. Parkin. Domain wall resistivity in epitaxial thin film microstructures. *Journal of Physics: Condensed Matter*, 13(25):R461–R488, 2001.

[152] L. J. van der Pauw. A method of measuring specific resistivity and Hall effect of discs of arbitrary shape. *Philips Technical Review*, 20(220), 1958.

[153] B. T. Matthias, T. H. Geballe, and V. B. Compton. Superconductivity. *Reviews of Modern Physics*, 35:1–22, 1963.

[154] Julian Eisenstein. Superconducting elements. *Reviews of Modern Physics*, 26:277–291, 1954.

[155] Jing Wang, Biao Lian, Xiao-Liang Qi, and Shou-Cheng Zhang. Quantized topological magnetoelectric effect of the zero-plateau quantum anomalous Hall state. *Physical Review B*, 92:081107, 2015.

[156] Takahiro Morimoto, Akira Furusaki, and Naoto Nagaosa. Topological magnetoelectric effects in thin films of topological insulators. *Physical Review B*, 92:085113, 2015.

[157] Andrew M. Essin, Joel E. Moore, and David Vanderbilt. Magnetoelectric polarizability and axion electrodynamics in crystalline insulators. *Physical Review Letters*, 102:146805, 2009.

[158] Liang Fu and C. L. Kane. Superconducting proximity effect and Majorana fermions at the surface of a topological insulator. *Physical Review Letters*, 100:096407, 2008.

[159] Xiao-Liang Qi, Taylor L. Hughes, and Shou-Cheng Zhang. Chiral topological superconductor from the quantum Hall state. *Physical Review B*, 82:184516, 2010.

[160] Xiao-Liang Qi and Shou-Cheng Zhang. Topological insulators and superconductors. *Reviews of Modern Physics*, 83:1057–1110, 2011.

[161] Jing Wang, Quan Zhou, Biao Lian, and Shou-Cheng Zhang. Chiral topological superconductor and half-integer conductance plateau from quantum anomalous Hall plateau transition. *Physical Review B*, 92:064520, 2015.

[162] Ettore Majorana. Teoria simmetrica dell'elettrone e del positrone. *Nuovo Cimento*, 14:171, 1937.

[163] Frank Wilczek. Majorana returns. *Nature Physics*, 5:614, 2009.

[164] Biao Lian, Xiao-Qi Sun, Abolhassan Vaezi, Xiao-Liang Qi, and Shou-Cheng Zhang. Topological quantum computation based on chiral Majorana fermions. *Proceedings of the National Academy of Sciences*, 115(43):10938–10942, 2018.

Appendix A

Specifications of SPM tips

The specifications of the SPM tips used in this thesis are listed in this appendix. The parameters are from the data sheets provided by the manufacturers, and may be slightly different for individual tips.

1. Nanosensors PPP-MFMR: tips used in the measurements described in Sec. 5.3.

   - Parameters:

   Table A.1: Nanosensors PPP-MFMR

Property	Nominal value	Range
Resonance frequency (kHz)	75	45 - 115
Force constant (N/m)	2.8	0.5 - 9.5
Thickness (µm)	3.0	2.0 - 4.0
Mean width (µm)	28	20 - 35
Length (µm)	225	215 - 235
Tip cone height (µm)	N/A	10 - 15
Tip cone radius (nm)	N/A	< 30

   - Materials:
     The cantilever and tip are made of n^+ silicon with a resistivity $\sim$ 0.01-0.02 Ω·cm. An Al coating is deposited on the detector side of cantilever for enhancing the reflectivity. A hard magnetic coating (CoCr alloy with a high fraction of Co) is deposited on the tip side. The nominal parameters for the magnetic coating are coercivity $\sim$ 300 Oe, remanence magnetisation $\sim$ 300 emu/cm^3, and effective magnetic moment $\sim$ 10-13 emu.

2. Nanoworld NCHPt: tips used in the measurements described in Sec. 5.4.

- Parameters:

Table A.2: Nanoworld NCHPt

Property	Nominal value	Range
Resonance frequency (kHz)	320	250 - 390
Force constant (N/m)	42	21 - 78
Thickness (µm)	4.0	3.5 - 4.5
Mean width (µm)	30	25 - 35
Length (µm)	125	120 - 130
Tip cone height (µm)	N/A	10 - 15
Tip cone radius (nm)	N/A	< 25

- Materials:
  The cantilever and tip are made of monolithic silicon which is highly doped to dissipate static charges. A layer of Pt/Ir alloy with thickness ~ 23 nm is deposited on both sides of the cantilever.

3. Nanoworld CDT-FMR: tips used in the measurements described in Sec. 5.4.

- Parameters:

Table A.3: Nanoworld CDT-FMR

Property	Nominal value	Range
Resonance frequency (kHz)	105	80 - 130
Force constant (N/m)	6.2	3 - 11.4
Thickness (µm)	3.0	2.5 - 3.5
Mean width (µm)	27.5	22.5 - 32.5
Length (µm)	225	220 - 230
Tip cone height (µm)	N/A	10 - 15
Tip cone radius (nm)	N/A	100 - 200

- Materials:
  The cantilever and tip are made of monolithic silicon which is highly doped to dissipate static charges. An Al coating is deposited on the detector side of cantilever for enhancing the reflectivity of the laser beam. A conductive diamond coating is deposited on the tip side for enhancing the hardness of the tip. The conductive diamond coating consists of a $\sim$ 100-nm-thick polycrystalline diamond which is highly doped with boron, resulting in a macroscopic resistivity of 0.003-0.005 $\Omega\cdot$ cm.

Appendix B

Instrument information and experiment details

B.1 SPM measurements in Chapter 5

The SPM measurements in Chapter 5 were mostly carried out in an Oxford Instruments Kelvinox MX100 dilution refrigerator, except for the SHPM measurements, which was performed in Prof. Simon Bending's lab in the University of Bath.

The Kelvinox MX100 dilution refrigerator has a base temperature of 30 mK (measured at the mixing chamber stage) and a superconducting magnet that can generate up to 8 T out-of-plane magnetic field. The probe of this dilution refrigerator is equipped with a home-made scanning probe system, which has a tip holder that allows users to load various kinds of tips for different SPM experiments, such as AFM, EFM, MFM, and SGM. The coarse and fine adjustment of the position of the SPM system were controlled by the Attocube ANC150 Piezo Step Controller and ANC200 Piezo Scan Controller, respectively. The Specs Nanonis OC4, SC4, and RC4 were implemented for supplying the AC and DC voltage to the piezoelectric scanners of the SPM system as well as controlling the communication between the instruments and the PC. The cantilever of the tip can be shaken by a piezoelectric actuator ("dither"). The oscillation of the cantilever can be probed by the heterodyne interferometry using the laser generated from an ARP100 laser/detector module. Hence, any phase change in the oscillation due to tip-sample interactions can be demodulated, which then can be used to produce the contrast associated with the interactions and displayed as SPM images.

The cryostat used for the SHPM experiments is an Oxford cryostat with a base temperature of 5 K and a superconducting magnet that can generate up to 7 T out-of-plane magnetic field.

B.2 Transport measurements in Chapter 5

The transport measurements described in Chapter 5 were performed in several different cryostats using a variety of measurement setups.

The transport measurements at millikelvin temperatures were carried out in the same Oxford Instruments Kelvinox MX100 dilution refrigerator used for the SPM experiments. Standard lock-in techniques were performed using two Signal Recovery 7265 DSP lock-in amplifiers and one EG&G Instruments 7220 DSP lock-in amplifier. In some cases, a Stanford Research Systems SR560 voltage pre-amplifier and a SR570 current pre-amplifier were used in the measurement circuits to reduce the noise level.

The transport measurements above 1.5 K in Chapter 5 were carried out in three different cryostats: the aforementioned Kelvinox MX100, the Oxford cryostat in the University of Bath and an Oxford cryostat in our lab. The transport measurements carried out in Kelvinox MX100 were performed using the same instruments as introduced above. For the transport measurements carried out in the other two cryostats, the lock-in amplifiers used were the Stanford Research Systems SR830 DSP lock-in amplifiers. The Oxford cryostat in our lab has a base temperature of 1.4 K and a superconducting magnet that can generate up to 8 T out-of-plane magnetic field.

The backgate voltage for the devices in all measurements was applied by a Keithley 2400 Source Measure Unit (SMU), which has a maximum output of 200 V.

B.3 Transport measurements in Chapter 6

The transport measurements in Chapter 6 were performed in a Bluefors LD400 cryogen-free dilution refrigerator, which has a base temperature of 10 mK (measured at the mixing chamber stage) and a superconducting magnet that can generate up to 12 T out-of-plane magnetic field. The highest magnetic field sweep rate allowed is 6 T/hr. A separate sample thermometer was installed near the sample holder to accurately measure the actual temperature of the sample space.

Standard lock-in techniques and multi-terminal measurements were performed with two Zurich Instruments MFLI lock-in amplifiers and one Signal Recovery 7265 DSP lock-in amplifier. In most cases, the Stanford Research Systems SR560 voltage pre-amplifiers and the SR570 current pre-amplifier were used in the measurement circuits to reduce the noise level. The backgate voltage for the devices was supplied by a Keithley 2400 SMU with a maximum output of 200 V.

In the AC + DC measurements described in Chapter 6, a National Instruments CompactDAQ system was employed to supply the DC voltage.